Synthesis-Structure-Property Relationships in Lead-Free Piezoelectric Materials

Deepam Maurya

Dissertation submitted to the faculty of the Virginia Polytechnic Institute and State University in partial fulfillment of the requirements for the degree of

Doctor of Philosophy

In

Materials Science and Engineering

Shashank Priya, Committee Chair

Dwight Viehland

Alex Aning

Carlos Suchicital

Jeane Heremans

Blacksburg, VA 24061

November, 12th 2012

Keywords: Lead-free, piezoelectric, ferroelectric, domain, transmission electron microscopy, neutron diffraction, X-ray diffraction

Synthesis-Structure-Property Relationships in Lead-Free Piezoelectric Materials

Deepam Maurya

Abstract

Piezoelectric materials find applications in multitude of devices such as sensors, actuators and energy harvesters. However, most of these piezoelectric materials utilize lead-based systems which are becoming serious problem owing to the restrictions imposed by regulatory agencies across the globe. In the functional ceramics community, currently there is no problem more important than to find a replacement for lead-based piezoelectrics used for actuators. The electromechanical properties required for actuators (high piezoelectric constant, high coupling factor, low loss, and high transition temperatures) for known lead-free compositions are, however, far inferior to those of lead-based systems. There are three lines of research for addressing this fundamental problem – (i) search for new systems through a combination of theory-based prediction followed by experimental effort (doping, solid solutions having a morphotropic (M) or polymorphic (P) phase boundary (PB), (iii) stabilization of metastable phases or finding the high temperature triclinic systems, and (iii) improving the properties of known compositions through microstructure optimization, domain engineering and multilayering. All these approaches are challenging and require innovation to make a significant impact on the current state-of-the-art. In this thesis, the later line of research was focused which is promising for near future applications, as it builds upon the known material systems with high depoling temperatures that have demonstrated the potential to be practical.

In the first chapter, a novel method for the synthesis of lead-free (1-x)($Na_{0.5}Bi_{0.5}$)TiO_3 – x$BaTiO_3$ piezoelectric ceramics was investigated. Initially, multiple compositions around morphotrpic phase boundary (MPB) were synthesized to identify the optimum composition 0.93$Na_{0.5}Bi_{0.5}TiO_3$-0.07$BaTiO_3$ (NBT-BT) for electromechanical effect. The new synthesis method starts with the synthesis of $Na_2Ti_6O_{13}$ (NTO) whiskers which are then transformed into lead-free NBT-BT ceramics. Synthesis of NTO whiskers was performed using molten salt synthesis (MSS) method. Tape casting method was used to align the whiskers in base matrix powder and subjected to various processing temperatures to elucidate the microstructure and texture evolution. For this, scanning electron microscopy (SEM), high resolution transmission electron microscopy (HRTEM), atomic force microscopy (AFM) and energy dispersive spectroscopy (EDS) analysis were used as principal tools. The sintering process can be understood by dividing it into three stages, namely (i) transformation of monoclinic whiskers in to NBT-BT perovskite phase through topochemical reaction (<800^oC), (ii) localized sintering confined on single whisker (800-1050^oC), and (iii) liquid phase sintering as densification and grain growth occurs in the whole matrix (>1050^oC). The concentric growth ledges observed on grain surfaces were found to be preferably confined on the corners of cubical grains indicating <111> growth direction. The Lotgering factor (f_{100}) for the sintered matrix was found to decrease with increase in sintering temperature. The longitudinal piezoelectric constant (d_{33}) of samples sintered for 20h at 1175^oC, 1200^oC and 1225^oC was measured to be ~153 pC/N, ~216 pC/N and ~180 pC/N, respectively.

Next, a novel method was developed for the synthesis of nanostructured lead-free ferroelectric NBT-BT whiskers with high aspect ratio using NTO as a host structure. High energy x-ray diffraction coupled with atomic pair distribution function (PDF) and Raman

scattering analyses were used to confirm the average structure of lead-free NBT-BT whiskers as rhombohedral, i.e. a ferroelectricity enabling type. The HRTEM analysis revealed local monoclinic-type structural distortions indicating a modulated structure at the nanoscale in the MPB composition of lead-free NBT-BT whiskers. The structural rearrangement during the synthesis of lead-free NBT-BT whiskers was found to occur via translation of edge shared octahedra of NTO into a corner sharing coordination. The high temperature morphological changes depicting disintegration of isolated whiskers into individual grains due to higher grain boundary energy have been found to occur in a close analogy with Rayleigh-type instability.

In lead-based ABO_3 compounds, with B-site disorder, the origin of enhancement of piezoelectric properties near MPB has been associated with the presence of an intermediate monoclinic/orthorhombic state that bridges the adjacent ferroelectric rhombohedral and tetragonal phases. However, the origin of high piezoelectric response in lead-free ABO_3 compounds with A-site disorder has not been conclusively established. In this thesis, a microscopic model derived from comparative analyses of HR-TEM and neutron diffraction was developed that explains the origin of high piezoelectric response in lead – free MPB compositions of NBT-BT. Direct observation of nanotwins with monoclinic symmetry confirmed the presence of an intermediate bridging phase that facilitates a pathway for polarization reorientation. Monoclinic distortions of an average rhombohedral phase were attributed to localized displacements of atoms along the non-polar directions. These results provide new insight towards design of high performance lead – free piezoelectric materials.

Microstructure and domain structure play dominant role towards controlling the magnitude of piezoelectric coefficient and hysteretic losses in perovskites. Brick-wall like microstructure with large grain size and small domain size can provide significant enhancement

in the magnitude of piezoelectric coefficient. A synthesis technique for lead-free piezoelectric NBT-BT system that can provide $[001]_{pc}$/$[012]_{Rh}$ grain oriented ceramics with large grain size and an electrical poling technique that results in smaller domain size will have significant impact on the electromechanical response. In this research, a synthesis technique was developed and the processing variables that play deterministic role in achieving the large grain brick-wall like microstructure were expplained. Interfaces in the microstructure were found to be coherent at the atomic scale facilitating the domain wall motion with applied electric field. The piezoelectric response was found to increase monotonously with the incease in the degree of texturing and optimized microstructure was found to provide 200% enhancement in the magnitude of piezoelectric coefficient as compared to its random form.

In order to understand mechanim of enhanced piezoelectric response in textured NBT-BT, *in-situ* neutron diffraction experiments revealed that characteristically different structural responses are induced in textured and randomly-oriented NBT-BT ceramics upon application of electric fields (*E*), which are likely related to the varying coherence lengths of polar nano regions and internal stresses induced by domain switching.

In conjunction to focus on NBT-BT, new lead-free piezoelectric materials with enhanced piezoelectric response were synthesized. This study provides fundamental understanding of the enhanced piezoelectric instability in lead-free piezoelectric (1-x) $BaTiO_3$-x$A(Cu_{1/3}Nb_{2/3})O_3$ (A: Sr, Ba and Ca and x = 0.0-0.03) solid solutions. These compositions were found to exhibit large d_{33} of ~330 pC/N and electromechanical planar coupling constant (k_p)~ 46% at room temperature. The piezoelectric instability in these compositions was found to increase with x despite monotonous decrease in the long range polar ordering. High energy X-ray diffraction coupled with *PDF*s indicated increase in local polarization. Raman scattering analysis revealed

that substitutions on A and B-site both substantially perturbed the local octahedral dynamics and resulted in localized nano polar regions with lower symmetry. These localized polar distortions were found to persist much above the Curie temperature (T_c). Polarization – electric field (*P-E)* hysteresis loop analysis indicated presence of the internal bias that was found to be correlated with the formation of polar defects. This defect structure was found to modulate the domain structure resulting in nano domains and broad domain walls with higher mobility as revealed through analysis from HR-TEM and piezoresponse force microscopy (PFM). The presence of nano domains and local structural distortions smears the Curie peak resulting in diffuse order-disorder type phase transitions. The electron paramagnetic resonance (*EPR*) investigations revealed that substitution of Cu^{2+} takes place on octahedral sites that are distorted due to Jahn-Teller effect. The A-sites were distorted by substitution of Sr and Ca on Ba-site possessing different ionic radii and electronegativity. The effect of these distortions on the variations in physical property was modeled and analyzed within the context of nanodomains and phase transitions.

As an application, the solid solution with nominal composition of $(1\text{-}x)BaTiO_3$-$xBa(Cu_{1/3}Nb_{2/3})O_3$ (BCN) (x = 0, 0.025) was synthesized by conventional mixed oxide route, followed by compositional modification with varying concentration of Sn, as given by the formulation: $0.975\ BaTi_{1-y}Sn_yO_3 - 0.025\ Ba(Cu_{1/3}Nb_{2/3})O_3$ (y = 0.05, 0.06, 0.075, 0.1). Room temperature XRD patterns showed decrease in tetragonality of BT after modifying with BCN (BT-BCN). Modifications with Sn lead to further decrement in tetragonality and the room temperature structure became cubic at 6.0 at% doping level. The decrement in tetragonality was accompanied by lowering of T_c. BT-BCN doped with 6 and 7.5 at% Sn were found to exhibit diffuse phase transition accompanied by high dielectric constant $\geq$ 7000, low loss tangent $\leq$ 1%

and grain size in the submicron regime (≤ 1 μm). These compositions were found to be promising for Y5V type multilayer ceramic capacitors (MLCCs).

Lastly, the dielectric and ferroelectric responses of compositionally graded bilayer and trilayer composites consisting of BT and $0.975BaTiO_3$-$0.025Ba(Cu_{1/3}Nb_{2/3})O_3$ (BT-BCN) were investigated. Two types of graded bilayer samples were synthesized, one with same thickness of BT and BT-BCN while other with different layer thicknesses. The graded trilayer sample consisted of BT layer sandwiched between two BT-BCN layers of equal thickness. SEM and TEM images showed a sharp interface with needle-shape domains across the interface. The domain size on BT-side was found to be larger than that on BT-BCN-side. The temperature dependence of dielectric response for all composite systems was found to exhibit shifting of characteristic Curie peak compared to constituent material which was associated to coupling between layers. Moreover, the differences in grain size, tetragonality, domain mobility of each layer was found to perturb the electrical response of composite. The polarization mismatch between uncoupled BT and BT-BCN established internal electric field in composite specimen and defined new polarization states in each layer by perturbing free energy functional of the composite specimen. Dynamic hysteresis behaviors and power-law scaling relations of all specimens were determined from *P–E* field hysteresis loop measurements as a function of frequency. All systems were found to exhibit similar dynamic scaling relationships. Hysteresis area $<A>$, P_r and E_C decreased with increasing frequency due to delayed response, but increased with increasing applied electric field due to enhancement of driving force. Trilayer system was found to exhibit strong internal-bias field and double hysteresis behavior. The coupling effect resulting due to polarization mismatch between layers had substantial influence on the dynamic hysteresis behavior and power-law scaling relations.

Acknowledgements

I take this opportunity to thank all the people who have helped me and would remain a source of inspiration.

Firstly, I am deeply indebted to my advisor Prof. Shashank Priya for invaluable discussions, great suggestions and encouragement during the entire course of this thesis. He always taught me to aim high and embrace scientific challenges with passion and enthusiasm. His endless quest to perform highest quality research has made a deep impression on me. I hardly know any person who could lead so much by example and I feel myself lucky to have such a role model. His capability of reducing complexities to simpler forms has enormously helped me in the smooth progress of this research. Again, I express my profound sense of gratitude to my teacher and advisor.

I would like to express my profound thanks to Prof. Dwight Viehland, Prof. Alex Aning, Prof. Carlos Suchicital and Prof. Jeane Heremans for serving in my committee and their effort in evaluating my dissertation. I am very thankful for their help, useful discussions and suggestions. Thanks are also due to Prof. W. T. Reynolds for helpful discussions. I am very thankful to Prof. M. Murayama for helpful discussion and training with TEM. I would like to express sincere thanks to Prof. Valeri Petkov, Department of Physics, Central Michigan University, Mount Pleasant, for his valuable help and discussion with high energy x-ray diffraction, synchrotron x-ray diffraction and atomic pair distribution function analysis. I am very thankful to Dr. Abhijit Pramanick, Chemical and Engineering Materials Division, Oak Ridge National Lab, for fruitful discussions and kind help with neutron diffraction measurements. I would like to express my gratitude to Dr. Ashok Kumar, National Physical Laboratory, New Delhi, India, for his help with Raman spectroscopy. I am very thankful to Prof. J. E. Mahaney, Edward Via College of Osteopathic Medicine, Blacksburg, for his help with electron paramagnetic resonance spectroscopy. I would like to thank Prof. Shujun Zhang, Materials Science and Engineering, The Pennsylvania State University, University Park, for his kind help with the dielectric measurements. I would like to express my gratitude to Prof. Toshihiko Tani, Toyota Technological Institute, for useful discussions and suggestions related to synthesis of grain oriented ceramics. I would like to express my gratitude to Prof. Haosu Luo, Shanghai Institute of Ceramics, China, for providing me opportunity to learn top seeded solution single crystal growth.

I am very thankful to Dr. C. –W. Ahn, Dr. C. -S. Park, Dr. V. Bedekar, Dr. Y. Tadesse, Dr. K.-H. Cho, Dr. Y. Yan for their help and discussions. I have been really very fortunate to have lab mates and friends like Su-Chul, Keyur, Natthapong, Alex, Ron, Shashaank, Yuan, Dragan, Tony, Yu, Ashok, Daniel and Elliot. I am thankful to Dr. N. Monsegue, John Mcintosh and William Wu for their help with TEM training and sample perpetration. I am thankful to Stephen McCartney for providing scanning electron microscopy training at NCFL, Virginia Tech.

It is beyond my words to thank my dear parents Mr. Siyaram Maurya and Mrs. Asha Maurya for the opportunity they have provided me and for the love, affection and unconditional support bestowed on me throughout my academic career. I would like to express my profound gratitude to my wife Ananya for her patience, encouragement and unconditional support. I sincerely thank to my sisters and younger brothers for their continuous support. At this juncture, I can't forget the support and inspiration provided by my late grandparents. My deepest gratitude will always be there for my mentors who have shown right direction.

Finally, I would like to thank the financial support from National Science Foundation, Office of Basic Energy Science, Department of Energy, Fundamental R&D Program for Core Technology of Materials funded by the Ministry of Knowledge Economy, Republic of Korea.

Table of contents

List of Figures

List of tables

List of symbols and acronyms

Symbols

$Ba_{Ba}^{\times}$	Ba^{2+} sitting on Ba-site with neutral effective charge
Cu_{Ti}''	Cu^{2+} sitting on Ti^{4+} site
d_{33}	longitudinal piezoelectric constant
E_c	Coercive field
ε	Relative permittivity
ε_o	Permittivity of free space
F_L	Landau potentials
F_G	Ginzburg energy
γ_b	Grain boundary energy
γ_s	Surface energy
γ_t	Domain wall energy density
ΔG^*	Energy barrier for 2D nucleation
h	Height of the growth step
j	Current density
j_L	Leakage current density
j_D	Displacement current density
k_p	Planar electromechanical coupling factor
k_B	Boltzman constant
λ_o	The average distance between two growth steps
λ	Wavelength of radiation
μ_m	Bohr magneton
μ_n	Nuclear magneton
$Nb_{Ti}^{\bullet}$	Nb^{5+} sitting on Ti^{4+} site
P_s	Saturated polarization
P_r	Remnant polarization
tanδ	Loss tangent factor
T_c	Curie temperature
T_d	Depoling temperature
T_m	Temperature of maximum relative permittivity
$V_o^{\bullet\bullet}$	Oxygen vacancy

List of acronyms

AFM	Atomic force microscopy
BT-ACN	$BaTiO_3$-$A(Cu_{1/3}Nb_{2/3})O_3$; A = Ba, Sr and Ca
BTBCN	$BaTiO_3$-$Ba(Cu_{1/3}Nb_{2/3})O_3$
BIT	$Bi_4Ti_3O_{13}$
CCD	Charge coupled device
CIP	Cold isostatic press
DPT	Diffuse phase transition
EBSD	Electron backscattered diffraction
EDS	Energy dispersive spectroscopy
EPR	Electron paramagnetic resonance
FE-PE	Ferroelectric-paraelectric
FeRAM	Ferroelectric random access memory
FeMFET	Ferroelectric metal oxide field effect transistor
FFT	Fast Fourier transform
FIB	Focused ion beam
GSAS	General Structure and Analysis System
HAADF	High angle annular dark field
HR-TEM	High resolution transmission electron microscopy
IPF	Inverse pole figure
JCPDS	Joint Committee on Powder Diffraction Standards
KBT	$K_{0.5}Bi_{0.5}TiO_3$
KNN/NKN	$K_{0.5}Na_{0.5}NbO_3$
KNN-LF4:	$(K_{0.44}Na_{0.52}Li_{0.04})(Nb_{0.86}\ Ta_{0.10}\ Sb_{0.04})O_3$
LPS	Liquid phase sintering
LO	Longitudinal optic
ME	Magnetoelectric
MLCC	Multilayer ceramics capacitor
MPB	Morphotropic phase boundary
NBT-BT	$Na_{0.5}Bi_{0.5}TiO_3$-$BaTiO_3$
NTO	$Na_2Ti_6O_{13}$
PDF	Pair distribution function
P-E	Polarization–electric field
PFM	Piezoresponse force microscopy
PNR	Polar nano region
PZT	$Pb(Zr_{0.52}Ti_{0.48})TiO_3$
ME	Magnetoelectric
PZN-PT	$Pb(Zn_{1/3}Nb_{2/3})O_3$–$PbTiO_3$
PMN-PT	$(PbMg_{1/3}Nb_{2/3})O_3$-$PbTiO_3$
RTGG	Reactive templated grain growth

SAED	Selected area electron diffraction
SBTBCN	Sn doped $BaTiO_3$-$Ba(Cu_{1/3}Nb_{2/3})O_3$
SEM	Scanning electron microscopy
SNS	Spallation neutron source
STEM	Scanning transmission electron microscopy
TSSG	Top seeded solution growth
TEM	Transmission electron microscopy
TGG	Templated grain growth
TCC	Temperature coefficient of capacitance
TO	Transverse optic
XRD	X-ray diffraction
Y5V	Y5V are class 2 ceramics capacitor with temperature range of −30 to +85 °C and % capacitance Change +22% to -82%

Chapter-1 Introduction

1.1 Piezoelectricity

Piezoelectricity was discovered in 1880 by Jacques and Pierre Curie. Since that discovery, piezoelectric effect has been sucessfully utilized across industry and academia. Piezoelectric materials find a wide range of applications in our daily lives like gas ignitors, microphones, speakers and ink jet printer etc. to various cutting edge technologies including sonar, medical ultrasound trasducers and energy harvestors[1].

The prefix 'Piezo' was derived from Greek word for 'press' or 'sqeeze'[2]. The piezoelectric effect is considered as linear interaction between mechanical and electrical systems in non-centric crystals. There are two types of piezoelectric effect namely 'direct piezoelectric effect' and 'converse piezoelectric effect'. The direct piezoelectric effect implies the generation of electric charge under applied stress; however, converse piezoelectric effect is the generation of mechanical strain in response to the applied electric field. The basic equations describing piezoelectric effects are [3,4]:

$$D_i = d_{ijk}X_{jk} + \varepsilon_{il}^{T}E_l \quad \text{(Direct piezoelectric effect)} \tag{1.1}$$

$$x_{ij} = s_{ijkl}^{E}X_{kl} + d_{mij}E_m \text{ (Converse piezoelectric effect)} \tag{1.2}$$

where X_{jk} and X_{kl} are the stress applied to a piezoelectric material, D_i is the induced charge density, E_l and $E_m$are the applied electric field, x_{ij} is the strain developed, ε_{il}^{T} is the dielectric constant (permittivity) at constant stress, and s_{ijkl}^{E} is the material compliance at constant electric field. Both d_{ijk} and d_{mij} are the piezoelectric coefficients of the third rank tensors with units of C/N and m/V, respectively. These equations are based on Einstein reduced tensor notation.

Generally, piezoelectric equations use reduced-suffix notation for the piezoelectric coefficients [4]:

$$D_i = d_{im} X_m \tag{1.3}$$

$$x_m = d_{mi} E_i \tag{1.4}$$

where i =1,2,3 and m = 1, 2, 3,…….6. As strain and stress tensors are symmetric, the piezoelectric coefficient tensor is also symmetrical with respect to the same indices, i.e. $d_{im} = d_{mi}$. The equations (1.3) and (1.4) describe directional properties which are usually specified with subscripts to identify the condition of their determination [5], e.g. d_{33} indicates the induced polarization generated in direction 3 (parallel to the direction in which piezoelectric materials is polarized) under the application of stress in direction 3, or the induced mechanical strain in direction 3 when electric field is imposed in the same direction. Another important parameter for characterization of piezoelectric materials is the electromechanical coupling factor (e.g. k_p, k_t and k_{33} etc.), which depicts the ability of materials to convert one kind of energy to another. The general form of coupling factor is defined as:

$$k = \sqrt{\frac{Stored\ electrical\ energy}{Supplied\ mechanical\ energy}} \tag{1.5}$$

or

$$k = \sqrt{\frac{Stored\ mechanical\ energy}{Supplied\ electrical\ energy}} \tag{1.6}$$

The value of *k* is always less than unity due to incomplete conversion of energy. The expression of k depends on the dimensions of the specimen. For a thin disc of piezoelectric material, the planar coupling factor (k_p) is measured. The values of k_p depicts the coupling

between an electric field applied parallel to the direction in which the piezoelectric specimen is polarized (direction 3) and the mechanical effects that produce the radial vibrations (direction 1 and 2). Generally, piezoelectric materials having high values of *d* coefficient and *k* factor are desired for actuator applications.

1.2 Ferroelectricity

Ferroelectric materials possess spontaneous electric polarization P_s, which can be switched under applied field. Every dielectric material cannot be ferroelectric. Ignoring translation repetitions, the crystals can be classified in to 32 point groups. There are 21 point group which do not have a center of symmetry. Out of these 21 point groups, 20 were found to show piezoelectric effect. Among those a group of materials having temperature dependent spontaneous polarization, called pyroelectric materials. A sub group of pyroelectric materials is *ferroelectric materials* which display switchable spontaneous polarization.

The spontaneous polarization (P_s) in ferroelectrics can be reoriented between two or more equilibrium states under the applied electric field [6]. Ferroelectric materials possess crystallographically allowed directions of spontaneous polarizations called polar axis. Moreover, the region having uniform polarization is called ferroelectric domain [7]. These domains are formed to minimize the electrostatic energy of depolarizing field and elastic energy associated with mechanical constraints produced upon cooling through phase transitions [7]. The interface between two domains is called a domain wall.

As mentioned above, the most important characteristic of ferroelectric materials is polarization reversal by applied electric field [3]. A typical P-E hysteresis loop in ferroelectrics is depicted in Figure 1.1. When the field is small, the polarization increases linearly with the field.

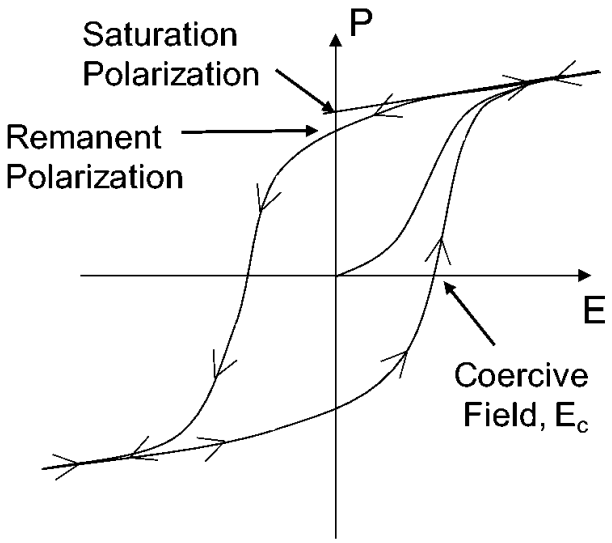

Figure-1.1 A typical P-E hysteresis loop displayed in ferroelectric materials

This is mainly due to field induced polarization, because the field is not large enough to cause orientation of the domains. On further increasing the field, the polarization increases nonlinearly with increasing field, because all domains start to orient in the direction of field. At high field, polarization will reach a state of saturation in which most domains are aligned in the direction of applied field to achieve a mono-domain state. The extrapolation of the linear segment of the curve at high field to the polarization axis gives the value the spontaneous polarization (P_s). However, in polycrystalline materials all domains in various grains cannot be aligned in direction of electric field and the true spontaneous polarization equal to that of single domain state cannot be achieved. In this case, the P_s value displayed in Fig. 1.1 is more correctly termed as 'saturated polarization' [3]. Moreover when the external field is reversed, some domain cannot return to

original state giving rise to remanent polarization (P_r) at zero electric field. The remnant polarization can be removed by further applying electric field in opposite direction and the critical field require for this is called coercive field 'E_c'. On further increasing electric field in negative direction, all domains will be aligned in this negative direction and the cycle can be completed by switching the field direction gain.

With the increase in temperature (T), the spontaneous polarization of a typical ferroelectric generally decreases. If the polarization suddenly becomes zero at some critical temperature (Curie temperature, T_c) [6], the system is said to have first order phase transition. On the other hand if value of spontaneous polarization decreases continuously with increase in temperature, the system is characterized by second order phase transition. When the system cools down through Curie temperature, structural transformation occurs and the system loses the center of symmetry and becomes ferroelectric with more than one possible polarization state as depicted in Figure 1.2 (a) by two minima separated by a potential energy barrier ΔG[8]. However, in paraelectric state ($T > T_c$) only one minimum is available denying the presence of switchable spontaneous polarization as shown in Figure 1.2 (c).

At the phase transition temperature, the dielectric, elastic, optical and thermal properties show anomalies [7]. The temperature dependence of a dielectric depicts very high value of relative permittivity at Curie temperature. The high dielectric permittivity in the vicinity of Curie temperature can also be explained by the free energy diagram by assuming reduced potential barrier among the equivalent polarization states. Due to which even a small external impact might induce a strong response from the dipoles, i.e. a high dielectric permittivity. However in different phase or temperature region, different mechanism may contribute to the dielectric permittivity. Sometimes, the high dielectric permittivity at T_c is shifted towards room

temperature by doping to get high relative permittivity at room temperature. The shifting of *T*c towards RT is often accompanied with an enhanced piezoelectric response suggesting the important role played by structural instability. However for piezoelectric materials high Curie

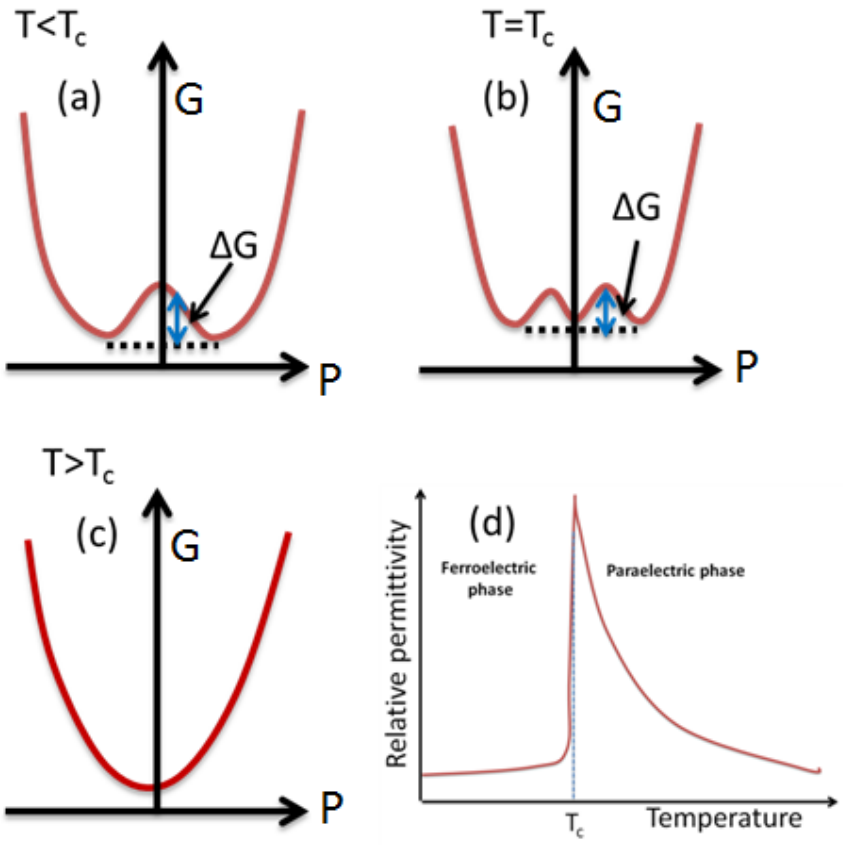

Figure-1.2 (a) –(c) Schematic of Free energy (G) versus polarization (P) plots at various temperatures in case of first order phase transitions [8], (d) Schematic of relative permittivity versus temperature for a normal ferroelectric

temperature is desired to get wide temperature range of operation. The structural instability has been considered an important factor in enhanced piezoelectric response in solid solutions near MPB. In this thesis, we therefore investigated the effect of structural instability on piezoelectric

response with respect to lead free materials. Next section provides description of MPB and the established mechanism for achieving enhanced piezoelectric response around MPB.

1.3 Piezoelectric materials with morphotropic phase boundary

Morphotropic phase boundary (MPB) is an intrinsic region of a phase diagram where two or more phases coexist. The solid solution of piezoelectric materials having MPB show enhanced piezoelectric and dielectric responses at this phase boundary. For example, the phase diagram of PZT with $PbTiO_3$ and $PbZrO_3$ as end members is provided in Figure 1.3 (a) [9]. The change in piezoelectric coefficients and electromechanical coupling constant of PZT with compositions near MPB are shown in Figure 1.3(b) and (c), respectively. Traditionally, the high piezoelectric response has been attributed to the enhanced number of polar axis in MPB composition [1, 9]. In a particular crystallographic symmetry, there are always a fixed number of equivalent polar axes in which the dipoles can be switched. The Ti-rich side of MPB in PZT possesses the tetragonal crystal symmetry with 6 equivalent [001] directions as polar axes. However on the Zr-rich side of the MPB, PZT with rhombohedral symmetry possesses 8 equivalent [111] directions as polar axes. Because at MPB two different phases coexist, the switching of polar axes in PZT has 14 available directions under applied *E*-field. This phenomenon was considered to be responsible for giving rise to high piezoelectric response at MPB. Noheda et al discovered the monoclinic phase between tetragonal and rhombohedral phase at MPB of PZT and thereby the phase diagram of PZT was modified by showing the monoclinic phase [10] (Figure 1.3(d)). Some well-known piezoelectric materials having MPB are $(1\text{-}x)Pb(Mn_{1/3}Nb_{2/3})O_3\text{-}xPbTiO_3$, $(1\text{-}x)Pb(Zn_{1/3}Nb_{2/3})O_3\text{-}xPbTiO_3$, and $(Na_{0.5}Bi_{0.5})TiO_3\text{-}BaTiO_3$, etc. High resolution X-ray diffraction investigations suggested that the major intrinsic contribution from both rhombohedral and tetragonal phase comes from the tilting of the P_s vectors [11]. The monoclinic phase with 24

permitted orientation states is expected to provide bridging polarization continuity leading to enhanced piezoelectric response [11].

In addition, it has been shown that enhanced piezoelectric response can be related to the presence of miniaturized ferroelectric domains (< 1μm) with high mobility [12]. Wada et al. [12] were able to synthesize miniaturized domain structure in $BaTiO_3$ single crystal by applying *E*-field along non polar $[111]_C$ direction through a poling process conducted above T_c. The high piezoelectric response (d_{31} = - 230 pC/N) observed in this system was attributed to the high density of domain walls [12]. Wang et al. [13] have performed theoretical calculations and have confirmed that the enhanced piezoelectric response in the specimen with miniaturized domains was correlated with domain wall broadening under applied *E*-field [13]. Further, the enhanced piezoelectric response in non-polar directions was also attributed to the domain wall broadening mechanism [13]. Building upon these prior studies, investigations were conducted on MPB composition of NBT-BT with respect to domain shape and size to understand the mechanism for enhanced piezoelectric response.

1.4 Relaxor ferroelectrics

The ferroelectric materials with compositionally induced disorder exhibit relaxor behavior. The diffused phase transition (DPT) and the frequency dependence of the Curie peak is the characteristics of relaxor-type materials. This kind of behavior has been observed in disordered ABO_3 type perovskite ferroelectrics, hydrogen bonded ferroelectrics and anti-ferroelectrics [14].

In perovskites the functional response is highly dependent on the A and B-site cation chemistry like charge, ionic radii, electronegativity. Bismuth strontium titanate $(Bi_{2/3x}Sr_{1-x})TiO_3$,

sodium bismuth titanate $Na_{0.5}Bi_{0.5}TiO_3$-$BaTiO_3$ and lead lanthanum zirconate titanate, $(Pb_{1-x}La_{2/3}x)(Zr_yTi_{1-y})O_3$(PLZT) are the typical examples of A-site substitutions. For the B-site substitution, the compounds lead magnesium niobate, $(PbMg_{1/3}Nb_{2/3})O_3$ (PMN) and lead scandium tantalate, $Pb(Sc_{1/2}Ta_{1/2})O_3$ (PST) are well-known relaxor materials discovered by Smolensky's group [15]. Figure-1.4 shows the temperature dependence of permittivity plot for PMN showing strong frequency dispersion of relative permittivity with broad Curie peak[16], which is in contrast to the purely displacive transition shown in Figure-1.2(d). In these materials, relative permittivity could reach up 20,000 near T_c and T_m shifts up with the increase in frequency. In relaxor-type ferroelectric materials polarization does not vanish immediately after T_m, but decreases gradually. Moreover, the relaxor-type ferroelectric materials do not exhibit macroscopic symmetry change during transition at T_m[14]. However at local length scales symmetry breaking polar nano regions (PNRs) or nano domains exist well above T_m strongly affecting the functional response [15]. These PNRs are also considered as ordered regions in disordered matrix [1]. The relaxor-type ferroelectrics exhibit high dielectric constant, large electrostrictive coefficients and temperature stability of functional response due to diffuse phase transition. The A-site disordered $Na_{0.5}Bi_{0.5}TiO_3$-based lead-free piezoelectric also exhibit DPT, however the origin of DPT is not clear. In this thesis, investigations were conducted on PNRs in NBT-BT in order to understand the DPT exhibited by these materials systems. Studies were also conducted on the newly developed BT-based piezoelectric materialsto establish a correlation among the phase transition behavior, domain structure and PNRs.

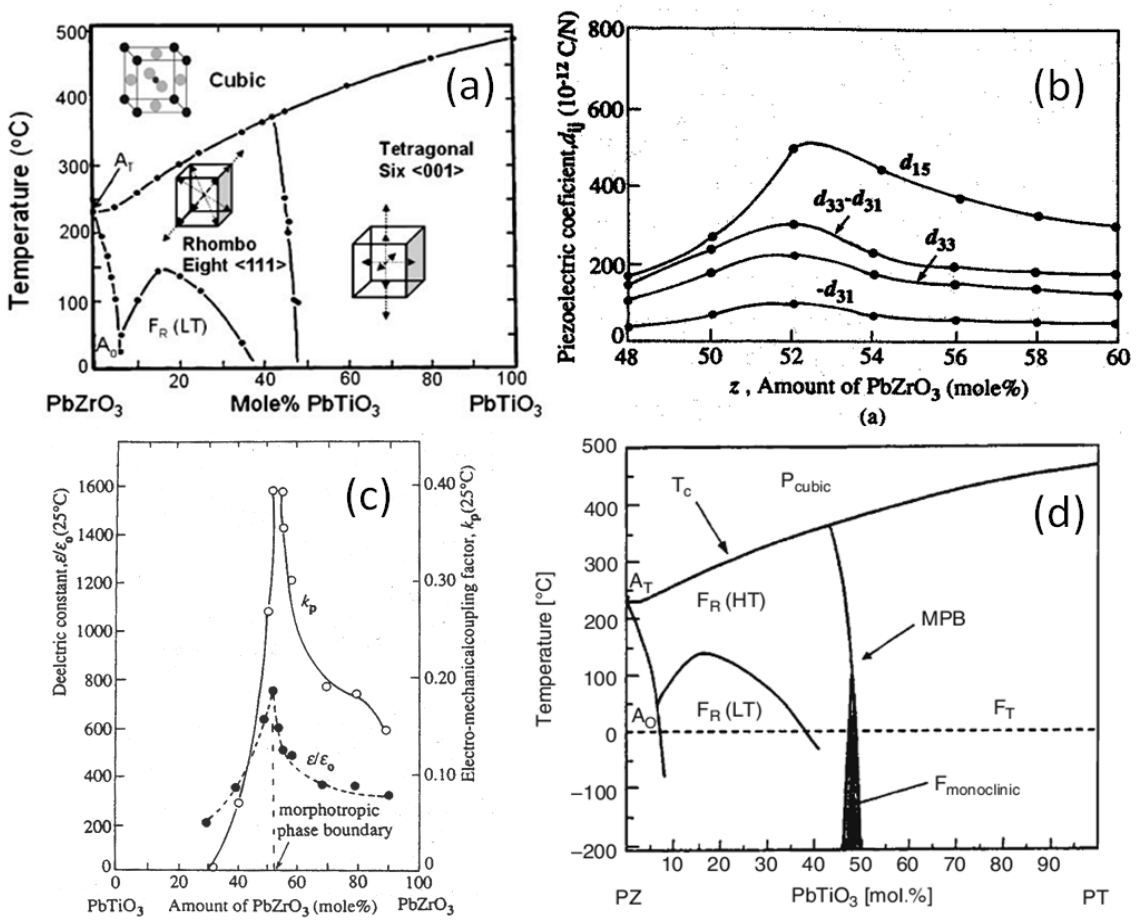

Figure-1.3 (a) Morphotropic phase boundary of PZT. Reprinted with permission from[9]. Copyright [1971], Academic press, an imprint of Elsevier. (b) Enhanced piezoelectric response at MPB. Reprinted with permission from[9]. Copyright [1971], Academic press, an imprint of Elsevier. (c) Enhanced electromechanical coupling factor and dielectric constant. Reprinted with permission from[9]. Copyright [1971], Academic press, an imprint of Elsevier. (d) Revised phase diagram of PZT showing monoclinic bridging phase [10]. Reprinted with permission from [16]. Copyright [2008], Springer Science + Business Media.

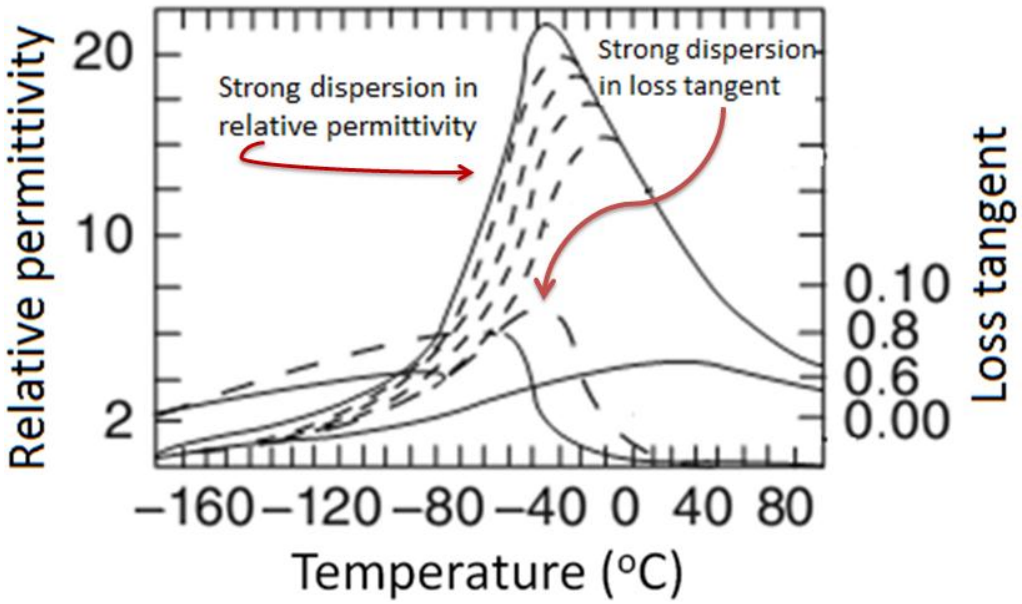

Figure-1.4 Temperature dependence of relative permittivity at various frequencies for $(PbMg_{1/3}Nb_{2/3})O_3$(PMN). Reprinted with permission from [16]. Copyright [2008], Springer Science + Business Media.

1.5 Lead-free piezoelectric materials

Piezoelectric materials find a myriad of applications in various cutting-edge technologies as discussed in the previous section. However, most of the currently used piezoelectric materials are lead-based and hence are matter of environmental concern. Recently, lead-free $Na_{0.5}Bi_{0.5}TiO_3$ (NBT) based piezoelectric materials have emerged as potential candidate to replace lead based piezoelectric materials.

NBT was discovered by Smolenskii[17] in 1961. It was reported that NBT is a relaxor ferroelectric with diffuse phase transition from rhombohedral to tetragonal phase between 200^{o}C and 320^{o}C and from tetragonal to cubic phase at 540^{o}C[18-21]. The temperature range of 200-320^{o}C has been subject of intense discussions related to the existence of antiferroelectric phase. Some researchers have suggested coexistence of rhombohedral and tetragonal phases in this

temperature range with PNRs [22]. However in a recent in-situ temperature dependent TEM investigation [23], it was reported that phase transition from ferroelectric rhombohedral to anti-ferroelectric orthorhombic phase proceeded via an antiferroelectric modulated phase consisting of orthorhombic sheets in a rhombohedral matrix in the temperature range from 200 - 300^{o}C. A second phase transition from O-T (Orthorhombic-Tetragonal) phase occurs near 320^{o}C, which corresponds to the antiferroelectric/paraelectric phase transition.

The solid solution of NBT with various tetragonal compounds has been investigated including $K_{1/2}Bi_{1/2}TiO_3$ (KBT), $BaTiO_3$, $CaTiO_3$, $SrTiO_3$ and $PbTiO_3$ [24-27]. Takenaka et al. [24] presented the phase diagram of NBT-BT showing the existence of MPB as shown in Figure 1.5. The d_{33}, k_{33} and loss tangent factors for NBT- 6% BT composition were found to be ~125 pC/N, 55% and 1.3%, respectively. However, T_c and ferroelectric to anti-ferroelectric transition temperature (T_d, also referred as depoling temperature) decreased at MPB. In comparison to lead-based perovskites, NBT has higher elastic modulus (~110 GPa vs 70 GPa) and lower density (6 g/cm^3) which makes it favorable for light-weight actuation applications [25]. Modification with $BiScO_3$ and $BiFeO_3$ lead to increment in T_c of NBT and NBT-BT up to 400^{o}C together with an improvement of remnant polarization (P_r)[28-30]. Li et al.[31] have reported the dielectric and piezoelectric response of $(1-x)(Na_{0.5}Bi_{0.5})TiO_3$-$xNaNbO_3$ ceramics. The samples in composition range of 0.01 to 0.02 were found to exhibit d_{33} ~ 80 – 88 pC/N. In a recent work, the effect of Na nonstochiometry in $Bi_{0.5}Na_{0.5-x}TiO_3$ ceramics was investigated [32]. The grain size was found to decrease with increase in Na nonstoichiometry. However, d_{33} was increased from 74 pC/N (T_d ~ 190^{o}C) at x =0.0 to 91 pC/N (T_d ~ 112^{o}C) at x=- 3.5 and then dropped with further Na deficiency. The effect of bismuth excess was studied on NBT-BT ceramics near MPB and compositions with x ≤0.505 were found to exhibit large P_r ~ 37.5-41.1 μC/cm^2 , d_{33} ~ 171-

176 pC/N at RT with moderate depoling temperature (T_d) ~ 85°C[33]. Wang et al[34] have studied (0.95-x)($Bi_{1/2}Na_{1/2}$)TiO_3-x($Bi_{1/2}K_{1/2}$)TiO_3-0.05$BaTiO_3$; x= 0 – 20 mol% compositions and specimen with x = 5 mol% was found to exhibit d_{33} ~ 148 pC/N, k_p~ 34 %, k_t~49.2 % and T_d ~125°C. However, these modifiers also increased the magnitude of coercive field (E_c) which

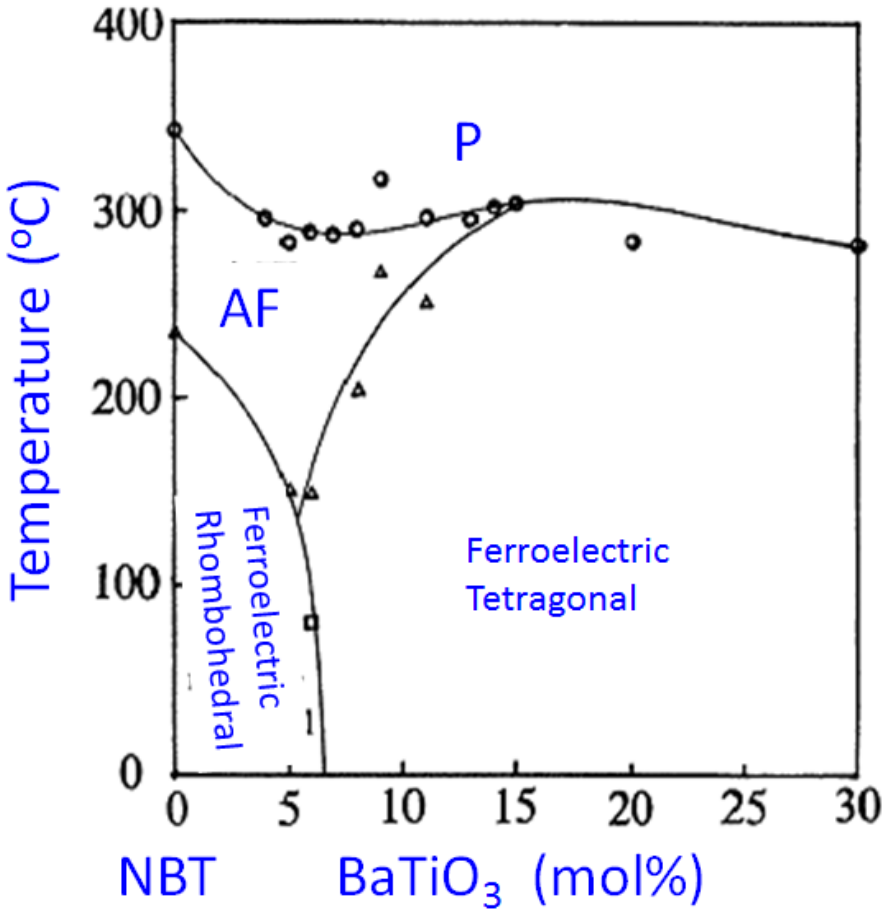

Figure 1.5 Phase diagram of (1-x)($Bi_{1/2}Na_{1/2}$)TiO_3-x$BaTiO_3$ (NBT-BT) reported by Takenaka et al. Reprinted with permission from [24]. Copyright [1991], The Japan Society of Applied Physics.

makes the poling difficult. Generally, E_c and T_d are lower in doped materials, however cobalt doping was found to enhance T_d by 20°C [35,36]. High piezoelectric properties in these Bi-based compounds are always accompanied with the lowering of T_d as shown in Fig. 1.6. Lower T_d

leads to unstable domains which are easy to switch and hence giving rise to higher piezoelectric constant [35]. Li doping of 4 at% in NBT-BT has been found to improve the piezoelectric coefficient as d_{33}= 176 pC/N, k_{33} = 0.6 and T_d= 171^{o}C[37]. In order to further improve the piezoelectric response without lowering the T_d various researchers have used reactive template (RTGG) and template (TGG) grain growth method [38-44]. The <100>$_c$ textured NBT-BT ceramics [40] were found to exhibit improved response given as: d_{33} ~ 241 pC/N, k_p ~ 41.2 % and k_t ~ 66.5% at RT with T_d ~ 115^{o}C.

Investigations on growth of lead-free single crystals in NBT-BT systems have shown that near MPB compositions congruently melt and can be grown by flux growth[45] and top seeded solution growth (TSSG) method[46]. Recently, d_{33} as high as 457 pC/N with k_{33} ~ 68.5 % was reported on Mn-doped NBT-BT single crystal grown by TSSG method. Piezoelectric properties of some NBT-based materials along with other lead-free piezoelectric materials are listed in Table 1.1. In order to demonstrate the practical feasibility, Chen et al. [47] have investigated the performance of high frequency ultrasonic transducers consisting of NBT-BT single crystal as active element. The [001] oriented NBT-BT crystal was found to exhibit thickness electromechanical coupling coefficient k_t of ~ 0.52 and low clamped dielectric constant of ~ 80. They further demonstrated that -6–dB bandwidth of transducer was 46.16 % and the insertion loss at the center frequency was -31.89 dB indicating NBT-BT single crystal as promising candidate for ultrasonic transducer application.

Recently, high electric field induced strain (~0.45%) was observed in (1-x-y) $(Bi_{0.5}Na_{0.5})TiO_3$-x$BaTiO_3$-y$(K_{0.5}Na_{0.5})NbO_3$ceramics[48-50]. The MPB composition 0.94$(Bi_{0.5}Na_{0.5})TiO_3$ –6mol% $BaTiO_3$ was found to exhibit field induced ferroelectricity and remained ferroelectric after field removal[51]. On addition of KNN, these ceramics were found

to exhibit high strain (up to 0.45%) due to the full recovery of original dimensions for every electric cycle [52,53]. It turned out that addition of KNN lowered the transition temperature (T_d) from the low-temperature ferroelectric to the high-temperature antiferroelectric phase [54]. Moreover, large electric field-induced strain in BNT-BT-KNN was attributed to a field induced transition from the antiferroelectric to the ferroelectric phase and explained in terms of change in the unit cell volume.

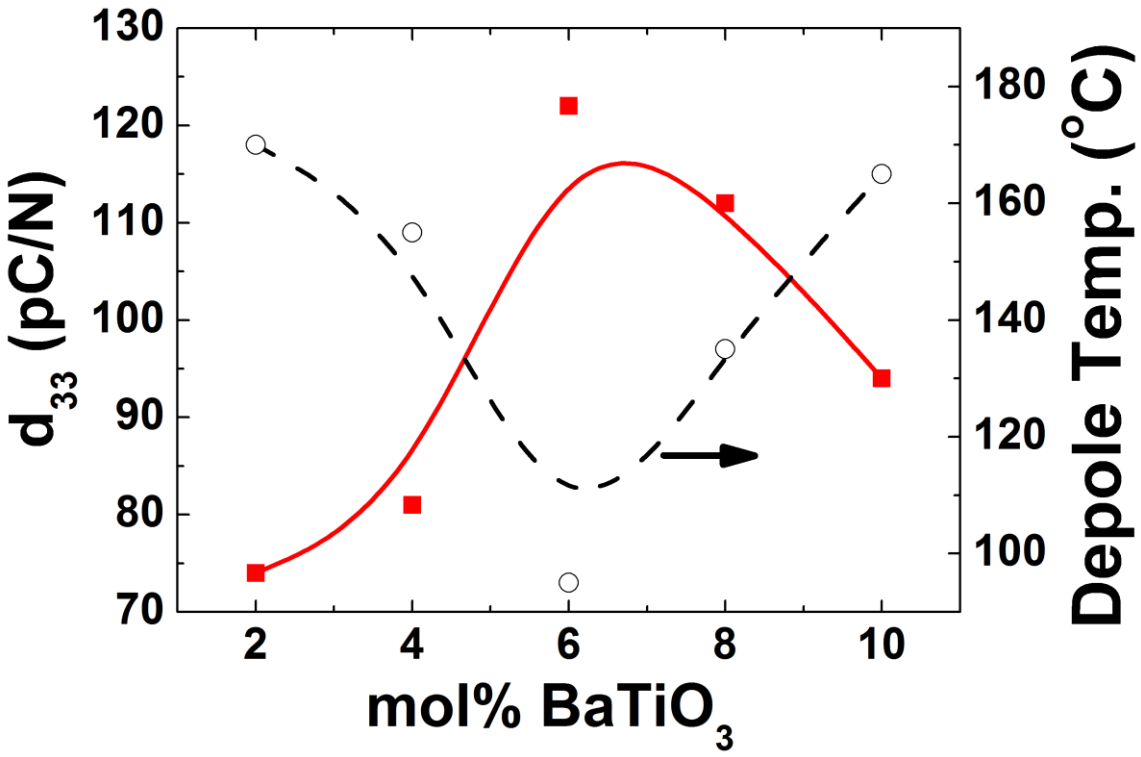

Figure 1.6. Variation of the piezoelectric constant and transition temperature (ferroelectric to antiferroelectric phase mentioned as depolarization temperature) as a function of $BaTiO_3$ concentration in NBT– BT system[55].

Also, in NBT-based lead-free piezoelectric materials, the effect of doping has not been very successful as opposed to PZT based systems where d_{33} up to 600 pC/N could be achieved by doping. However in this thesis, synthesis of grain oriented NBT-BT materials with composition near MPB was successfully accomplished by overcoming barriers related to processing. The

synthesis of grain oriented NBT-BT composition near MPB has been challenging due to the presence of multiple phases. These grain oriented specimen were found to depict enhanced piezoelectric response. To understand the nature of *E*-field induced phase transitions in textured and randomly oriented NBT-BT, *in-situ* neutron diffraction experiments were performed under E-field.

Table 1.1 Dielectric and piezoelectric properties of the prominent lead free systems [55]

Materials	**d_{33}**	**k_p**	**k_{33}**	**T_c**	**T_{o-t}/T_d**	**Ref**
$BaTiO_3$	190	0.36	0.5	115	0	[56]
BT-BCN	330	0.43	----	80	--	[57]
NBT-KBT-LBT	216	0.401	---	350	160	[58]
NBT-KBT-BT	183	0.367	0.619	290	100	[59]
NBT-xBT; x =6 - 8%	122-176	0.21-0.36	---	225-228	90-105	[60-64]
NBT-6BT+7.5L	208	0.368	---	260	85	[65,66]
NBT-6BT-2NKN	30	---	---	260		[49,50]
NBT-20KBT (MPB)	140-190	0.27-0.35	---	280-300	130-170	[67-72]
$(K_{0.5}Na_{0.5})NbO_3$ (H.P.)	127	0.46	0.6	420	---	[73,74]
$(K_{0.5}Na_{0.5})NbO_3$	80	0.35	0.51	420	195	[75]
NKN-Li (7%)	240	0.45	0.64	460	~20	[76]
NKN (Textured)	410	0.61	-	253	25	[39,77]
NKN-$SrTiO_3$ (5%)	200	0.37	--	277	27	[78,79]
NKN-$LiTaO_3$(5%)	200	0.36	--	430	55	[80]
NKN-$LiNbO_3$ (6%)	235	0.42	--	460	70	[81]
NKN-$LiSbO_3$ (5%)	283	0.50	--	392	45	[82]

Chapter-2

Purpose of research and organization of thesis

2.1 Purpose of research

The objective of this research is to design, synthesize and characterize lead-free piezoelectric ceramic materials with enhanced functional properties and to understand their structure-property relationships. Conventionally, NBT based lead-free piezoelectric ceramics have been synthesized by mixed-oxide sintering route leading to random polycrystalline grain structure. It is well-known that the piezoelectric properties are higher in oriented single crystals. However, the processing of single crystal is complicated and is not cost-effective. Further, the stoichiometry in single crystals is difficult to control and often variation in composition leads to changes in properties across the diameter and length of the ingot.

An alternative to single crystal is texturing of the piezoelectric ceramics. In this case, selection and synthesis of suitable template is the critical issue. The process for achieving texturing in alkali-based ceramics is challenging due to diffusion and low melting oxides. It would be extremely beneficial if certain degree of texturing can be achieved during the normal course of ceramic fabrication without using the complex multi-step template grain growth method (TGG) and reactive template grain growth (RTGG) method. In this thesis, one such possibility was investigated by using $Na_2Ti_6O_{13}$ single crystal whiskers that were aligned in the base matrix powder during tape-casting stage. Texturing of new composition required in-depth understanding of phase transformation, microstructural development and high temperature chemical reactivity of base matrix powder with templates. An in-depth understanding of transformation mechanism of $Na_2Ti_6O_{13}$ into $Na_{0.5}Bi_{0.5}TiO_3$-$0.07BaTiO_3$ (NBT-BT) was developed and overall densification mechanism for all sintering stages was investigated using

high resolution microscopy and diffraction. This new method for synthesizing the NBT-BT ceramics opens the possibility of achieving varying grain shape and sizes with certain degree of texturing.

Ferroelectric nanostructures with high aspect ratio are highly desired but their synthesis is extremely challenging since at reduced dimensions most perovskites adopt a structure with cubic symmetry resulting in a highly isotropic shape during high temperature processing. A novel molten salt synthesis process was developed for the synthesis of lead-free NBT-BT ferroelectric whiskers with high aspect ratio. This method utilizes topochemical transformation using $Na_2Ti_6O_{13}$ as a host structure. Furthermore, a model was developed to understand mechanism the structural transformation mechanism from edge-sharing octahedral coordination in NTO to vertex sharing octahedral coordination of NBT-BT.

The ABO_3 type perovskite piezoelectric compositions near the MPB are known to exhibit high piezoelectric response. Polarization rotation through intermediate monoclinic phase has been considered to be an important mechanism resulting in enhanced electromechanical response in lead-based B-site disordered piezoelectric systems near MPB. However, the mechanism of high piezoelectric response in A-site disordered lead–free systems at MPB is not well understood. In this thesis, we describe a microscopic model derived from comparative analyses of HRTEM and neutron diffraction that explains the origin of high piezoelectric response in lead – free MPB compositions of NBT-BT. Samples of high purity single crystals and polycrystalline ceramics were used for the high resolution microscopy and diffraction studies.

Texturing enables the polycrystalline ceramics to resemble their single crystal counterparts so that favorable domain engineered states can be obtained for composition close to

MPB. Texturing of lead-free MPB compositions is an extremely challenging problem due to several fundamental constraints – volatility of the alkali elements, chemical reactivity with seed templates, poor sinterability of the base compositions, and cubical equilibrium grain shape. All these problems were solved and more than 90% grain oriented ceramics were achieved which lead to 200% improvement in the piezoelectric properties as compared to the random ceramics of same composition. This is significant advancement in the field of lead-free piezoelectrics opening the pathway for actuation applications.

Investigations on the textured samples using *in-situ* bulk neutron diffraction patterns revealed that the pseudo-cubic nature of the bulk lattice was maintained subsequent to the application of *E*-field. In contrast, significant distortions in diffraction peak profiles were observed in the randomly oriented specimen, indicating coexistence of phases with rhombohedral and tetragonal symmetries. Although the $(001)_{PC}$ textured specimen exhibits no electric-field-induced phase transformation, it shows a much higher d_{33} (~ 320 pC/N) than that of the randomly oriented specimen (~160 pC/N). Based on these observations, It could be asserted that structural instability, at least on a bulk scale, is not a necessary prerequisite to obtain large piezoelectric properties in NBT-BT ceramics. This result indicates that the enhanced piezoelectric behavior of the $(001)_{PC}$ textured specimen is partially due to it's domain engineered state, as well as due to preservation of the "relaxor" nature due to existing PNRs.

Compositional modification of piezoelectric materials is a principal technique used for tuning the magnitude of electromechanical response. These compositional modifications perturb the atomic-scale structure and global microstructure, modulate the phase transition behavior and influence the evolution of the domain structure. However, comprehensive studies accounting for compositional effect on local dynamics/distortion and further on the domain structure and

microstructure and their correlation with functional response are limited for lead – free relaxor piezoelectrics. A novel lead-free piezoelectric (1-x) $BaTiO_3$ – x $A(Cu_{1/3}Nb_{2/3})O_3$ (A: Ba, Sr and Ca) compositions was synthesized. In order to provide fundamental understanding of A-site instability on piezoelectricity, the local structural distortions, phase transition behavior, microstructure, domain structure and associated changes in functional response of the system were investigated. This study provides fundamental understanding about the origin of enhanced piezoelectric instability in BT-based materials and its correlation with the average and local structural changes. The microstructure – domain structure – defect chemistry – physical property relationships were investigated in complex perovskite solid solutions given by the formulation (1-x)$BaTiO_3$-*x*$A(Cu_{1/3}Nb_{2/3})O_3$ (BT-*x*ACN, x = 0.0-0.03, A=Ba, Sr, Ca).

Multilayer ceramic capacitor (MLCC) technologies require continuous development of high dielectric constant material in order to meet the growing demand of miniaturization, high volume efficiency, lifecycle, and low cost. In order to meet these requirements, thickness of each layer is a critical factor. Dielectric layers less than 3.0 μm thickness require sub-micron grain size with good densification. There has been limited success in achieving large relative permittivity with smaller grain sizes. A novel Sn-modified system [0.975 $BaTi_{1-y}Sn_yO_3$ – 0.025 $Ba(Cu_{1/3}Nb_{2/3})O_3$] was developed in this thesis that exhibited dielectric constant higher than 7000 (with TCC suitable for Y5V type MLCCs), dielectric loss factor less than 1% and grain size less than 1 μm.

Graded structures offer the possibility of tuning the hysteresis loops by modulating the parameters such as leakage current, sharpness of the interface and ferroelectric – anti-ferroelectric exchange coupling. Using tape-casting based process, bulk graded ferroelectric structures of $BaTiO_3$ and 0.975$BaTiO_3$-0.025$Ba(Cu_{1/3}Nb_{2/3})O_3$ were synthesized for two specific reasons: (i) to

better understand the physics governing the dynamic hysteresis behavior, and (ii) to deterministically model the hysteretic scaling relationships. It was observed that coupling resulting due to polarization mismatch between layers changes the free energy function and influences the dynamic hysteresis behavior and power-law scaling relations.

2.1 Organization of thesis

Chapter-1 Introduction

This chapter summarizes the fundamental concepts of piezoelectricity and ferroelectricity. The concepts related morphotropic phase boundary, intermediate bridging phases and relaxor-type ferroelectrics were included in the discussion. This chapter also presented a detailed review of various prominent lead-free piezoelectric systems.

Chapter-2 Purpose of research and organization of thesis

After summarizing the current state-of-the-art in the Chapter 1, the need for new investigations related to lead-free piezoelectrics was identified with clear pathway towards design of composition and microstructure. The data reviewed in Chapter 1 also indicated the need to continue the search of new lead-free compositions.

Chapter-3 Experimental procedure

This chapter summarized the details of main experimental procedures used throughout the dissertation. The chapter explained the synthesis method for ceramics adapted in this thesis. It also provided details on the characterization techniques such as x-ray/neutron diffraction, Rietveld refinement and PDF analysis, used throughout this dissertation. The description of Raman spectroscopy, TEM, electrical characterization and PFM measurements was presented to inform the readers about the necessary background.

Chapter-4

In this section, synthesis, microstructural evolution and electrical characterization of lead-free (1-x)$Na_{0.5}Bi_{0.5}TiO_3$-x$BaTiO_3$ (NBT-BT) ceramics with x = 0.05, 0.06, 0.07, 0.08, 0.09 was reported. The piezoelectric response was optimized by synthesizing the compositions around the MPB given as 0.93$Na_{0.5}Bi_{0.5}TiO_3$-0.07$BaTiO_3$. Next in this chapter, a novel method for the synthesis of NBT-BT was presented. This method starts with the synthesis of monoclinic $Na_2Ti_6O_{13}$ (NTO) whiskers and then transforms them to NBT-BT ceramics.

Chapter-5

This chapter discusses the synthesis process for achieving nanostructured ferroelectric NBT-BT whiskers with high aspect ratio using NTO as a host structure. A microscopic model was developed by conducting comparative analyses through HR-TEM and neutron diffraction that explains the origin of high piezoelectric response in lead – free MPB compositions of NBT-BT. Extensive structural investigations on high purity single crystals and polycrystalline samples were conducted to validate the model. NBT-BT whiskers with a diameter of ~2-3 grains (grain size ranging 300-500 nm) were used in the structural analysis to avoid the influence on the domain migration in a given grain from the domains in neighboring grain.

Chapter-6

This chapter described the synthesis method for grain oriented NBT-BT ceramics. The mechanism for grain transformation and its influence on piezoelectric response was explained in detail by using results from XRD, TEM and PFM analysis. This chapter also provided a comparative description of the properties of textured and randomly oriented polycrystalline lead-free piezoelectric 0.93($Na_{0.5}Bi_{0.5}TiO_3$)-0.07$BaTiO_3$ (NBT-BT) ceramics by using data from *in-situ field-dependent* neutron diffraction experiments.

Chapter-7

This chapter provides the fundamental understanding of the enhanced piezoelectric instability in new lead-free piezoelectrics given as: (1-x) $BaTiO_3$-x$A(Cu_{1/3}Nb_{2/3})O_3$ (A: Sr, Ba and Ca and x = 0.0-0.03) through detailed structural and electromechanical analysis.

Chapter-8

This chapter provides the approach for the synthesis of new $BaTiO_3$ (BT) based high dielectric compositions that are promising for Y5V type multilayer ceramic capacitors (MLCCs).

Chapter-9

This chapter investigates the dielectric and ferroelectric response of compositionally graded bilayer and trilayer composites consisting of $BaTiO_3$ (BT) and 0.975$BaTiO_3$-0.025$Ba(Cu_{1/3}Nb_{2/3})O_3$ (BT-BCN). Two types of graded bilayer samples were synthesized by varying the layer thicknesses. The graded trilayer sample consisting of BT layer sandwiched between two BT-BCN layers of equal thickness was also synthesized.

Chapter-10 Summary and future work

This chapter summarizes the significant results of the thesis. It also describes about the future work that needs to be pursued to successfully transition the NBT based ceramics into practical applications.

Chapter-3 Experimental procedure

3.1 Synthesis of piezoelectric ceramics:

3.1.1 Solid state reaction:

In order to synthesize polycrystalline piezoelectric ceramics, solid state reaction method was adapted. This method can be categorized into two broad steps: (i) synthesis of ceramics powder, (ii) sintering of the compact ceramics body.

3.1.2 Synthesis of ceramics powders:

For the synthesis of $(1-x)Na_{0.5}Bi_{0.5}TiO_3$-$xBaTiO_3$, the stoichiometric amounts of starting materials (Na_2CO_3, Bi_2O_3, TiO_2, $BaCO_3$) were weighed followed by first ball milling for 24h. The ball milling was performed under ethanol in polyethylene bottles with Yttria-stabilized ZrO_2 balls as milling media. The resulting mixture was dried in an electric oven at 80^oC for 12h. The powder thus obtained was calcined in alumina crucibles covered with alumina plate at higher temperatures. The temperature of calcination was optimized to achieve perovskite phase. After calcination the powder gets agglomerated and to break this agglomeration a second ball-milling was performed for 24h. After finishing the second ball-milling, the slurry was kept for drying in an oven for 12h at 80^oC. Finally, after drying, the powder was sieved with a sieve having 300 μm opening and used for ceramic fabrication.

3.1.3 Sintering process:

The powder obtained after calcination was uni-axially pressed into pellets using a steel die. These pellets were covered with the powder of the same composition and processed at high temperature (less than the melting temperature) to obtain a highly dense ceramic body. The reduction of the excess surface energy associated with particle surfaces is the macroscopic driving force operating during this process [83]. This is achieved by (i) reduction of the total surface area by an increase in the average size of the particles leading to coarsening (Figure 3.1 (b)), and/or (ii) the elimination of solid/vapor interfaces and the creation of grain boundary area, followed by grain growth, which leads to densification (Figure 3.1 (a))[83]. These two mechanisms are usually in competition. If the atomic process that leads to densification dominates, the pores get smaller and disappear with time. This process is called sintering.

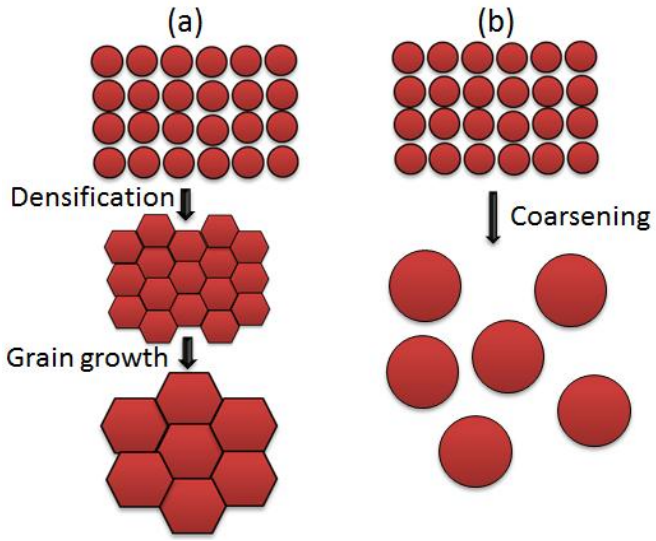

Figure-3.1 Schematic diagram depicting two possible paths through which collection of particles can lower its energy[83]. (a) Densification followed by grain growth. In this case shrinkage of the compact has to occur. (b) Coarsening where the large grains grow at the expense of the smaller ones.

However, if the atomic process leading to coarsening is faster, both the pores and grains coarsen

and get larger with time [83]. After optimization of sintering temperature of NBT-BT, all the materials were sintered at 1200^{o}C for 2h with heating and cooling rate of 5^{o}C/min

3.2 Structural characterization

3.2.1 X-ray diffraction

X-ray diffraction (XRD) can be used to characterize any crystalline specimen. However this method is most sensitive to the high-Z elements, because the diffracted x-ray intensity is stronger from heavier nuclei [84]. It can easily be used with a resolution in the sub-angstrom range. Figure 3.2 shows the Bragg reflection from the set of crystal planes with spacing *d*. A beam of parallel x-rays is impinging on the crystal surface at an angle θ and diffracted at an exit angle θ.[84] The condition for constructive interference is that the path difference between the

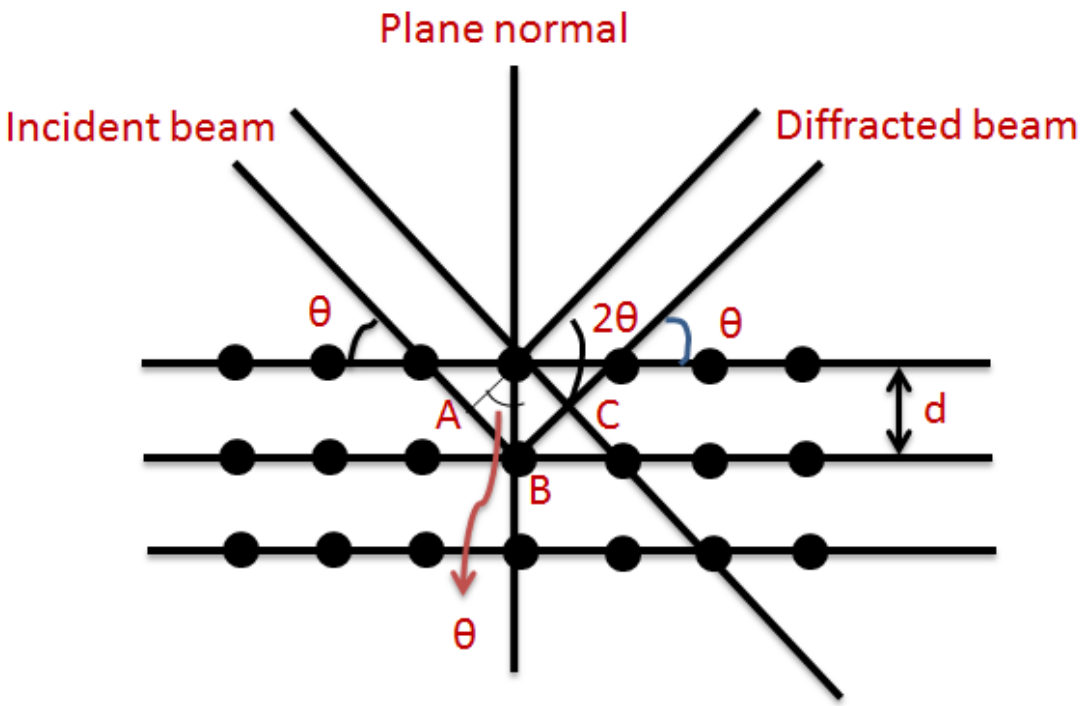

Figure-3.2 Bragg reflection from the set of crystal planes with a spacing *d*.

two rays shown in the figure is equal to an integral number n of wavelengths:

$$AB + BC = d\sin\theta + d\cos\theta = n\lambda \quad (2.1)$$

Rewriting this formulates the famous Braggs law as:

$$n\lambda = 2d\sin\theta \quad (2.2)$$

where λ is the wavelength of incident x-rays and n is the order of diffraction[84].

A powder XRD spectrum of a specimen provides *d*-spacing of the line and their intensity. High intensity is desirable for getting high quality spectrum. The d-spacing is important as it is directly related to unit cell parameter of the specimen. Therefore, the XRD spectrum can be used to determine a change in crystal symmetry and confirm the formation of desired phase [84]. For example, when a crystal structure changes from cubic to tetragonal, the inter-axial angles remain unchanged, however the length of unit cell changes: a=b≠c. In XRD spectra, {111} reflections would be identical in cubic and tetragonal phase and there would be only one {111} Bragg peak. However, the single {100} Bragg peak now splits in to two (100) and (001) Bragg peaks. Because in tetragonal symmetry, lattice parameters a = b, Bragg reflections from (100) and (010) are detected at the same 2θ angle, resulting in intensity of (100) peak nearly twice that of (001) peak. In case of rhombohedral phase, {111} Bragg peaks splits in to two peaks (111) and (-111), however {100} Bragg reflections remains unchanged. XRD experiments (Cu Kα radiation) were conducted using PANalytical X'Pert Pro powder X-ray diffractometer at operating voltage of 45 *kV* and current of 40 *mA*.

3.2.2 Neutron diffraction

The X-rays are mainly scattered by heavier cations however neutrons are scattered by all the ions. Therefore combined use of two probes could be helpful in separating the cation-cation correlation from the cation-oxygen correlation. Neutrons are the fundamental particles with zero charge, mass m, and spin ½. The relation between the wave vector $\vec{K}$ and the momentum $\vec{P}$ is given by: $\vec{P} = \hbar\vec{K}$.[84, 85]] The de Broglie wavelength of the neutron is given as: $\lambda = \frac{h}{p} = \frac{9.045}{\sqrt{E}}$, where E is the energy of the neutron in units of MeV[85]. In this thesis, the neutron powder diffraction patterns of the NBT-BT whiskers were collected at the VULCAN diffractometer of the Spallation Neutron Source (SNS), Oak Ridge National Laboratory[86]. The diffraction pattern was collected with an incident neutron beam in the time-of-flight mode. Rietveld refinement on the diffraction pattern was performed using the GSAS software package [87].

3.2.4 Rietveld refinement

In 1969, Rietveld[88] presented a method for the analysis of the powder XRD data. In this method the whole pattern of diffracted intensity and the diffraction profile as a function of the angle 2θ is calculated. The profile get modified due to experimental effects such as the peak shape, absorption, polarization correction, the Debye-Waller factor, sample geometry, and the background[89]. The profile of calculated intensity I_{calc} (Q), is compared to the experimental data. In order to obtain the best-fit structural model, each parameter of the model is refined [89]. The R-factor (residual function), which is the difference between the model and experiment [89],

$$R = \frac{\int [I_{meas}(Q) - I_{calc}(Q)]^2 dQ}{\int [I_{meas}(Q)]^2 dQ} \qquad (2.3)$$

is minimized through least square fitting. The ideal value of *R* should be zero, however various errors results in non-zero *R* values. Generally R value of a few % is considered as excellent fitting, while 10% represents a poor fitting. Another common R factor is weighted profile R-factor (R_{wp}), which deals with the statistical significance of each data-point by weighing its contribution to the residual function. The weighted residual function is defined as [89]:

$$R_w = \frac{\int (\frac{1}{\sigma(Q)})^2 [I_{meas}(Q) - I_{calc}(Q)]^2 dQ}{\int \frac{I_{meas}(Q)^2}{\sigma(Q)^2} dQ} \quad (2.4)$$

where $\sigma(Q)$ is the estimated random error on each data-point at the level of one standard deviation.

3.2.4 Atomic pair distribution function (PDF) analysis:

Generally, the Bragg peaks and diffuse scattering intensities have been treated separately during the crystallographic analysis. The position and intensity of Bragg peaks have been used to determine the structure; however diffuse scattering has been used to obtain more information in regard to structural deviations from the perfect lattice [89]. In case of small deviations, this approach is useful, however this method fails if the structure is disordered [89]. In this case atomic PDF analysis comes in to play as it deals with the Bragg and diffuse scattering on equal basis[89,90]. The atomic PDF, G(r), gives the number of atoms in a spherical shell of unit thickness at a distance r from a reference atom as [90]:

$$G(r) = 4\pi r[\rho(r) - \rho_o] \quad (2.5)$$

where ρ(r) and ρ_o are the local and average atomic number densities, respectively, and r is the radial distance. G(r) is one dimensional function that oscillates around zero and shows positive

peaks at distances separating pairs of atoms [90]. The negative valleys in G(r) correspond to real space vectors lacking atoms at either ends[90].G(r) is a Fourier transform of the experimentally observable total structure function S(Q)[90] given as:

$$G(r) = (\frac{2}{\pi}) \int_{Q=0}^{Q_{max}} Q[S(Q) - 1] \sin(Qr)\, dQ, \qquad (2.6)$$

where Q is the magnitude of wave vectors ($Q = 4\pi\sin\theta/\lambda$), 2 θ is the angle between the incoming and outgoing X-rays, and λ is the wavelength of X-rays used. The structure function is related to the coherent part of the total scattered intensity as[90]:

$$S(Q) = 1 + [I^{coh}(Q) - \sum c_i |f_i(Q)|^2 / |\sum c_i f_i(Q)|^2 \qquad (2.7)$$

where I^{coh} is the coherent scattering intensity per atom in electron units and c_i and f_i are the atomic concentration and X-ray scattering factor, respectively, for the atomic species of type *i*[91]. The equations (2.6) and (2.7) consider the total scattering (Bragg scattering and diffuse scattering) in PDF [90]. Therefore, average and longer range atomic structure (manifested in Bragg peaks) and the local structural distortions (manifested in diffuse component of the diffraction pattern) are incorporated in PDF[90].

3.2.5 Raman spectroscopy

Raman spectroscopy is a versatile tool to investigate the local structural distortions due to shorter characteristic length[92]. The dynamic behavior of the lowest wavenumber transverse optical mode (soft mode) has been of great interest in ferroelectric materials [93]. Raman scattering is very sensitive to the subtle structural modifications and can be used to detect low concentration impurity phases which remain unperceived to normal diffraction methods. Moreover, the chemical heterogeneity at sub-micrometer levels [94] can be easily probed

through spatially resolved Raman spectroscopy. The Raman spectra usually contains intensity versus the difference in wave number between incident and the scattered beam and the peaks are related to the corresponding phonon frequency[92]. Because of small wave vector of optical photons, the phonons involved in the Raman scatetring of crystalline solids have very small momentum compared with the Brilloiun zone[92]. Therefore, only zone-centered phonons participate in the Raman scattering[92]. Raman spectroscopy is very useful for investigating the role and origin of structural and chemical factors.

In this thesis, Raman studies were conducted in the backscattering geometry using a Jobin-Yvon T6400 Triplemate instrument utilizing laser radiation of 514.5 nm from a coherent Innova 99 Argon source. The green laser light was focused in ~2μm-diameter by using a Raman microprobe with a 50X objective. A charge-coupled device (CCD) system collected and processed the scattered light. The integration time of the spectrum and the slit width and laser beam power were adjusted in order to achieve a high signal to noise ratio. The typical spectral resolution for the Raman system with an 1800 grooves/mm grating and 1-in CCD was less than 1 cm^{-1}. The system was calibrated with Si spectra at room temperature before and after recording the spectra.

3.2.6 Transmission electron microscopy

The Philips EM 420 electron microscope was used to record selected area electron diffraction (SAED) and bright field images. This microscope could be operated with the variable acceleration voltage from 40 to 120 kV. This microscope is equipped with slow scan CCD camera for BF/DF imaging and electron diffraction pattern recording. The HR-TEM experiments were performed on FEI TITAN 300 electron microscope operated 300 kV. While doing HR-

TEM imaging, the specimens were tilted to particular zone axis. The analysis of the images was performed using ImageJ and DigitalMicrograph^{TM} (Gatan Inc., Pleasanton, CA, USA) software. The simulation of SAED was performed using CrystalKit program.

3.3 Electrical characterization

3.3.1 Measurements of dielectric properties

Piezoelectric materials are generally dielectrics. The dielectric constant and loss tangent factor are important parameters for characterization of a piezoelectric material. The temperature dependence of dielectric constant and loss tangent factor provides vital information about nature of phase transition of these materials. Generally these measurements are performed in parallel plate capacitor configuration. Suppose a parallel plate capacitor is filled with a dielectric medium. On applying an alternating electromotive force $\mathcal{E}$ with frequency ω onspecimen, an alternating current *i* flows through the capacitor [95],

$$i = j\omega\varepsilon_r C_o \mathcal{E} \ (\mathrm{j} = \sqrt{-1}\,), \tag{2.8}$$

where C_o is the capacity of the parallel plate condenser without any medium (in vacuum) and ε_r is the relative dielectric constant is a function of ω. As the dielectric loss (including leakage current) exists in a dielectric material, ε_r could be written as a complex number [95]:

$$\varepsilon_r^* = \varepsilon'(\omega) - j\varepsilon''(\omega), \tag{3.9}$$

where, $\varepsilon'(\omega)$ is the real part of the dielectric constant (which is sometimes denoted as relative permittivity in this thesis) and $\varepsilon''(\omega)$ is the imaginary part. The imaginary part represents the dielectric loss. Generally, loss tangent factor (tanδ) is used to represent the dielectric loss and is defined as:

$$tan\delta = \varepsilon''/\varepsilon' \quad (3.0)$$

The electric current density [95] in a parallel plate capacitor can be written as:

$$J = j\omega\varepsilon_o\varepsilon' E + \omega\varepsilon_o\varepsilon'' E,$$

where *E* is the electric field strength. The real part of the ratio J/E is the electric conductivity σ [95] in dielectric materials:

$$\sigma(\omega) = \omega\varepsilon_o\varepsilon''(\omega)$$

σ(ω) represents the total dielectric losses caused by various mechanisms. Therefore, ε' and $tan\delta$ are sufficient for characterizing the dielectric response of a material. For electrical measurements, silver electrodes were applied on flat faces of sintered pellets of piezoelectric ceramics. Computer controlled HP 4192A impedance analyzer coupled with high temperature oven was used to measure the dielectric constant and loss tangent factor as a function of temperature at various frequencies with oscillation level of 500 mV.

3.3.2 P-E hysteresis measurements

The polarization-electric field (P-E) measurements were recorded using the computer-controlled ferroelectric tester Precision Pro with Vision-Pro software from Radiant Technology Inc. The P-E hysteresis curves were generated with a standard bipolar profile with parameters of 0 offset and pre-loop delay of 100 ms.

3.3.3 Piezoelectric measurements

Prior to poling, ferroelectric materials do not show piezoelectric properties because of the random orientation of ferroelectric domains in the ceramics. During poling process, a DC electric

field is applied on ferroelectric ceramic sample to align domain in the direction of electric field. In order to avoid the electric arcing, the poling process was performed in silicone oil bath. For effective poling, the temperature, time and E-field was optimized. Theoretically, when the *E*-field is larger than the coercive field of a ferroelectric sample, most of the domains will be aligned along the applied field direction. However, the experimental results show that poling field should be 3x or 4x higher than that of coercive field [95] to obtain optimum piezoelectric response. The longitudinal piezoelectric coefficient (d_{33}) was measured using a Berlincourt APC YE 2730A d_{33} meter. The electromechanical properties were measured using the frequency dependent impedance spectrum measured by HP 4194A impedance analyzer. The electromechanical coupling factor, mechanical quality factor, piezoelectric voltage constants were calculated from these measured parameters.

3.3.4 Piezo-response force microscopy (PFM)

The PFM is a scanning probe microscopy (SPM) based technique used to investigate domain structure. In this study, a Bruker atomic force microscope was used. In order to perform PFM measurements, the piezoelectric samples were grinded to ~ 100 μm thickness and polished to be optically flat. This specimen was glued on the sample stage using conducting silver epoxy and the other surface was scanned by the conducting SPM tip. For this an AC modulation voltage (peak to peak) with a frequency was applied between the conducting tip and the bottom electrode of the specimen.

Chapter-4

4.1 Structural and electrical characterization of lead free (1-x)$Na_{0.5}Bi_{0.5}TiO_3$-x$BaTiO_3$ ceramics[a]

In this chapter, the synthesis method, microstructural and electrical characterizations of lead-free (1-x)$Na_{0.5}Bi_{0.5}TiO_3$-x$BaTiO_3$ (NBT-BT) ceramics with x = 0.05, 0.06, 0.07, 0.08, 0.09 were investigated. The piezoelectric response was optimized by synthesizing the compositions around morphotropic phase boundary (MPB). These NBT-BT ceramics were synthesized using conventional solid state reaction method. These samples were subjected to room temperature XRD measurements for structural characterization. Scanning electron micrographs were recorded for all the compositions to check morphology, while measured density using Archimedes principle comes out to be more than 96% of theoretical density for all specimens. The values of free permittivity ($\varepsilon^{T}_{33}/\varepsilon_{o)}$ and longitudinal piezoelectric constant (d_{33}) for x = 0.07 were found to be 1027 and 160 pC/N, respectively along with the electromechanical coupling constant factor k_p ~ 22(%). However for x = 0.08, values of d_{33} and k_p were found to be 151 pC/N and 35%, respectively. The longitudinal piezoelectric constant (d_{33}) in x=0.07 composition was found to be around 28% higher than that of reported for same composition.

4.1.1. Background:

The profound increase of scientific research in piezoelectric materials is growing very fast due to their diversified potential application in many cutting edge technologies. But, the piezoelectric response of lead-based piezoelectric materials like PZT is much higher. Therefore, there is strong urge to develop lead-free piezoelectric materials equally efficient as lead based.

[a] Reproduced with permission from [174]. Copyright 2010, The American Ceramic Society.

Various methods are used to improve piezoelectric response of the materials; construction of solid solution near morphotropic phase boundaries, doping of aliovalent cations, grain size control, and synthesis of textured ceramics. Further, construction of solid solution around MPB is also very popular method to improve the piezoelectric response of an underline system. $Na_{0.5}Bi_{0.5}TiO_3$ have been in picture since a long time[15], recently these materials have been the point of attraction as "eco-friendly" lead free piezoelectric with potential industrial application [19,20]. The sodium bismuth titanate $Na_{0.5}Bi_{0.5}TiO_3$ (NBT) belongs to $A'A''BO_3$ - type complex perovskites with *A* sublattice occupied by ions of different species having different valence states.

Moreover, solid solutions of $Na_{0.5}Bi_{0.5}TiO_3$ (NBT) with $BaTiO_3$ (BT); (1-x) $Na_{0.5}Bi_{0.5}TiO_3$–x $BaTiO_3$, have been studied to improve the dielectric and piezoelectric properties of NBT. A morphotropic phase boundary (MPB) between a rhombohedral ferroelectric relaxor structure (NBT) and a tetragonal ferroelectric (BT) structure has been found at x = 0.06–0.07[24,96,97]. At MPB, materials show structural coexistence of the two phases in a large temperature range and improved electromechanical and piezoelectric properties [24]. It has been reported for (1-x) $Na_{0.5}Bi_{0.5}TiO_3$–x $PbTiO_3$ system that MPB may be shifted due to lattice distortion [98]. In present chapter, the synthesis of various (1-x)$Na_{0.5}Bi_{0.5}TiO_3$-x$BaTiO_3$ ceramics around MPB was performed using conventional solid state reaction method. These specimens were further subjected to structural analysis followed by optimization of piezoelectric and electrical response.

4.1.2. Experimental

The synthesis of (1-x)$Na_{0.5}Bi_{0.5}TiO_3$-x$BaTiO_3$ (x = 0.05, 0.06, 0.07, 0.08, 0.09) randomly oriented ceramics were performed using solid state reaction method. For this, stoichiometric amounts of high purity Na_2CO_3, TiO_2, $BaCO_3$ and Bi_2O_3 were mixed and ball milled for 24h with ZrO_2 balls in polyethylene bottle. The ball milled powders were subjected to two step calcination (800 - 900^{o}C for 2h). Calcined powder was again ball milled, pelletized, and sintered at 1100 - 1200^{o}C for 2h. XRD-patterns were recorded at RT to confirm the phase evolution in all samples using X-*Ray Diffraction System (Philips Xpert Pro)*. SEM images were collected using *LEO (Zeiss) 1550* microscope for thermally etched samples. The density was measured using *Archimedes* principle. For electrical and piezoelectric measurements, silver paste was applied on flat surfaces of the ceramic disks and fired at 650^{o}C. These samples were poled at 5 kV/mm for 1h at 60^{o}C. The d_{33} values were measured using by Berlincourt meter using a d_{33}-meter, while HP 4194A impedance analyzer was utilized to measure electrical response. Relative permittivity (ε) (and tangent loss factor was determined as a function of temperature at selected frequencies using HP 4284A LCR meter connected to a computer-controlled high temperature furnace.

4.1.3. Results and discussion

Figure-4.1 represents XRD-spectra recorded at RT for all the (1-x) NBT-xBT ceramics. It was observed that all (1-x)NBT-xBT compositions crystallize in pure perovskite phase. Figure-4.2(a) and Figure-4.2(b) depict variations of (200) and (111) peaks of NBT-BT samples with various $BaTiO_3$ content at RT, respectively. It can be seen in Figure-4.2(b) that with increasing amount of $BaTiO_3$, the shape of (200) rhombohedral peak becomes asymmetric and finally get split in to (002) and (200) tetragonal peaks along with the presence of rhombohedral (200) peaks. The tetragonality (c/a) calculated for x = 0.07, 0.08, 0.09 comes out to be 1.0087, 1.0101, 1.0153, respectively. Moreover, c/a ratio could not be calculated for x = 0.06 as tetragonal (200)

peak get merged with rhombohedral (200) peak, but one can still observe (002) peak, which further get merged with the rhombohedral (200) peak. Thus, one can observe decrease in tetragonality with decreases in $BaTiO_3$ content in the base matrix. The obvious rhombohedral split in (111) peak can be clearly observed for x = 0.05 composition, which get merged in to one peak indicating transition of structure from rhombohedral to tetragonal with the increase in the $BaTiO_3$ content in the base matrix. Figure-4.2(c) shows trend of variations of (220) peaks with the change in $BaTiO_3$ content in NBT-BT. It is observed that the intensity of rhombohedral (220) peaks decreases gradually with the increase in the $BaTiO_3$ content along with the evolution of the tetragonal (220) peaks for increased $BaTiO_3$ content. Thus, one can observe coexistence of two phases rhombohedral and tetragonal in a same composition indicating the underline composition at (MPB).

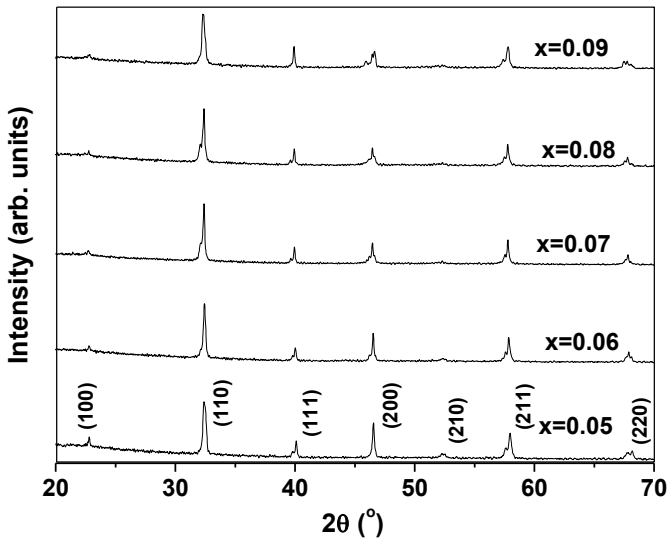

Figure 4.1- XRD-patterns recorded at RT for various compositions of (1-x)$Na_{0.5}Bi_{0.5}TiO_3$-x$BaTiO_3$ ceramics

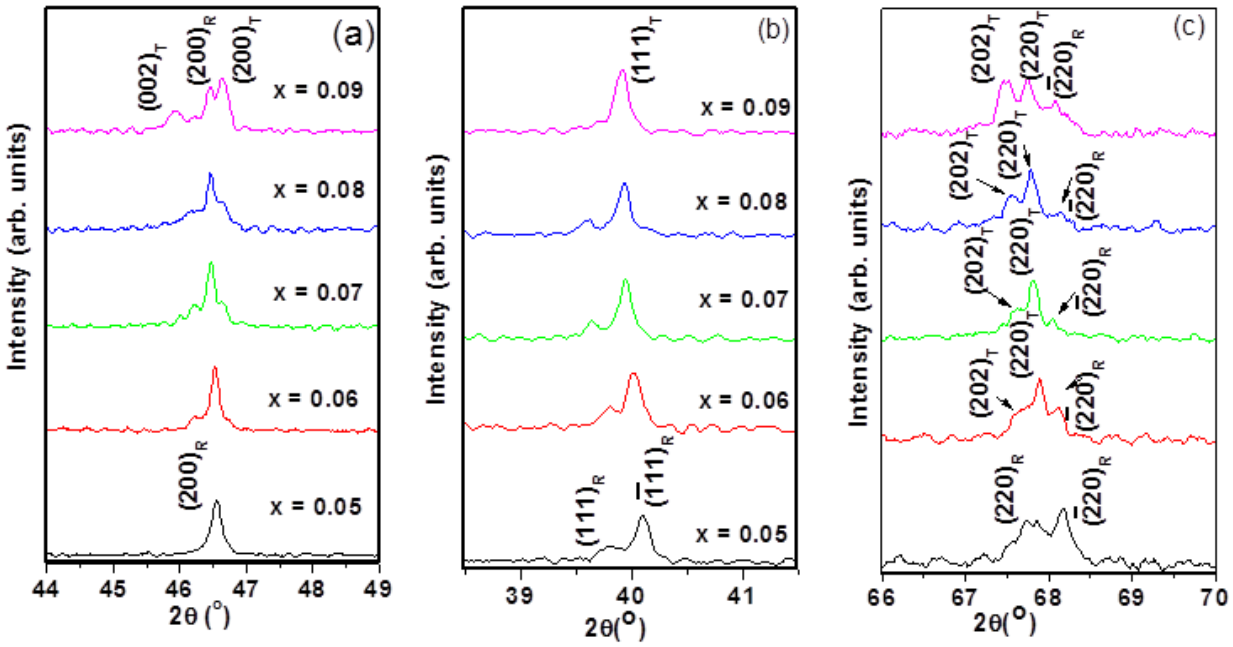

Figure 4.2 Effect of compositional change on various Bragg reflections in (1-x)$Na_{0.5}Bi_{0.5}TiO_3$-x$BaTiO_3$: (a) {200}, (b) (111) and (c) (220).

Figure-4.3 shows the scanning *e*lectron micrographs of thermally etched (1-x) NBT-xBT; x= 0.05, 0.06, 0.06, 0.07, 0.08, 0.09 compositions. These micrographs clearly indicate the highly dense ceramics body. The density of all NBT-BT specimens is higher than 96% of theoretical density (Figure-4.4). The increasing trend of theoretical density with respect to increase in $BaTiO_3$ can be noticed.

Figure -4.5 depicts relative permittivity (ε) and loss tangent factor (tan δ) as a function of temperature at 100 kHz for unpoled (1-x)NBT-xBT; x=0.07 specimen. The presence of diffuse transition can be observed in terms broad transition peaks. Three regions are marked as ferroelectric, antiferroelectric and paraelectric phase in wide temperature range of ε(T) and tanδ(T) plots .

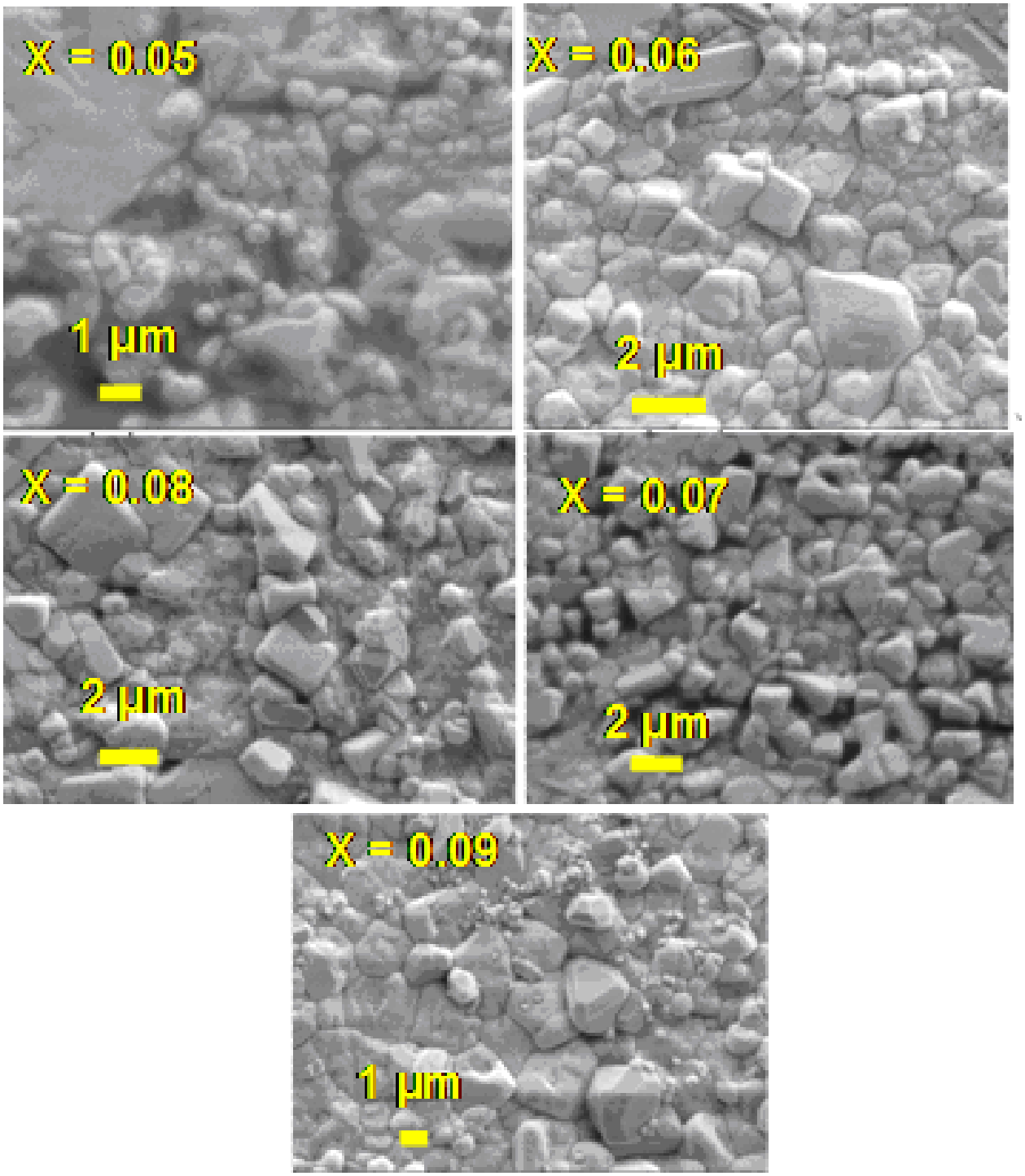

Figure- 4.3 SEM micrographs of (1-x)NBT-xBT ceramics

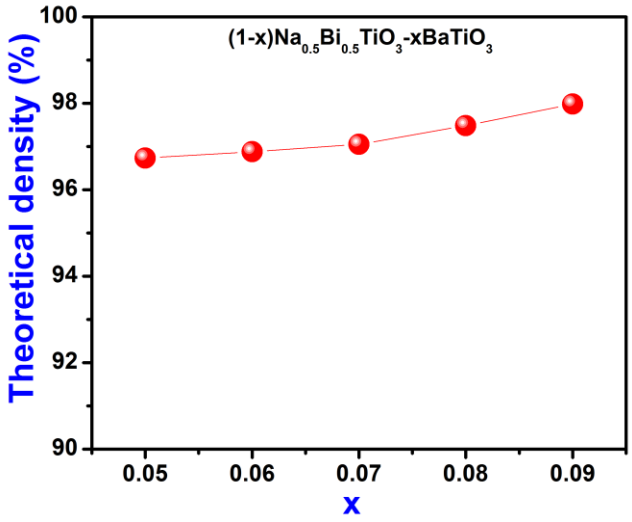

Figure 4.4 Theoretical density versus composition in (1-x)NBT-xBT ceramics

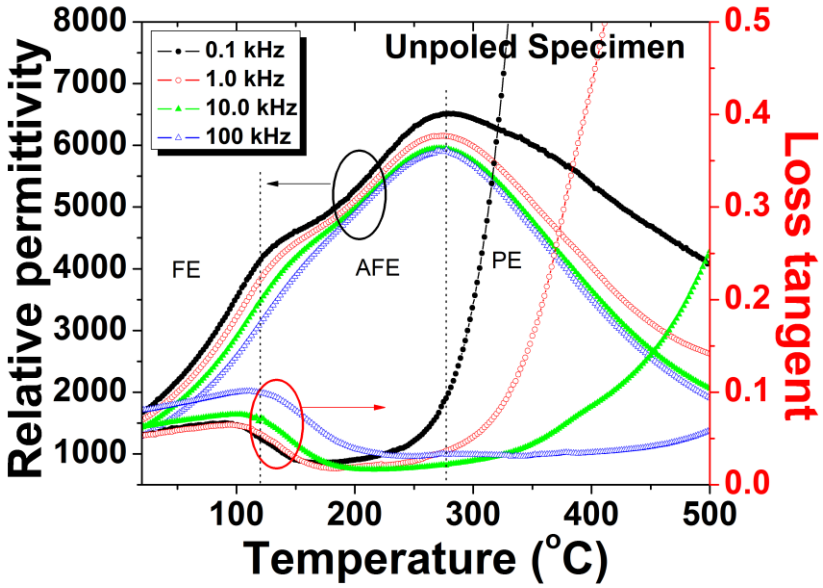

Figure-4.5 Permittivity (ε) and loss tangent (tan δ) versus temperature plot for unpoled 0.93NBT-0.07BT ceramics

Figure- 4.6 (a) shows free permittivity ($\varepsilon^{T}_{33}/\varepsilon_o$) and tangent loss factor tanδ (%) as a function of $BaTiO_3$ content (x). All values are average values measured on three samples prepared in different batches. $\varepsilon^{T}_{33}/\varepsilon_o$ and tanδ(%) are found to be maximum for x = 0.07 composition, which lies around morphotropic phase boundary (MPB) in NBT-BT system.

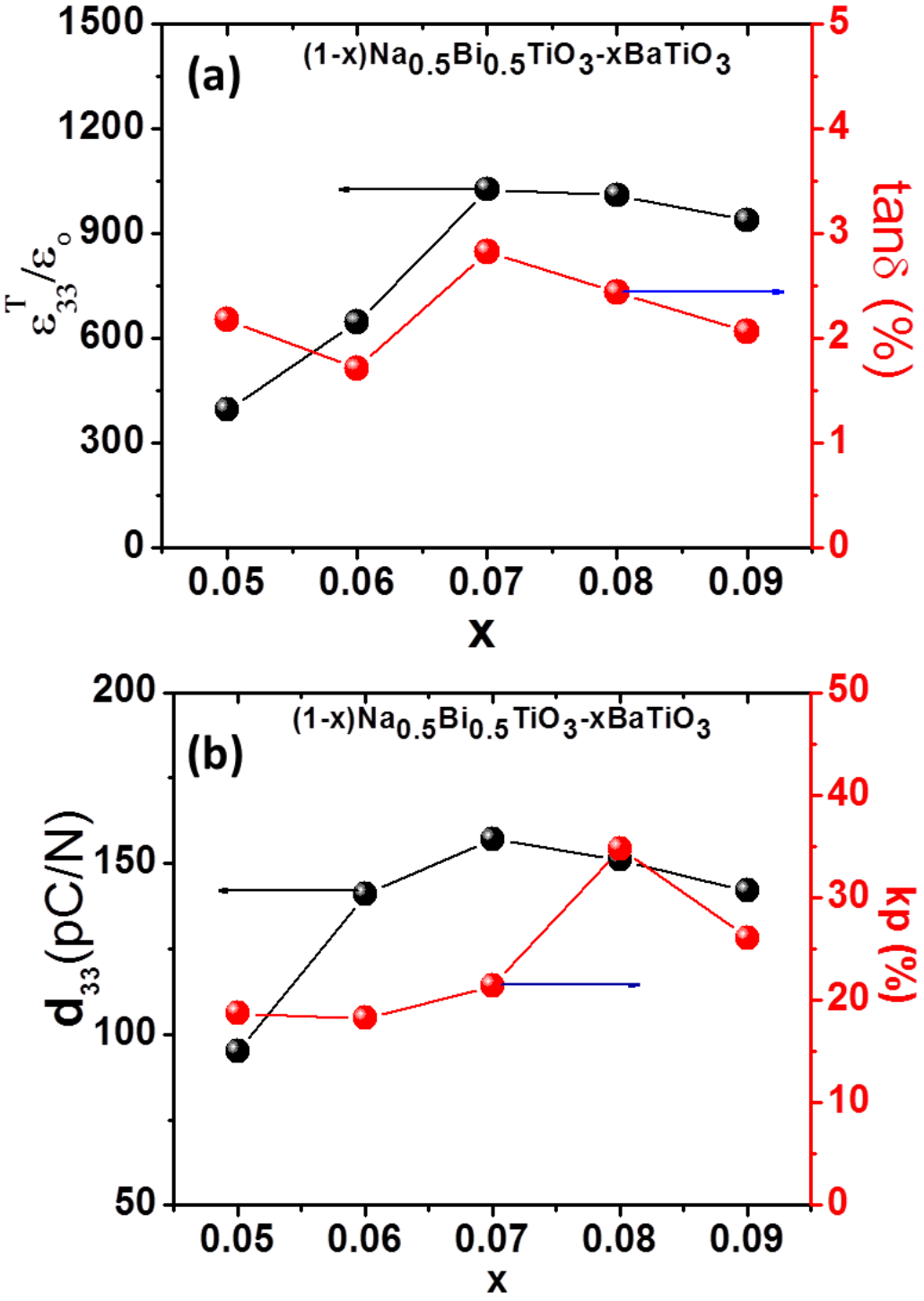

Figure- 4.6 dependence of dielectric response (a) and piezoelectric response (b) at room temperature for (1-x)NBT-xBT ceramics

Figure 4.6(b) depicts compositional dependence of longitudinal piezoelectric constant (d_{33}) and and electromechanical coupling constant factor k_p. The value of d_{33} increases up to 160 pC/N for x =0.07 and then drops on further increase in $BaTiO_3$ content, while k_p assumes the maximum value ~35(%) for x =0.08. The longitudinal piezoelectric d_{33} value observed in this composition is much higher than d_{33} value observed in NBT-BT ceramics reported in literature (d_{33}~125 pC/N) [24,35] synthesized by conventional solid state reaction method. Higher d_{33} (~160 pC/N) value can be ascribed to the existence of this composition at MPB, which is composed of two phase rhombohedral and tetragonal. Rhombohedral structure possess eight (111) polar axis and tetragonal phase possess six (100) polar axis and hence there are 14 polar axis in MPB composition, which increases the probability of alignment of diploes along the polar axis giving rise to decent piezoelectric properties.

4.1.4. Chapter summary:

The (1-x) NBT-xBT composition near MPB was optimized by synthesizing x = 0.05, 0.06, 0.07, 0.08, 0.09 compositions. All these compositions crystallize in single perovskite phase with the variation in (200) (111) and (220) peaks indicating presence of composition at MPB. All the specimens are showing > 96% of theoretical density. Composition x = 0.07 was found to show higher d_{33} value ~ 160 pC/N and k_p ~ 22% along with value free permittivity value ($\varepsilon^T_{33}/\varepsilon_o$) of 1027. However, d_{33}, kp and $\varepsilon^T_{33}/\varepsilon_o$ value found to be 151 pC/N, 35 % and 1010, respectively for x = 0.08 compositions.

4.2 Synthesis and characterization of $Na_2Ti_6O_{13}$ whiskers and their transformation to (1-x) $Na_{0.5}Bi_{0.5}TiO_3$-x$BaTiO_3$ ceramics [b]

In previous chapter, the composition around morphotrpic phase boundary in (1-x)NBT-xBT was optimized. The composition $0.93Na_{0.5}Bi_{0.5}TiO_3$-$0.07BaTiO_3$ was identified as MPB composition. However, the sintering of NBT-BT is has some issues due to presence of elements having low melting temperature. In this chapter, a novel method for the synthesis of NBT-BT has been presented. This method deals with the synthesis of monoclinic $Na_2Ti_6O_{13}$ whiskers and their transformation to lead-free $0.93Na_{0.5}Bi_{0.5}TiO_3$-$0.07BaTiO_3$ (NBT-BT) ceramics. Synthesis of $Na_2Ti_6O_{13}$ templates was performed using molten salt synthesis (MSS) method. These whiskers were further characterized using XRD, SEM, TEM and HRTEM for structural analysis. Tape casting method was used to align the whiskers in a base matrix powder and subjected to various processing temperature to elucidate the microstructure and texture evolution. For this, SEM, HRTEM, AFM and EDS analysis were used as principal tools. The sintering process can be understood by dividing it into three stages, namely (i) transformation of monoclinic whiskers in to NBT-BT perovskite phase through topochemical reaction (<800^{o}C), (ii) localized sintering confined on single whisker (800-1050^{o}C), and (iii) liquid phase sintering as densification and grain growth occurs in the whole matrix (>1050^{o}C). The concentric growth ledges observed on grain surfaces were found to be preferably confined on the corners of cubical grains indicating <111> growth direction. The Lotgering factor (f_{100}) for the sintered matrix was found to decrease with increase in sintering temperature. The longitudinal piezoelectric constant (d_{33}) of samples sintered for 20h at 1175, 1200 and 1225 ^{o}C was measured to be ~153, ~216 and ~180 pC/N respectively.

[b] Reproduced with permission from [177]. Copyright 2010, the American Ceramic Society.

4.2.1. Background

Current generation piezoelectric actuators, sensors and transducers are fabricated mainly using lead-based piezoelectric composition [5,15,99]. However, there is growing environmental concern in use of lead which has prompted research in finding alternative lead-free compositions. $Na_{0.5}Bi_{0.5}TiO_3$-$BaTiO_3$ solid solution is considered as one of the promising lead-free candidate for possible replacement of lead-based ceramics [24]. This system consists of a morphotropic phase boundary (MPB) and it has been shown that the compositions close to MPB exhibit excellent electromechanical properties [24]. Considering the technological relevance of $Na_{0.5}Bi_{0.5}TiO_3$ (NBT) based ceramics, various methods have been adopted to synthesize this material including hydrothermal synthesis method [100,101], stearic acid gel method[102], the citrate method[103], mixed oxide route[104], and slurry synthesis with a transient Aurivillius–type structure[105]. In a recent work, in-situ high temperature diffraction measurements were performed in order to investigate the formation of NBT phase during the course of sintering [106]. Several researchers have also investigated the role of dopants such as Nd_2O_3, La_2O_3, Sm_2O_3, Nb_2O_5, Eu_2O_3, $MnCO_3$, Fe_2O_3, and Dy_2O_3 to achieve higher density and ferroelectric properties [107-112]. Most of the dopants are found to improve the electrical characteristics but at the same time shift the depoling temperature (T_d) towards room temperature (RT). The optimized composition in this system has been shown to be (1-x)$Na_{0.5}Bi_{0.5}TiO_3$-x$BaTiO_3$; x= 0.07 (denoted as NBT-BT in this chapter).

Conventionally, NBT ceramics are synthesized by mixed-oxide sintering route leading to random polycrystalline grain structure. It is well-known that piezoelectric properties are higher in oriented single crystals. However, the processing of single crystal is complicated and not cost-effective. The composition in single crystals is difficult to control and often leads to

variation of properties across the diameter and length of the ingot. The other alternative to achieve high property is by texturing of the piezoelectric ceramics [38]. Texturing refers to the orientation of grains with similar crystallographic orientation normally conducted using template grain growth (TGG) or reactive templated grain growth (RTGG) approaches. Both of these methods require templates having shape anisotropy with high aspect ratio [40,42-44,113,114]. Textured NBT-BT based ceramics processed using RTGG method by using $Bi_4Ti_3O_{12}$ templates were reported to exhibit d_{33} of 241 pC/N with lotgering factor f_{100} of 96%[41]. The ceramics processed using TGG method by using $SrTiO_3$[40] and NBT[115] templates were found to exhibit d_{33} of 200 pC/N at f_{100} of 94% and 299 pC/N at f_{100} of 87%.

The selection and synthesis of suitable template is the critical issue in fabrication of textured ceramics. However, the process of achieving texturing still remains a challenge which has limited its use across the laboratories and industry. It will be very interesting if certain degree of texturing can be achieved during the normal course of ceramic fabrication without using the complex multi-step TGG and RTGG process. One such possibility was investigated by using $Na_2Ti_6O_{13}$ single crystal whiskers that were aligned in the base matrix powder during tape-casting stage. Texturing of new composition requires in-depth understanding of phase transformation, microstructural development and high temperature chemical reactivity of base matrix powder with templates.

In this chapter, in-depth understanding of transformation mechanism of $Na_2Ti_6O_{13}$ into NBT-BT, microstructural development and overall densification mechanism for sintering stages was provided. Detailed discussion was provided on the synthesis and microstructure of $Na_2Ti_6O_{13}$ whiskers and subsequently their transformation in to NBT-BT ceramics. $Na_2Ti_6O_{13}$ whiskers were synthesized using molten salt synthesis method and characterized using SEM,

XRD, TEM and HR-TEM. A physical understanding of interaction between $Na_2Ti_6O_{13}$ whiskers and base matrix powder was performed using the results from microscopy and chemical analysis which provides insight on the transformation of whiskers with monoclinic phase to perovskite phase of $Na_{0.5}Bi_{0.5}TiO_3$-0.07$BaTiO_3$. The electrical response of these NBT-BT ceramics was investigated and correlated with the microstructure. This new method for synthesizing the NBT-BT ceramics opens the possibility of achieving varying grain shape and sizes with certain degree of texturing.

4.2.2. Experimental

4.2.2.1 Synthesis of $Na_2Ti_6O_{13}$ whiskers: The molten salt synthesis method was used to synthesize $Na_2Ti_6O_{13}$ whiskers. For this purpose, stoichiometric amount of Na_2CO_3 and TiO_2 (Rutile) powder was ball-milled for 24h followed by addition of controlled amount of NaCl. The ball-milling was performed using Y-stabilized ZrO_2 balls in polyethylene bottle. Various combinations of oxide to salt ratio (1:1, 1:2, 1:3) were investigated, however 1:2 ratio was found to provide required aspect ratio of the template whiskers and hence it was used for further experiments. The salt mixed oxide powders were heated at 1100^oC for 10h followed by cooling to RT. The mixture was then washed with deionized water several times to remove the trace salt. The basic mosaic of rutile structure is TiO_6 octahedron where octahedra share parallel edges and form chain if viewed along c-axis and the chains are connected by sharing the vertices, however orientation of chains are different[116] Rutile (TiO_2) reacts with Na_2CO_3 leading to reconstruction of octahedra to produce $Na_2Ti_6O_{13}$ whisker. The octahedra chain in the rutile is combined as three units to produce $Na_2Ti_6O_{13}$ [116].

4.2.2.2 Sample preparation: In order to prepare the perovskite specimen, the stoichiometric amount of raw powder was batched according to following chemical reaction:

$$0.93[Na_2Ti_6O_{13}+1/2Na_2CO_3+3/2Bi_2O_3] + 6[0.07(BaCO_3+TiO_2)] \longrightarrow 6[0.93Na_{0.5}Bi_{0.5}TiO_3\text{-}0.07BaTiO_3] + 0.885CO_2 \quad (4.1)$$

Table 4.1 List of the amount of various starting materials used for the synthesis NBT-BT using $Na_2Ti_6O_{13}$.

$Na_2Ti_6O_{13}$ (g)	Bi_2O_3 (g)	Na_2CO_3 (g)	TiO_2 (g)	$BaCO_3$ (g)	Total weight (g)
12.5869	16.2504	1.2321	0.8390	2.0722	32.9805

The ball milling of mixture consisting of Na_2CO_3 (Alfa Aesar, 99.8 %), Bi_2O_3 (Alfa Aesar, 99.9 %), $BaCO_3$ (Alfa Aesar, 99.8 %) and TiO_2 (Alfa Aesar, 99.5 %) powders was performed in polyethylene bottles using yttria-stabilized ZrO_2 balls as milling media and high purity ethanol as solvent. The resulting matrix powder was mixed with $Na_2Ti_6O_{13}$ whisker templates in commercial binder system 'B73225' (Ferro Corporation) to form slurry which was tape casted on polymer sheet with 200 µm opening of the doctor blade. After drying, the tape was cut in to 20 x 20 mm size and then laminated at 80^{o}C for 1h. The laminated tape was then cut in to desired shape and subjected to binder burn out at 400^{o}C for 4h with heating rate of ~0.5 ^{o}C/min. Subsequently, these specimens were subjected to two step heating cycle; 800^{o}C for 2h followed by 1175^{o}C for 20h. In order to characterize the phase and microstructual change with texture evolution, samples were subjected to sequential heating in the range of 800 – 1175^{o}C with temperature interval of 100^{o}C. The microstructural evolution between 1000 – 1100^{o}C was closely monitored with temperature interval of 25^{o}C. In order to elucidate the grain growth and

densification mechanism, samples were subjected to isothermal heating at 1175^{o}C for varying time periods. The density of sintered specimens was measured by using Archimedes principle. The surface morphology of the sintered samples was observed using a LEO Zeiss 1550 (Zeiss, Munich, Germany) scanning electron microscope equipped with HKL Nordlys II Electron Back Scatter Diffraction (EBSD) system. In order to investigate the structure of $Na_2Ti_6O_{13}$ whiskers, single whisker was mounted on FIB grid using focused ion beam (FIB) machine (FEI Helios 600 NanoLab) and subsequently characterized by a FEI Titan 300 (FEI, Hillsboro, USA) transmission electron microscope (TEM). The degree of orientation was determined from the XRD pattern in the range of $2\theta = 20 - 60^{o}$ by Lotgering's method. The Lotgering factor *f* is defined as the fraction of area textured with required crystallographic plane using the formula [117]:

$$\text{Lotgering Factor } f_{h00} = \frac{P - P_o}{1 - P_o}, P = \frac{\Sigma I(h00)}{\Sigma I(hkl)}, P_o = \frac{\Sigma I_o(h00)}{\Sigma I_o(hkl)} \quad (4.2)$$

where I and I_o are intensity of the diffraction lines (hkl) of textured and randomly oriented specimens, respectively. For electrical measurement, silver electrode was applied on the flat faces of the rectangular specimen and then fired at 650^{o}C for 30 minutes. Samples were poled at 5 kV/mm at 60^{o}C in a silicon oil bath. The longitudinal piezoelectric constant (d_{33}) was measured by Berlincourt d_{33}-meter.

4.2.3. Results and discussion:

4.2.3.1 Structural characterization of $Na_2Ti_6O_{13}$:

Figure 4.7(a) shows the XRD patterns of $Na_2Ti_6O_{13}$ whiskers measured at room temperature. It can be seen that $Na_2Ti_6O_{13}$ whisker crystallizes in pure monoclinic phase.

$Na_2Ti_6O_{13}$ belongs to the family of $M_2Ti_nO_{2n+1}$ compounds, where n = 6 or 3 and M = Na or K. $Na_2Ti_6O_{13}$ has a base centered monoclinic structure with parameters, a = 1.51310 nm, b= 0.37450 nm, c = 0.91590 nm and β = 99.3°C with spatial group C2/m[118]. Figure 4.7(b) shows the microstructure of $Na_2Ti_6O_{13}$ whiskers synthesized using molten salt method with 1:2 oxide to salt ratio. These whiskers were found to exhibit high aspect ratio suitable for aligning in the base matrix. The estimated average length of whisker was found to be ~10-20 μm and thickness was in the range of 0.5 – 1.0 μm.

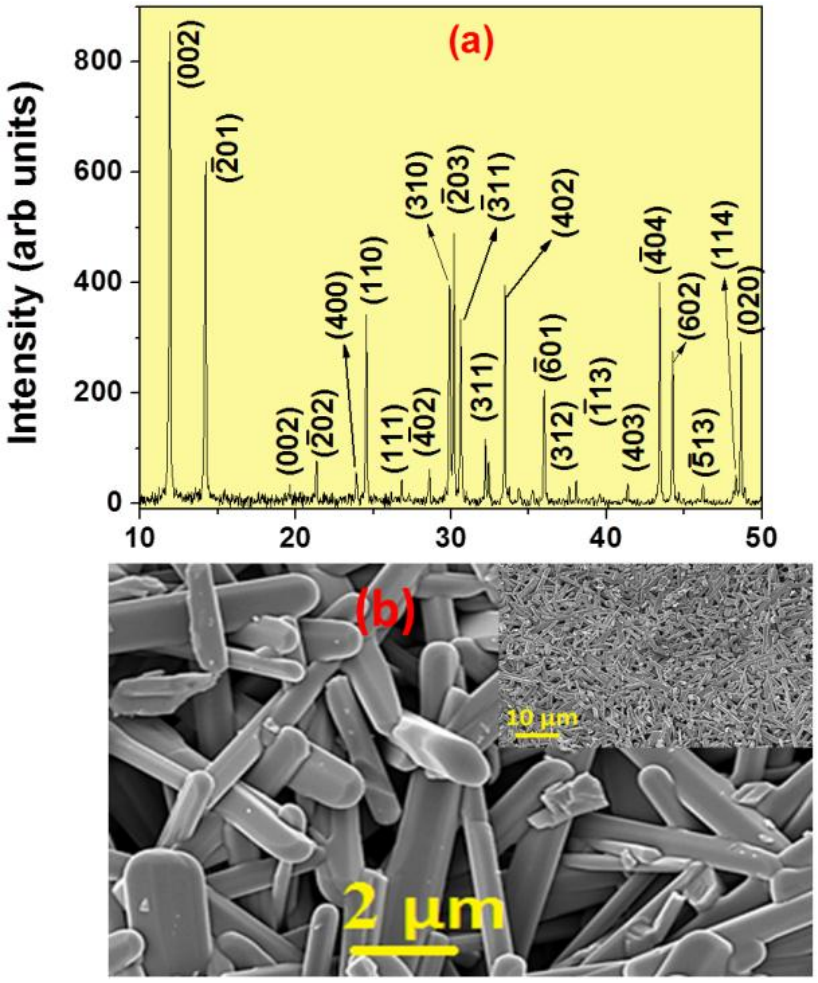

Figure 4.7: (a) XRD-patterns of $Na_2Ti_6O_{13}$ whiskers recorded at RT, (b) SEM images of $Na_2Ti_6O_{13}$ whiskers synthesized using molten salt synthesis method.

Figure 4.8(a) shows the TEM image of whisker mounted on the FIB grid (inset of Fig. 4.8(a) representing the sample). HR-TEM image of this whisker is shown in Fig. 4.8(b). Two dimensional lattice fringes are clearly seen in this image with interplanar spacing of fringes of 0.90 and 0.62 nm corresponding to the d-spacing of (001) and (201) planes respectively. The

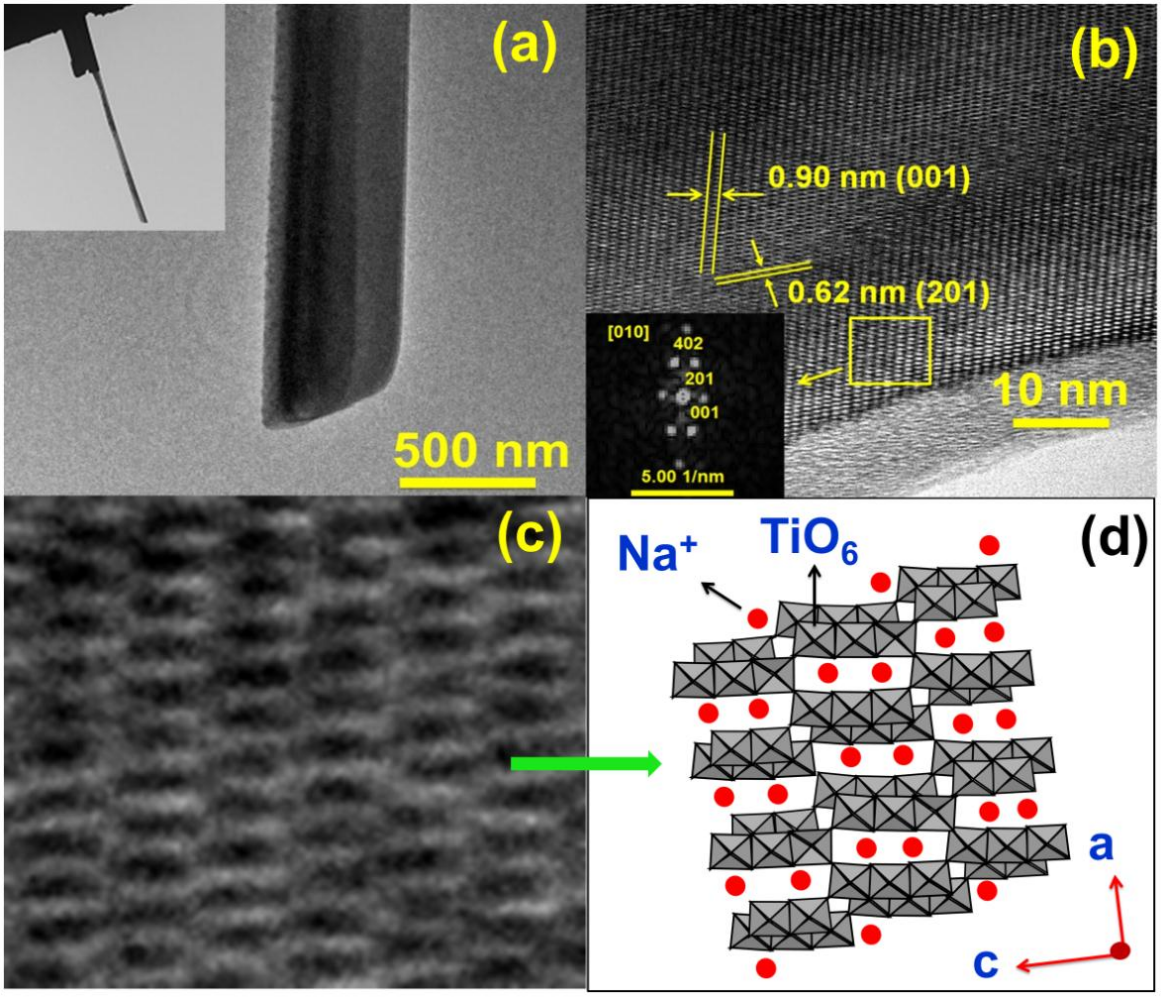

Figure 4.8 : (a) TEM image of $Na_2Ti_6O_{13}$ whisker, (b) HR-TEM image of $Na_2Ti_6O_{13}$ whiskers from [010] zone axis (inset is showing the FFT of selected portion), (c) magnified view of the lattice image depicted in (b), and (d) schematic representation of structure of $Na_2Ti_6O_{13}$ whisker**.**

(001) lattice plane is parallel to the length of whisker. Fast Fourier transform (FFT) of selected area from lattice image was indexed with [010] zone axis in which plane (201) can be observed with interplanar spacing of 0.62 nm. This HR-TEM (Fig.4.8 (b)) analysis shows microstructure

of planes extending without any grain boundaries depicting single crystalline nature of $Na_2Ti_6O_{13}$ whiskers. Figure 4.8 (c) is a magnified view of the lattice image and Fig. 4.8(d) represents the schematic structure model of $Na_2Ti_6O_{13}$ crystals**.** In $Na_2Ti_6O_{13}$ structure, a 3-D network of TiO_6 octahedron joined by corners and edges form a zig-zag structure with rectangular tunnels along y-axis, where sodium ions are located. To elucidate further about crystalline structure of whisker, selected area electron diffraction (SAED) patterns were measured by tilting the $Na_2Ti_6O_{13}$ crystal to different zone axes (Figure 4.9). Figure 4.9(a) shows the SAED pattern indexed with (201)

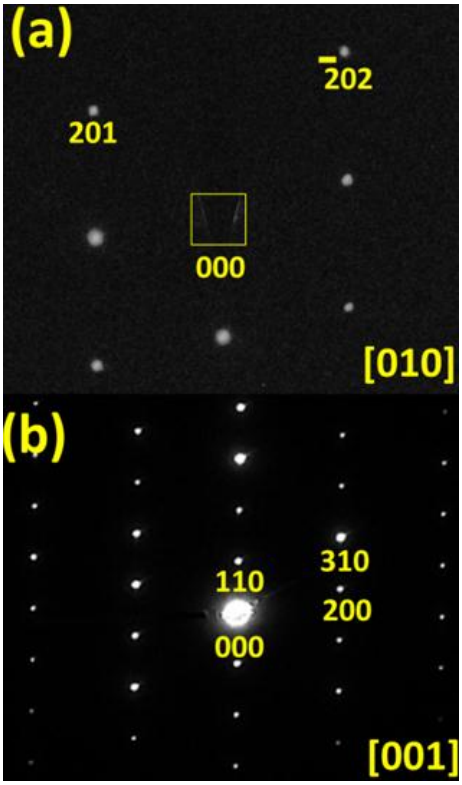

Figure 4.9: SAED patterns recorded on whisker from various zone axes**.**

and $(\bar{2}02)$ planes observed from [010] zone axis. Figure 4.9(b) shows the SAED pattern measured from [001] zone axes with planes indexed as (200), (310) and (110). Both SAED patterns (Fig. 4.9(a) - (b)) were found to exhibit single crystalline nature of whiskers.

4.2.3.2 Transformation of $Na_2Ti_6O_{13}$ whiskers in to NBT-BT ceramics

4.2.3.2.1 XRD analysis and density measurements:

Figure 4.10 (a) depicts the microstructure of single tape of matrix containing $Na_2Ti_6O_{13}$ template whiskers along with binder system. Whiskers were found to be embedded in base matrix powder along with the binder system and were mostly arranged in the direction parallel to the tape casting. The XRD-spectrum recorded at RT on this tape is shown in Fig. 4.10 (b). The change in intensity of the powder peaks with respect to $Na_2Ti_6O_{13}$ peaks indicates the preferred orientation of whiskers in the tape. Figure 4.11 (a) shows the XRD patterns measured at various stages of heat treatment process. Up to 400^{o}C (which corresponds to the binder burnout temperature) no reaction occurred between $Na_2Ti_6O_{13}$ whiskers and powder matrix. XRD-spectra recorded on specimen heated for 2h at 800^{o}C indicates that whiskers reacted with powder matrix leading to structural transformation to perovskite phase NBT-BT. Figure 4.11 (b) depicts the variation of Lotgering factor f_{100} (fraction of area textured in (100) plane) with change in temperature. It was found that in the range of 800 – 900^{o}C, the magnitude of f_{100} was around 20% which decreases upon heating to higher temperatures. Thus after transformation to NBT-BT perovskite phase at 800 and 900^{o}C, specimens were found to exhibit lower but significant degree of orientation (texture) ~20% in (100) plane. This 20% texture was found to decrease rapidly with further increase in temperature which can be associated with rapid microstructural changes as discussed in detail later.

In order to investigate the sintered phase, specimens processed at 1175 ^{o}C for 20h were crushed to fine powder and XRD analysis was conducted as shown in Fig. 4.11 (c).

Inset of Fig. 4.11 (c) depicts the magnified view of (111) and (200) peak. The splitting of (111) peak indicates rhombohedral phase, however the splitting of (200) indicates tetragonal

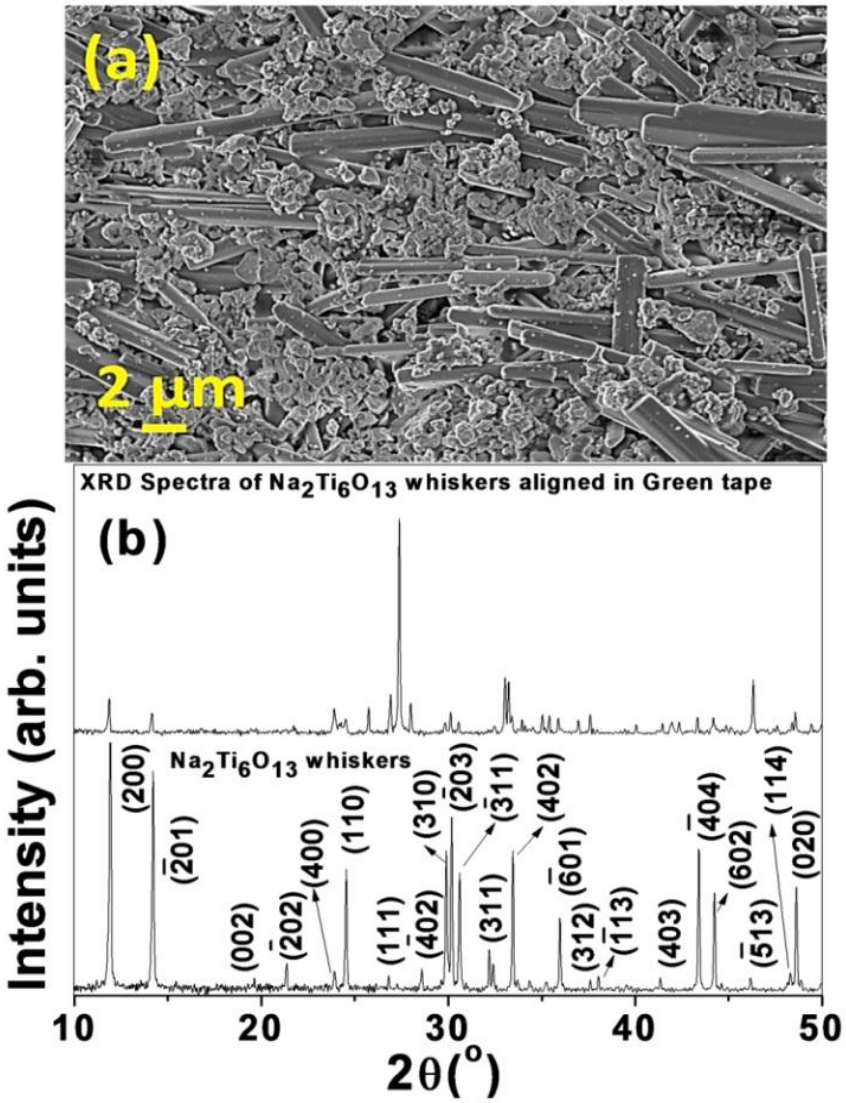

Figure 4.10: (a) SEM image of single tape containing template whiskers embedded in the base matrix powder, and **(**b) Comparative change in intensities of various reflections observed in XRD-spectra recorded for aligned whiskers embedded in green tape with respect to that of powder XRD-spectra of whiskers.

nature of the specimen. Therefore, Fig. 4.11 (c) suggests that this composition was close to

morphotropic phase boundary (MPB)[119]. The XRD spectra recorded on powdered specimens processed at further higher temperatures (1200^{o}C and 1225^{o}C for 20h) were found to be similar.

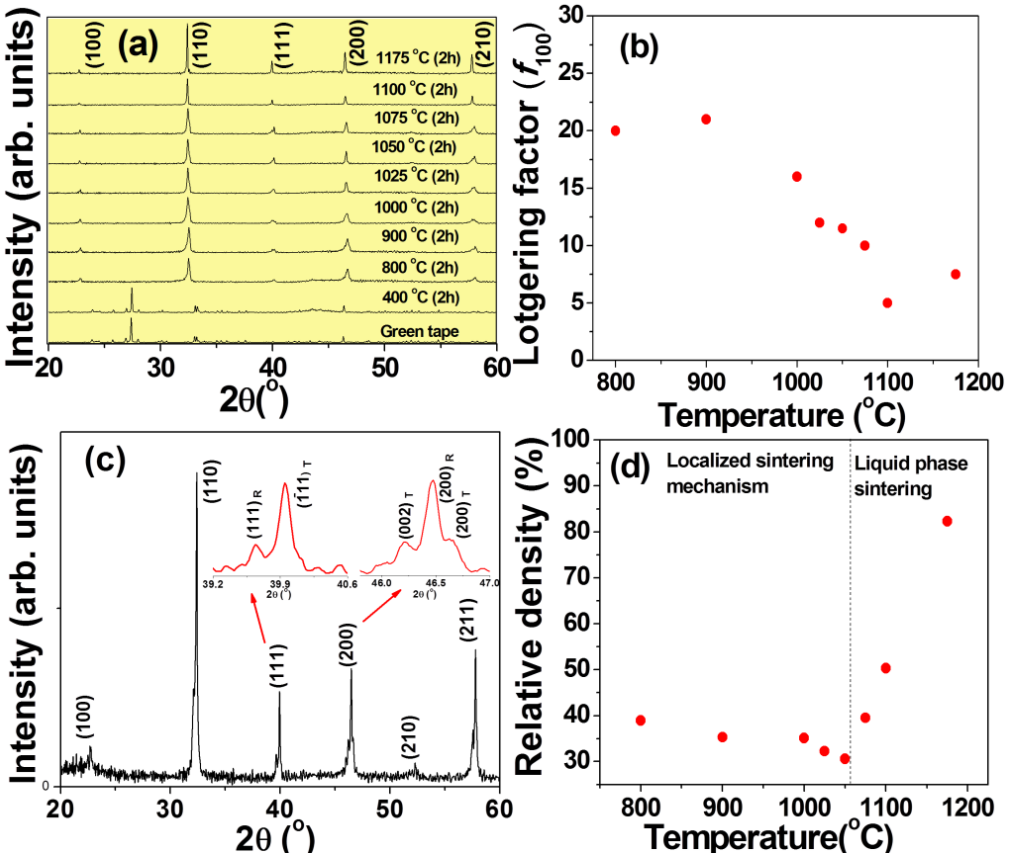

Figure 4.11 : (a) XRD spectra measured at RT for the specimen heated at various temperatures, and (b) Lotgering factor (f_{100}) as a function of temperature, (c) RT XRD-spectra of the powdered NBT-BT specimen processed at 1175C for 20h, Inset of this plot indicates magnified view of {111} and {200} reflections, (d) Relative density as a function of sintering temperature.

The characteristic XRD pattern of NBT-based random ceramics exhibited highest intensity for {110} reflections [120]. The relative intensity of powder diffraction lines can be given as [121]:

$$I = |F|^2 \, p \left(\frac{1+\cos^2 2\theta}{\sin^2 \theta \cos \theta} \right) e^{-2M} \qquad (4.3)$$

where I is relative integrated intensity (arb. units), F is structure factor, p is multiplicity factor, and θ is Bragg angle. The trigonometric terms given in the parenthesis are Lorentz-polarization factor and e^{-2M} is the temperature factor with M dependent on amplitude of thermal vibration and scattering angle. The intensities can be changed through [121]: (i) preferred orientation i.e. grains in polycrystalline matrix are aligned in preferred crystallographic orientation, and (ii) extinction i.e. decrease in the integrated intensity of diffracted beam as the crystal (or individual grains in case of polycrystalline specimens) becomes nearly perfect. In present investigation, XRD-spectrum recorded on specimens after phase transformation was similar to characteristic XRD-spectrum of randomly oriented ABO_3 type perovskite with highest intensity for {110} reflections, though relative intensities for various reflections were found to vary. This further confirms the texture evolution in the sintered specimens.

The relative density as a function of temperature on all the specimens subjected to heat treatment for 2h is shown in Fig. 4.11(d). It can be observed that the density of NBT-BT ceramic synthesized with $Na_2Ti_6O_{13}$ whiskers was about 40% of theoretical density at 800^{o}C which is the phase transformation temperature. On further increasing the temperature, relative density decreases slowly up to 1050^{o}C. However, when specimens were heated above 1050^{o}C, the density starts to increase and reaches to 82% of the relative theoretical density at 1175^{o}C (2h). Due to low density, the specimens were difficult to pole and suffered electrical breakdown at very low field. However, after heating the specimen at 1175^{o}C for 20h, the relative density reaches up to 93% of theoretical density but the Lotgering factor was as small as 7%. The specimens sintered at 1200^{o}C for 20h were found to have density of 97% whereas specimens sintered at further higher temperature were characterized by relatively smaller density ~95% due to loss of volatile elements. Both these specimens were characterized by small degree of

texturing 6-7%. The electrical response measured on these specimens is presented in section 4.2.3.2.6.

Generally, densification occurs with increase in processing temperature up to certain extent. But in this case, the density first decreases and then increases upon further heating. Therefore Fig. 4.11(d) can be divided in two temperature range sections: (i) area where density decreases with increase in temperature, and (ii) the area where density increases with increase in temperature. In order to understand the variation of density with temperature, a systematic study of microstructural evolution and texture was conducted at various processing temperatures.

4.2.3.2.2 Scanning electron microscopy:

Figure 4.12 (a) – (b) shows the microstructure of specimen after binder burn-out process (400^{o}C), leaving behind $Na_2Ti_6O_{13}$ whiskers embedded in base matrix. Smooth surface of the whiskers embedded in the powder matrix can be clearly observed indicating absence of secondary reaction on the surface at this stage. On further heating the system to 800^{o}C for 2h, whiskers in the sample could be found without much change in morphology (Fig. 4.13(a)-(c)). The microstructure at this temperature was porous. However, RT XRD-spectrum indicates conversion of monoclinic whiskers to ABO_3 type perovskite phase after reacting with the base matrix (Figure 4.11(a)). Figure 4.13 (d) - (f) show the micrographs of specimen heated at 900^{o}C for 2h. Microstructures were characterized by large porosity along with the intact shape of whiskers, which are now perovskite.

In the magnified images of Figure 4.13(c) and (f), we can notice the rough surface of whiskers after transformation. These samples were further heated to 1000^{o}C resulting in grain

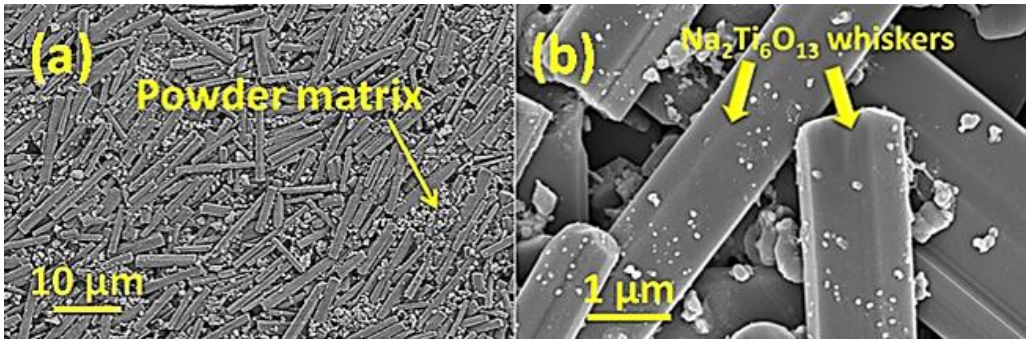

Figure 4.12(a)-(b): Microstructure of the specimen containing $Na_2Ti_6O_{13}$ whiskers in powder matrix after binder burnout process at 400 ^oC.

coarsening on whisker with size in the range of 100 – 300 nm indicating polycrystalline nature as shown in Fig. 4.13 (g)-(i). After 1000^oC, there was rapid change in microstructure and thus the SEM imaging was performed on specimens heated in small temperature intervals of $\Delta 25^oC$, from 1000 to 1100^oC. Figures 4.13 (j-l) and (m-o) show the microstructure of specimen heated at 1025 and 1050^oC, respectively. One can clearly observe the interconnected grains giving rise to bamboo type structure (Fig. 4.13 (o)), however the magnified view of these interconnected grains show presence of growth steps on grain surfaces (Fig 4.13 (p)). The microstructure of the specimen heated at 1075, 1100 and 1175^oC is shown in Fig.'s 4.14 (a-c), (d-f) and (g-i), respectively. These microstructures have residual porosity. But interestingly as this system was further heated to 1100^oC for 2h, the morphology got completely changed into net-like structure consisting of grains connected through neck. Moreover, microstructure of the specimen processed at 1175^oC (2h) was much denser as also observed in the temperature dependence of density plot.

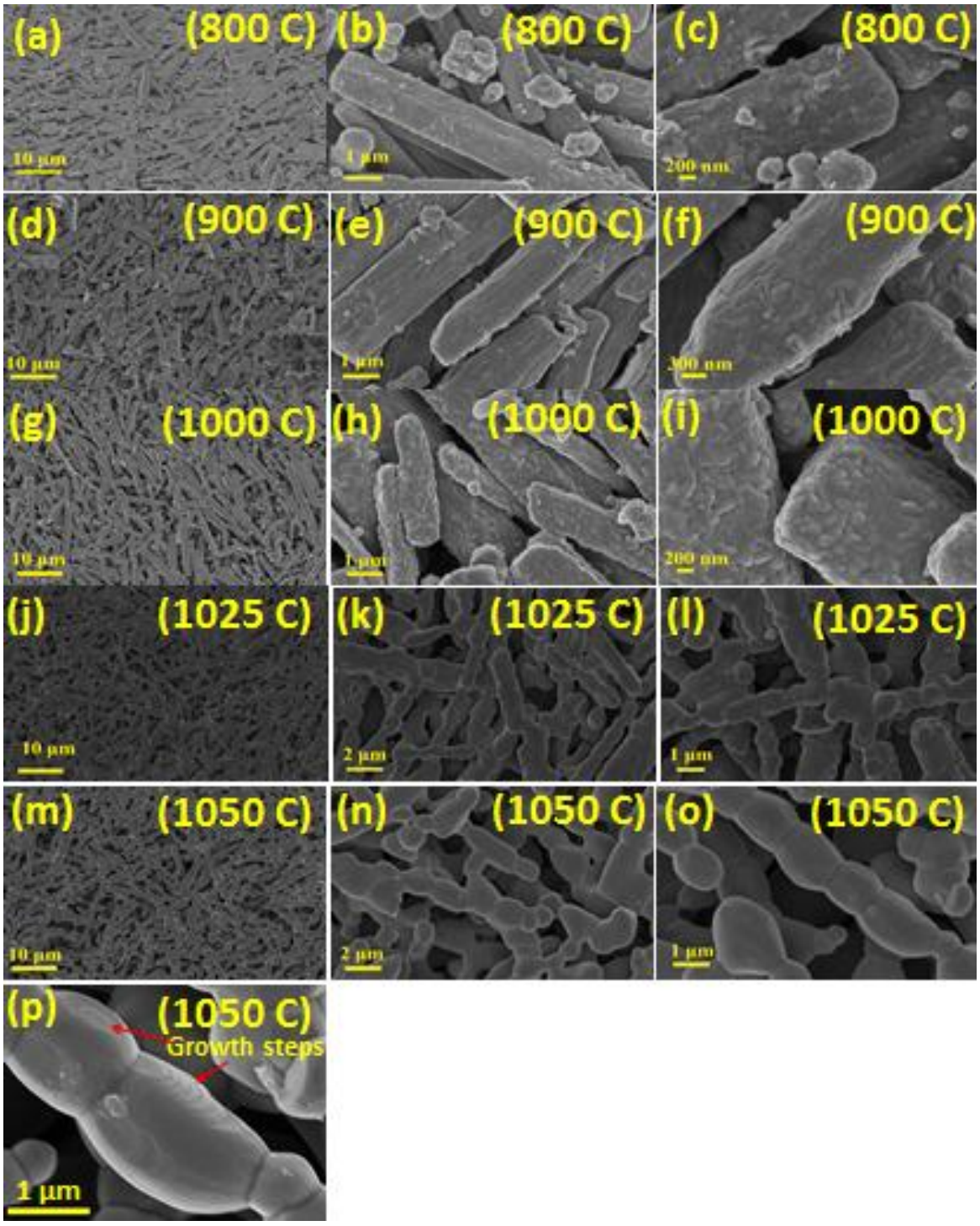

Figure 4.13: Microstructure of the specimen at various stages of heat treatment: (a-c) 800 ^{o}C (2h), (d-f) 900 ^{o}C (2h), (g-i) 1000 ^{o}C (2h), (j-l) 1025 ^{o}C (2h), (m-o) 1050 ^{o}C (2h), (p) magnified view of the micrograph (o) depicting the grain boundary regime

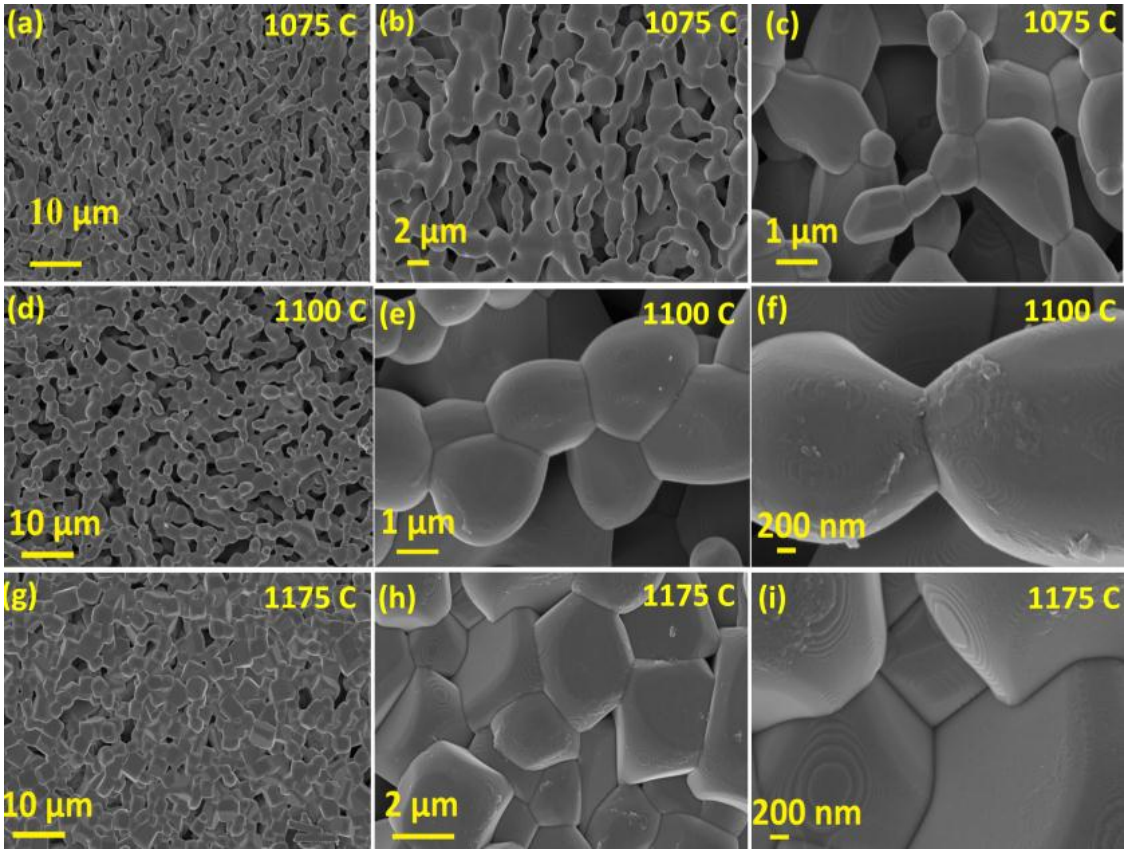

Figure 4.14: Microstructure of the specimen at various stages of heat treatment: (a-c) 1075^{o}C (2h), (d-f) 1100^{o}C (2h), (g-i) 1175^{o}C (2h).

Figure-4.15 (a) shows the microstructure of the specimen sintered at 1175^{o}C for 20h. Figure 4.15 (b) shows the EBSD (Electron backscattered diffraction image) image of same specimen while Fig. 4.15(c) is the inverse pole figure (IPF) of corresponding EBSD orientation map shown in Fig. 4.15(d) for specimen processed at 1175^{o}C for 20h. This orientation map (indexed using $Na_{0.5}Bi_{0.5}TiO_3$ R3c space group) clearly depicts the spread in orientation of grains. The morphology of specimens sintered at 1200^{o}C and 1225^{o}C for 20h is shown in Fig. 4.15 (e) and 4.15(f) respectively. One can see the presence of abnormal grain growth in the specimen processed at 1200^{o}C for 20h as few bigger grains were found to be embedded in matrix of smaller grain. On further increasing the temperature, uniformly distributed larger grains were

observed as a result of Ostwald ripening mechanism due to formation of liquid phase[122]. The average grain sizes measured for specimen sintered at 1200^{o}C and 1225^{o}C for 20h was found to be ~15 and ~152 µm. Next, the specimens were subjected to isothermal heat treatment at 1175^{o}C for different length of time. Figure 4.16(a) depicts the variation in grain size and rate of grain growth with time at 1175^{o}C. As can be observed from this figure that grain size increases rapidly when the sample was heated for 80 min, after which the grain growth rate (dG/dt) decreases exponentially and almost becomes constant for prolonged exposure of heat treatment.

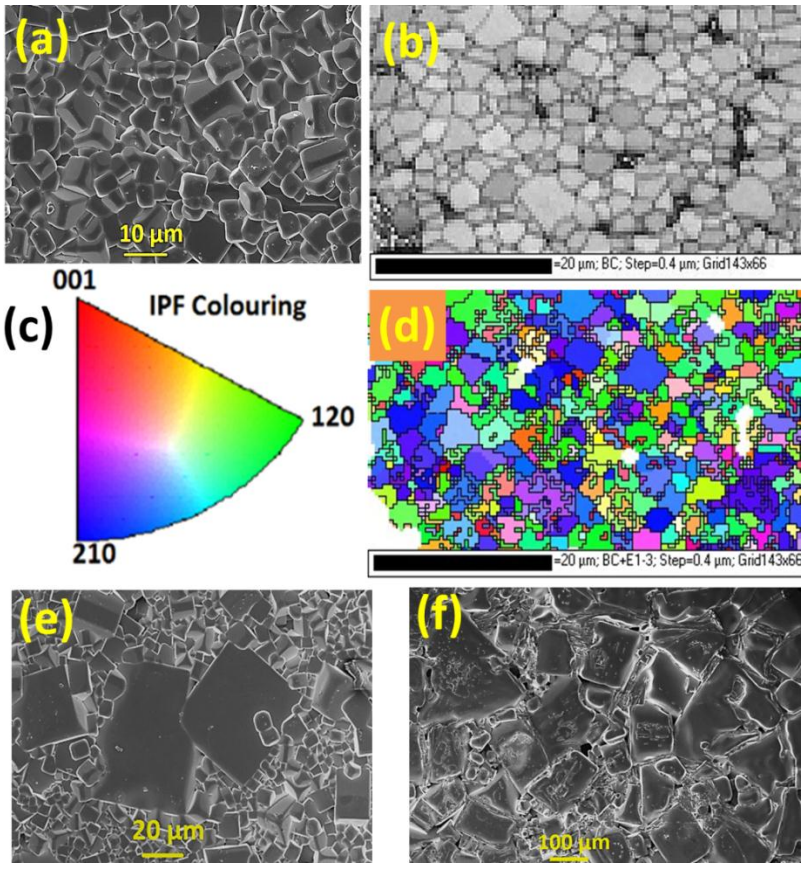

Figure 4.15 (a) SEM micrographs of specimen sintered at 1175 ^{o}C for 20 h, (b) EBSD image of this specimen (1175^{o}C, 20h), (c) Inverse pole figure (IPF) corresponding to grain orientation map presented in (d) for specimen processed at 1175 ^{o}C for 20h, (e) SEM image of the specimen processed at 1200 ^{o}C for 20h, and (d) SEM micrographs of the specimen processed at 1225 ^{o}C for 20h.

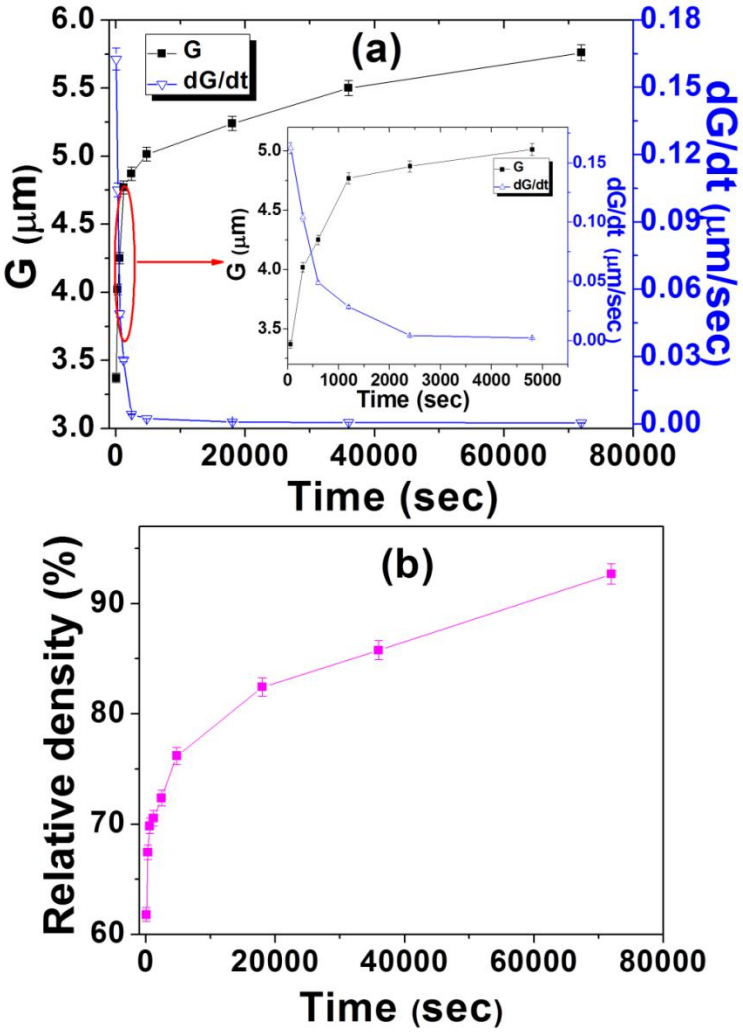

Figure 4.16: (a) Variation of grain size and grain growth rate with respect to change in temperature, and (b) temperature dependence of relative density with respect to the change in time.

If the rate of grain boundary migration V_p (sometimes called grain boundary velocity) is taken to be approximately equal to the instantaneous rate of grain growth then one can relate them as[123]:

$$V_p = \frac{dG}{dt} = M_b F_b \qquad (4.4)$$

where G is the average grain size, M_b is the boundary mobility and F_b is the driving force for boundary migration. It was found that the specimen exposed to prolonged heat treatment has lower driving force F_b and decreasing grain growth rate. This was expected due to the fact that increase in grain size leads to decrease in grain-boundary area per unit volume, which in turn reduces the interfacial energy per unit volume. Therefore, the driving force for grain growth is lower which further leads to reduction in growth kinetics. Figure 4.16(b) depicts the change in density with respect to time for isothermal heat treatment. It was found that the trend in variation of density with respect to time of isothermal heat treatment is similar to that of grain size variation. Initially, densification occurs very fast and then slows with the time, which is similar to that observed in liquid phase sintering [124]. Thus, densification and coarsening compete with one another and densification slows down after prolonged exposure to heat treatment. In order to understand the role of crystalline structure and chemical composition across the grain boundary towards sintering, detailed HR-TEM and EDS analyses were performed on the specimen heated at 1075^{o}C and 1175^{o}C for 2h.

4.2.3.2.3 Transmission electron microscopy (TEM):

For this analysis, specimens were prepared by standard polishing technique, i.e. mechanical grinding, dimpling and Ar ion beam milling. Figure 4.17(a) shows a TEM image of a specimen heated at 1075^{o}C for 2 h depicting interconnected grains with bamboo like structure. Figure 4.17 (b) shows a HRTEM image around grain boundary region revealing lattice structure. The top inset on the right side of Fig. 4.17 (b) depicts the low magnification image of region-of-interest. The change in contrast in the grain boundary region indicates that boundary plane is not vertical rather inclined at an angle. However, the grain boundary at this temperature was not as sharp as that formed at higher temperature. Lattice image depicting plane with various

orientations marked with arrows can be seen in high resolution image. The yellow arrows show planes with larger interplanar spacing than those marked with red arrows. The magnified view of lattice image from spot A and spot B is depicted in the inset marked with A and B, respectively. The interplanar spacing at spot A and B was found to be 0.83 nm and 0.42 nm, respectively.

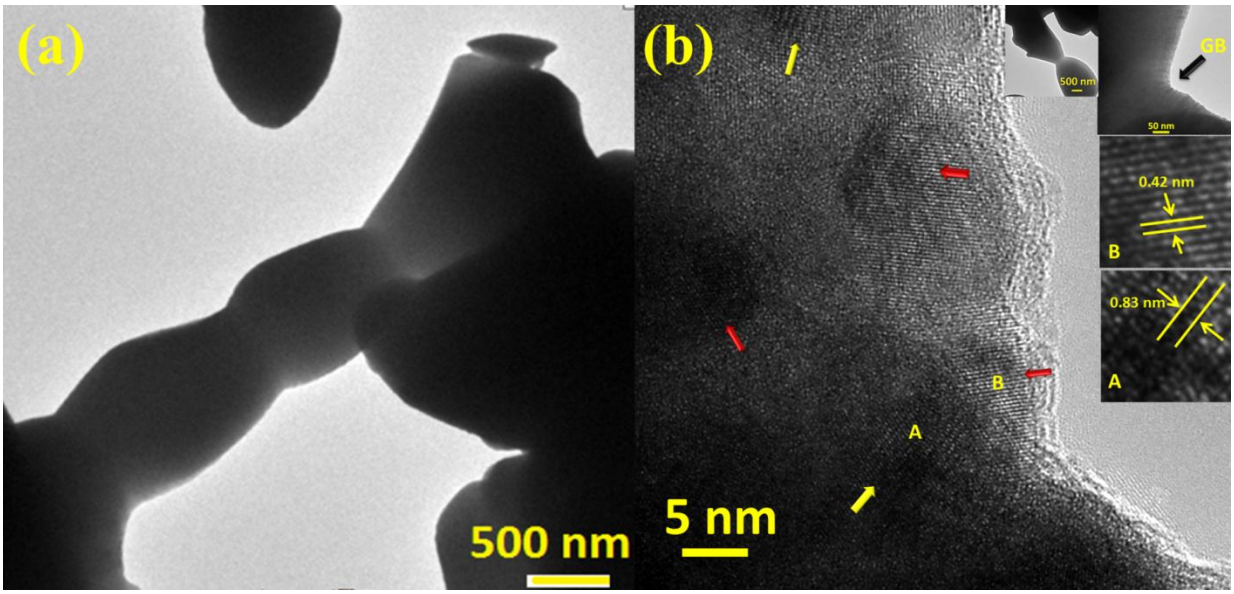

Figure 4.17: (a) TEM image of specimen heated at 1075^{o}C (2h), (b) HR-TEM lattice image at the grain boundary region of the same specimen (arrows indicate planes with different orientation, inset depicting the low magnification image, magnified view of spot A and spot B of lattice image)

The interplanar spacing of 0.42 nm is close to 0.4242 nm of (110) plane of the rhombohedral $Na_{0.5}Bi_{0.5}TiO_3$ (NBT) phase [120] (JCPDS # 85-0530). However, the interplanar spacing of 0.83 nm is much larger than that of for NBT phase and can be attributed to the presence of metastable intermediate phase during the transformation process. The presence of planes with various orientations suggests that system is in transient state. Thus, the system requires further thermal activation to increase diffusion of various species in order to achieve more ordered and homogenous state.

In order to investigate the chemical homogeneity across grain boundary and to identify preferred diffusion path of corresponding chemical species, EDS line scan was performed across the grain boundary as marked red line in a STEM-HAADF image (Fig. 4.18 (a)). While recording EDS spectra, drift correction was used to achieve higher accuracy in measurements. Figure 4.18 (b) shows the variation in ratio of atomic percent of Na/Ti and Bi/Ti across the grain boundary region marked with red line in Fig. 4.18 (a). It can be observed form this plot that Na/Ti ratio is

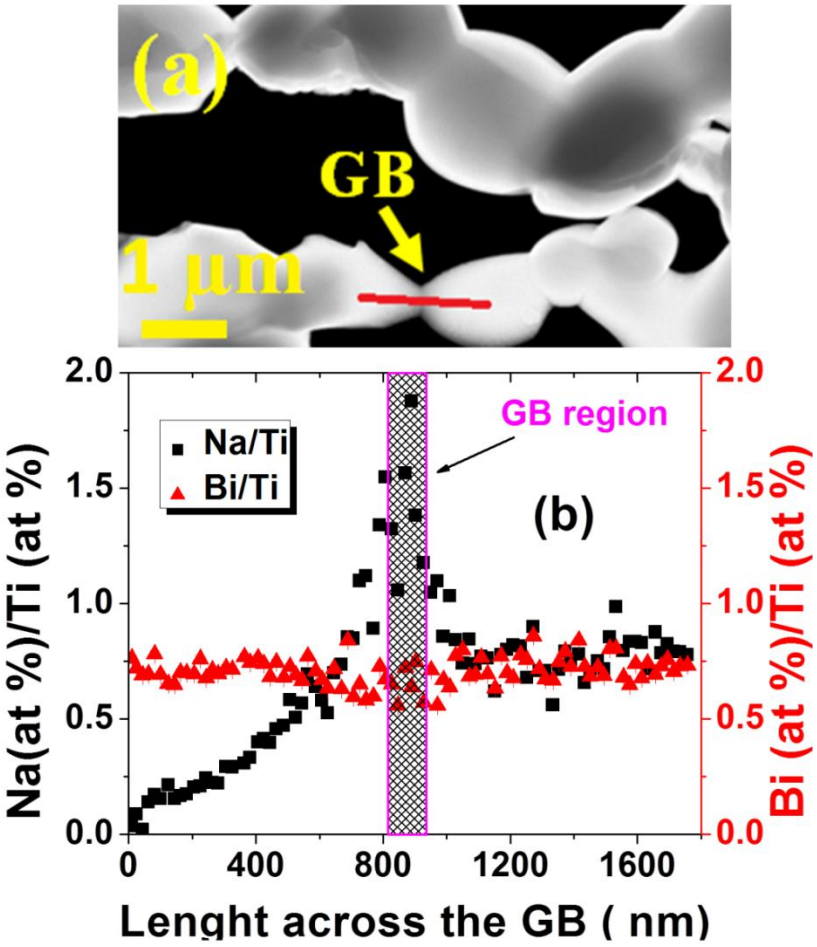

Figure 4.18: (a) STEM-HAADF image of the grain boundary region indicating region of EDS line analysis, (b) variation of atomic % ratio of Na/Ti and Bi/Ti

highest in the vicinity of grain boundary region and decreases on either side of the grain boundary regime, which indicates that grain boundaries are Na-rich resulting in chemical potential gradient across the grain boundary. Generally, Na ions have tendency of segregation on to grain boundary [125-127]. Na segregation in the grain boundary regime could be more prominent during liquid phase sintering as observed in the present investigation. However, Bi/Ti ratio remained almost constant across region of measurement. This chemical inhomogeneity further leads to rapid microstructural change observed around 1075^{o}C and indicates the presence of liquid phase sintering which facilitates rapid mass transport of Na and Bi.

Figure 4.19(a) depicts a lattice image across the grain boundary in a region of interest for specimen heated at 1175^{o}C for 2h. The inset in the lower corner on left side of this figure indicates STEM-HAADF image of the corresponding region. The spot EDS analysis was conducted on both sides of the grain boundary regime using the STEM mode (Table -4.2). This analysis was found to show that Bi and Na deficient phase exists at one side of grain boundary, while other side of the grain boundary possess Na and Bi rich phase [marked on lattice images in Fig. 4.19(a)]. Well-defined grain boundaries with grains possessing highly crystalline nature were observed. The indexing of HR-TEM image of Bi and Na deficient phase side of grain boundary was found to correspond with triclinic $Ba_2Ti_9O_{20}$ phase[128,129], while indexing of Na and Bi rich phase was found in accordance with tetragonal $Na_{0.5}Bi_{4.5}Ti_4O_{15}$ phase[130-132]. In Na and Bi deficient side region, $(\bar{1}10)$ plane was marked with interplanar spacing of 1.00 nm, while in Bi and Na rich region the (008) plane was found to exhibit interlayer spacing of 0.51 nm. The Fast Fourier transformation (FFT) image of Na and Bi-rich region and Na and Bi-deficient region are shown in Fig. 4.19 (b) and (c) respectively. These FFT images were indexed using tetragonal $Na_{0.5}Bi_{4.5}Ti_4O_{15}$ and triclinic $Ba_2Ti_9O_{20}$ for Na and Bi-rich and deficient phases,

respectively. $Ba_2Ti_9O_{20}$ possess hollendite-like structure[c] but additional barium ions replace oxygen ions and disrupt the tunnel walls leading to formation of cavities which contains two barium ions per tunnel [128,129]. $Na_{0.5}Bi_{4.5}Ti_4O_{15}$ is a four layer ferroelectric with Curie temperature of 655^oC and crystal structure similar to the pseudo tetragonal $BaBi_4Ti_4O_{15}$ phase [130-132]. However, these phases were not uniformly distributed but rather localized entities resulting from compositional fluctuation due to liquid phase sintering. One might also expect these kinds of localized phases in sample processed at higher temperature and longer processing time. Moreover, the contribution of these localized phases towards diffuse nature of phase transition (DPT) in addition to polar nano regions (PNR) cannot be ruled out which is explained further for ε(T) plots presented in section 4.2.6.

Table-4.2 List of atomic % of various elements detected by EDS

Elements	**Na and Bi deficient phase**	**Na and Bi rich phase**
	Atomic %	**Atomic %**
Na	0.33 ±0.09	5.56 ±0.21
Bi	0.12 ±0.44	11.92 ±1.72
Ba	4.54 ±1.35	0.00
Ti	31.31 ±1.04	19.28 ±0.55
O	63.68±0.94	63.23±0.81

Figure 4.20 (a) shows the STEM-HAADF image of the microstructure depicting presence of liquid phase. To examine chemical composition on various spots marked in STEM image, EDS analysis was performed as shown in Fig. 4.20 (b). The ratio of Na/Ti, Bi/Ti and Ba/Ti was

[c] Hollandite structure is made of rutile mosaic with edge sharing and have large square tunnel [116].

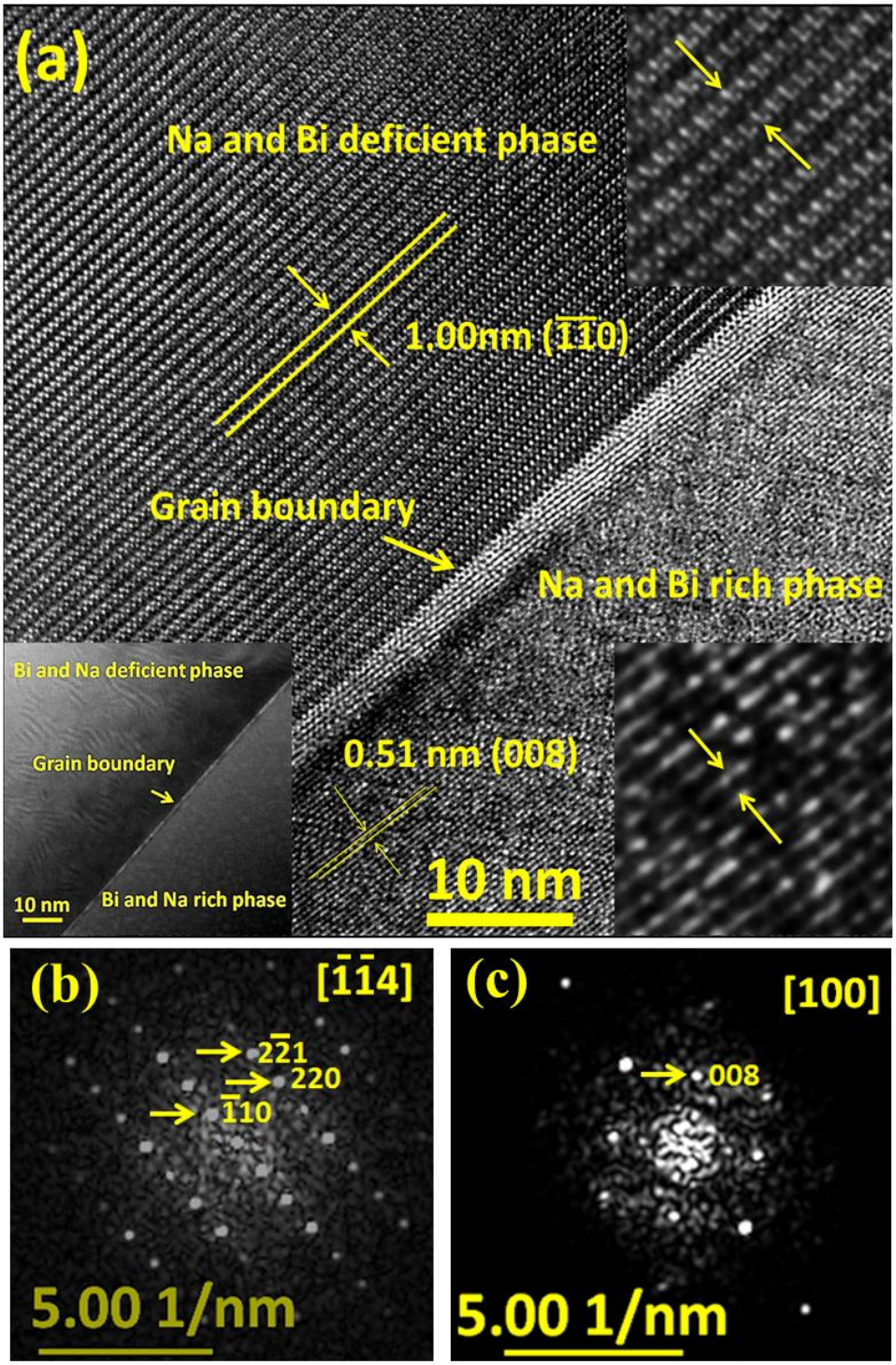

Figure 4.19: (a) HR-TEM image of the lattice across the grain boundary (inset on the right side of upper and lower corner of the image showing magnified view of corresponding region, while inset on left side of lower corner depicts STEM-HAADF image of region of interest), (b) FFT of the Bi and Na deficient phase, and (c) FFT of the Bi and Na rich phase.

highest on spot-1 and decreases for spot-2 and spot-3, indicating the presence of liquid phase with high content of Na, Bi and Ba. The observation of liquid phase confirms the argument about liquid phase sintering at higher temperatures.

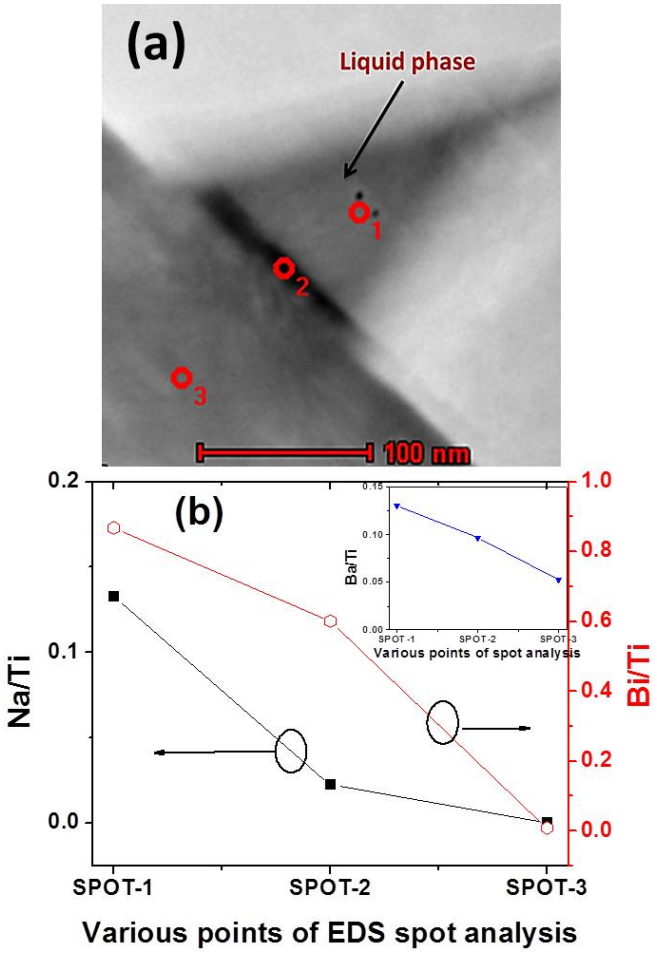

Figure 4.20: (a) STEM-HAADF image depicting presence of liquid phase in the specimen heated at 1175C (2h), (b) Variation of Na/Ti and Bi/Ti on various points of EDS spot analysis. Inset of Fig. 4.20 (b) showing Ba/Ti ratio on various points.

4.2.3.2.4 Equilibrium shape and growth mechanism:

The γ-plot is a polar diagram where the length of the radius coordinate is proportional to the magnitude of interface energy. The isotropic interface energy gives rise to spherical shape at equilibrium as a sphere has small surface area to volume ratio. However in case of anisotropic

surface energy, the shape of the crystal depends on the polar γ-plot. The condition for equilibrium is given by [133]:

Total surface energy$E_s = \int \delta(\gamma dA) = minimum$ (4.5)

Assuming equilibrium shape of NBT-BT grains in Fig. 4.21 (a), the schematic γ-plot and Wulff construction can be used to elucidate the difference in surface energy along <111> and <100> crystallographic direction. According to Wulff theorem[134,135], if planes are drawn perpendicular to the radius vectors where they cut γ-plot, the inner most envelope of these planes corresponds to the equilibrium grain shape. It can be observed from Fig. 4.21 (b), that the surface energy in <100> direction is lower than that of <111> direction giving rise to larger (100) faces. Thus, the 3D growth process of these crystalline grains was confined on the corners of pseudo cubic grains (Fig. 4.21 (a)) along the <111> direction [136].

The shape of growth patterns was found to be hexagonal suggesting growth direction is along <111> direction (Fig. 4.21(c)). The schematic of (111) plane is shown in Fig. 4.21(d). The morphology of the specimen heated for 20 h at 1175^{o}C was similar to that of specimen heated for 2h except larger grain size and higher density. It has been reported that grain growth is fastest along <111> direction [137-141] and therefore exhibits smallest (111) plane. Based on these prior results, the growth direction observed in these figures could be along <111>. However, these grains are randomly distributed in specimen (as observed in orientation map of EBSD image) giving rise to characteristic XRD-spectrum for NBT based ceramics as explained in previous section. The formation of these types of growth steps has been considered as a result of layer growth mechanism and can be explained by using the relationship for the formation of steps due to growth along screw dislocation[142]. Figure 4.21(e) shows that the step spreads out

with velocity v_{step} along the surface and with $\dot{R}$ in direction perpendicular to surface. In this case, the growth rate of the surface can be given by [143]:

$$\dot{R} = hv_{step}/\lambda_o \quad (4.6)$$

where h is step height, λ_o is the average distance between two steps, and v_{step} is the velocity. In the case of 2D nucleation, the growth rate is given by [144]:

$$\dot{R} = v_{step}\exp(-\frac{\Delta G^*}{kT}) \quad (4.7)$$

where ΔG^* is the energy barrier for 2D nucleation. Comparing equations (3.6) and (3.7), one obtains:

$$h/\lambda_o = \exp(-\Delta G^*/kT) \quad (4.8)$$

This equation is plotted in Fig. 4.21 (f) for h/λ_o from 0 to 0.5 at 1175^{o}C (1448K). It can be seen that with increase in value of ΔG^*, h/λ_o decreases exponentially indicating reduction in growth rate normal to the grain surface. In order to measure the step height (h) and average separation between the two steps (λ_o), atomic force microscopy (AFM) was performed.

Figure 4.22 (a)-(d) shows AFM images of surface morphology for specimen heated at 1000^{o}C (2h), 1050^{o}C (2h), 1175^{o}C (2h) and 1175^{o}C (20 h), respectively. The growth steps can be easily seen in these images. The measured step height h was found to be ~3.5 nm with ~ 46 nm of separation between two consecutive steps (λ_o) for both the specimen heated at 1175^{o}C. However, the average values of h and λ_o for the specimen heated at relatively lower temperature (1050^{o}C) was found to be ~ 11 nm and 94 nm, respectively. The higher average value of λ_o than that of h indicates that $\dot{R}$ is much slower than that of v_{step} and thus steps spread out faster leading

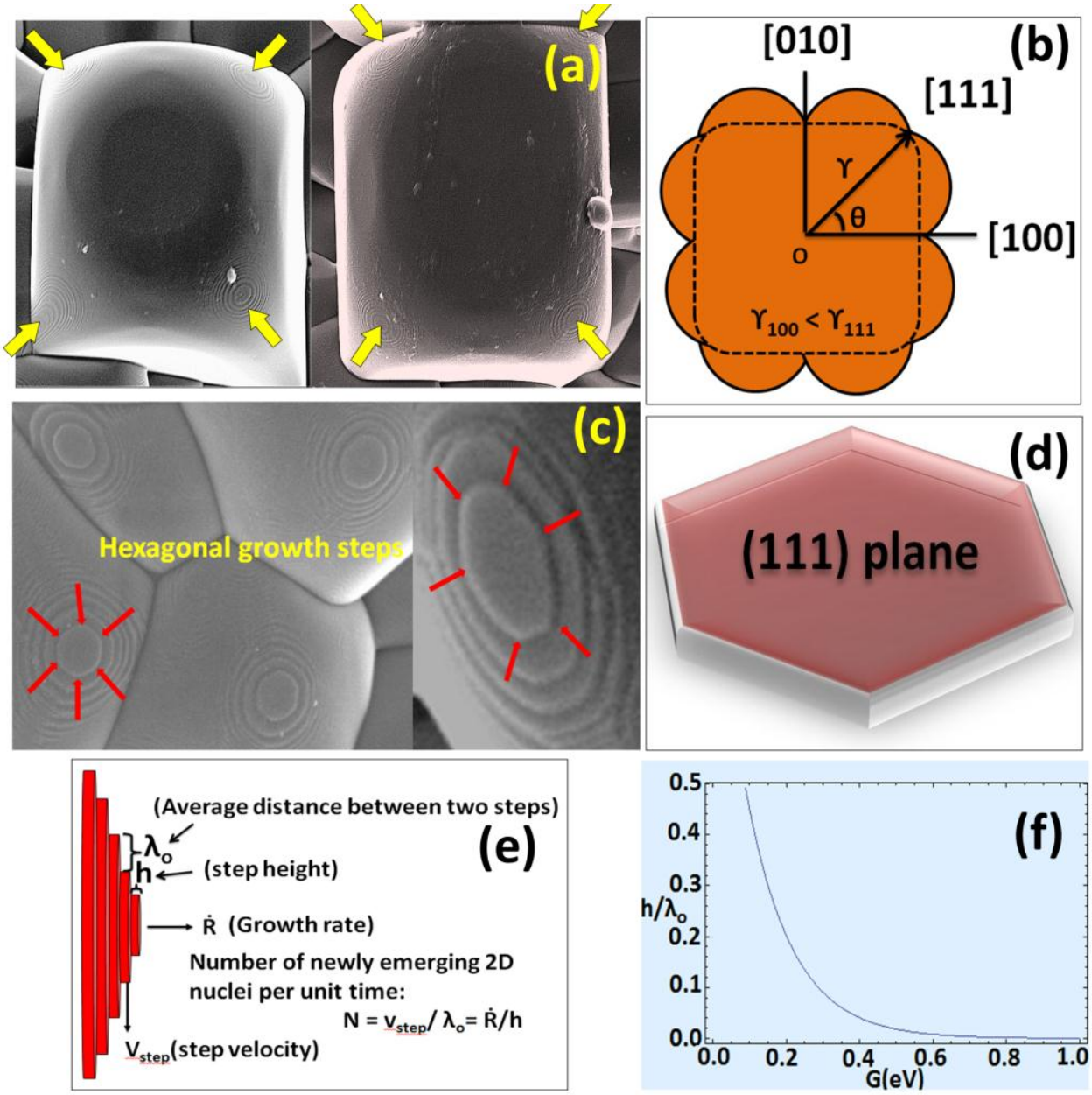

Figure 4.21: (a) Magnified view of the NBT-BT grains of the specimen heated for prolonged period (~20h), arrow indicates concentric growth steps preferably confined on corners of the grain, (b) a schematic polar γ-plot and the Wulff construction of equilibrium shape of NBT-BT grains, (c) surface of the grains depicting the shape of hexagonal growth patterns as corners of these patterns are marked with arrows, (d) schematic of (111) plane, (e) schematic representation of the growth step's mechanism observed on the grain surface, and (b) variation of h/λ_o as a function of energy barrier for 2 D nucleation at 1448K.

to 3D growth process. In the present case, the ratio h/λ was measured to be ~0.08 and the corresponding energy barrier calculated from Eqn. (3.8) for 2D nuclei was ~0.32 eV for the specimen heated at 1175^{o}C.

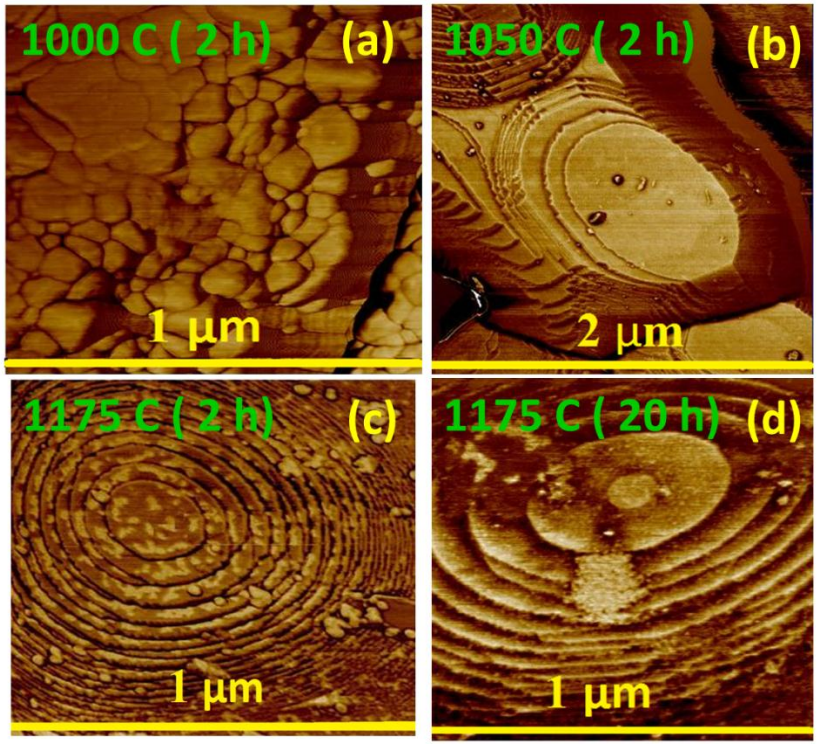

Figure 4.22 (a-d): AFM image of the growth steps observed on the grain surface of the specimen heated at various temperatures.

4.2.3.2.5 Sintering of NBT-BT ceramics with monoclinic whiskers:

Combined these results indicate that the complete sintering process can be divided in to three parts: (i) transformation of monoclinic whiskers to perovskite phase (ii) localized sintering, and (iii) liquid phase sintering.

(i) Transformation of monoclinic whiskers to perovskite phase: After binder burn out the samples were exposed to heat treatment for 2h at 800^{o}C. The XRD spectrum measured at RT confirmed

the formation of perovskite phase indicating transformation of monoclinic whiskers into ABO_3-type perovskite whiskers. According to the chemical reaction proposed in the experimental section, Bi_2O_3 and Na_2CO_3, $BaCO_3$ and TiO_2 react with $Na_2Ti_6O_{13}$ whiskers. Due to difference in chemical potential across matrix powder and whisker, Bi^{3+} and Ba^{2+} diffuse in to the $Na_2Ti_6O_{13}$ whisker leading to rearrangement of the octahedra chain which results in the formation of perovskite structure. The shape of whiskers remained intact (Fig. 4.13(a-c)) in the matrix which indicates topochemical reaction between the base powder matrix and $Na_2Ti_6O_{13}$ whiskers. $Na_2Ti_6O_{13}$ structure was characterized by 3-D network of edge and corner sharing octahedra [116,118]. The structures with apex sharing of octahedra at an angle 180^o are most stable among other type of geometrical connections as in this case the separation between adjacent Ti^{4+} is higher resulting in lower energy configuration. The screening effect from the anions (oxygen) is also higher for this condition [116]. This type of geometrical arrangement of octahedra provides thermodynamic stability to perovskite structure and thereby facilitates the structural transformation. After topochemical transformation, small equiaxed grains were formed on perovskite whiskers as shown in SEM images. The growth of these small grains with isotropic perovskite structure can be explained by assuming Rayleigh instability [145,146]. The small grains on a given whisker should have same crystallographic orientation[146] which gives rise to partial texturing (~20%) as observed from the samples sintered at 800^oC [Fig. 4.11(b)]. However on further increasing the sintering temperature, the degree of texturing decreased because of random grain growth [Fig. 4.11(b)]. Ideally to preserve the orientation, coalescence among the grains on a given whisker should occur without leaving void [146].

(ii) Localized sintering: The microstructural evolution up to 1050^oC can be described using the experimental results described in previous sections. After formation of pure perovskite phase at

800^{o}C, as the specimen was further heated to 1000^{o}C for 2h, small grains ranging from 100 – 300 nm can be observed on the surface of whisker as explained in previous section. These grains grow with increasing temperature as is evident from the microstructures of the specimen processed at 1025^{o}C and 1050^{o}C for 2h. The grain growth was observed to result in division of the long whiskers into integral connection of grain-network, where individual grains were connected through neck presenting bamboo type structure (Fig. 4.13(o)). Interestingly, this phenomenon was localized on a single whisker. The microstructural evolution in polycrystalline system has been commonly attributed to grain boundary migration, however the possibility of grain rotation in evolution of such microstructures cannot be ruled out. The excess energy of a polycrystalline system is the product of the grain boundary area and grain boundary energy, and the system can minimize its energy either by reducing its area or through grain rotation [147]. In the present case, small grain size on whiskers gives rise to high grain boundary area. Thus the system tries to minimize the grain boundary area resulting in grain coarsening, which was confined locally on a whisker. Grain coarsening termed as thermodynamically driven migration of grain boundary, occurs in order to reduce the total surface area. Generally grain growth is propelled by the chemical potential gradient across the curved boundary [123], which was confirmed by the line scan EDS performed across the grain boundary depicting chemical inhomogeneity (Fig. 4.18(b)). The growth steps observed on the grain surface are shown in Fig.'s 4.13(p) and 4.22(b). The growth steps formed in this region were found to have higher values of h and λ_o than that observed on the grain surface at 1175^{o}C. These growth steps on the grain surface indicate polynuclear growth mechanism, which suggests that the formation of nucleation steps on the particle surface is fast enough to create a new layer before the previous one has been

completed [123]. Furthermore, these growth steps reduce kinetic barrier for nucleation [148,149] which in turn increases the growth rate.

(iii) Liquid phase sintering mechanism: On further increasing the sintering temperature above 1050^{o}C, grain coarsening occurs to create a net type microstructure and the conventional liquid phase sintering (LPS) mechanism starts. The LPS leads to reduction of porosity and enhances the grain growth in order to minimize the surface area and to achieve lowest energy configuration and equilibrium shape of NBT-BT grains [150]. In this temperature range, fast densification of whole volume was observed as indicated in the temperature dependence of the density plots. In SEM micrographs of specimen heated for 2h at 1175^{o}C, the complete change in morphology and development of cubical grains could be noticed. The HR-TEM image (Fig. 4.19 (a)) of specimen heated at 1175^{o}C for 2h presents well defined grain boundary separating two different phases. The presence of liquid phase in STEM-HAADF image indicates the liquid phase sintering. The liquid phase formation was facilitated by Na and Bi mass transport. The hexagonal growth steps preferably confined on corners of pseudo cubical grains suggest <111> growth direction, which in turn leads to formation of 3D structure of grain with larger (100) plane. The assumed equilibrium shape of grains indicate that the surface energy along <100> direction is lower than that of <111> direction for NBT-BT grain.

4.2.3.2.6 Electrical properties:

After poling, specimens processed at 1175^{o}C, 1200^{o}C and 1225^{o}C for 20h were found to exhibit longitudinal piezoelectric constant (d_{33}) of ~ 153, 216 and 180 pC/N respectively. The larger piezoelectric constant for specimen processed at higher temperature can be attributed to ease in domain wall motion in larger grains [151]. However, the decrease in d_{33} value for the

specimen processed at 1225°C for 20h can be attributed to the defects formed due to loss of volatile elements and changes in stoichiometry which results in drop of relative density (~95%).

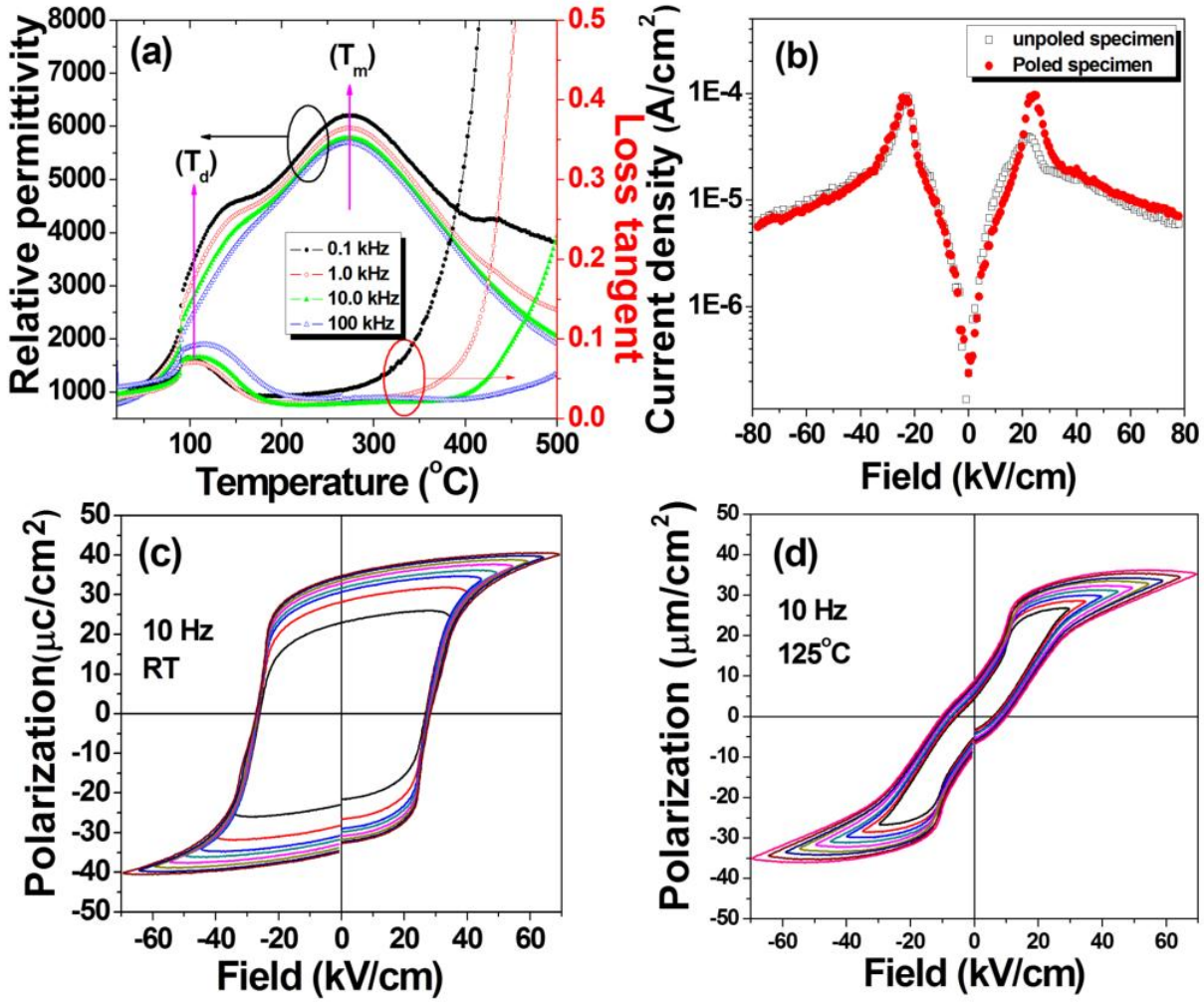

Figure 4.23 (a) Temperature dependence of dielectric constant and loss tangent at various frequencies for poled specimen (1175°C, 20h), (b) Current density (j) versus electric field plot for poled and unpoled specimen (1175°C, 20h) in forward and reverse bias, PE-hysteresis for the same specimen recorded at (c) RT and (d) 125°C.

The temperature dependence of relative permittivity ε(T) and loss tangent factor tanδ (T) at various frequencies for poled specimen (1175°C (20h)) is shown in Figure 4.23 (a). The appearance of two broad peaks in ε(T) plots, one frequency dependent peak at lower temperature ~104°C (more pronounced in tanδ(T) plots) and another at higher temperature ~ 275°C, can be

noticed. The peak at lower temperature corresponds to depoling temperature (T_d) which represents ferroelectric to antiferroelectric phase transition[27] while broad maximum (T_m) in high temperature regime corresponds to antiferroelectric to paraelectric phase transition. This broad peak observed at ~275^{o}C indicates diffuse phase transition (DPT) characteristic of relaxors [16]. The relaxor behavior is commonly attributed to the absence of macroscopic phase (symmetry) change at the transition. However, there is symmetry breaking at nano scale leading to the formation of polar nano regions (PNRs), that exists well beyond the peak in *ε(T)* plots perturbing electrical response[152]. These PNRs have also been considered by various researchers as embryos of the ferroelectric phase and believed to be essential for relaxors[153]. Besides these PNRs, localized distribution of $Ba_2Ti_9O_{20}$ and $Na_{0.5}Bi_{4.5}TiO_3$ (HR-TEM analysis in previous section) also contributes to the diffuse phase transition (DPT).

Figure 4.23 (b) shows the current density (*j*) vs. electric field (*E*) measurements in forward and reverse bias with delay time of 10 ms on poled and unpoled specimen at room temperature. In case of piezoelectrics, the total current density is the sum of leakage current density (j_L) and displacement current density (j_D)[154]:

$$j = j_L + j_D = j_L + \frac{dP}{dt} \tag{4.9}$$

where p is the polarization of the sample and t is the time. The sign of j_D differs for increasing and decreasing fields. A maximum due to switching of domains was observed for forward and reverse bias. The peak height under forward bias was found to be lower than that in reverse bias for unpoled specimen, however the plots were symmetric under reverse and forward bias for poled specimen. In case of unpoled specimen during the forward bias, application of electric field aligns randomly oriented domains resulting in poling of specimen. Thus, under reverse bias

higher peak current asymmetricity is obtained. It can be further noticed that electric field up to ~80 kV/cm could be applied on this specimen without any electrical breakdown, which shows high breakdown strength. *P-E* hysteresis loops were measured at 10 Hz for specimen processed at 1175^{o}C for 20h. A well saturated *P-E* loop with coercive field ($2E_c$) = 54 kV/cm and $2P_r$ = 70 μC/cm^2 was observed as shown in Figure 4.23(c). P-E loop measurements performed at 125^{o}C (above depoling temperature T_d) with 10 Hz were found to exhibit pinched loop behavior as shown in Figure 4.23(d). This kind of behavior has been attributed to anti-ferroelectric nature in these materials, however the mechanism of their origin is not well understood.

4.2.4. Chapter summary:

Synthesis of $Na_2Ti_6O_{13}$ template whiskers was performed by molten salt synthesis method and it's structure was characterized using TEM. The template whiskers were aligned in base powder matrix of NBT-BT using tape casting and subjected to various sintering temperatures. The sintering process occurred in three stages: transformation of monoclinic whiskers to perovskite phase through topochemical reaction (<800^{o}C), localized sintering which was confined on now polycrystalline single whisker (800-1050^{o}C), and liquid phase sintering resulting in densification and grain growth over the whole volume (>1050^{o}C). The concentric hexagonal growth patterns were preferably confined on the corners of cubical grains indicating <111> growth direction. The specimens processed at 1175^{o}C, 1200^{o}C and 1225^{o}C for 20h were found to exhibit longitudinal piezoelectric constant (d_{33}) ~ 153, 216 and 180 pC/N, respectively.

Chapter-5

5.1 Nanostructured lead–free ferroelectric $Na_{0.5}Bi_{0.5}TiO_3$-$BaTiO_3$ whiskers: synthesis mechanism and structure [d]

Nanostructured lead-free ferroelectric $Na_{0.5}Bi_{0.5}TiO_3$-$BaTiO_3$ (NBT-BT) whiskers with high aspect ratio were synthesized topochemically using $Na_2Ti_6O_{13}$ (NTO) as a host structure for the first time. High energy x-ray diffraction coupled with atomic pair distribution function (PDF) and Raman scattering analyses were used to confirm the average structure of lead-free NBT-BT whiskers as rhombohedral, i.e. a ferroelectricity enabling type. The HRTEM analysis revealed local monoclinic-type structural distortions indicating a modulated structure at the nanoscale in the MPB composition of lead-free NBT-BT whiskers. The structural rearrangement during the synthesis of lead-free NBT-BT whiskers was found to occur via translation of edge shared octahedra of NTO into a corner sharing coordination. The high temperature morphological changes depicting disintegration of isolated whiskers into individual grains due to higher grain boundary energy have been found to occur in a close analogy with Rayleigh-type instability.

5.1.1 Background

Ferroelectric perovskite oxides in the form of single crystals, polycrystalline ceramics, and thin or thick films constitute an important class of materials widely used in capacitors, electro-mechanical systems, ferroelectric memories, etc. [155]. Moreover, in recent years owing to the shrinking size of electrical and electromechanical components, fabrication and characterization of micro and nano-sized perovskite oxides have attracted much attention[156-

[d] Maurya et al., Dalton Trans., 41 (2012), 5643. Copyright 2012, Reproduced by permission of The Royal Society of Chemistry.

161]. Ferroelectric nanostructures with high aspect ratio are highly desired but their synthesis is extremely challenging since at reduced dimensions most perovskites adopt a structure with cubic symmetry resulting in a highly isotropic shape during high temperature processing. There have been several approaches to obtain nano-structured materials with anisotropic shape such as template-directed method [162], vapor phase synthesis [163], vapor-liquid-solid (VLS) growth,[164] solution –liquid-solid (SLS) technique,[165] solvothermal synthesis,[166] solution phase growth based on capping reagents,[167] self-assembly,[168] and lithography[169]. These techniques require multiple processing steps and controlled environment limiting their large scale application. Therefore, a new powder processing based technique capable of providing ferroelectric perovskite structures of high aspect ratio morphology is highly desired.

Furthermore, current generations of ferroelectric devices and resonators are fabricated mainly using lead-based ferroelectric compositions. However, there is growing environmental concern in the use of lead which has prompted research in finding alternative lead-free compositions. The present chapter addresses both these issues and demonstrates molten salt synthesis of lead-free NBT-BT ferroelectric whiskers through a topochemical transformation using NTO as a host structure. This technique is highly cost-effective and can provide large quantities of lead-free NBT-BT whiskers with controlled morphology at relatively low synthesis temperature [170,171]. The topochemical reaction involves introduction of guest species (ions) into a host structure resulting in a product with different structure but morphology similar to that of guest structure. In prior work, this method has been successfully used for synthesis of shape anisotropic ABO_3 type perovskite using Aurivillius type $PbBi_4Ti_4O_{15}$ and $Bi_4Ti_3O_{12}$ oxides as host structure[172,173].

$Na_{0.5}Bi_{0.5}TiO_3$ is a well-known lead-free ferroelectric material. A Solid solution of $(Na_{0.5}B_{0.5}TiO_3)_{(1-x)}$-$(BaTiO_3)_x$ (NBT-BT) exhibits a MPB for x =0.05-0.08 providing enhanced piezoelectric properties[24]. As reported in chapter-4, the composition near MPB of $(Na_{0.5}B_{0.5}TiO_3)_{(1-x)}$-$(BaTiO_3)_x$ was optimized [174], and x = 0.07 was selected for synthesis of NBT-BT whiskers (hereafter in this chapter whiskers having composition $(Na_{0.5}B_{0.5}TiO_3)_{(1-x)}$-$(BaTiO_3)_x$ with x=0.07, will be denoted as NBT-BT. In MPB region both tetragonal and rhombohedral phases co-exists as the space group symmetry of these two ferroelectric phases is not connected by direct group theoretical correlation [175]. The piezoelectric/ferroelectric materials at MPB are characterized by enhanced piezoelectric response. The enhancement in piezoelectric properties at MPB has been attributed to increased spontaneous polarization and near degeneracy of the tetragonal and rhombohedral states which facilitates domain orientation under applied electric field [176].

The structural and morphological characterizations of NBT-BT whiskers were performed using high-energy XRD and SEM to elucidate the phase, grain size and grain boundary morphology. Furthermore, HRTEM analysis was used to understand the change in the local microstructure and the mechanism of the topochemical transformation to lead-free NBT-BT whiskers. The high temperature behavior and morphological changes of these lead-free NBT-BT whiskers were investigated to elucidate the role of surface energy.

5.1.2 Experimental

NTO whiskers were synthesized by molten salt synthesis method [177]. Molten salt synthesis method is suitable for realizing crystallites of complex oxides with shape anisotropy at low temperatures and with smaller reaction time due to enhanced diffusion of reactants in molten

salts. In this method starting materials are mixed together with a suitable salt (NaCl in present case) and heated at temperature higher than the melting point of salt. After completion of reaction, the product is washed several times with hot deionized water to remove salt. In this case, stoichiometric amounts of Na_2CO_3 and TiO_2 (Rutile) powders were ball-milled for 24h in polyethylene bottle with Yttria-stabilized ZrO_2 balls as milling media and high purity ethanol as solvent. The resulting slurry was dried in an oven at 80^{o}C for 6h. This dried mixture was mixed with NaCl followed by ball milling for 24h to achieve homogeneous mixing. After drying, the homogenous mixture was crystallized at 1100^{o}C for 2h in a covered platinum crucible with heating and cooling rate of 5^{o}C/min. The resulting product was 6-7 times with hot deionized water to achieve NTO whiskers without trace of salt. Various combinations of oxide to salt ratio (1:1, 1:2 and 1:3) were investigated, however 1:2 ratio was found to provide high aspect ratio of the host NTO whiskers. The concentration of the host matrix powder and whiskers for the MPB composition of lead–free $(Na_{0.5}B_{0.5}TiO_3)_{(1-x)}$–$(BaTiO_3)_x$ with x=0.07 (denoted as NBT-BT) was calculated using the chemical reaction equation (3.1). Stoichiometric amount of oxide powders were mixed in 1:2 weight ratios with salt and stirred for 6h at RT in ethanol for proper mixing. This mixture was dried in an oven for 24h followed by heating (heating rate 5^{o}C/min) in a covered platinum crucible at 200^{o}C, 500^{o}C, 600^{o}C, 700^{o}C, 800^{o}C and 900^{o}C for 2h followed by cooling (cooling rate 5^{o}C/min) to room temperature (RT). All the high temperature experiments were done in an electric muffle furnace. The resulting whiskers were washed with deionized water several times and dried at 80^{o}C for 24h in an oven. XRD experiments (Cu Kα radiation) were conducted on these whiskers to confirm the formation of perovskite phase at RT using a powder X-ray diffractometer at operating voltage of 45 *kV* and current of 40 *mA*. The morphological investigations were performed using a scanning electron microscope at 5 *kV*

accelerating voltage. In order to record the SEM image, NBT-BT whiskers were dispersed on a platinized silicon substrate followed by conductive gold palladium coating. HRTEM analysis was performed using a transmission electron microscope. For TEM analysis the whiskers were mixed with G_2- epoxy (Gatan Inc.) and then filled in brass tubes of 3 mm in diameter. The tubes were then sliced to thin sections that were mechanically polished. Finally, dimple grinding followed by Ar ion milling was performed to obtain TEM transparent foils.

Table-5.1: List of the amount of various chemicals used to synthesize the NBT-BT whiskers

$Na_2Ti_6O_{13}$ (g)	**Bi_2O_3 (g)**	**Na_2CO_3 (g)**	**TiO_2 (g)**	**$BaCO_3$ (g)**	**Total weight (g)**	**NaCl (g)**
12.5869	16.2504	1.2321	0.8390	2.0722	32.9805	65.9609

Room temperature micro Raman studies were conducted in the backscattering geometry using a Raman spectrometer instrument utilizing laser radiation of 514.5 nm from a coherent Argon source. The green laser light was focused in ~2μm-diameter by using a Raman microprobe with a 50X objective. A charge-coupled device (CCD) system collected and processed the scattered light. The integration time of the spectrum and the slit width and laser beam power were adjusted in order to achieve a high signal to noise ratio. The typical spectral resolution for the Raman system with an 1800 grooves/mm grating and 1-in CCD was less than 1 cm^{-1}. The system was calibrated with Si spectra at room temperature before and after recording the sample spectra. Raman spectra of all the samples were taken at different geometrical positions; the results presented here were same throughout the matrix.

5.1.3 Results and discussion

5.1.3.1 High energy XRD and atomic pair distribution function (PDF) analysis:

Figure 5.1 shows the powder diffraction patterns of pure NTO matrix and products of chemical reaction (see equation (4.1)) carried out at different temperatures (^{o}C). The data was taken with Ag Kα radiation (λ=0.56 Å) up to Bragg angles 2θ of 120 deg., i.e. to wave vectors $q = 4\pi \sin(\theta)/\lambda$ of approximately 20 Å $^{-1}$. Only the range of XRD data up to 2θ = 80 deg. is shown here for the sake of clarity. The XRD patterns for pure NTO and NBT-BT obtained at 800 ^{o}C show sharp Bragg peaks indicating good crystallinity. The Bragg peaks in the XRD patterns of the reaction products (e.g. sample treated at 200 ^{o}C) are very broad indicating low degree of crystallinity. This data was then reduced to atomic pair distribution functions (PDF)s shown in Figure 5.2. According to recent studies, high-energy XRD and atomic PDFs analyses are very suitable for studying materials structured at the nanoscale[178]. The experimental PDFs peak at real space distances where well defined atomic coordination spheres exist in the material under study and so can be easily used to test and refine structural models. Figure-5.2 depicts the atomic pair distribution functions *G(r)* (solid line in black) extracted from the full 2θ range of the XRD patterns shown in Fig. 5.1. The pair distribution functions (PDFs) for pure NTO and NBT-BT (800 ^{o}C) show series of well-defined peaks to high interatomic distances reflecting the presence of a sequence of well-defined coordination spheres in these crystalline materials. These PDFs of the starting and ending products of the reaction are very well approximated with structure models (dotted line in red) featuring the monoclinic (S.G. C2/m) and rhomobhedral (S.G. *R3c*) structures of crystalline $Na_2Ti_6O_{13}$ (NTO) [118] and $Na_{0.5}Bi_{0.5}TiO_3$ (NBT) [120], respectively. The PDFs of the samples treated at 200 ^{o}*C* show only few peaks at relatively low

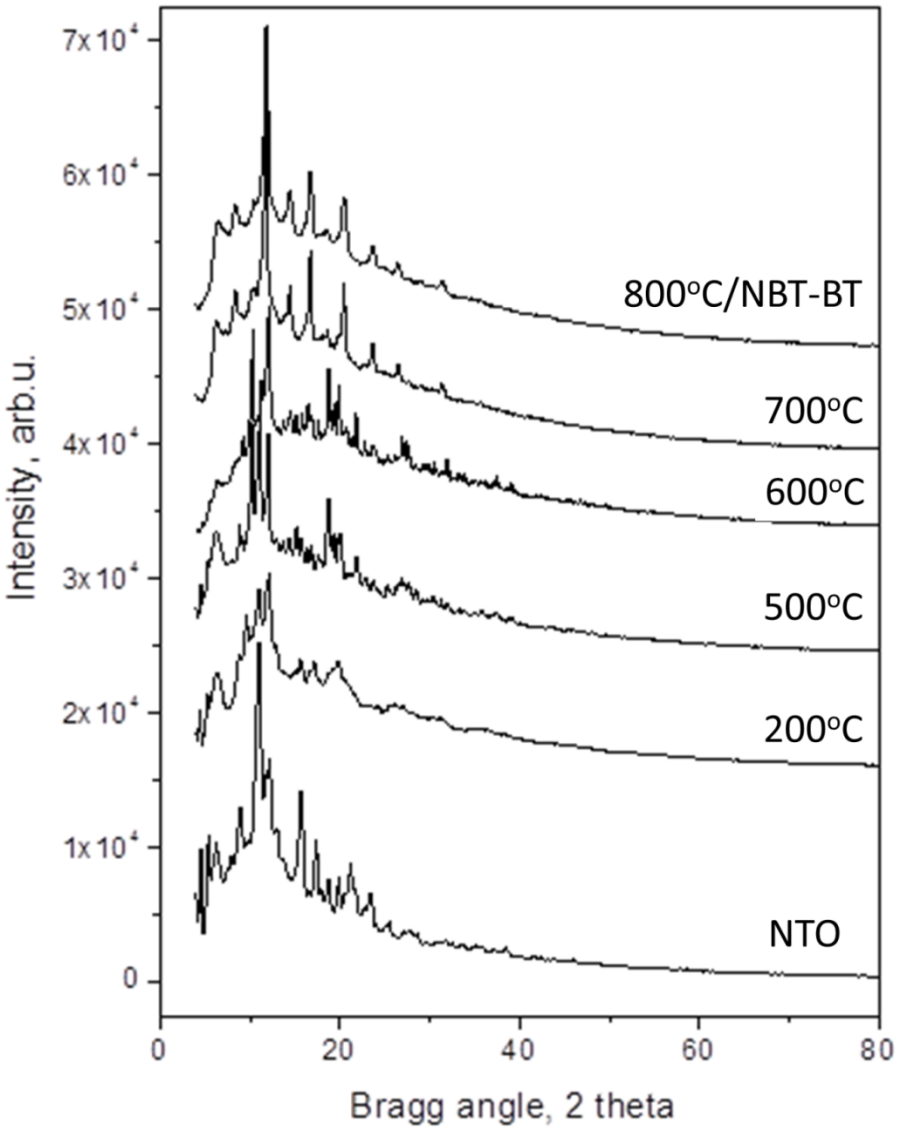

Figure 5.1- Powder x-ray diffraction patterns of pure NTO matrix and products of its reaction (see eq. 4.1). Experiment was conducted at different temperatures (^{o}C) in the increasing order to understand the transformation sequence. Note the XRD patterns of pure NTO and NBTO obtained at 800 ^{o}C show sharp Bragg peaks indicating good crystallinity. The Bragg peaks in the XRD patterns of the reaction products (e.g. sample treated at 200 and 500 ^{o}C) are very broad indicating a low degree of crystallinity.

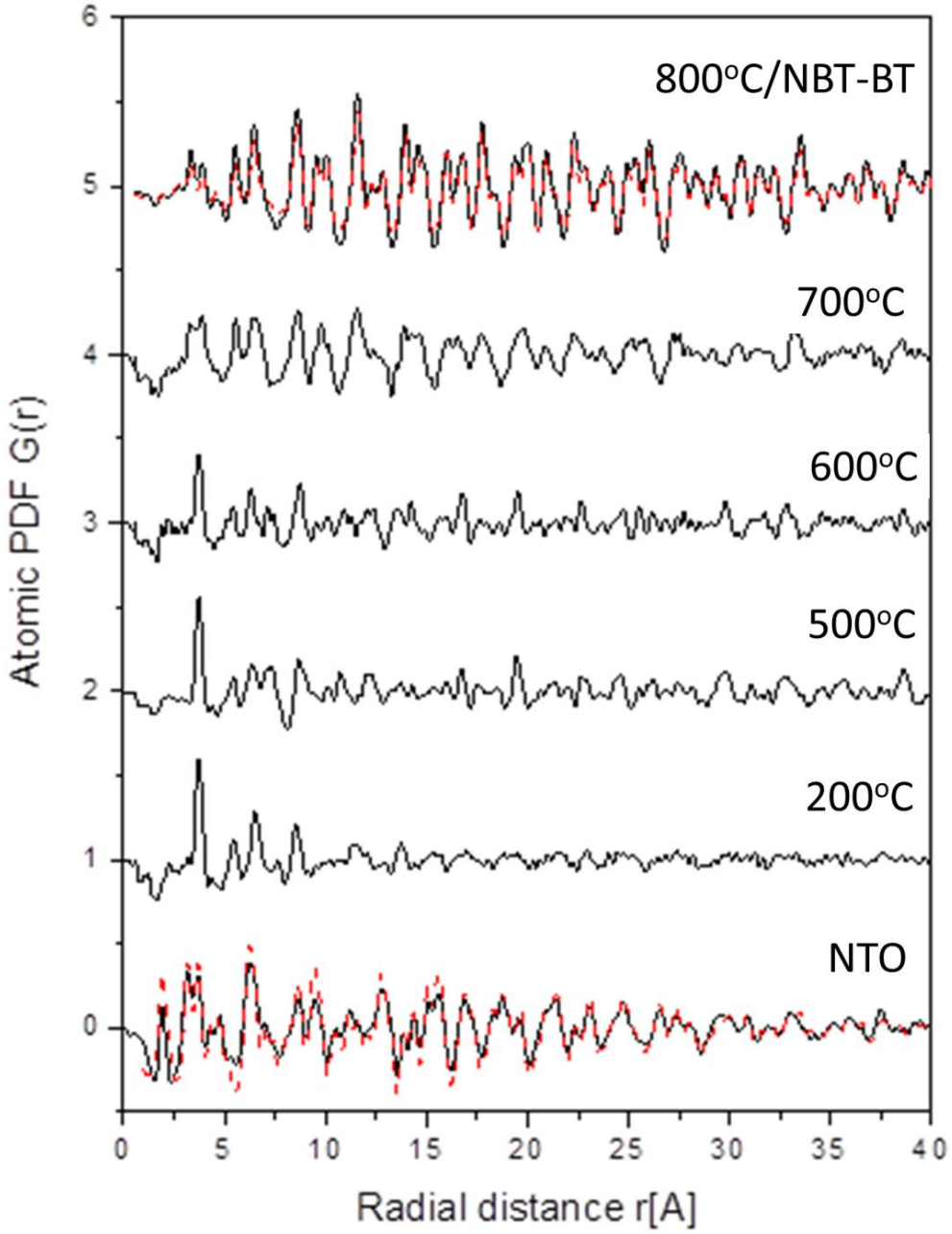

Figure 5.2- Atomic pair distribution functions G(r) (full line in black) extracted from the full 2θ range of the XRD patterns shown in Fig. 5.1. The PDFs for the starting NTO and resulting NBTO are very well approximated with structure models (broken line in red) featuring the monoclinic (S.G. C2/m) and rhomobhedral (S.G. R3c) structures of crystalline $Na_2Ti_6O_{13}$ (NTO) and $Na_{0.5}Bi_{0.5}TiO_3$ (NBTO), respectively.

interatomic distances reflecting a poor crystalline state. Crystallinity improves with reaction temperature as manifested by the increased sharpness of the peaks in the PDFs of the samples treated at temperature higher than 200 ^{o}C. Figure-5.3(a)-(b) represents the schematic of fragments from the structures of NTO and NBT-BT, respectively. TiO_6 octahedra are in blue, Na/Bi/Ba atoms in yellow. Several interatomic distances between connected TiO_6 octahedra are marked with arrows. The low-r part of the experimental atomic PDFs of Fig. 5.2 is depicted in Figure-5.4. Arrows mark several distances between atoms sitting on the vertices of corner sharing TiO_6 units (see Fig. 5.3) that exist in NTO and persist in the products of its reaction (see eq. 4.1) until a perovskite structure NBT-BT is formed. The result indicates the existence of a topochemical relationship between NTO and lead-free NBT-BT. These kind of layered titanates have been found to be suitable precursors of framework perovskites in other studies as well [179].

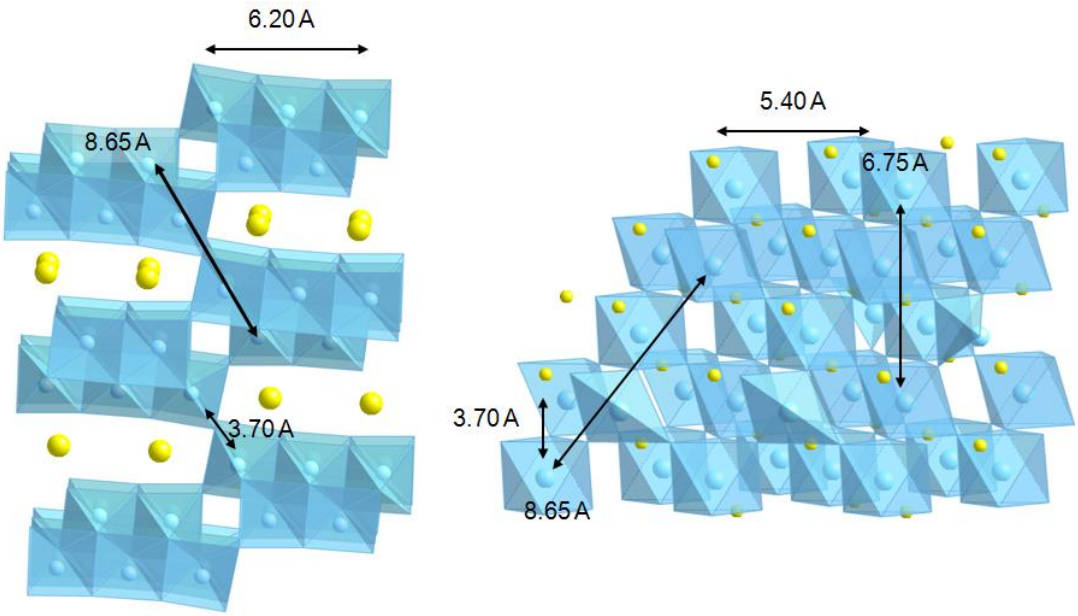

Figure-5.3 The schematic of fragments from the structures of NTO (left) and NBTO (right). TiO_6 octahedra are in blue, Na/Bi atoms in yellow. Several interatomic distances between connected TiO_6 octahedra are marked with arrows.

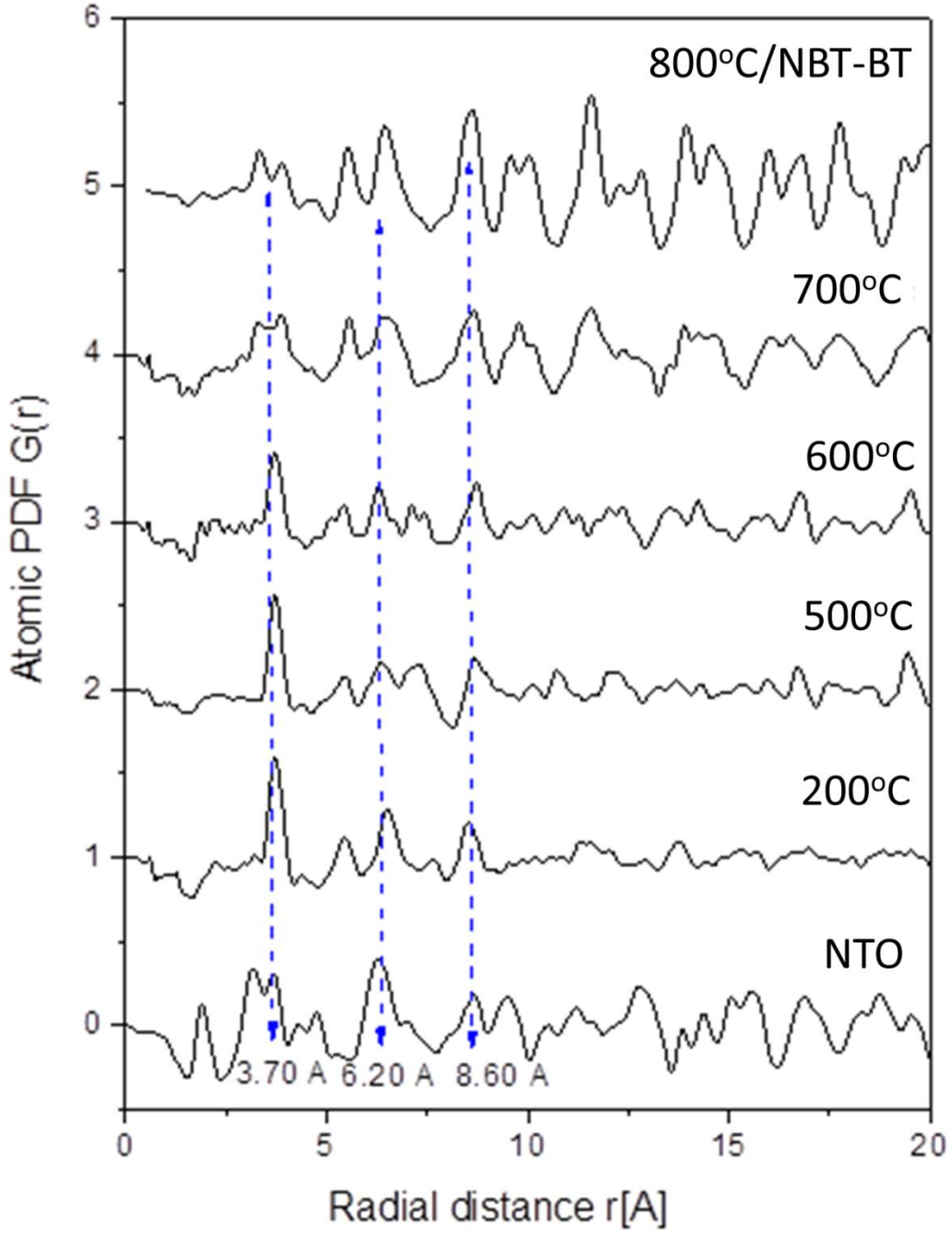

Figure-5.4 Low-r part of the experimental atomic PDFs of Fig. 5.2. Arrows mark several distances between atoms sitting on the vertices of corner sharing Ti-O_6 units (see Fig. 5.3) that exist in NTO and persist in the products of its reaction (see equation (4.1)) until a perovskite NBTO is formed.

Figure 5.5(a) shows XRD patterns of the $Na_2Ti_6O_{13}$ (NTO) whiskers taken with Cu Kα radiation allowing better resolution in reciprocal space. The data confirms that these whiskers are crystallized in monoclinic phase [118]. Figure 5.5(b) and (c) show the Cu Kα XRD patterns of NBT-BT whiskers synthesized topochemically at 800 and 900^{o}C revealing the formation of a perovskite phase for these whiskers. However, small impurity peak marked with '*' in the XRD-pattern of the sample synthesized at 800^{o}C suggests more than 95% transformation occurs at this temperature. The magnified view of $\{111\}_C$ and $\{200\}_C$ Bragg peaks for the sample processed at 900^{o}C is shown in the inset of Figure 5.5(c). The subscript c stands for cubic crystal system. A small shoulder appearing in the $\{111\}_C$ and $\{200\}_C$ peaks indicates that the composition is near the MPB. In order to determine the structure type of the whiskers processed at 900^{o}C, higher energy XRD patterns were recorded again using AgKα radiation [Fig. 5.5(d)]. This data was then reduced to an atomic PDF shown in Fig. 5.5(e). The experimental PDF for the whiskers [see Fig. 5.5(e)] shows well defined peaks to high real space distances. The PDF peaks decay to zero at distances of about 10-15 nm which may be considered to be the length of structural coherence, also known as crystallite domain size, in this material. These XRD/PDF results indicate that the larger grains observed in these whiskers by SEM (discussed later in this manuscript) are made of relatively small size crystallites. Furthermore, the data in Fig. 5.5(f) shows that the PDF can be well fitted with a model based on the rhombohedral structure of NBT perovskite [120] confirming that the whiskers are a single phase ferroelectric material.

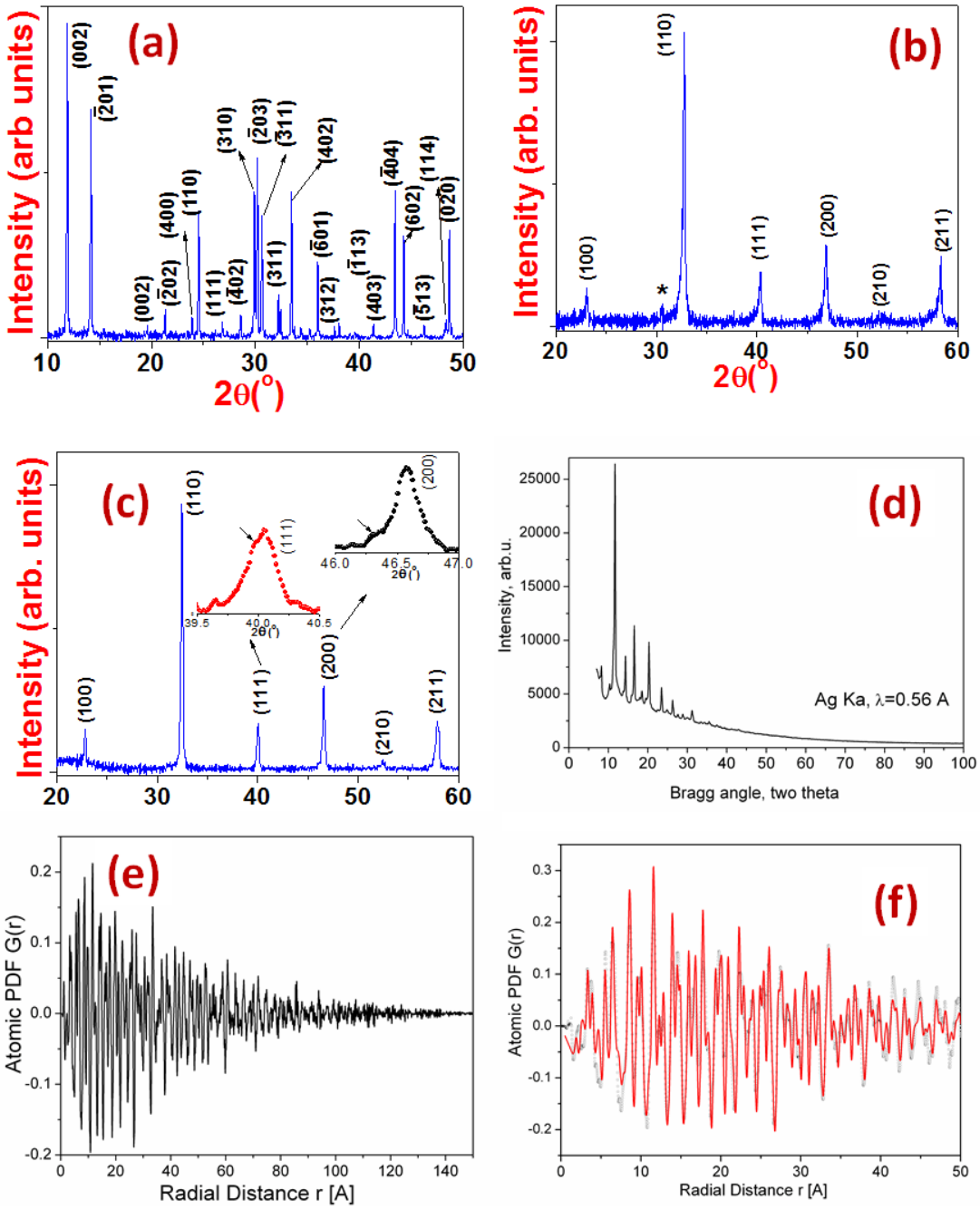

Figure-5.5 Cu Kα x-ray diffraction data at RT for (a) NTO powder whiskers with monoclinic symmetry, (b) NBT-BT processed at 800 ^{o}C indexed with reference to cubic phase, (c) NBT-BT processed at 900 ^{o}C with inset depicting a magnified view of the $\{111\}_c$ and $\{200\}_c$ reflections, where c stands for cubic phase. The high energy x-ray diffraction data of NBT-BT/900 ^{o}C (d) and the respective atomic PDF (e). The low-r part of the experimental PDF data is shown in Fig. 5.5f (open circles). The data can be fitted very well with a structure model (line in red) based on the rhombohedral (S.G *R3c*) structure of NBT perovskite.

5.1.3.2 Raman spectroscopy:

Figure-5.6 shows Raman spectra of NTO matrix and of specimens after reaction at different temperatures (in deg. Celsius). The Raman spectra of pure NTO and sample processed at 200^{o}C are similar indicating no change in the structure of NTO. The peaks observed in Raman spectra of NTO in the present study are similar to those reported earlier [180]. The Raman spectra of NTO depict modes at 276 and 334 cm^{-1} due to vibration of Na-O-Ti [181]. The Raman modes in the region of 600 – 700 cm^{-1} have been attributed to the Ti-O-Ti stretch in edge shared octahedra. However, the mode observed at 743 cm^{-1} is the characteristic of corner sharing octahedra in NTO [182]. The mode at 872 cm^{-1} was attributed to short Ti-O bonds in the distorted TiO_6 octahedra of NTO [183]. Furthermore in the specimen processed at 500^{o}C and higher temperatures, *Bi* and *Ba* start diffusing inside the system in the presence of molten salt. This can be seen in terms of new bands that appeared at 55 cm^{-1} and the peak around 91 *cm*$^{-1}$ (observed in NTO) becomes asymmetric indicating appearance of a shoulder. Another small peak appeared as shoulder in the main peak observed at 137 cm^{-1}. At 600^{o}C, the increase in the intensity of band observed at 55 *cm*$^{-1}$ was noticed and, the peaks at about 91 *cm*$^{-1}$ and 137 *cm*$^{-1}$ give rise to doublet, which could be attributed to increased inharmonicity of vibration and change in the local symmetry due to the substitution of heavier Bi on Na site. The decrease in the intensity of various peaks below 200 *cm*$^{-1}$ could be result of the substitution of Bi and Ba on the Na-site. However, the effect of substitution of Ba would be smaller due to its smaller concentration. A mode at 276 *cm*$^{-1}$ becomes broad and diffuse indicating appearance of two more peaks for samples processed at 600^{o}C, which appears to be perturbation in Na-O-Ti vibrations due to the Na-site substitution. A noticeable change occurs in the intensity of the Raman peak at 525 *cm*$^{-1}$ which increases with the reaction temperature. The bands in the range of 400 – 600cm^{-1}

are attributed to the bending motion of TiO_6 octahedra [184]. Therefore, the increase in the intensity of the peak at about 525 cm^{-1} with the reaction temperature could be attributed to the enhanced TiO_6 bending motion in the process of the transformation from TiO_6 octahedra edge sharing to corner (vertex) sharing. Moreover with increase in the reaction temperature, the gradual decrease in the intensity of modes appearing within 657 – 680 cm^{-1} regime could be interpreted as loss of the edge sharing coordination that is prevailing in NTO type system (see Fig. 5.3a). The decrease in the intensity of the mode observed at 748 cm^{-1} is likely due to Ti-O-Ti corner sharing coordination; it shows subtle changes with increase in the reaction temperature. However, this band appears to be still present, but buried under a broader band observed in the regime of 700-850 cm^{-1} in the Raman spectra observed for the 700, 800 and 900^oC treated samples. The persistence of modes observed in the higher wavenumber regime 700 -850 cm^{-1}(that are attributed to corner-shared TiO_6 octahedra), also suggests a topo-chemical type conversion in line with the results of high-energy XRD and PDF analysis. The poorly resolved Raman spectra of the specimens processed at 700^oC resembles a density of states spectrum because the disorder due to the random distribution of Na, Bi and Ba ions breaks $k=0$ selection rule and permits phonons from the entire Brillouin zone to become Raman active. The Raman spectra of the specimen processed at 800 and 900^oC are similar to those previously reported for NBT based system (space group *R3c* (C_{3V}^6) with broad modes due to local disorder in the structure[185]. This confirms the successful transformation of NTO made of mostly edge sharing octahedra to lead-free NBT-BT system made of corner sharing octahedra (see Fig. 5.3(a) and 5.3(b), respectively).

5.1.3.3 SEM and HRTEM analysis:

Figure 5.7(a) shows the morphology of $Na_2Ti_6O_{13}$ whiskers prepared using the molten salt synthesis method at 1100^oC. Figures 5.7(b), (c) and (d) show the micrographs of the ferroelectric

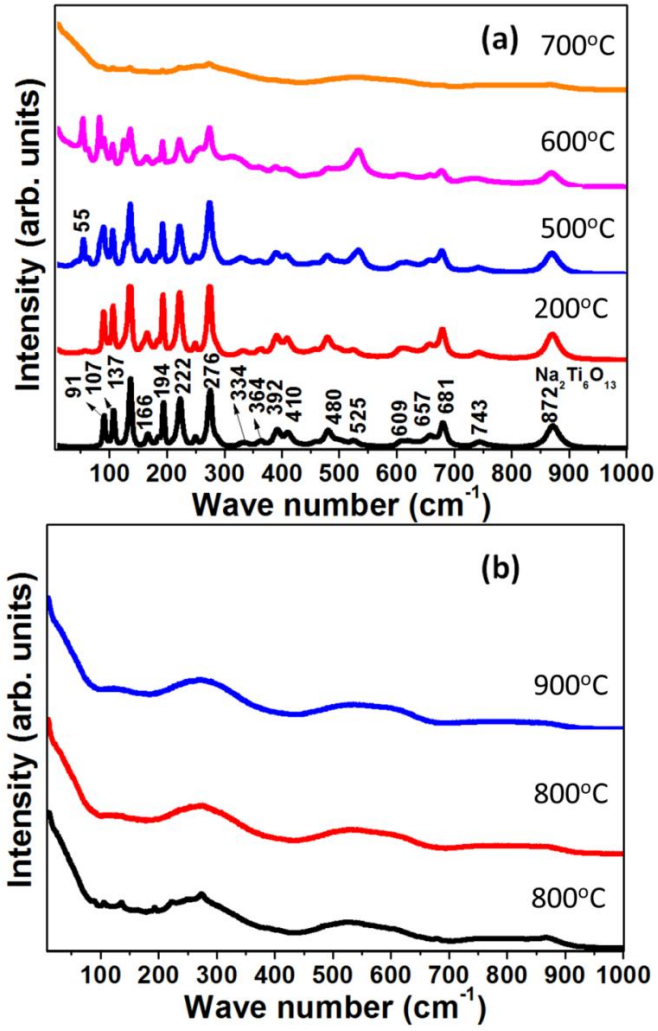

Figure-5.6 (a) Raman spectra of pure NTO matrix and products of its reaction (see eq. 3.1). Synthesis experiments were conducted in the temperature range of 200 – 700 ^oC. The Raman spectra of NTO and the specimen processed at 200 ^oC is similar. Note the systematic changes in the intensity of various peaks in spectra of specimens reacted at and above 500^oC. (b) Raman spectra of samples reacted at 700, 800 and 900 ^oC. The spectra of the specimen reacted at 800 ^oC and 900 ^oC are similar to typical Raman scattering behavior observed for NBT based systems.

NBT-BT whiskers synthesized at 700, 800 and 900^{o}C, respectively. It can be clearly seen from these micrographs that despite the structural transformation, the overall morphology of the whiskers is maintained up to 900^{o}C. For the sake of clarity, the magnified view of the surface morphologies of whiskers treated at various temperatures is presented in Figure 5.8(a)-(f). As can be seen in this figure, the lead-free NBT-BT whiskers processed at 900^{o}C (Fig. 5.8(f)) are composed of densely packed grains revealing their polycrystalline nature. However, this kind of grain growth in the sample processed at relatively lower temperatures (<900^{o}C) is not very obvious. Still the surface is clearly showing the change in morphology (Fig. 5.8) due to diffusion of Ba^{2+} and Bi^{3+} during the reaction. The NTO with tunnel structures (see Fig. 5.3 (a)) have excellent ion exchange property due to which the Na^{+} atom can be easily replaced by Ba^{2+} and Bi^{3+}. The presence of these ions with higher positive charge further facilitates the structural transformation from NTO to lead-free NBT-BT. The estimated grain size on the NBT-BT whiskers after reaction at 900^{o}C was found to be in the range of 100-500 nm (Fig. 5.8(f)). In order to analyze the local microstructure and identify the phase content at the various stage of thermal processing, HR-TEM was performed.

Figure 5.9(a) shows the lattice fringes of $Na_2Ti_6O_{13}$ whiskers viewed along the $[010]_M$ zone axis, where the subscript M stands for monoclinic system. The $\{001\}_M$ planes parallel to the length of the whiskers were found to run along the growth direction. Figure 5.9(b) - (d) shows the HRTEM image of the sample processed at 800^{o}C. The EDS analysis conducted on the edge marked as A and towards the core marked as B in Fig. 5.9(b) shows atomic % ratio of Na/Ti =13.3 and 1.50, respectively. This indicates that during the topochemical reaction, Na ions diffused outward. At the same time, Ba and Bi ions diffused inside the whiskers due to

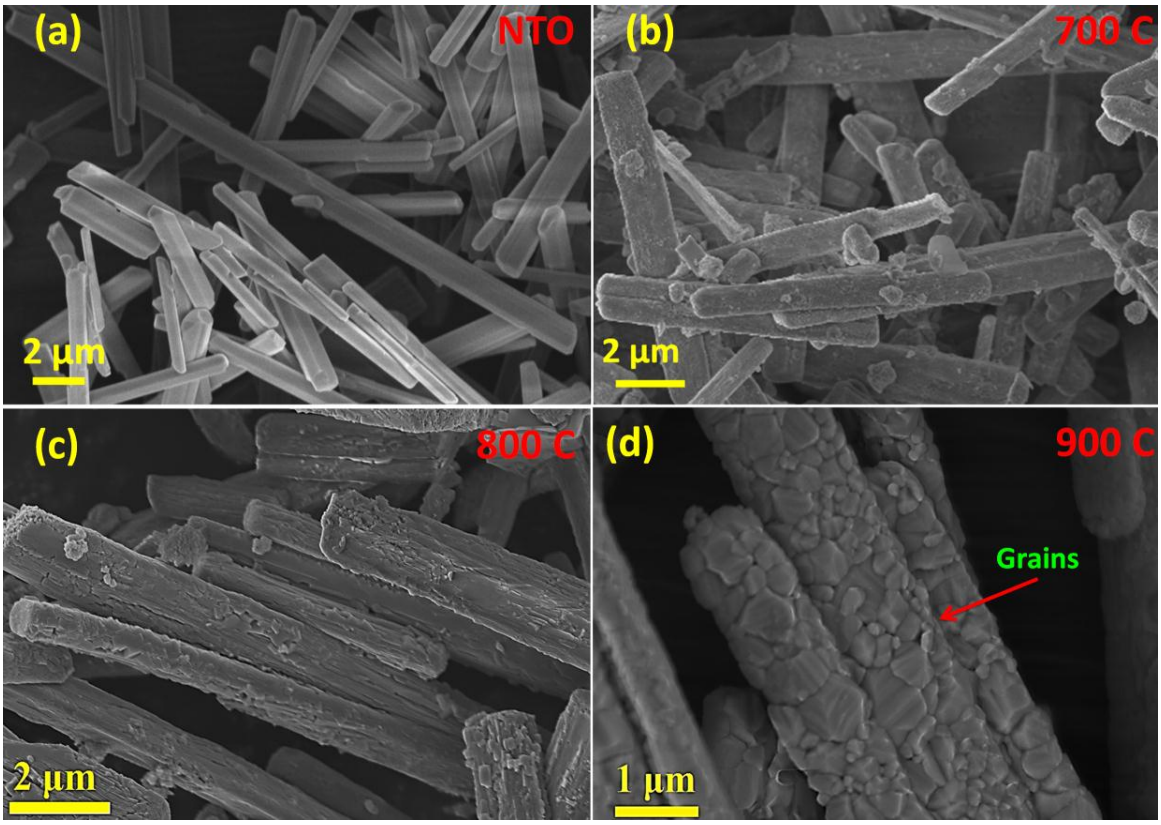

Figure-5.7 SEM micrographs of (a) NTO whisker matrix. Whiskers after reaction at (b) 700°C, (c) 800°C and (d) 900°C. The length of whiskers varies from 7.0-20 µm and the width varies from 0.30 – 1.0 µm. The overall shape of the whiskers was maintained even after reaction at different temperatures despite of noticeable change in surface morphology.

difference in the chemical potential [186]. This results in rearrangement of the octahedra building blocks as explained in forthcoming paragraph. A lattice image showing atomic planes with an interplanar spacing ~0.80 nm from the vicinity of the region marked with B on Fig. 5.9(b) is shown in Fig. 5.9(c). The interplanar spacing is smaller than d_{001} ~ 0.903 nm of the host $Na_2Ti_6O_{13}$ matrix. This change of the interplanar spacing is expected due to the outward diffusion of Na atoms from the core of the sample and the concomitant inward diffusion of Bi/Ba atoms due to difference in the chemical potential. This state can be related to a transient intermediate phase. Since this ion exchange is carried out in a molten salt and is of a topochemical type, it can produce a metastable intermediate state which is otherwise inaccessible

by high temperature reactions[187]. Moreover, molten salt (NaCl) provides strong oxidizing atmosphere which helps in stabilizing a higher oxidation state of Ti^{4+} in the system. The area towards the edge marked as "A" in Fig. 5.9(b) is enlarged in Fig. 5.9(d). The lattice fringes with planes of various orientations can be observed showing a polycrystalline transient state and nucleation sites. The planes are marked with arrows and the area near the arrow head is magnified in the figures next to Fig. 5.9(d). The edge type dislocation marked in the magnified figure of "region 3" acts as a potential site for nucleation and growth of grains [188]. Thus, only partial transformation occurs at 800^{o}C and further thermal treatment is required to obtain a homogeneous phase. Figure 5.9(e) shows the microstructure of the NBT-BT whiskers processed at 900^{o}C for 2h. The inset in the lower corner of the figure shows the fast fourier transform (FFT) of the image in Fig. 5.9(e). The spots in the FFT can be indexed in a monoclinic-type structure [Joint Committee on Powder Diffraction Standards (JCPDS) #460001]. The zone $[2\bar{2}1]_M$ was obtained by indexing this FFT. Interestingly, the average NBT-BT structure obtained by high energy XRD and PDF analysis was found to be of a rhombohedral type. The results indicate the presence of a difference between the local and average lead-free NBT-BT structure implying an incommensurate-type modulated structure at the nano-scale. Furthermore, the intermediate phases with monoclinic distortions are considered to be responsible for enhanced piezoelectric response in MPB compositions of lead-based oxide solid solutions including $Pb(Zr_{1-x}Ti_x)O_3$(PZT), PZN-PT, and PMN-PT[10,189-191]. Various studies employing high energy probing techniques have shown that local symmetry of the MPB compositions can be different from the average bulk symmetry. In perovskite ferroelectric materials these local distortions are generally found to be of a monoclinic type [192]. Therefore, the observed local

monoclinic distortion in NBT-BT appears to be main cause of the enhanced ferroelectric/ piezoelectric response at MPB in this system.

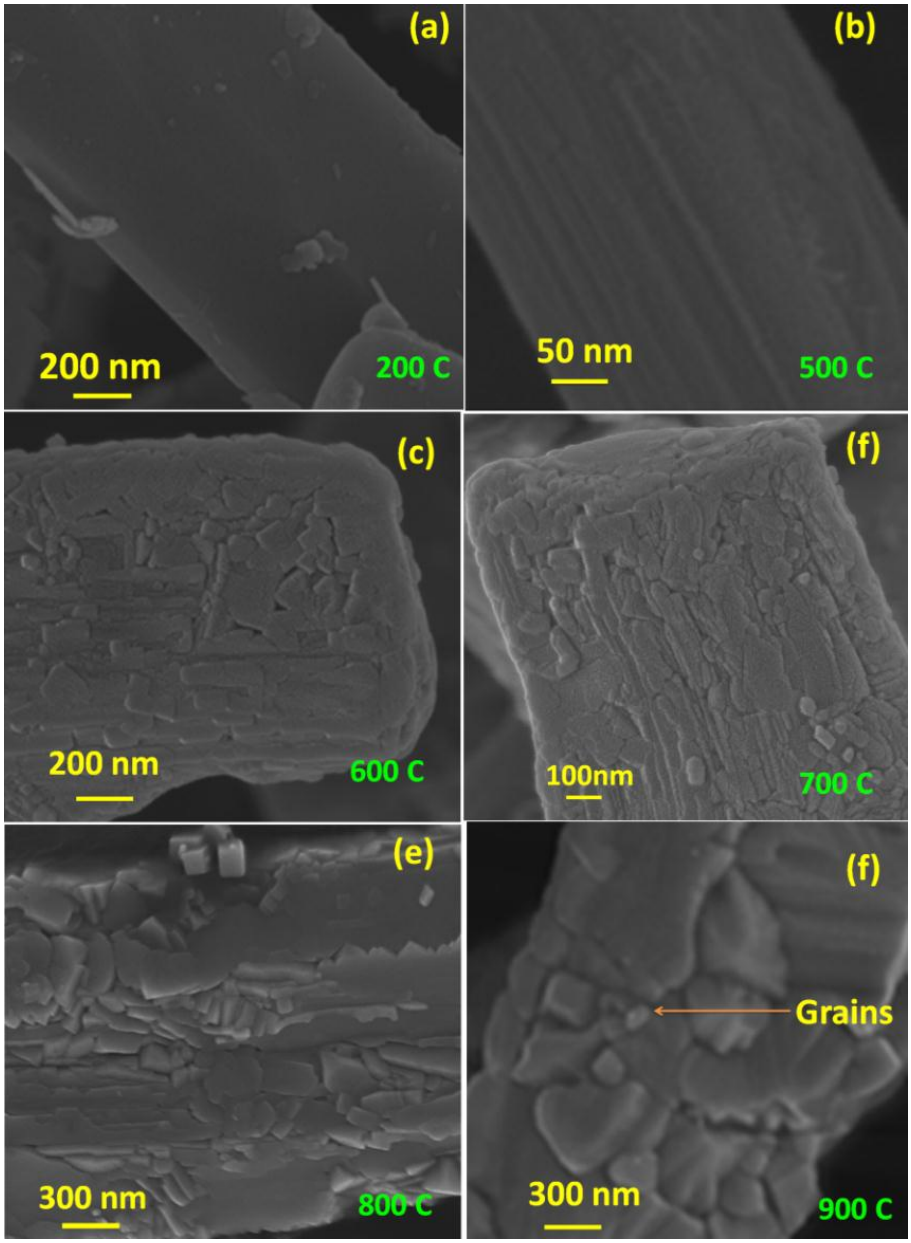

Figure-5.8 Magnified SEM micrographs depicting morphological changes of the whiskers reacted at (a) 200^{o}C, (b) 500^{o}C, (c) 600^{o}C, (d) 700^{o}C and (e) 800^{o}C and (f) 900^{o}C. Note the effect of reaction temperatures on the surface morphology leading to development of nano size grains at 900^{o}C.

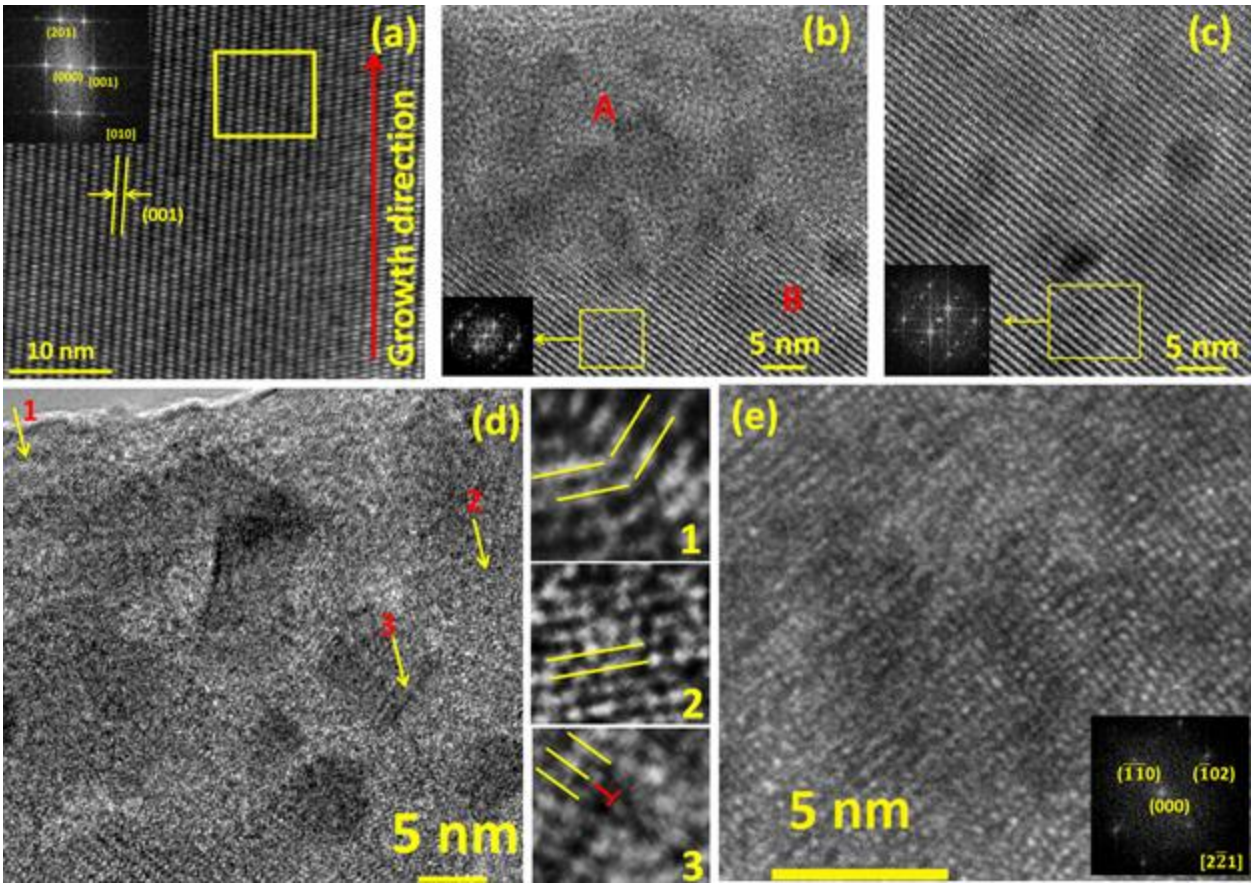

Figure-5.9 Lattice fringe of (a) $Na_2Ti_6O_{13}$ matrix whiskers synthesized at 1100 ^oC, (b) HRTEM image of NBT-BT whisker processed at 800^oC, (c) Lattice fringes corresponding to region marked as 'B' in Fig. 5.9(b) depicting core of the whiskers with larger interplanar spacing than that of NBT based systems. (d) Lattice fringes corresponding to the region 'A' (marked in Fig. 5.9(b)) near the edge of NBT-BT whisker processed at 800 ^oC and the regions marked with 1, 2 and 3 depicting planes with various orientation on the same whisker and symbol (⊢) depicts edge type dislocation in Fig. 5.9(d) are magnified next to Fig. 5.9(d), (e) lattice images of NBT-BT whiskers processed at 900^oC.

3.1.3.4 Model of structural transformation:

The detailed mechanism of the microstructural change and transformation of NTO host into the ABO_3 –type NBT-BT structure can be summarized as follows. When a stoichiometric amount of the starting materials mixed with NaCl is heated at 800 and 900^oC the salt melts, and the decomposing $BaCO_3$ and Bi_2O_3 provide Ba^{2+} ions and Bi^{3+} ions. These ions react with the

host NTO matrix due to difference in the chemical potential resulting in the formation of ABO_3 type perovskite structure. NTO belongs to the family of $M_2Ti_nO_{2n+1}$ compounds, where n = 6 or 3 and M = Na or K. It has a base centered monoclinic structure with lattice parameters, a = 1.51310 nm, b= 0.37450 nm, c = 0.91590 nm and $\beta = 99.3^oC$ of space group C2/m [118]. NTO structure is a 3-D network of TiO_6 octahedra joined by corners and edges resulting in a zig-zag structure (see Fig. 5.3(a)) with rectangular tunnels along the y-axis of the monoclinic lattice, where sodium ions are located. On the other hand, the ABO_3 perovskite structure features a simple cubic lattice in which the octahedra shares only corners and the B cation is at the origin of the Bravais cell[193]. In the present case the A-site is shared by $Na^+/Ba^{2+}/Bi^{3+}$ ions and the B–site is occupied by Ti^{4+}. The process of NTO to NBT-BT transformation can be rationalized as follows:

(i) During synthesis, Ba^{2+}/Bi^{3+} diffuse in the host lattice of $Na_2Ti_6O_{13}$ through ion exchange mechanism with Na^+ resulting in a rearrangement of the octahedra sharing scheme to minimize the energy for obtaining a thermodynamically stable configuration. The schematic of NTO to NBT-BT transformation (ABO_3 type perovskite) is shown in Figure 5.10(a) and the coordination of the octahedra in the perovskite structure is presented in Figure 5.10(b). The geometrical connection of the octahedra plays an important role in this transformation. The perovskite structure is composed of corner (vertex) sharing octahedra[116] at 180^o and any deviation from this angle decreases the distance between Ti-Ti atoms (Fig. 5.10(b)) resulting in increased repulsion potential experienced by the Ti atom and the screening effect from the negative charge of oxygen atoms would be smaller. As a result the free energy of this structural configuration increases and the structure becomes unstable. The equation describing the distance between two Ti-Ti (Fig. 5.10b)) atoms can be given as:

$$d = a(\sqrt{[2(1-\cos\theta)]}) \quad (5.1)$$

where θ is the angle between the Ti-O-Ti in the corner sharing octahedra and "a" is the Ti-O bond length in the Ti-O-Ti bonding bridge between octahedra sharing two vertices. The order parameter η = 180-θ with two limiting values of 180^o and 0^o where θ is the deviation of the bond angle from 180^o in the Ti-O-Ti bonding bridge i.e. in the geometrical connection of vertex sharing octahedra. Therefore, the system will be most stable for η =0^o i.e. θ =180^o. Figure 5.10(c) plots the Eq. (5.1) with θ ranging from 0 to 180^o. However, in reality the inclination angle can vary from 131.8^o to 180^o [116]. The bond length 'a' of Ti-O was taken to be 2.009 Å from the archetype perovskite $BaTiO_3$ with a cubic phase [194] as the reaction occurred at high temperature where most of the ABO_3 type perovskite have cubic structure. This plot (see Fig. 5.10c) shows the change in perpendicular distance between two Ti atoms with the angle between the vertex sharing octahedra. It can be noticed here that this distance is optimal for θ =180^o. The mechanism of rearrangement of $Na_2Ti_6O_{13}$ into the ABO_3 type NBT-BT structure can be further comprehended as follows. The energy of edge shared octahedra configuration is higher than that of corner sharing configuration, and consequently the edge sharing octahedra are driven into a more energetically favorable coupling scheme during the reaction. According to the model proposed in this research, during the reaction, octahedra with shared edges in $Na_2Ti_6O_{13}$ move in {100} direction to achieve the corner sharing connection of the ABO_3 type structure. This rearrangement is shown schematically in step 2 of Fig. 5.10(a) and is supported by the findings of the atomic PDFs analysis that indicates the existence of a relationship between the NTO and NBTO (see Figs. 5.3 and 5.4) structures. The arrows marked in step 2 indicate the direction of the translational motion of the octahedra.

(ii) The perovskite structure is isotropic and, therefore, after the topochemical conversion, the sample at higher temperature exhibits well-defined grain morphology, which could be understood by assuming Rayleigh type instability [177] as observed in Fig. 5.7(d) and 5.8(f).

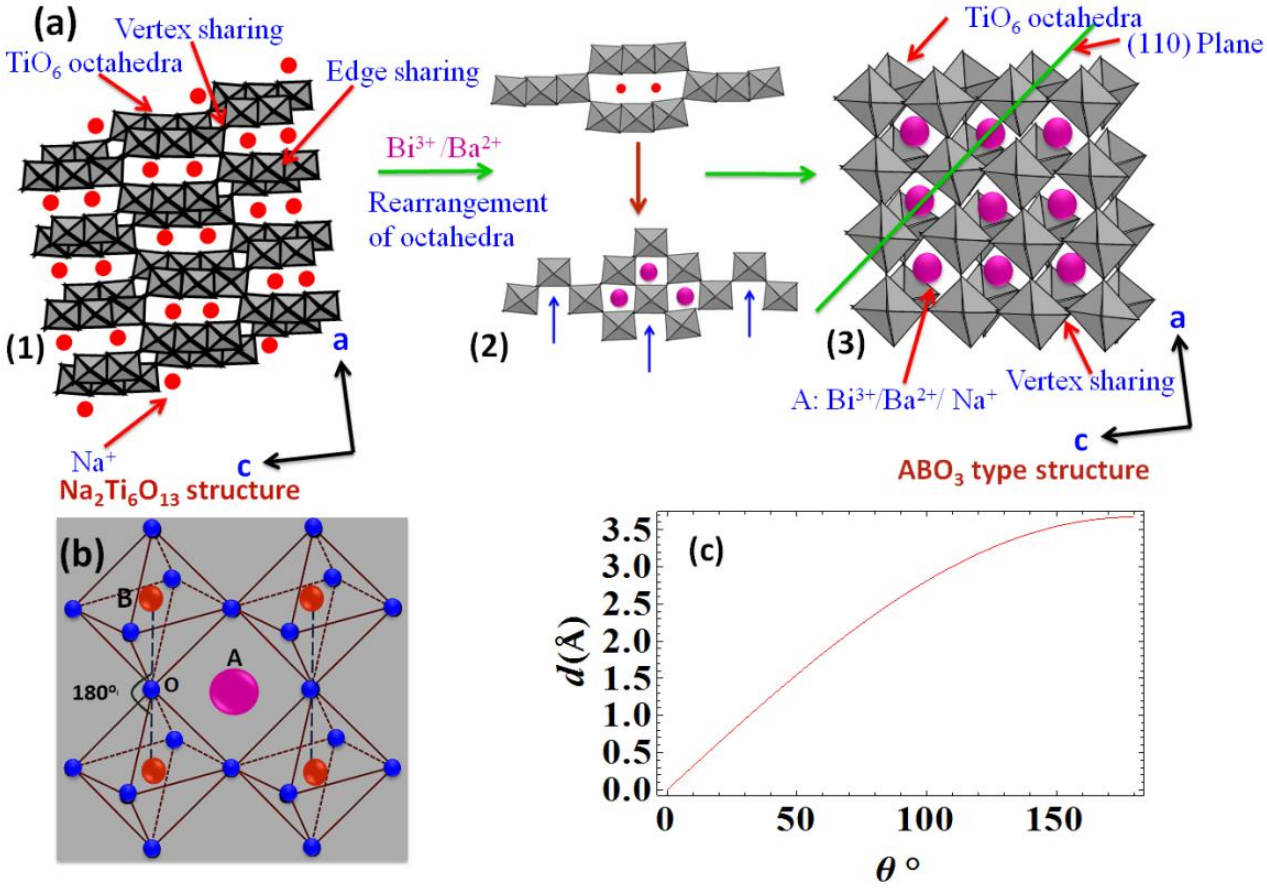

Figure -5.10: (a) Schematic of the transformation of $Na_2Ti_6O_{13}$ structure into ABO_3 type perovskite structure of NBTO through rearrangement of the octahedral connectivity type, (b) Schematic representation of the perovskite structure (ABO_3) (c) The change in the distance between two Ti-Ti atoms with the tilt angle of corner sharing octahedra depicting optimum distance between two Ti-Ti atom at 180^o as in ABO_3 type perovskite

The schematic representation of the ABO_3 type structure depicted in Fig. 5.9 (b) shows the presence of O^{2-} -T^{4+} -O^{2-} triples parallel to the x, y and z axes. In the ABO_3 type perovskite with no center of symmetry, under the application of electric field along z axis, the O^{2-} -T^{4+} -O^{2-}

chains parallel to the z-axis get polarized without a significant effect on the chains parallel to other two axes. The whisker polarized in the direction of z-axis imparts ferroelectricity to the system. Moreover, when configuration of A-site cation suffers a distortion (i.e. A-site atom displaces from its average position) during the displacement of oxygen ions in above process, the shape of unit cell would change resulting in a piezoelectric effect [116]. However in NBT-BT, the distortion would be different for A-site occupied with different atoms (Bi^{3+}, Ba^{2+} and Na^{+}) that have different charges and ionic radii resulting in disorder in the lattice as also indicated by the broad Raman modes.

3.1.3.5 High temperature morphological changes:

Furthermore, NBT-BT whiskers were dispersed on an alumina plate and subjected to heat treatment in air at various temperatures for 2h in order to investigate the high temperature morphological transformation and the role of the surface and grain boundary energy (Figure-4.11). On heat treatment at 1000^{o}C, coalescence occurred among the grains of the whiskers as small grains (Fig. 5.8(e-f)) observed at RT are not visible due to high dihedral angles. Further increase in temperature leads to the appearance of relatively larger grains within the whiskers forming a bamboo type structure at 1100^{o}C and 1175^{o}C (Fig. 5.11(b) and (c)). At 1175^{o}C, the whisker starts to get thinner in the vicinity of the grain boundaries showing grain boundary grooving as a result of the surface/grain boundary diffusion and local evaporation-condensation[195] [Fig. 5.11(c)]. According to the Mullins model [196]: $\gamma_b = 2\gamma_s \sin\theta$, where, γ_b and γ_s is grain boundary and surface energy, respectively and θ is surface inclination at the root of groove (Fig. 5.11(c)). In the present case θ is measured from the SEM micrograph (Fig. 5.11(c)) and comes out to be 41^{o} and therefore γ_b/γ_s equals to 1.31. Thus, the system has unusually higher grain boundary energy as compared to the surface energy. As a result, on

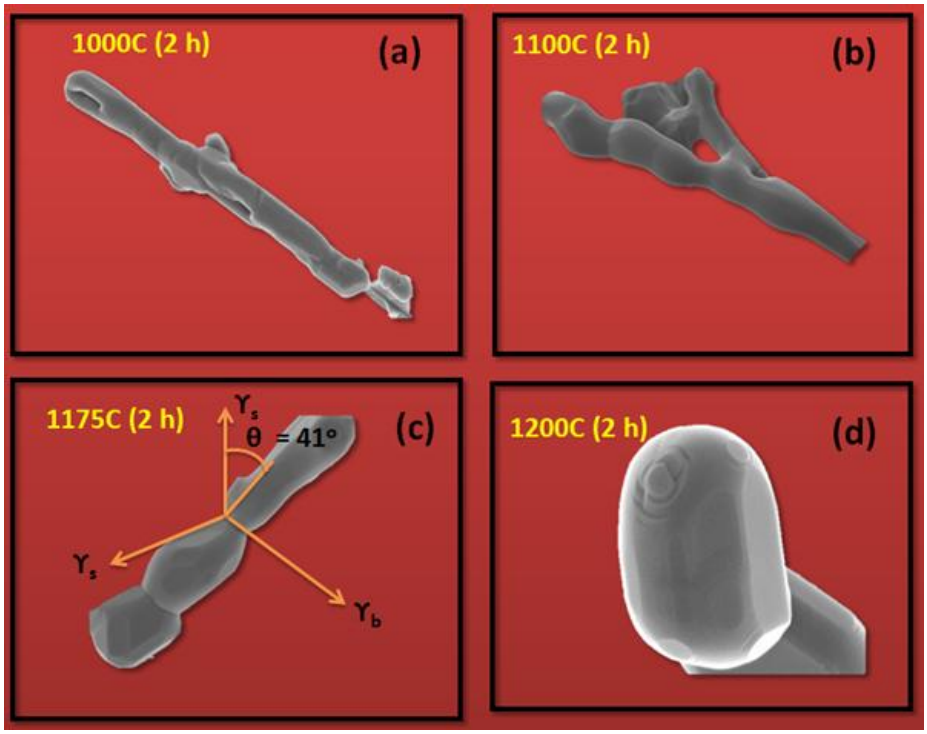

Figure-5.11 Change in the morphology of isolated whiskers heated on alumina plate in air at various temperatures (a) 1000^{o}C, (b) 1100^{o}C, (c) 1175^{o}C and (d) 1200^{o}C. The higher grain boundary energy leads to disintegration of whiskers to achieve equilibrium cubical shape.

further heating at 1200^{o}C, the whiskers eventually disintegrate into individual grains, in close analogy with the Rayleigh-type instability[177,197,198], so that the grain boundary energy is minimized by thermal grooving i.e. grain boundary grooving (Fig. 5.11(d)) to achieve an equilibrium cubical shape of the grain. Originally developed to explain breaking of liquid jet into small droplets, Rayleigh type instability has been used to explain phenomena like disintegration of nanowires into small beads [199] and fission of charged finite systems such as atomic nuclei or liquid droplets[200]. The grain boundary grooving and Rayleigh type instability both could lead to disintegration of polycrystalline whisker with bamboo type structure as both these mechanisms are driven by surface energy[201]. However in present case, grain boundary

grooving is considered to be dominant mechanism. Figure 5.12 depicts the schematic representation of disintegration of lead-free NBT-BT whiskers into isolated cubical grains.

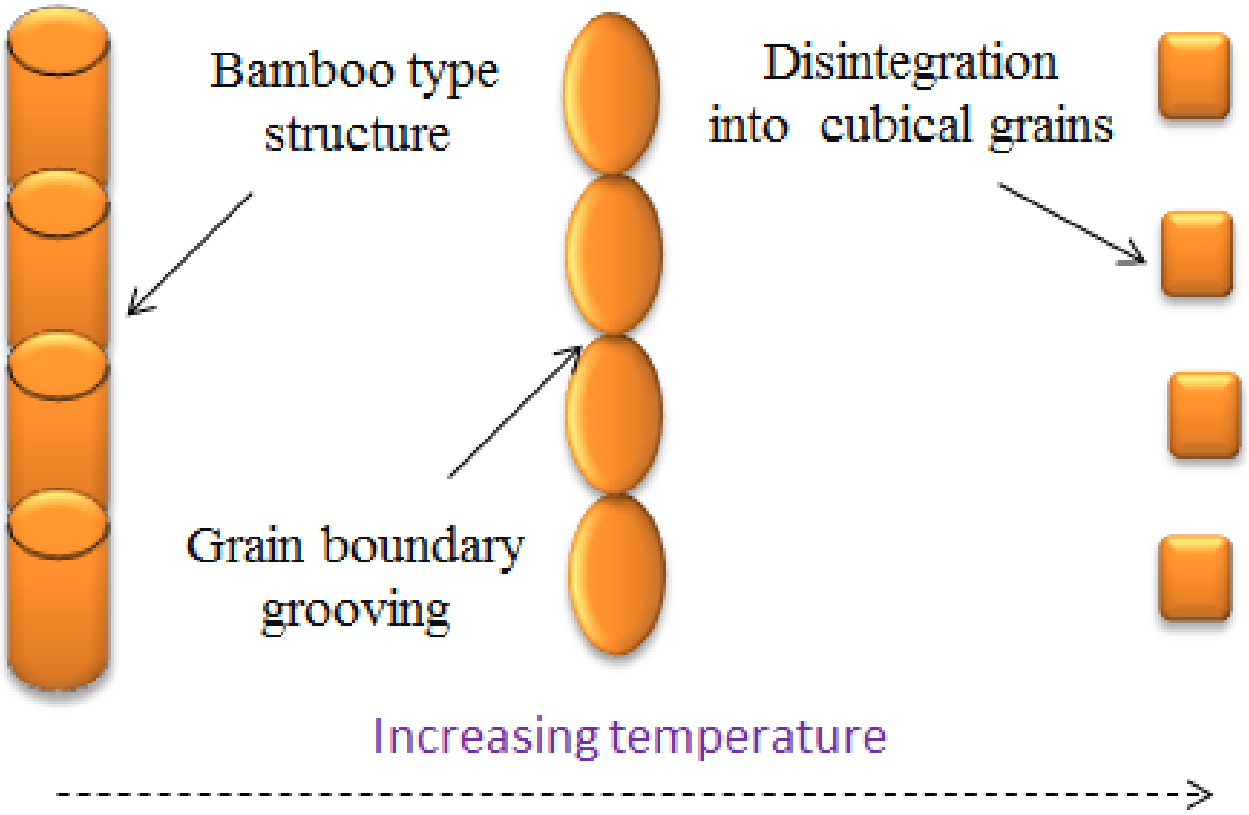

Figure 5.12 Schematic representation of change in morphology during disintegration of NBT-BT whisker with increase in tempretaure. The polycrystalline whisker disintegrates into isolated cubic grains via grain boundary grooving in analogy with Rayleigh type instability.

5.1.4 Chapter summary

The reaction route adopted in this research allows a topochemical conversion and structural rearrangement via translation of edge shared octahedra of the starting NTO material leading to the formation of nanostructured NBT-BT ferroelectric whiskers. These whiskers have a rhombohedral type average structure of the perovskite phase indicating their ferroelectric

nature as confirmed by high energy x-ray diffraction coupled with PDF analysis and Raman scattering. The HRTEM analysis reveals a local monoclinic structural distortion of NBT-BT whiskers suggesting a presence of modulated structure at the nanoscale. Upon high temperature treatment morphological changes take place resulting in breaking of the whiskers into individual grains as a consequence of a thermal grooving effect driven by minimization of the higher grain boundary energy. The lead free NBT-BT ferroelectric whiskers have potential applications in environmentally benign devices in microelectronic.

5.2 Origin of high piezoelectric response in A-site disordered morphotropic phase boundary systems

Perovskite piezoelectric compositions near the MPB are known to exhibit high piezoelectric response. In lead-based ABO_3 compounds, with B-site disorder, the origin of this enhancement has been associated with the presence of an intermediate monoclinic/orthorhombic state that bridges the adjacent ferroelectric rhombohedral and tetragonal phases. However, the origin of high piezoelectric response in lead-free ABO_3 compounds with A-site disorder has not been conclusively established. Moreover, a microscopic model derived from comparative analyses of HR-TEM and neutron diffraction that explains the origin of high piezoelectric response in lead – free MPB compositions of NBT-BT. Direct observation of nano-twins with monoclinic symmetry confirmed the presence of an intermediate bridging phase that facilitates a pathway for polarization reorientation. Monoclinic distortions of an average rhombohedral phase are attributed to localized displacements of atoms along the non-polar directions.

5.2.1 Background

Environmental restrictions in many parts of the world are demanding the elimination of lead from all consumer electronics. This has prompted global investigations on finding lead – free piezoelectric compositions with high electromechanical coupling. In the past decade, enhanced piezoelectric properties have been discovered in $(Na_{0.5}Bi_{0.5})TiO_3 - (K_{0.5}Bi_{0.5})TiO_3$ (NBT-KBT) and $(Na_{0.5}Bi_{0.5})TiO_3 - BaTiO_3$ (NBT-x%BT) compositions close to their morphotrophic phase boundary (MPB) [Figure-1.5]. Particularly, $Na_{0.5}Bi_{0.5}TiO_3$ (NBT) with R3c symmetry has emerged as a rhombohedral substitute for the lead–based counterpart similar to that of $PbZrO_3$ in $Pb(Zr,Ti)O_3$ [9,202]. However, some recent studies have indicated that the

NBT the end member in NBT-BT phase diagram instead exhibits a monoclinic Cc symmetry [203,204]. The solid solution (1-x)$Na_{0.5}Bi_{0.5}TiO_3$ – x$BaTiO_3$ (NBT-BT) exhibits MPB for x = 0.05-0.07. The magnitude of electromechanical coefficients measured at MPB for NBT-BT are d_{33} =125 pC/N, d_{31} = 40 pC/N, k_{31} =0.19, and $\varepsilon_{11}^{T}/\varepsilon_o$= 733[24]. However, the origin of piezoelectric property enhancement in lead-free ABO_3 compounds with A-site compositional disorder is unclear.

Earlier theoretical and diffraction studies on lead-based solid solutions established the relation between the presence of an intermediate phase with monoclinic/orthorhombic symmetry near the MPB and enhancement in piezoelectric properties. The intermediate phase bridges the end-members of a phase diagram with tetragonal and rhombohedral symmetries. Fu and Cohen[205] proposed that for a monoclinic symmetry, the polarization can easily adjust along the applied electric field providing strong coupling between degrees of freedom for polarization and crystallographic strain that leads to high piezoelectric response. Subsequent X-ray diffraction studies confirmed the importance of a monoclinic phase during polarization rotation [206]. For example, when electric field is applied along the pseudocubic [001] direction of rhombohedral PZN-PT with polarization vector along pseudocubic [111], the zero field rhombohedral state irreversibly changes first to an monoclinic M_C phase and then to an orthorhombic phase with a_m=c_m[Ref. 207].This intermediate monoclinic phase facilitates continuous rotation of the polarization vector between the T <001> and R <111> directions resulting in enhanced electromechanical response under external stimuli. Traditionally, at MPB, rhombohedral and tetragonal phases are assumed to coexist as the space group symmetries of these two ferroelectric phases are not connected by any direct group theory correlation [208,209]. The co-existence of

different ferroelectric phases at the MPB was attributed to the enhanced piezoelectric response in these compositions. Additionally, such type of two-phase coexistence has been considered to give rise to residual strains at the hetrophase boundaries, which could lead to lowering of symmetry at smaller length scales.

Unlike lead-based ferroelectrics that have varying occupancies on the B-site of an ABO_3 compound, NBT-based piezoelectrics exhibit disorder on the A-site. Different site-specific disorders can lead to lowering of crystal symmetry in ABO_3 compounds at nano-scales. For example, in well-known $Pb(Zr,Ti)O_3$ with B-site disorder, a monoclinic phase was evident from synchrotron X-ray diffraction under applied electric field. Establishment of a long-range monoclinic order in $Pb(Zr,Ti)O_3$ could be explained as a condensation of local displacements of Pb ions along non polar directions in the tetragonal phase[210]. In ABO_3 perovskite type systems, the A-site cation has stronger interaction with oxygen anions and hence a change in the A-site cation can strongly perturb the crystal symmetry. The different interionic interactions can be understood by considering the differences in the local environment of A and B cations in the ideal perovskite structure. In case of $Pb(Zr,Ti)O_3$, for A-site cations, the oxygen nearest neighbor shell has 12-fold symmetry. This symmetry is however broken for the B-cation next nearest neighbor shell. Zr is a larger ion than Ti, and thereby purely repulsive interaction between Pb and B cation (Zr^{4+}/Ti^{4+}) has been considered to be stronger for Pb-Zr than Pb-Ti [211]. On the other hand, all B-cation distribution do not display a strong dependence on the local structure and are aligned closely with the Pb ion distributions [211]. Grinberg et al. [211] considered Pb distortions, produced by a hierarchy of interactions, as determining factor for the average structure of the material. The effect of disorder on the different sites in the perovskite structure is schematically illustrated in Figure 5.13.

Figure 5.13(a) shows the schematic of long range ordering due to cooperative displacement of Ti in archetype piezoelectric $BaTiO_3$. The displacement of B-site cation is shown by arrow. However when B-site is substituted by Zr^{4+} and Ti^{4+}, the local displacement of Pb^{2+} is substantially perturbed by the presence of the neighboring ions. The Pb^{2+} tend to go away from Zr^{4+} and close to the Ti^{4+}. However, on average Pb^{2+} distortions were found to be in $[001]_c$ direction[211] leading to long range monoclinic phase in $Pb(Zr,Ti)O_3$ at MPB. The schematic representations of ionic displacements in $Pb(Zr,Ti)O_3$ [211] are depicted in Figure 5.13(b). The perforated circles and small arrows are showing the tendency of Pb^{2+} displacements and Ti/Zr displacements in polar direction, respectively.

The situation in NBT-BT is more complex because the A-site is occupied by three types of atoms (Bi^{3+}, Ba^{2+} and Na^{+}) with different chemistry like charge, ionic radius and electronegativity etc, as illustrated in Figure 5.13(c). The B-site Ti^{4+} would have stronger repulsive interaction if surrounded predominantly by the Bi^{3+}. This interaction would vary significantly depending on the type of neighboring ions Ba^{2+} or Na^{+}. As discussed above, the A-site cation has stronger interaction with oxygen anions and hence a change in the A-site cation can strongly perturb the crystal symmetry. These local structural distortions could reduce local symmetry. For NBT-BT systems of MPB compositions, local-scale monoclinic symmetry from an overall rhombohedral symmetry has been proposed from diffused anelastic and dielectric spectra, NMR spectra and diffuse X-ray patterns[212,213]. However, no direct microstructural evidence for such localized distortions has been reported. Therefore, it is still debatable whether the perceived significance of local monoclinic distortions, as observed in lead-based piezoelectrics, could be extended as a general principle to other systems as well. Here, the direct evidence from high-resolution TEM and neutron diffraction measurements was provided for

localized monoclinic distortion of an overall rhombohedral symmetry in NBT-BT in form of nanoscale twins. The importance of the nano-twins towards enhanced piezoelectric properties is discussed.

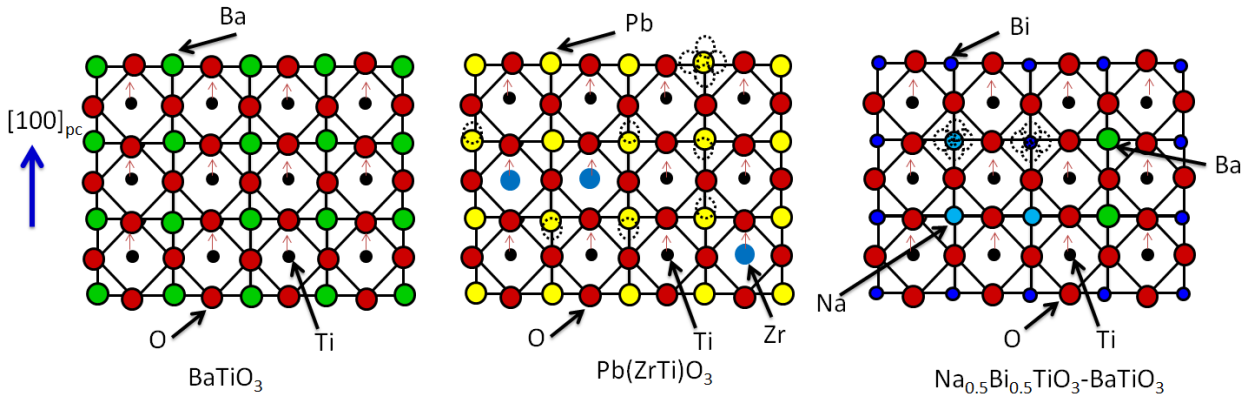

Figure-5.13 (a) Long range polar lattice distortions in $BaTiO_3$, (b) polar lattice distortions in Pb(ZrTi)O3, (c) polar lattice distortions in $Na_{0.5}Bi_{0.5}TiO_3$-$BaTiO_3$. The dotted circles marked represent possible distortion direction of A-site atoms depending on the neighboring atoms.

An understanding of the crystallographic distortions near the MPB also could help to clarify the phase transition behaviors that have been reported for NBT-BT. During cooling from high temperature, NBT undergoes a sequence of phase transitions from a high temperature cubic (C) phase to ferroelastic tetragonal (T) phase at 540°C, and a diffuse phase transition (DPT) from ferroelastic tetragonal (T) to rhombohedral (R) phase between 200°C and 320°C [19]. Different variants of phase diagrams for NBT-BT have been proposed that consists of ferroelectric rhombohedral and tetragonal phases as end components, and an antiferroelectric or ferrielectric orthorhombic component as an intermediate phase[206,214-217]. Coexistence of rhombohedral and tetragonal phases has been observed over a broad range of temperatures and *E*-fields while the orthorhombic phase was proposed to exhibit antiferroelectric-like (AFE) characteristics [23,218]. Recent studies on the orthorhombic phase describe it as a relaxor phase with polar nanoregions [219,220]. The high piezoelectric response and *E*-field induced strain in NBT based

systems has been attributed to structural phase transitions under the application of an *E*-field [221]. However in a previous study, it has been demonstrated that *E*-field induced structural phase transition is not prerequisite for achieving high piezoelectric constant in NBT-BT [222]. Intriguingly, textured and randomly-oriented polycrystalline ceramics of the same composition of NBT-BT were found to exhibit drastically different phase transition behaviors under electric field which were tentatively associated with variance in coherence lengths of polar nanoregions and internal stresses induced by domain switching.

Based on these earlier results, it could be said that the role of nanoregions in the NBT-based system is quite special as compared to lead-based relaxors. For example, in case of PZN-0.1PT, the off centering of Pb cations containing a lone pair of electrons play an important role in the origin of polar nano regions and have been found to favor the polar displacement of corresponding nearest B-site cations[223]. During the application of *E*-field, the correlated displacement of Pb ions could be considered to result in long range polar phase with lower symmetry. However as discussed earlier, the case is very different in NBT-BT system with the A-site being shared by Bi, Na and Ba. The nature of local polar distortions created by Bi on the A-site containing a lone pair of electron would be different than that of due to Na and Ba without lone pair of electrons in terms of cation off centering and octahedral tilting disorder. Therefore in NBT-BT, the local distortions due to the substitution on A-site are more complex than that of B-site substituted lead-based relaxors and would behave differently under external stimuli. These short range local structural distortions can further couple with elastic degrees of freedom resulting hierarchical domain structures from mesoscopic lamellar domains to polar nano regions[224,225]. Moreover, NBT-BT exhibits a high temperature unique ferroelastic phase transition followed by low temperature ferroelectric phase transition as discussed earlier. The

ferroelastic domain variants created during the high temperature ferroelastic phase transitions sustains up to room temperature and coexists with the nano sized ferroelectric domains[226]. The nano sized ferroelectric domains were found to be geometrically and elastically restricted within micro-sized ferroelastic domains [226]. Therefore, the percolation behavior of these polar nano regions under the influence of *E*-field in piezoelectric A-site disordered NBT-BT system can be influenced by the presence of ferroelastic domains. However, this kind of transition has not been reported in B-site disordered lead-based relaxor like PZT. Also, the percolation behavior of polar nano regions vary significantly with the different systems, as PZN-0.8PT was not found to show significant change in PNRs under applied E-field[227]. The percolation behavior and coupling between local polar distortions with the nonlinear elastic lattice [228] could play an important role in NBT based systems exhibiting interesting functional response and structural phase transition behavior.

In this chapter, structural investigations on high purity single crystals and polycrystalline samples were carried out. In order to account for the different types of perturbation of domain morphology expected in polycrystalline samples, a special type of samples was studied. For polycrystalline samples, whisker morphology was developed to clearly delineate the contribution from the crystallography. Most of the piezoelectric materials used in polycrystalline form consist of a large number of randomly oriented grains each with multiple domains of varying orientations as allowed by crystallographic symmetry[229]. The domain switching in one grain is constrained by differently oriented neighboring grains. Moreover, neighboring grains can also induce lateral stress on each other during the paralectric to ferroelectric (PE-FE) phase transition [230]. Therefore, the perturbation of domain behavior due to interaction with the differently oriented neighboring grains is a highly correlated collective process that is complicated to

quantify [229]. In order to overcome this problem, NBT-BT whiskers were synthesized with a diameter of ~2-3 grains (grain size ranging 300-500 nm) as shown in the inset of Fig. 5.16. With this morphology, the influence on the domain system in a given grain from the domains in neighboring grain will be negligible.

5.2.2 Experimental

Single crystals were grown using the molten flux method [231]. In order to grow single crystals of $0.93(Na_{0.5}Bi_{0.5})TiO_3 - 0.07BaTiO_3$ (after this point NBT-BT will be referred to this MPB composition in this chapter), pre-calcined (800- 900°C, 2h) powder was mixed with 30wt% Bi_2O_3 and 10wt% Na_2CO_3 and heated in sealed Pt crucible at 1300°C for 6h before slowly cooling down to RT (room temperature). The synthesis of NTO whiskers was performed by using the molten salt synthesis method as reported earlier. These NTO whiskers were used to synthesize NBT-BT whiskers of the same composition as explained in chapter 5.1. The composition of both types of specimens (single crystals and whiskers) was confirmed by energy dispersive spectroscopy. The XRD experiments were conducted on these NBT-BT whiskers (thickness $\sim 0.5 - 1.0\mu m$ and length $\sim 10 - 20\mu m$) to confirm the formation of perovskite phase at RT. These whiskers were pressed in to pellet and sintered at 1200^oC for 2h. The electromechanical coupling constants for various variants of NBT-BT like single crystals, whisker based polycrystalline ceramics and traditionally processed NBT-BT ceramics are listed in Table-5.2. The specimen processed using NBT-BT whiskers shows higher piezoelectric response than traditionally processed variant. For morphological investigations, Zeiss LEO 1550 scanning electron microscope was used. The high-resolution neutron powder diffraction patterns of the NBT-BT whiskers were collected at the VULCAN diffractometer of the Spallation Neutron Source (SNS), Oak Ridge National Laboratory [232]. The sample was loaded into a

cylindrical vanadium can and the diffraction patterns were collected with an incident neutron beam in the time-of-flight mode. Rietveld refinement on the diffraction pattern was performed using the GSAS software package [233].

Table 5.2- List of the piezoelectric properties for various variants of lead-free piezoelectric NBT-0.07BT

Sample	d_{33} **(pC/N)**	k_{31} **(%)**
NBT-0.07BT (single crystal)	300±5	40±2
NBT-0.07BT (whisker-based)	205±5	28±2
NBT-0.07BT(Conventional sintering)	160±5	18±2

5.2.3 Results and discussion

5.2.3.1 TEM domain structure analysis

The twin microstructure in the single crystals and whiskers of NBT-BT was first investigated. During transition from a higher symmetry phase to a lower symmetry phase, twin boundaries play an important role as twin boundaries are considered to be localized pseudo symmetries relating one twin domain to another by a lost symmetry operation. The twin domains are formed due to the loss of point group symmetry and the interaction between twin boundaries (walls) can give rise to a multitude of domain patterns creating difference between the local atomic structure of twin (domain) boundary and bulk[234]. The arrangement of domain patterns in this case are called hierarchical because it can be decomposed into simpler patterns until the most elementary unit ‘twin wall’ or ‘domain wall’, is found [234].

The multitude of domain structures of NBT-BT single crystal is depicted in the bright field TEM images of Figure-5.14(a)-(d) and Figure 5.15. The ferroelastic lamellar domains having width ~ 100-200 nm with planar $\{100\}_C$ domain walls can be observed in Figure 5.14(a). The magnified view of these lamellar domains is depicted in Fig. 5.14(b). A HR-TEM image of lattice fringes across domains and fast fourier transform (FFT) patterns of two regions in the image are presented in Figure 5.16(b). The FFT and nano probe electron diffraction patterns (Fig. 5.16 (d)) recorded on the two sides of different contrast regions of these domains were found to be similar indicating no significant structural changes across them. The bigger lamellar domains with domain wall planar on $(100)_C$ and $(010)_C$ intersect at angle ~90^o with plane of intersection $\{\bar{1}10\}_C$ giving rise to a herringbone-type domain structure as observed in modulated systems[235] (marked with the rectangle in Fig. 5.14(c)). The magnified image of these domains indicates that the thicker lamellar domains are composed of smaller domains (fig. 5.14(d)). The lamellar domain consists of two domains with a common domain wall attracting each other and this force of attraction decreases rapidly with the increase in the distance between the two domain walls [236] resulting in fine substructure ranging from submicron to nano scale in dimension that is represented as hierarchical structure of ferroelastic domains. Similar hierarchical domain structures were reported for ferroelastic lead phosphate [237]. Another region of interest showing domain structure is depicted in Figure 5.15, which shows polydomain plates with domain boundaries on different planes. In this image along with the larger sizedomains with thickness ~ 100-200 nm having domain walls planar on {100}c, another set of domain variants with smaller size domains (~50 nm) and boundaries planar on $\{1\bar{1}0\}_c$ were also observed. The thickness of polydomain plate δ having domains thickness d is marked in Fig. 5.15, which is ~400 nm. Hierarchical patterns with lamellar domains are formed depending on

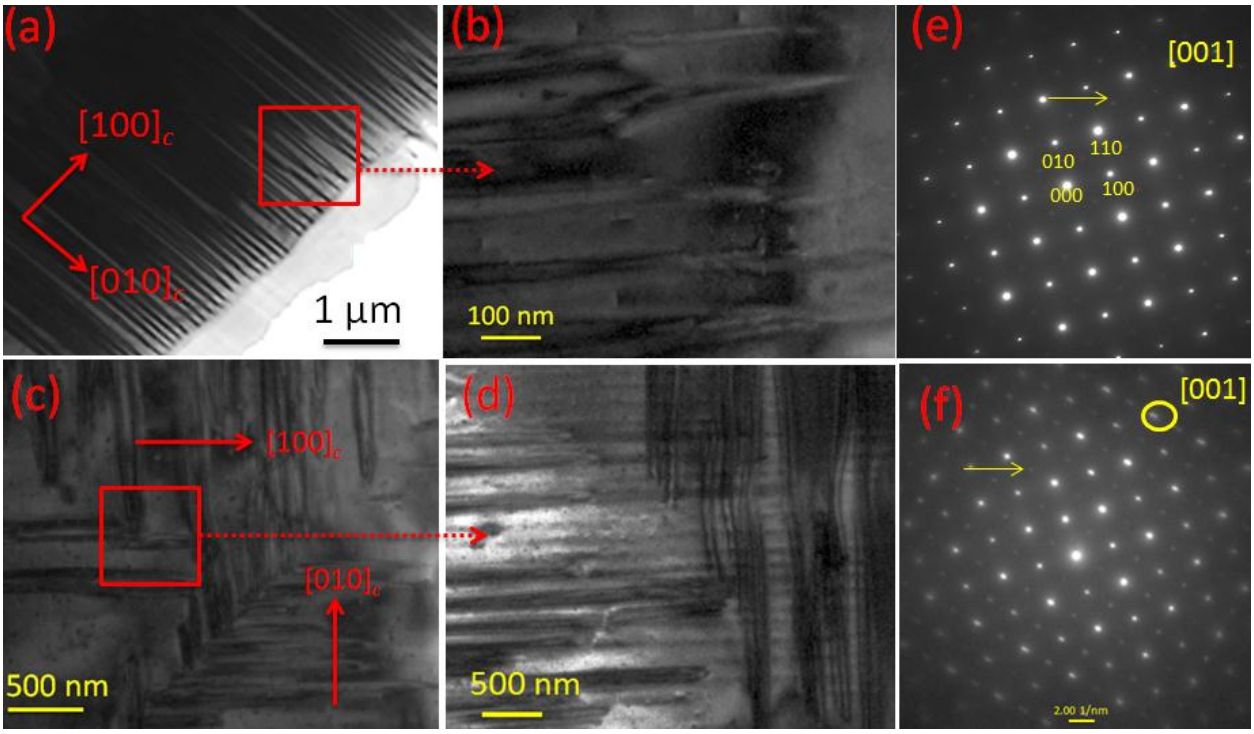

Figure-5.14 High purity single crystal studies. (a) TEM image of thin domains with domain walls planar on (100), the magnified view of these domains is depicted in Fig. 5.14(b). (c) The herringbone type domains structure composed of thin domains with domain walls planar on (100) and (010) and intersecting on (110) plane. The magnified view of these domains is depicted in Fig. 5.14(d). (e) SAED with large probe size, (f) electron diffraction with nano beam. The arrows marked in (e) and (f) indicates superlattice reflections. It was noticed that the $\boldsymbol{g}_{100}/\boldsymbol{g}_{010}$ =1 and the angle between these vectors was ~ 90^{o}, however the SAED with nano beams shows deviation in the ratio and the angles indicating lowering of symmetry.

the interaction between domains and the energy of the domain walls. According to Khachaturyan et al [238] the typical domain size in ferroelastic materials is related to the thickness of the poly domain plate δ and domain wall energy density γ_t:

$$d = \xi\sqrt{\frac{\gamma_t}{\mu\varepsilon_o^2}}\delta \qquad (5.2)$$

where ξ is a dimensionless constant, μ is the shear modulus, and ε_o is the twinning strain. This theory was extended to piezoelectric materials to explain miniaturized domain state and adaptive

phase in MPB compositions [239] and the thickness *d* of ferroelectric domains in a polydomain plate of thickness 'δ' was found proportional to $\sqrt{\gamma_t \delta}$. On decreasing the domain wall energy, the wall thickness would decrease [238]. Furthermore, Theissmann et al.[240] investigated change in domain structure across MPB of PZT. They reported miniaturized domain in MPB composition of PZT with polydomain plate (microdomain) having thickness δ ~ 250 nm containing nano-sized domains [240]. These nanodomains were found to respond to *E*-field instead of microdomains.

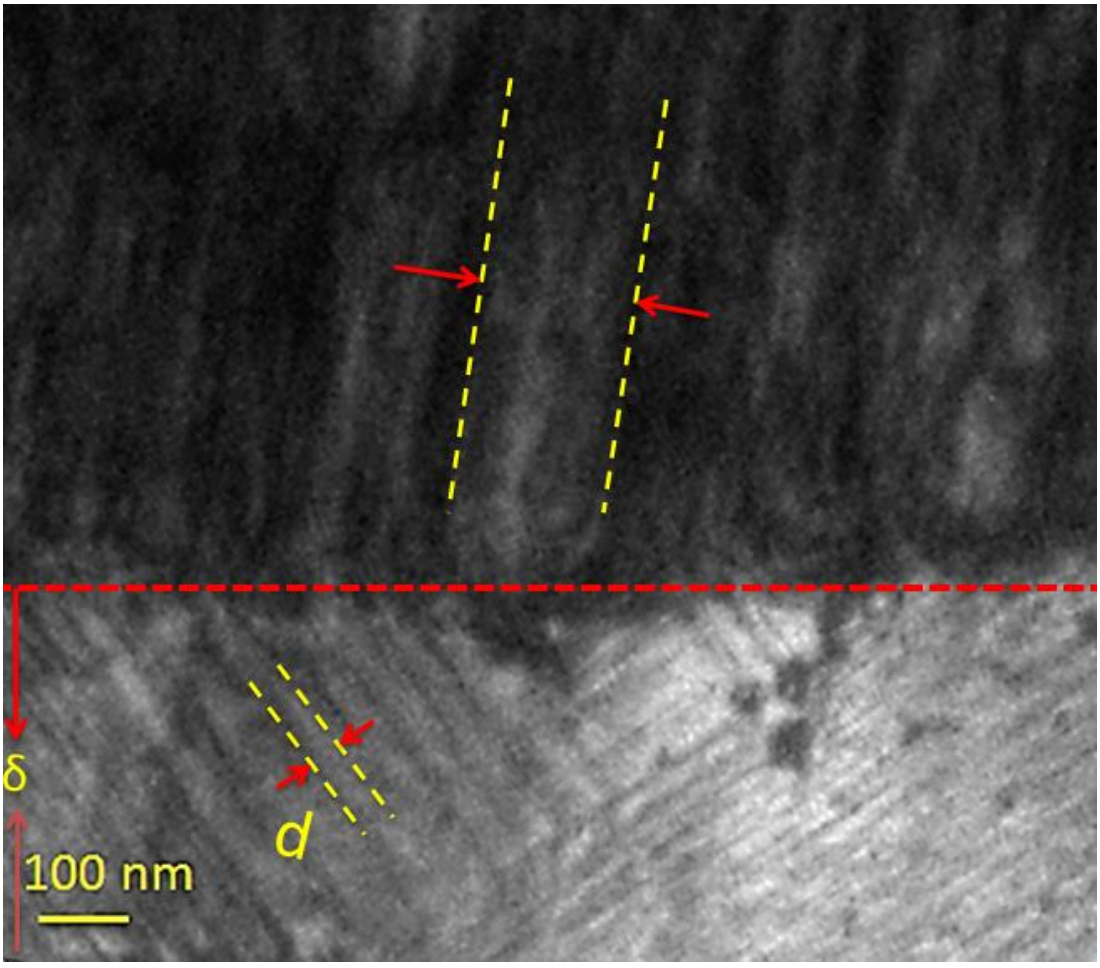

Figure-5.15 Bright field TEM image of various domain variants of NBT-BT single crystals viewed from $[001]_c$ zone axis.

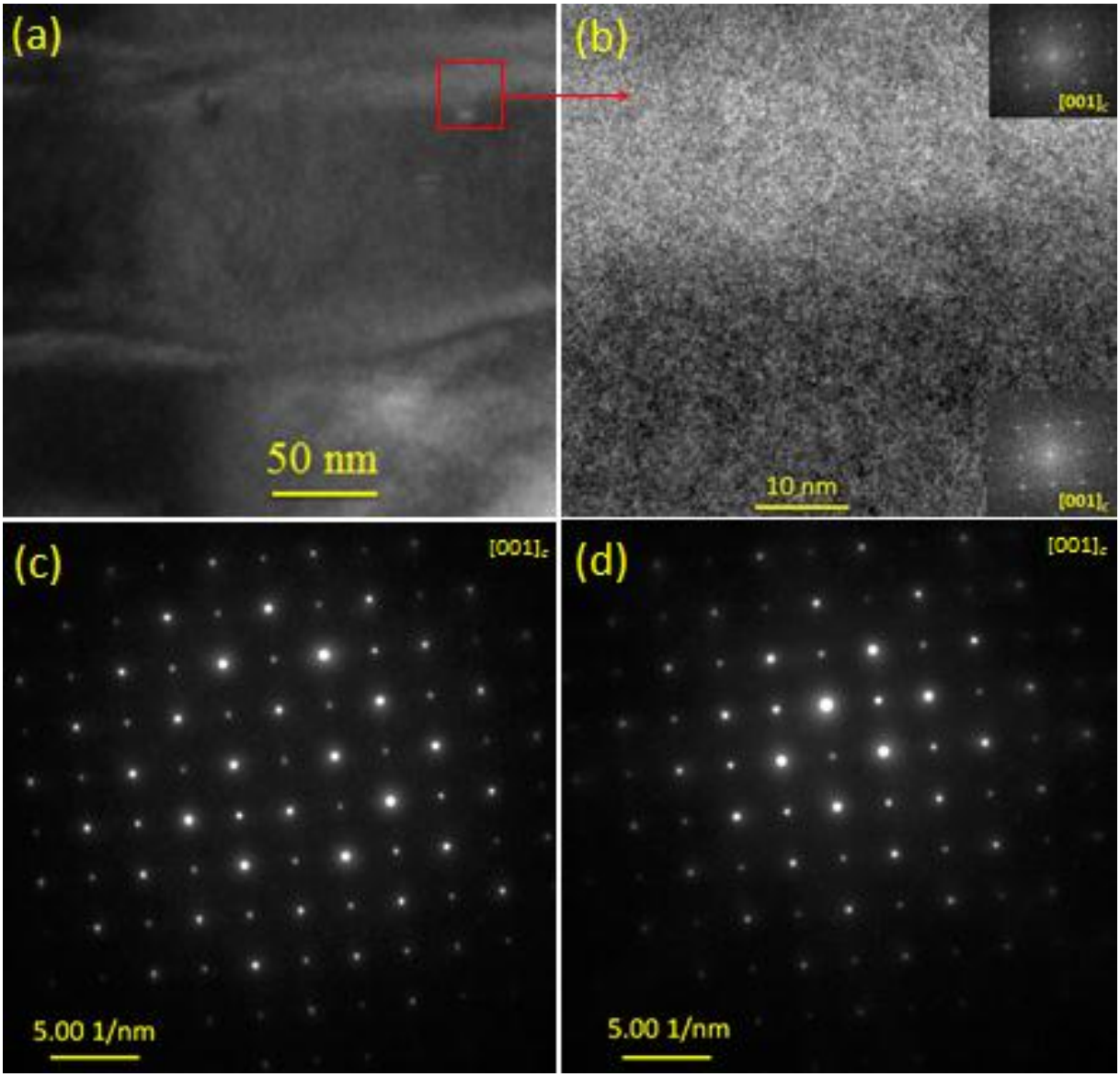

Figure 5.16 (a) TEM bright field image of the magnified view of edges of domains in NBT-BT single crystal, (b) HR-TEM image corresponding to rectangular region marked in (a), the FFTs in the inset depicts the FFT corresponding to respective regions indicating no sufficient deviation in atomic planes between two variants . (c) and (d) depicts the nano-beam diffraction between two variants.

The crystallographic details for the nanodomains are next elucidated from the electron diffraction patterns. Figure-5.14(e) shows a SAED pattern from the NBT-BT single crystal with $[001]_C$ zone axis with electron beam probe size ~ 400 nm. The ½ $\{ooe\}_C$ (*e* stands for even Miller indices and *o* for odd Miller indices) super-lattice reflections are marked with arrow in

Fig. 5.14(e). In this case the ratio of the magnitude of $\boldsymbol{g}$ vectors ($\boldsymbol{g}_{100}/\ \boldsymbol{g}_{010}$ =1) was found to be unity with 90^{o} phase difference between them. Interestingly, from the diffraction patterns recorded using nano beam (~ 5 nm) probe (Fig. 5.14(f)), deviations from the unity ratio of $\boldsymbol{g}$ vectors were observed, as well as the angle between the $\boldsymbol{g}$ vectors was found to deviate from 90^{o}. These changes suggest a lowering of symmetry locally [$\boldsymbol{g}_{100}/\ \boldsymbol{g}_{010}$ =0.98 and angle between them deviates by 0.75-1.0 ^{o} (Please note these deviations are much clearer when observed over several diffraction spots)]. The implications of this local deviation in crystal symmetry will be more apparent in later discussions. Also, the splitting in the higher order diffraction spots reveals the presence of twins with small shear displacement ~ 0.03 calculated from the splitting of higher order diffraction spot in Fig. 5.14(f). Similar magnitude of splitting in electron diffraction pattern was observed for PZT [241]. Such small shear displacements could be the result of only partial relaxation of stress in NBT-BT single crystals as there are various crystallographically allowed domain variants with collective interactions among them. It is therefore important to use NBT whiskers with diameter of only few grains so that interactions due to surrounding domain variants are reduced.

Next, HR-TEM analysis was performed on NBT-BT whiskers (inset of figure -5.17). HR-TEM analysis was repeated across several different samples and sample area to confirm the results. Figure 5.17 shows the HR-TEM image of lattice fringes exhibiting the presence of nanotwins. Yellow lines are drawn along several lattice planes as a visual guide to highlight the presence of a twin boundary. For comparison, FFT patterns were calculated from a twin free region (region-1) and the twinned region (region-2). These FFT patterns could not be indexed using a rhombohedral symmetry as has been suggested in earlier works [24,202]. Interestingly, both the FFT patterns can be indexed using a monoclinic symmetry (JCPDS #460001). The

lattice parameters of this monoclinic cell is: a = 0.5553(2), b = 0.6675 (3), c = 0.5520(1) nm, β = 120.54(2)°. The monoclinic crystal structure within the nanotwins is significant since monoclinic lattice can have more degrees of freedom to adapt local stress field in ceramics [241].

The zone axis $[2\bar{2}1]_M$ (M stands for monoclinic phase) was obtained from the indexed FFT pattern in Figure 5.17. The FFT pattern of twinned region clearly depicts an additional diffraction spot near $(\bar{1}02)_M$ and the inter-planer angle was measured to be 11°. The twinning plane (or "mirror plane") was parallel to the zone axis and is the boundary between two twinned domains. Next, the twin plane/ twin boundary was calculated, which was found to be $(\bar{1}\bar{1}0)_M$. The continuity of lattice planes across the boundary indicates that the twins were coherent. The arrow marked with N in the FFT pattern of region 2 points towards the shapes of twin spots. Two spots very close to each other suggest the presence of nanotwins with very small twinning shear of ~0.06. These nanotwins were present within boundaries of bigger nanotwin shown by yellow lines. Similar nanotwin structure with thickness about one atomic layer was observed in nanocrystalline copper [242]. The smaller size of nanotwins has been found to be associated with very small twin boundary energy [238] as discussed earlier According to Khachaturyan et al. [238] the lower surface energy and large strain energy leads to smaller size nano twins. However at certain smaller size (comparable to atomic scale size), the finite interaction among the twin walls constrain further miniaturization of twin domains. Randall et al. [243] calculated the surface energy (σ) of $\{100\}_R$ and $\{110\}_R$ twins in rhombohedral system following the work of Zirnov[244] and suggested that $\gamma_{100} \approx 3\gamma_{110}$. Therefore, the formation {110} twins is more energetically favorable than that of {100} twins.

The schematic representation of twinning is depicted in Figure 5.18(a). In present case, twinning gives rise to plane with same interplanar spacing but slightly deviated (11^o) from the

parent plane. The magnitude of shear can be given by tanθ = tan (11^o) = 0.19, which is much higher than that of twinning shear (0.06) of nanotwins having thickness of atomic layer as discussed above. The magnitude of shear observed in this case was comparable to martensitic materials [245]. The orientation of habit plane with respect to the parent lattice plane at a given point can be estimated geometrically [246] as:

$$sin\alpha = \frac{sin\theta}{\sqrt{2-2cos\theta}} = 84.5^o \; for \; \theta = 11^o \qquad (5.3)$$

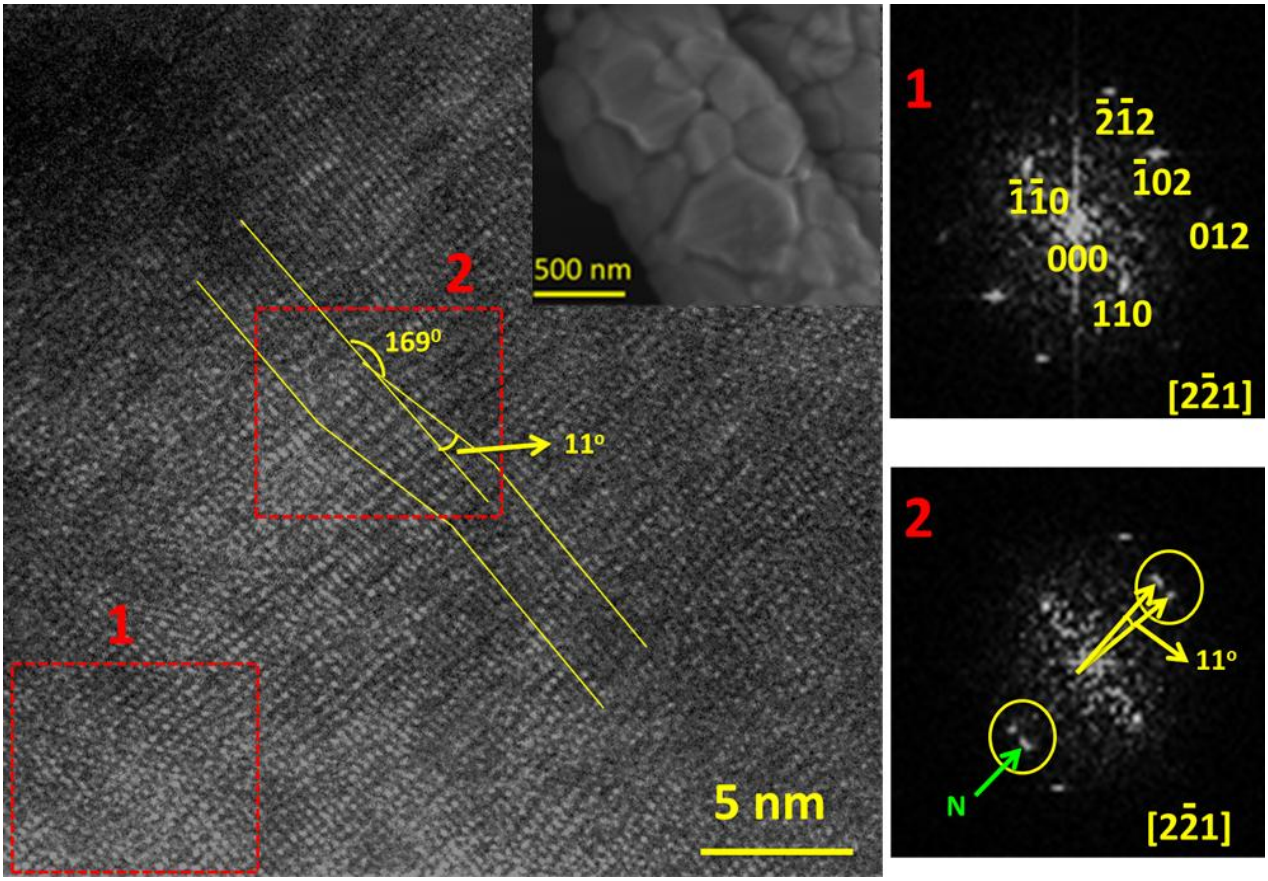

Figure 5.17 A HR-TEM image showing the presence of a nanometer twinned region in NBT-BT whiskers. The two patterns on the right labeled 1 and 2 are Fast Fourier Transform (FFT) patterns from the corresponding regions of the HR-TEM image marked 1 and 2; the split spots in the yellow circles of the FFT of region 2 indicates twinning of the atomic planes. The inset on the HR-TEM image is an SEM micrograph of NBT-BT whisker.

5.2.3.2 High resolution neutron diffraction analysis

Furthermore, the crystallographic symmetry of NBT-BT whiskers at larger length scales was characterized from neutron diffraction. The high resolution neutron diffraction pattern was fitted separately for two possible space groups - *R3c* and *Cc*. The rhombohedral space group *R3c*, with antiphase oxygen octahedral tilts, has been reported previously for NBT-BT solid solutions [18,216]. The space group *Cc* is a monoclinic subgroup of the *R3c* which also allows tilting of

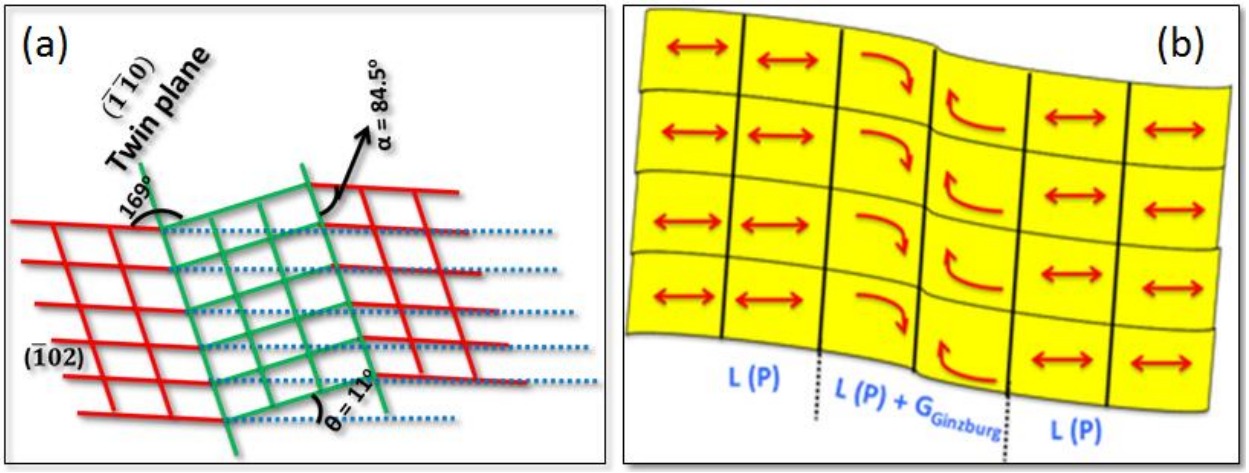

Figure 5.18 (a) A schematic representation of the twin arrangement observed in fig.-5.17, (b) Schematic plot of bent lattice planes indicating the various energy contributions (After Salje [237). The lattice on either end of the plot is distorted due to PE-FE phase transition. The spontaneous strain is symbolized by the double arrows. The relevant energy is Landau potential. When the planes are bent additional gradient energy occurs as described by the Ginzburg energy. The single arrow represents bending of the planes

the oxygen octahedral, and has been mentioned in a previous report [247]. The Rietveld refinement for space group *R3c* yielded the following lattice parameters: a_H = 0.54999 (2) nm, c_H = 1.35583 (9) nm, V = 0.35519 (2) nm^3, with Rp = 0.057, wRp = 0.0738 and reduced χ^2 = 3.415; the starting variables for the fitting were taken from Jones et al. (Figure 5.19(a)) [18]. In comparison, Rietveld refinement for space group *Cc* yielded the following lattice parameters: a_M

= 0.95368 (11), b_M = 0.54921 (7), c_M = 0.55154 (7), β = 124.956 (8), with Rp = 0.072, wRp = 0.097 and reduced χ^2 = 5.909 (Figure 5.19(b)); the initial setting for this refinement was taken from *Cc* structure of PZT [248]. The *R3c* space group yielded better fit to the diffraction pattern which is evident from a 20% improvement in the value of Rp for the *R3c* phase. Furthermore, examination of the high intensity (111) peak (see insets) clearly reveals the better fit for the R3c model. A mixture of tetragonal and rhombohedral phases was also tested; however it did not provide a stable fit.

Neutron diffraction of NBT-BT whiskers indicates an average rhombohedral structure with *R3c* space group in contrast to monoclinic symmetry observed in HR-TEM analysis. Therefore, although the material has a monoclinic symmetry at a local scale, it retains an average rhombohedral structure, as revealed by bulk powder neutron diffraction. It was observed that even though the *R3c* model provides a good fit to the neutron diffraction profile in terms of overall statistics, slight broadening of the measured Bragg peaks with respect to the calculated pattern was observed (for example see peaks 111 and 3/2 1/2 1/2 in Figure 5.19). Such broadening could arise from local monoclinic distortions of the crystal in the matrix. This is consistent with previous report in which polar nano regions of ~20 nm were estimated from diffuse X-ray scattering, although the average structure retained *R3c* symmetry[249]. It was suggested from the diffused X-ray scattering measurements that the displacements of Bi^{3+}, Ba^{2+} and Na^{+} away from $[111]_R$ (R stands for rhombohedral phase) direction towards $[100]_T$ (T stands for tetragonal phase), can give rise to local monoclinic symmetry.

A lowering of the crystal symmetry within the twin domains at the nanoscale suggests that they are formed due to the loss of point group symmetry during the phase transition from the high temperature paraelastic cubic phase to an intermediate ferroelastic tetragonal phase in NBT

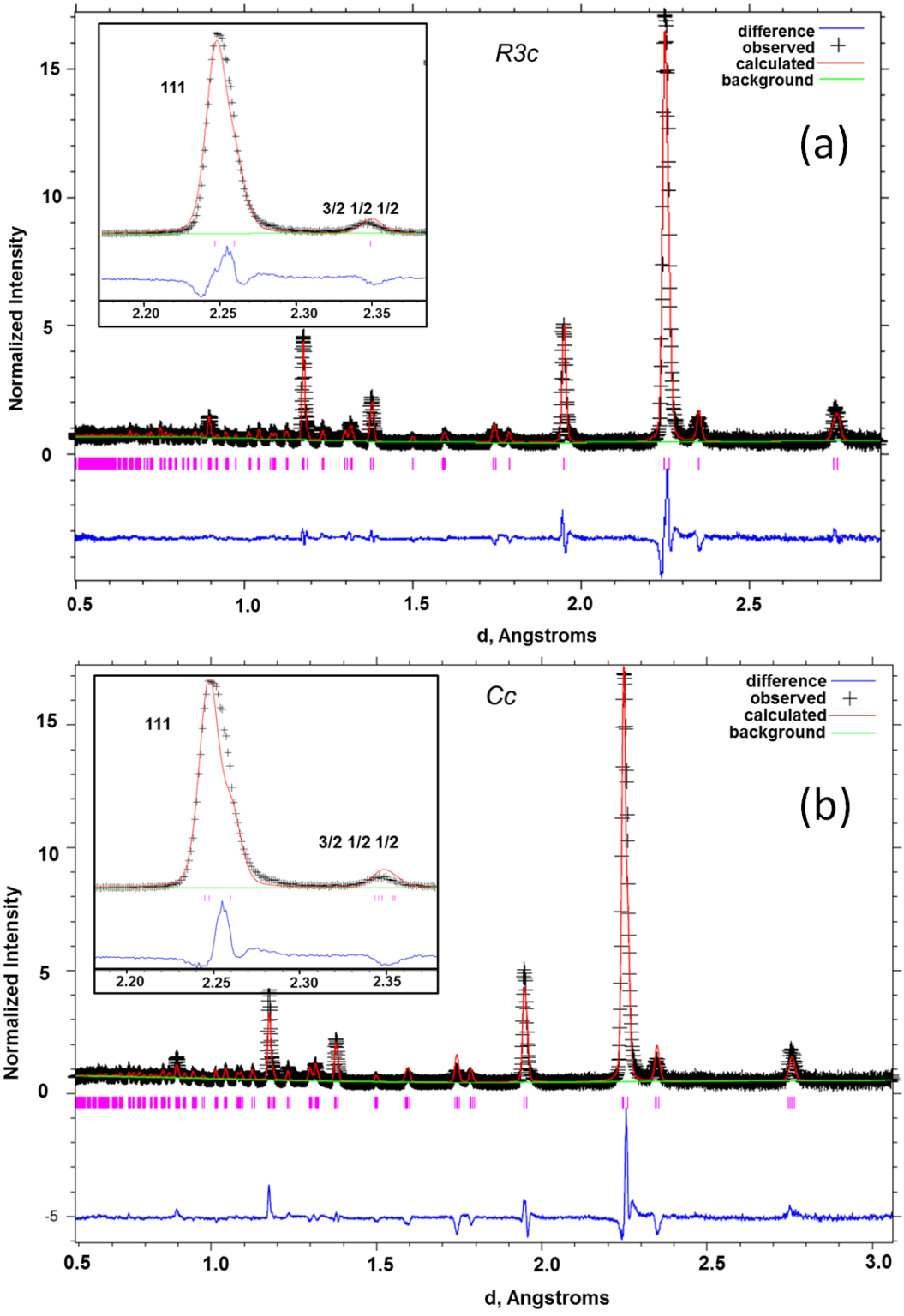

Figure 5.19 High resolution neutron diffraction patterns fitted with space group (a) R3c (b) Cc. Insets are showing {111} reflection was fitted well R3c space group.

based systems. Thus, recently observed structural phase transition in NBT based materials [250] under the application of electric field could be expected to be facilitated by the presence of nano twins. Next, SAED from different zone axis were recorded to investigate the nature of superlattice reflections in NBT-BT whiskers. Figure 5.20 depicts the SAED patterns taken along various zone axes on NBT-BT whiskers. The SAED patterns with zone axes $[001]_C$ and $[112]_C$ depicts superlattice reflections ½ $\{ooe\}_C$ and ½ $\{ooo\}_C$ (*e* stands for even miller indices and *o* for odd miller indices) as marked in Fig. 5.20 (a) and 5.20 (b), respectively. The observance of ½ $\{ooe\}_C$ and ½ $\{ooo\}_C$ superlattice reflections are consistent with the average rhombohedral phase with the *R3c* space group[251,252]. However, the origin of super lattice reflections can be attributed to disorder in octahedral tilting and cation-ordering [253], both of which could lead to local departure from the average rhombohedral symmetry [254] resulting in the formation of a localized monoclinic phase (Schematic showing cation displacement and antiphase octahedra tilting is depicted in Fig.5.21) with lower symmetry as observed in HR-TEM analysis. However, these local distortions with various tilting disorder and ionic displacements are compensated over longer length scales resulting in an average anti-phase tilting of octahedra in the rhombohedral structure [252,255]. The local displacements of the A-site cations along $[100]_T$ are also compensated over larger length scales giving rise to an average rhombohedral symmetry. This is illustrated through a simple model showing representation of $[001]_C$ projection of the perovskite structure is provided in Figure-5.22(a). The octahedra tilting are not shown in the schematic model. The unit cell is marked by the square with broken lines. The simulated SAED patterns based on rhombohedral phase with the *R3c* space group equivalent to $[001]_C$ zone axis is presented in Fig. 5.22(b). It can be noticed that the displacement of A-site cations along $[100]_C$ would lead to distortion in the lattice consequently affecting the diffraction pattern leading to

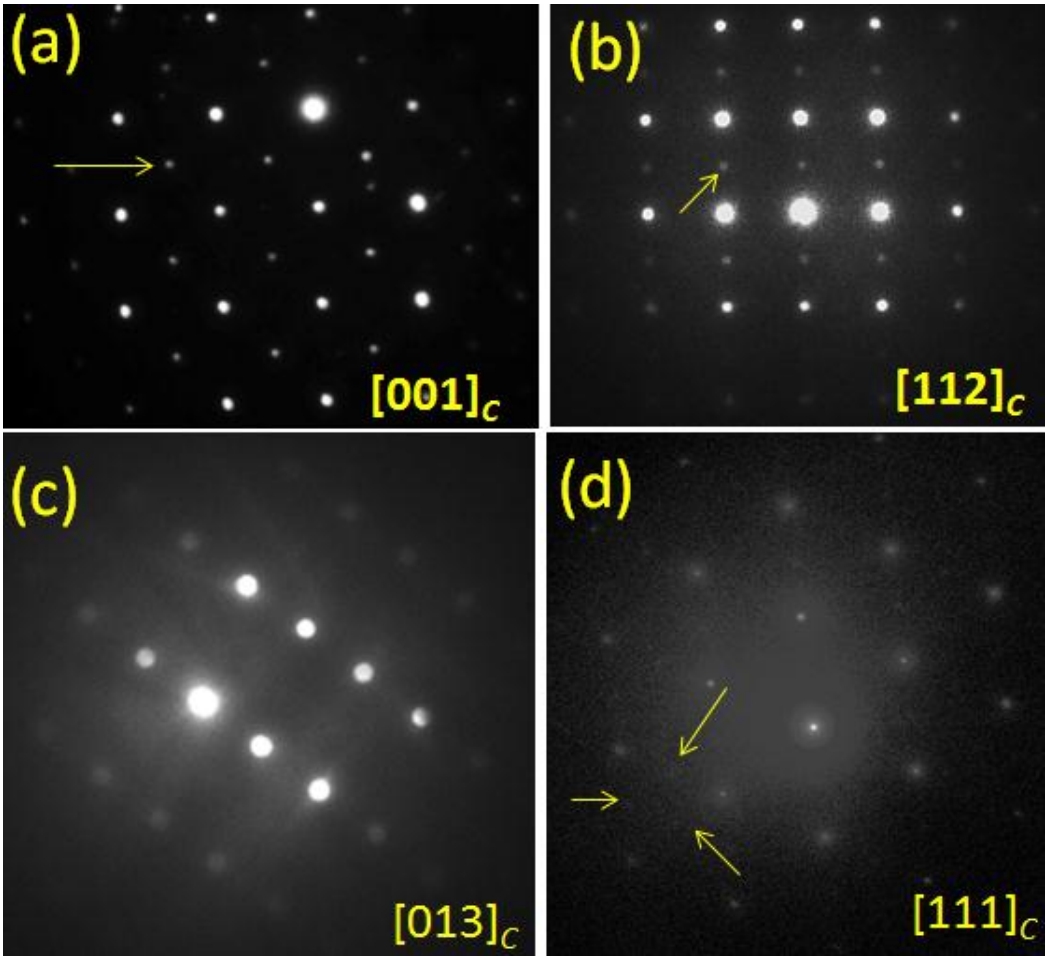

Figure 5.20: SAED patterns for NBT-BT whiskers taken along (a) $[001]_C$ and (b) $[112]_C$. The super lattice reflections ½ $\{ooe\}_C$ and ½ $\{ooo\}_C$ are marked with arrows in Fig. (a) and (b) respectively. (c) and (d) depicts the SAED taken with $[013]_C$ and $[111]_C$ zone axes, respectively. The superlattice reflection marked with arrows in (d), however the intensity is very small.

lowering of symmetry locally. However as discussed above, these distortions averaged over larger length scales lead to higher average symmetry as observed in high resolution neutron diffraction. Moreover, the small size of nanotwins gives rise to high density of twin boundaries, which makes material more deformable as twin boundaries can accommodate the macroscopic strain, induced by external electric field or applied stress[256]. The rearrangement of nanotwins with symmetry lower than the macroscopic symmetry results in giant strain and enhanced piezoelectric response under applied fields[257]. Furthermore, the higher mobility of these nano

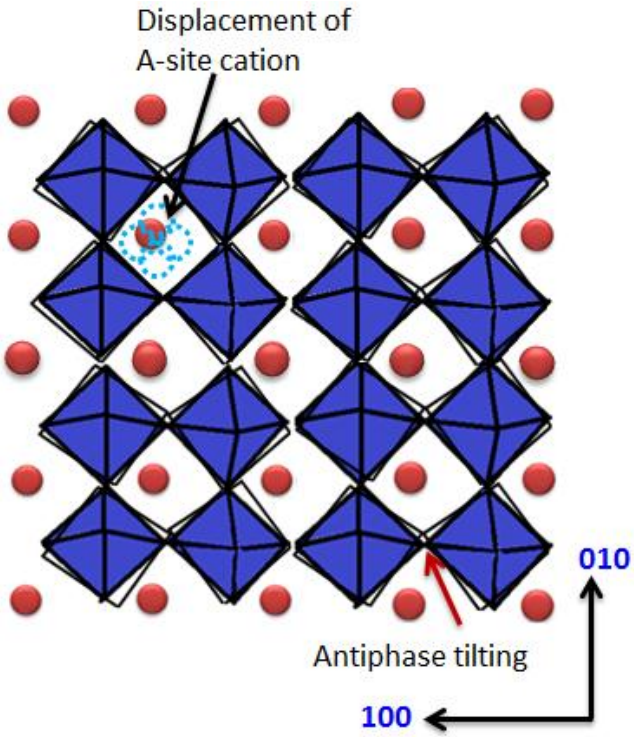

Figure 5.21 A schematic of the projection of [001] depicting cation displacement and antiphase octahedra tilting

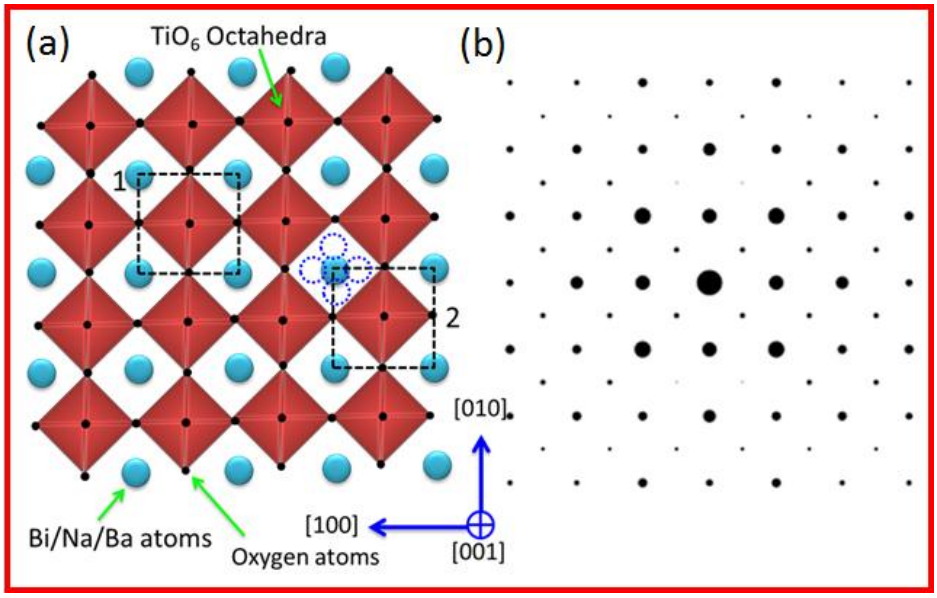

Figure 5.22: (a) A simple model showing $[001]_{pc}$ projection of ABO_3 type structure. The unit cell is marked as square 1 with broken lines. The displacement of A-site (indicated by solid circle with light blue color) cation depicted by the dotted circle in the unit cell 2, which could lead to lower local symmetry of the system. (b) The simulated SADP using R3c unit cell with $[001]_{pc}$ zone axis.

twins is expected to be responsible for giving rise to high strain energy density in MPB composition of NBT-BT [258,259]. Recently, *in-situ* TEM experiments under electrical biasing has also shown that in PZN, polarization reversal can occur by reorientation of nanoscale non-180° domain walls between monoclinic nanotwins[260].

5.2.3.3 Phenomenology and phase transitions

The local crystallographic distortions in the MPB composition of NBT-BT can be justified from thermodynamic considerations as explained below. NBT-BT is a ferroelastic-ferroelectric material, therefore thermodynamic description of NBT-BT requires at least two order parameters; polarization P_1 and strain P_2. The different symmetry for high temperature ferroelastic (tetragonal) and low temperature ferroelectric (rhombohedral) phase requires biquadratic coupling between the order parameters as reported by Salje [237]. The variation of the order parameters *P*(r) in space requires that the Ginzburg energy (F_G)term should be added to Landau potentials (F_L) and the Landau-Ginzburg potential for NBT-BT could be written as:

$$F = F_o + F_G + F_L$$

where, $F_G = \frac{a}{2}(\nabla P_1)^2 + \frac{b}{2}(\nabla P_2)^2$

and $F_L = \frac{1}{2}\alpha_1 P_1^2 + \frac{1}{4}\beta_1 P_1^4 + \frac{1}{6}\gamma_1 P_1^6 + \frac{1}{2}\alpha_2 P_2^2 + \frac{1}{4}\beta_2 P_2^4 + \frac{1}{6}\gamma_2 P_2^6 + \lambda P_1^2 P_2^2$ (2)

F_o is the energy in unconstrained paraelectric state. If the sign of coupling parameter (λ) is negative, the two order parameters strengthen each other and lower the Gibbs free energy as reported by Salje[237]. In this case, the temperature is considered to be control parameter. However, positive coupling parameter depicts competition between two order parameters and increases free energy [237]. The nature of coupling between these order parameters could modulate the order of the phase transition resulting in the relaxor-type diffused phase transitions

in NBT-BT systems. Figure 5.18(b) represents a schematic depicting lattice distortion. As shown in Fig. 5.18(b), the Landau potential causes the atoms to be displaced in the low-symmetry phase and Ginzburg energy leads to spatial variation of solitary waves [237]. In case of negative Ginzburg energy, the total Gibbs free energy is reduced by each twin boundary and the system tends to nucleate more twin boundaries to increase thermodynamic stability. However, the density of twin boundaries is controlled by the repulsion potential experienced by them resulting in incommensurately modulated phase at nano scale in terms of local monoclinic distortions observed in NBT-BT. Therefore, the Landau and Ginzburg energy appears to compete with each other resulting in lowering of energy via formation of twin boundaries.

5.2.4 Chapter summary

The local structural distortions coupled with elastic degrees of freedom results in hierarchical domain structure in MPB composition of NBT-BT. The local polar distortions with lower symmetry in A-site disordered NBT-BT systems are different than that of lead based B-site disordered relaxors and so as their percolation under external stimuli. The dynamics of ferroelectric nano domains could also be considerably constrained by ferroelastic domains in NBT-BT with unique high temperature ferroelastic phase transition. The nano beam electron diffraction revealed higher deviation in $\boldsymbol{g}$ vectors suggesting lower local symmetry, which were however found to be compensated over larger length scales. To delineate the contribution from interdomain interactions and surrounding numerous grains, polycrystalline NBT-BT whiskers with same compositions were investigated. The HR-TEM analysis revealed presence of a local monoclinic symmetry as monoclinic lattice with higher degree of freedom can easily adopt local stress. However, the neutron diffraction analysis suggested an average rhombohedral phase. Interestingly, monoclinic nanotwins (nanodomains) in NBT-BT whisker specimen were directly

observed. The presence of monoclinic domains in rhombohedral domains can easily transform to tetragonal acting as bridging phase responsible for high piezoelectric response in MBP based systems. Moreover, small size of nanotwins could make material more deformable due to easy accommodation of the macroscopic strain induced by external stimuli. The nanotwins with higher mobility could result high strain density and electromechanical response in MPB compositions of NBT-BT. These results emphasize the generic role of nanotwins with reduced symmetry towards enhanced piezoelectric properties of MPB compositions. The short range crystallographic distortions in NBT-BT can explain different phase transitions that have been reported for this material around the MPB.

Chapter-6

6.1 Giant piezoelectric response in grain-oriented lead-free piezoelectric $Na_{0.5}Bi_{0.5}TiO_3$-$BaTiO_3$ ceramics

Lead – free piezoelectrics are being demanded globally to meet the emergent need of greener and safer materials solutions. Finding lead-free piezoelectric materials for actuators has been fundamentally challenging and known lead-free compositions are known to display significantly inferior electromechanical response as compared to lead-based perovskites. Microstructure and domain structure play dominant role towards controlling the magnitude of piezoelectric coefficient and hysteretic losses in perovskites. Brick-wall like microstructure with large grain size and small domain size can provide significant enhancement in the magnitude of piezoelectric coefficient. A synthesis technique for lead-free piezoelectric system that can provide $[001]_{pc}$/$[012]_{Rh}$ grain oriented ceramics with large grain size and an electrical poling technique that results in smaller domain size will have significant impact on the electromechanical response. This chapter provides the details on such an synthesis technique and elaborate upon the processing variables that play deterministic role in achieving the large grain brick-wall like microstructure. Interfaces in the microstructure were found to be coherent at the atomic scale facilitating the domain wall motion with applied electric field. The piezoelectric response was found to increase monotonously with the incease in the degree of texturing and optimized microstructure was found to provide 200% enhancement in the magnitude of piezoelectric coefficient as compared to its random form (thus the term ˝giant˜)

6.1.1 Background

Piezoelectric materials find applications in multitude of devices such as sensors, actuators and energy harvesters. However, most of these piezoelectric materials utilize lead-based systems which are becoming serious problem owing to the restrictions imposed by regulatory agencies across the globe [202]. In the functional ceramics community, currently there is no problem more important than to find a replacement for lead-based piezoelectrics used for actuators. The electromechanical properties required for actuators (high piezoelectric constant, high coupling factor, low loss, and high transition temperatures) for known lead-free compositions are, however, far inferior to those of lead-based systems[261]. There are three lines of research for addressing this fundamental problem – (i) search for new systems through a combination of theory-based prediction followed by experimental effort (doping, solid solutions having a morphotropic (M) or polymorphic (P) phase boundary (PB), (iii) stabilization of metastable phases or finding the high temperature triclinic systems as reported by Ren et al.[262]), and (iii) improving the properties of known compositions through microstructure optimization, domain engineering and multilayering. All these approaches are challenging and require innovation to make a significant impact on the current state-of-the-art. In near future, the later line of research is expected to be more promising as it builds upon the known material systems with high depoling temperatures that have demonstrated the potential to be practical. In this scenario, what is required is a processing technique that can reproduce the ideal texture and microstructure for a wide range of compositions across the phase boundary.

In case of known lead-free compositions, $(1-x)(Na_{0.5}Bi_{0.5}TiO_3)-xBaTiO_3$; x=0.05-0.07 with morphotropic phase boundary (MPB) has emerged as a potential candidate [24,174,177,263]. The MPB in this system from present experiments was found to exist at

$0.93N_{0.5}Bi_{0.5}TiO_3$-$0.07BaTiO_3$ (NBT-BT) which is similar to that reported in literature [174]. Thus, this composition was used for synthesizing textured or grain-oriented specimen (synthesis details are provided in supplementary file). It is worthwhile to mention that the MPB composition is the most difficult choice for texturing but if the processing technique is able to handle this specific composition then it can be easily used for other compositions in the single phase region. Variety of other ways for improving the piezoelectric response of NBT-BT have been pursued, however, most of these prior efforts have shown limited success [264-270] (Figure-6.1(b)). Driving the material through electric-field induced phase transformation in certain compositions of NBT-BT that exhibit structural instabilities can provide large strain but this is challenging for practical applications due to the intrinsic non-linear behavior and high amplitude of the electric drive. It is known [271,272] that the piezoelectric properties of perovskites can be drastically enhanced by enforcing strong crystallographic texture.

Saito et al.[271] have reported the synthesis of textured modified $K_{0.5}Na_{0.5}NbO_3$ based ceramics using $NaNbO_3$ seeds and have demonstrated improved piezoelectric response in this system. This modified composition is quite complex, consists of expensive "Nb" element and is sensitive to sintering conditions in narrow range of temperature. However, their work clearly demonstrated that texturing process can provide significant jump in the electromechanical response. Texturing enables the polycrystalline ceramics to resemble their single crystal counterparts so that favorable domain engineered states can be obtained for composition close to MPB. Texturing of lead-free MPB compositions is an extremely challenging problem due to several fundamental constraints – volatility of the alkali elements, chemical reactivity with seed templates, poor sinterability of the base compositions, and cubical equilibrium grain shape. These problems were solved to achieve more than 90% grain oriented ceramics, which, lead to

200% improvement in the piezoelectric properties as compared to the random ceramics of same composition. This is significant advancement in the field of lead-free piezoelectrics opening the pathway for actuation applications.

6.1.2 Experimental

6.1.2.1 Synthesis of ceramics powder and slurry

In order to select the suitable composition for texturing, first the composition of morphotropic phase boundary (MPB) was determined using present processing technique and raw materials. For this, various compositions of $(1-x)Na_{0.5}Bi_{0.5}TiO_3$-$xBaTiO_3$; x = 0.05, 0.06, 0.07, 0.08, 0.09 using solid state reaction method were synthesized [174]. The stoichiometric amount of chemicals were mixed through ball milling with Yttria stabilized ZrO_2 (YSZ) balls under ethanol in polyethylene bottle. The resulting product was dried and sieved. Next, this NBT-BT powder was mixed with the binder system and ball milled for 24h to obtain homogenous slurry.

6.1.2.2 Synthesis of seed templates

$Bi_4Ti_3O_{12}$ (BIT) single crystal platelets were synthesized using molten salt synthesis method. For this, stoichiometric amounts of high purity precursors (Bi_2O_3 and TiO_2) were added with the equal weight of high purity salt mixture (56wt% KCl and 44wt% NaCl) and heated at 1100 ^oC and 1150 ^oC for 2h. The resulting product was washed several times with hot deionized water to remove trace of salts. NBT platelets were synthesized using topochemical microcrystal conversion [273] method. For this, stoichiometric amount of starting chemicals Na_2CO_3, $BaTiO_3$ and BIT templates (synthesized at 1150^oC) were mixed together. This mixture was added to NaCl salt in 1:1 weight ratio and heated for 2h at 1000^oC followed by washing with deionized

water to obtain $Na_{0.5}Bi_{4.5}Ti_4O_{15}$ platelets. The $Na_{0.5}Bi_{4.5}Ti_4O_{15}$ seed platelets were mixed with stoichiometric amounts of Na_2CO_3 and TiO_2 along with NaCl salt in 1:1 ratio. This mixture was heated at 950^oC for 2h to achieve $Na_{0.5}Bi_{0.5}TiO_3$ (NBT) platelets and then washed with the deionized water to remove salt.

6.1.2.3 Aligning seed template in powder matrix using tape casting and heat treatment to get textured ceramics

Next, the $0.93N_{0.5}Bi_{0.5}TiO_3$-$0.07BaTiO_3$ (NBT-BT) powder synthesized above was mixed with the binder system to make slurry and ball-milled for 24h. Resulting slurry was taken out in a beaker and 10 vol% of NBT platelets were added to the slurry followed by stirring for 6h using magnetic stirrer for proper mixing of seed platelets. This slurry was subjected to tape casting with the doctor blade height of 250 μm to align the NBT platelets in the powder matrix. These tapes were diced and stacked together to get desired thickness and size followed by binder burnout process at 400^oC (4h) with heating rate of 0.3^oC. After binder burnout process, the samples were found to assume smaller green density**.** To increase the green density, the samples after binder burnout process were subjected to the cold isostatic press (CIP). In order to promote texturing, the specimens were heated at 1175^oC for 5 -50h with heating and cooling rate of 10 ^oC/min. Furthermore, during high temperature processing, all the specimens were muffled with the powder of same composition in order to maintain the chemical composition. The EDS elemental analysis was performed on all the specimens at various spots to confirm the final composition.

6.1.2.4 Morphological and electrical measurements:

The surface morphology of the sintered samples was observed using a scanning electron microscope. The degree of orientation was determined from the XRD pattern in the range of 2θ =

$20 – 60^{o}$ by Lotgering method. The EBSD orientation mapping was performed using FEI Helios 600 Nanolab equipped with Hikari camera for EBSD. ME laminate composite was fabricated in the form of trilayer structure corresponding to Metglas/NBT-BT/Metglas. Both textured and random samples with dimensions of $4\times7\times0.3mm^3$ were poled at 3kV/cm. After aging for 24h, 0.15-mm-thick Metglas sheet (4 layers, 2605sA1, Metglas Inc., USA) with same dimension were laminated on both side of the NBT-BT plate by using epoxy resin (West System, USA) to form the trilayer laminates. The ME effect was measured in L-T mode (longitudinally magnetized and transversely poled) configuration with sample located in the center of the Helmholtz coil (H_{ac}=1Oe at 1 kHz) which itself was located in the center of large electromagnet (H_{dc}). The induced voltage was monitored using a lock-in amplifier. At 1 kHz, a ME coefficient of 222 $mV.cm^{-1}.Oe^{-1}$ was obtained.

6.1.3 Results and discussion

6.1.3.1 Piezoelectric and magnetoelectric properties:

For electrical measurement, silver electrode was applied on the flat faces of the rectangular specimen and then fired at $650^{o}C$ for 30 minutes. Samples were poled at 5 kV/mm at $60^{o}C$ in the silicon oil bath. The longitudinal piezoelectric constant (d_{33}) was measured by Berlincourt method. Figure 6.1 (a) and (b) clearly reveal the advantage of texturing over dopant engineering in achieving high piezoelectric response in lead-free NBT-BT system (with 7% BT) near MPB composition. Randomly oriented ceramics were found to possess d_{33} of 160 pC/N which increased to ~322 pC/N for 92 % textured specimens. The value of d_{33} for textured specimens was found to be almost comparable to that of the single crystal value of NBT-based systems [274,275] of similar composition and hard PZT (Ferroperm) ceramics

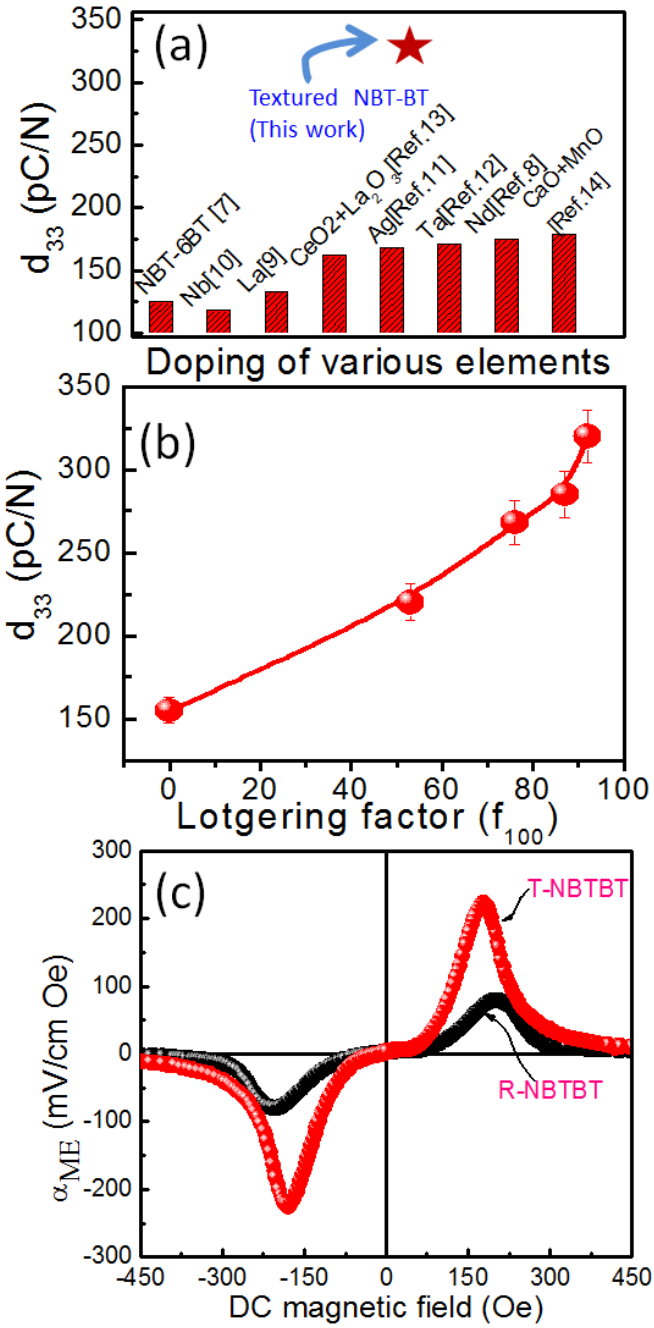

Figure-6.1: (a) d_{33} versus Lotgering factor. (b) d_{33} versus various dopants. (c) ME voltage coefficients for trilayer laminates of Metglas/NBT-BT/Metglas for randomly oriented (R) and textured NBT-BT (T) systems.

(Table 6.1). As an application, the textured specimen was found to exhibit 300% improvement in magnetoelectric response (Figure-6.1(c)) that is vital for sensors. It is worthwhile to

mention that the synthesis of textured NBT based systems has been attempted before but had very limited success [272,276]. Most of these prior reports attempted to synthesize the textured NBT based ceramics using $Bi_4Ti_3O_{12}$ (having very small piezoelectric response) and $SrTiO_3$ (having no piezoelectric response) seeds [40]. The crystal structure and lattice parameters of these seeds are very different from that of NBT. Thus, these heterogeneous seeds alter the composition and reduce the functional response despite higher degree of texture. The novelty of present texturing method lies in utilizing NBT seeds as a template. The NBT seeds were successfully synthesized, which were found to meet the requirements of shape, dimension, and interface stability. The template seed crystals should have a high aspect ratio and smaller lattice mismatch as shown in Fig. 6.2(a) and (b) [38].

6.1.3.2 Growth mechanism of grain oriented ceramics:

In the texturing processes, the epitaxial growth occurs on the template seeds which are aligned in the casting direction in the matrix powder. The best suitable template for texturing NBT based ceramics would be NBT seeds themselves; however, macroscopic cubic symmetry at high temperature leads to a highly symmetrical shape of the NBT based crystallites. These uniformly shaped crystallites cannot be aligned using a tape casting method. Therefore, NBT templates with strong shape anisotropy were synthesized through topochemical conversion from $Bi_4Ti_3O_{13}$ (BIT) platelets using a molten salt synthesis method. For this, the BIT platelets with high aspect ratio were synthesized using the process depicted in Figure-6.2(a). The formation of single phase BIT platelets was confirmed by indexing XRD pattern as shown in the inset of Figure 6.2(a). Next, the NBT platelet seed crystals (Figure 6.2(b)) were synthesized from these BIT platelets using topochemical conversion method. The XRD-

spectra recorded on NBT seeds confirmed the formation of ABO_3-type perovskite phase as shown in the inset of Figure 6.2(b).

Table-6.1 Piezoelectric and ferroelectric properties of PZ27 (PZT based polycrystalline ceramic, Ferroperm) ceramics and NBT-BT single crystal, Mn: NBT-BT (Pt) [single crystal Grown using Pt seed], and textured NBT-BT ceramics.

Sample	d_{33} (pC/N)	k_t (%)	k_{31} (%)	P_r ($\mu C/cm^2$)	E_c (kV/mm)
PZ27 ceramics (Ferroperm)	425	47	33	----	-----
NBT-BT single crystal[274]	280	56	-----	16.44	2.67
Mn: NBT-BT single crystal(Pt)[275]	287	55.6	39.7	35	2.91
Textured NBT-BT ceramics	322	57.3	----	35	1.8

These NBT templates were aligned in the base matrix by applying shear stress through tape casting. The schematic of tape casting process is shown in Figure-6.3. The ceramic tapes consisting of embedded seeds were diced into desired size and stacked to achieve required thickness followed by heat treatment for binder burnout. During binder burnout process, if the proper green body density is not achieved then there is possibility of NBT single crystal platelets becoming polycrystalline (Figure-6.2(c)) in close analogy with Rayleigh-type instability [277]. These polycrystalline templates will result in poor texturing. Form the microstructure shown in Figure-6.2(c), the vacuum/empty space between the NBT seeds and the polycrystalline matrix due to the lower density of the specimen could be observed.

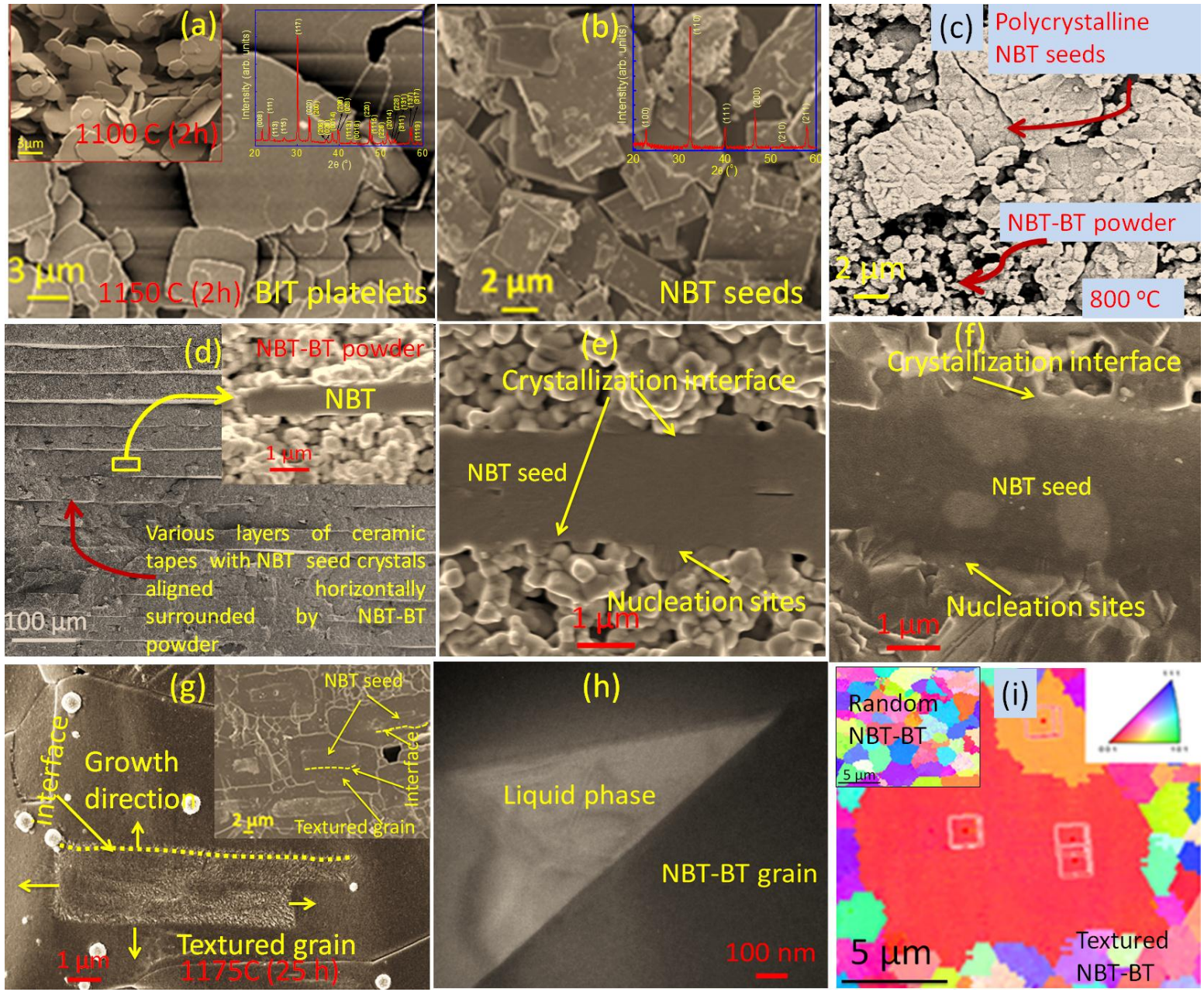
(a)
1100 C (2h)
3 µm
1150 C (2h) BIT platelets
(b)
2 µm
NBT seeds
(c)
Polycrystalline NBT seeds
NBT-BT powder
2 µm
800 °C
(d)
NBT-BT powder
NBT
1 µm
Various layers of ceramic tapes with NBT seed crystals aligned horizontally surrounded by NBT-BT powder
100 µm
(e)
Crystallization interface
NBT seed
Nucleation sites
1 µm
(f)
Crystallization interface
NBT seed
Nucleation sites
1 µm
(g)
NBT seed
Interface
Growth direction
2 µm
Textured grain
1 µm
Textured grain
1175C (25 h)
(h)
Liquid phase
NBT-BT grain
100 nm
(i)
Random NBT-BT
5 µm
5 µm
Textured NBT-BT

Figure-6.2 (a) Micrographs of $Bi_4Ti_3O_{12}$ platelets synthesized at 1150^{o}C(30 min), the left and right side inset show $Bi_4Ti_3O_{12}$ platelets with smaller size synthesized at 1100^{o}C (30 min) and the corresponding XRD spectra recorded at room temperature respectively. (b) NBT templates synthesized using topochemical conversion from BIT, inset shows XRD spectra recorded after conversion of BIT to NBT demonstrating perovskite structure. (c) Micrograph of the specimen without CIP heated at 800^{o}C (2h) after embedding seed inside. Note the polycrystalline nature of seed after processing at this temperature due to low density. (d) Low magnification cross-section image of the specimen with embedded seed heated at 800^{o}C (2h), inset depicts the magnified view of aligned NBT seed buried in NBT-BT powder inside ceramic tapes laminated to get desired thickness of final specimen. Micrographs of the cross-section of the specimen depicting various stages of textured grain growth on NBT seed during high temperature processing (e) 1000^{o}C (2h), (f) 1100^{o}C (2h), (g) 1175^{o}C (25h). Please note that at lower temperature (~800^{o}C), there is hardly any growth on the seed (inset of Figure 6.2(d)). But at elevated temperatures (≥1000^{o}C), nucleation and growth of epitaxial NBT-BT layer starts. Inset of 2(g) shows low magnification image of textured grains in the speciment heated at 1175 ^{o}C (10h). (h) TEM image of triple junction showing presence of liquid phase in textured specimen, (i) EBSD orientation map of $(100)_{pc}$ textured NBT-BT, right and left insets show EBSD mapping of randomly oriented NBT-BT ceramics and inverse pole figure showing color scheme.

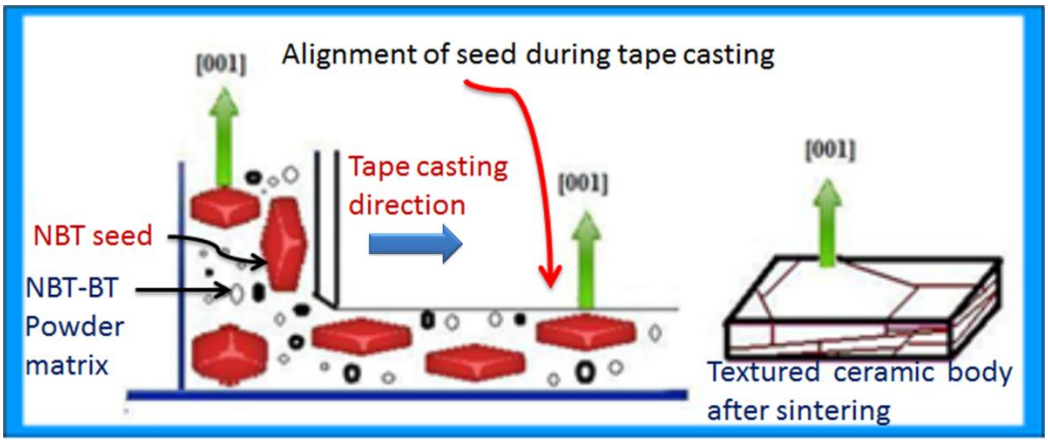

Figure-6.3: Schematic of tape casting process for synthesizing grain oriented ceramics.

In order to avoid this problem, all the specimens were subjected to cold isostatic pressing (CIP) after binder burnout process. After CIP, samples were subjected to high temperature heat treatment that resulted in epitaxial growth at the $[001]_{pc}$ / $[012]_{Rh}$ oriented surface of the seed template as shown in Fig.6.2 (f) – (h).

To understand the mechanism of microstructure transformation, SEM images of the cross-section of the specimen subjected to various processing temperatures are shown in Figures 6.2(d) - (g). Figure-6.2(d) shows the low magnification image of the ceramic processed at 800 ^{o}C for 2h revealing the layers of ceramics tapes with well-aligned NBT seeds in the NBT-BT powder. The approximate thickness of one layer was ~50-60 μm. The magnified view of the NBT seed and powder interface is depicted in the inset of Figure 6.2(d). The inset of Figure 6.2(d) shows that seeds are still single crystalline contrary to polycrystalline nature observed in the specimen processed at high temperature without CIP (Figure-6.2(c)). The close proximity of seed and powder could be observed in the inset which is crucial for achieving grain orientation. On further increasing the temperature ($\geq$ 1000^{o}C), nucleation at the matrix/seed interface can be observed as marked in Figure 6.2(e) and (f). According to previous study [177], contribution of liquid phase to sintering starts around this temperature. The liquid phase facilitates the nucleation and growth of epitaxial NBT-BT layer leading to grain-oriented ceramic body at 1175^{o}C during prolonged exposure (up to 50h) to heat-treatment (Figure 6.2(e) – (g)). The growth direction of textured grain on NBT seed are marked with arrows in Figure-6.2(g). The inset of Figure-6.2(g) shows the cross-sectional micrograph of the specimen processed at 1175 ^{o}C for 10h illustrating the formation of various textured grains. In textured specimen, the growth of NBT-BT epilayer of thickness 4 -5 μm on NBT seed could be noticed. Figure 6.2(h) shows the bright field TEM image of triple junction showing the presence of liquid phase. Similar results about the presence of liquid phase in NBT based systems has been reported earlier [177]. In order to provide a spread of grain orientations, EBSD maps of the top surface of textured and randomly oriented NBT-BT specimen are shown in Figure 6.2(i). It can be seen that $[001]_{pc}/[012]_{Rh}$ textured grain

dominate the microstructure. The color scheme is based on the inverse pole figure shown in the inset of Figure 6.2(i).

The schematic describing the mechanism of growth of textured grain on NBT seed is shown in Figure 6.4(a) – (c). As explained above, liquid phase sintering plays an important role in densification of grain-oriented NBT-BT piezoelectric ceramics by facilitating mass transport during growth process. In NBT-BT, the liquid phase (Figure-6.2(h)) is predominantly facilitated by the low melting point elements like Na and Bi. [177]. The growth of textured grain is similar to the Ostwald ripening-like process where larger grains grow at the expense of smaller ones because of difference in surface energy [38]. In order words, the boundary of seed crystal (or the crystallization interface) migrates through the polycrystalline matrix and the kinetics of this process is increased by the presence of liquid phase [38]. The growth occurs by dissolution of the polycrystalline matrix grain and deposition/precipitation on the lowest surface energy template. In case of NBT-BT, the $\{001\}_{pc}$ has low surface energy and therefore has potential for the growth to occur resulting in the formation of the textured grain. The process of dissolution and precipitation in presence of liquid phase can be interpreted in terms of epitaxial growth process.

The additional driving force for the growth is provided by the chemical potential difference between the stable NBT seeds and the metastable liquid phase. Because, NBT seeds have similar lattice parameter as that of matrix, the epitaxial growth occurs with minimal stress at the interface and the crystallization process is not expected to introduce significant misfit strain at the interface. Assuming a simple exchange process in which the atoms of the metastable liquid phase A and atoms of the solid crystalline phase B (NBT seeds or epilayer) pass from one phase to other, the difference in the chemical potentials of phase A and phase B

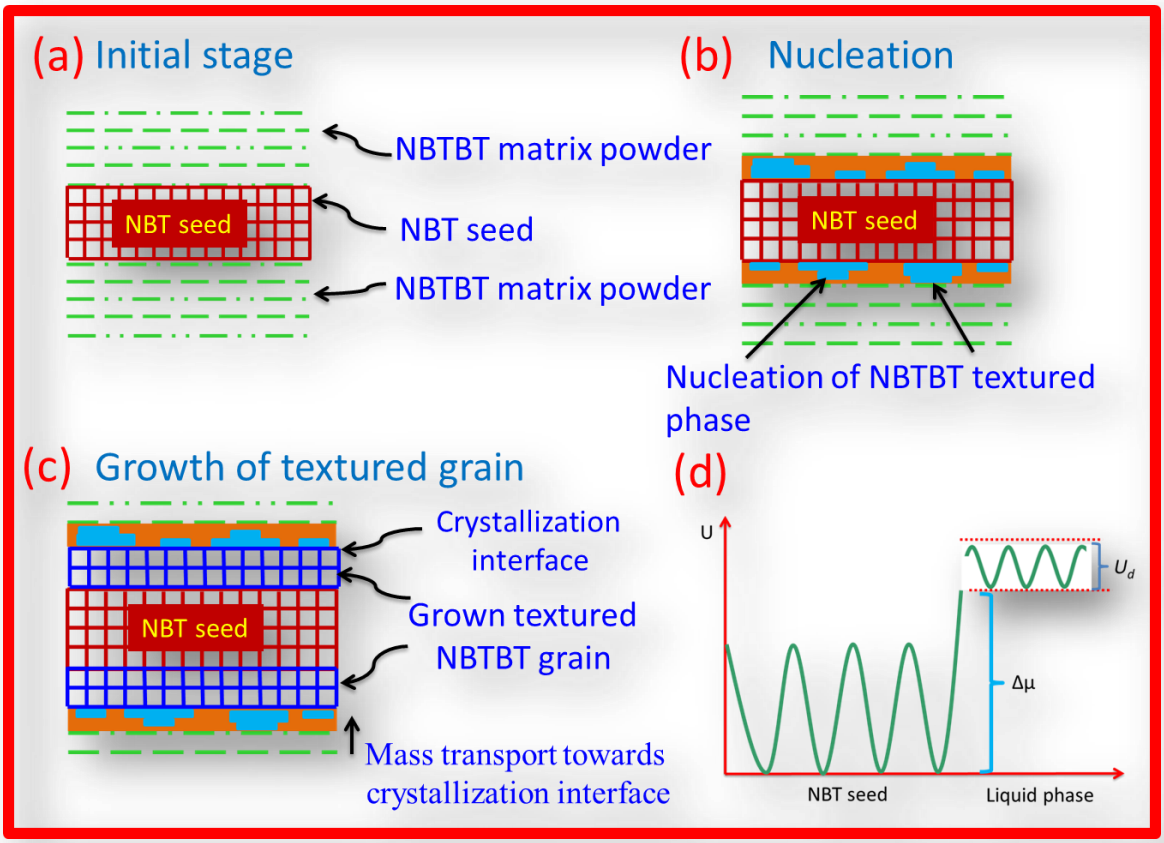

Figure-6.4 Schematic representation of the growth of textured NBT-BT grain on NBT template. (a) NBT seed surrounded by NBT-BT powder at intial stage. (b) Formation of the liquid phase in the vicinity of NBT seed and nucleation of new phase during sintering process. (c) Growth of $[001]_{pc}$ textured grain via epitaxial growth on NBT template on prolonged sintering process at ~1175^{o}C, (d) Schematics of potential barrier of NBT seed platelets and metastable liquid phase in polycrystalline matrix. The difference in the potential barrier indicates the activation energy for diffusion.

in addition to difference in surface energy would drive the epitaxial growth as: $\Delta\mu = RTln(\frac{a_A^e a_B}{a_A a_B^e})$, where a_A^e is the activity of phase A at the equilibrium [278]. Generally, the practical growth rate is considerably slower than that theoretically predicted and, therefore, it is difficult to establish equilibrium throughout the system. Thus, to achieve higher degree of texturing a prolonged heat treatment of more than 50h was needed. The growth rate was

limited by the mass transport occurring as a combination of convection, diffusion and surface reaction processes. The growth process of textured grains occurs through incorporation of atoms from the liquid phase into the template seed crystal by overcoming an energy barrier U_d (Figure 6.4(d)). The crystallization rate per unit time at temperature T could be represented by $vexp(-\frac{U_d}{k_B T})$, where v is the frequency of vibration of atoms around their average position and k_B is the Boltzman constant. Since, the texturing process takes place at higher temperature ~1175^{o}C, the formation of liquid phase from the NBT seed cannot be ruled out. However, the Gibbs free energy in liquid state is higher than that of solid state NBT seed by a factor of$(-\frac{\Delta\mu}{k_B T})$. This would lead to a higher crystallization rate and so the growth rate can be given as:[278] $V_g = a_t exp(-\frac{U_d}{k_B T})(1 - exp(-\frac{\Delta\mu}{k_B T}))$, where a_t is the thickness of the monatomic layer by which the crystallization interface/boundary of seed crystal moves.

6.1.3.3 TEM analysis of interface and microstructure:

Next, the mechanism of epitaxial growth of textured grains was described. The magnified view of the interface is shown in Figure 6.5(a). A close inspection of the interface indicates the presence of a coherent interface between the seed and textured grain. A coherent interface without defects can be attributed to the small lattice mismatch between the NBT template and the textured NBT-BT grain, which is an important factor towards obtaining superior functionality. This result further highlights the advantage of processing technique used in this chapter. If the lattice parameter of seed crystal and the matrix are not closely matched, defects will be created to accommodate the extra elastic energy. The simulated interfacial region of a cubic NBT seed and epitaxially grown textured NBT regions with

tetragonal symmetry is shown in the inset of Figure-6.5(e). The simulation was performed using CrystalKit software. Due to

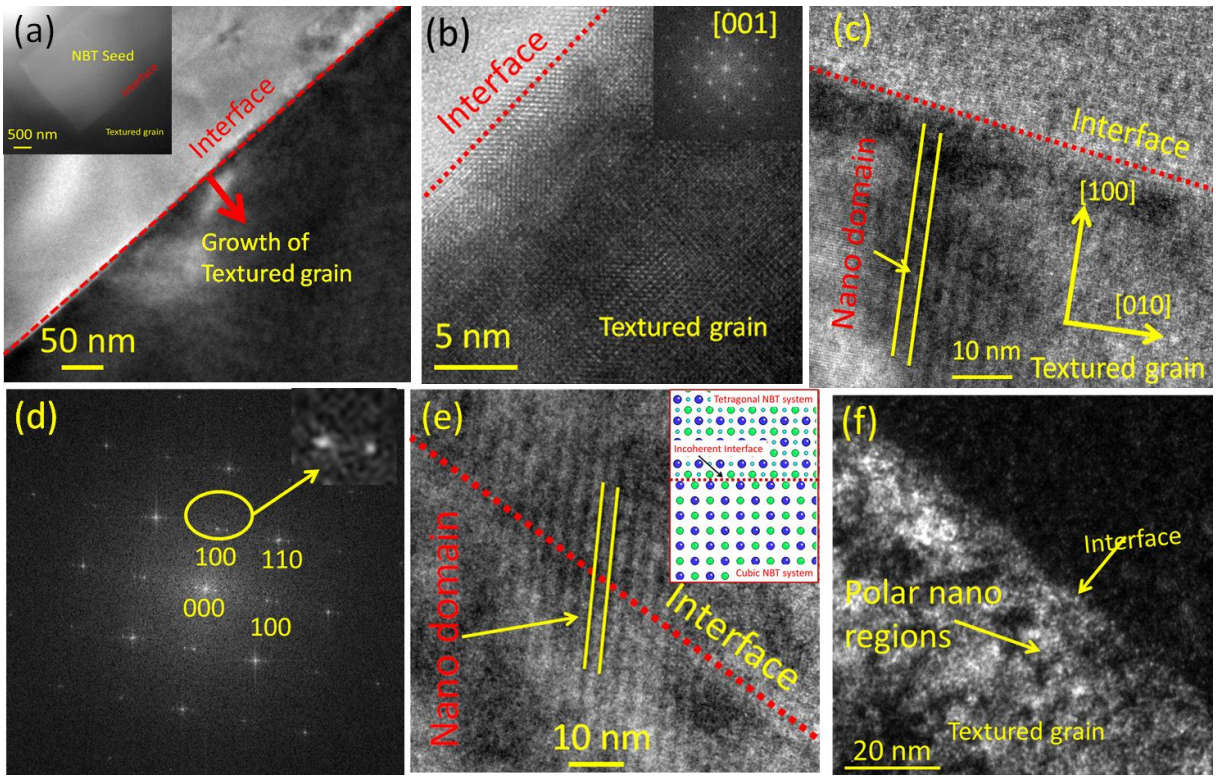

Figure-6.5 (a) Bright field image depicting magnified view of the interface, inset is showing low magnification TEM image of NBT seed and grown textured grain. (b) Lattice fringes near the interface of the seed and textured grain. (c) Nano domain in the textured grain near interface region. (d) FFT pattern corresponding to nano domain regions in (c) showing splitting of spot in the inset. (e) Nano domain running across the interace without deviation, the inset of (e) shows simulated interface between cubic NBT seed and grown tetragonal NBT region viewed down from [001] zone axis, blue circles represent Na and Bi atoms, green circles represent Ti atoms, cyan circles represent oxygen atoms. (f) Dark field images depicting the contrast change due to polar nano regions.

slight mismatch in the crystal structure, one can observe the displacement of lattice planes leading to incoherent interface (inset of Figure 6.5(e)). In this example, the defects act as pinning sites of the ferroelectric domain walls leading to reduced functional response. Figure 6.4(b) shows the lattice fringes across the coherent interface of the NBT seed and the textured grain. The FFT patterns obtained from the textured grain show its $(001)_{pc}/[012]_{Rh}$ orientation.

Figures 6.5(c) shows the presence of nanodomains in the textured grains, however, on defocusing it can be observed that these domains actually run across the coherent interface (Figure 6.5(e)). The FFT pattern obtained from the area related to the domain structure in Figure 6.5(c) shows signatures of splitting of the spots due to the presence of nano-sized twins (Figure 6.5(d)). A dark field image corresponding to the same region reveals the presence of polar nano regions (PNRs) in Fig. 6.5(f). The contrast change is related to the PNRs distributed in the matrix. The presence of a range of such PNRs modulates the Curie point resulting in a diffuse-type phase transition. The high piezoelectric response and low coercive field in textured NBT-BT could be thus attributed to the domain engineered state and the nano domains with higher mobility.

6.1.3.3 X-ray diffraction analysis:

Figure 6.6(a) shows the XRD patterns recorded at room temperature for NBT-BT specimens with different degree of texturing. The relative increase in the intensity of $\{100\}_{pc}$ Bragg reflections clearly indicates increase in the strength of texture which was quantified using Lotgering factor[117] (f_{100}). The temperature and time of processing to further achieve high degree of texturing was optimized. The longitudinal piezoelectric constant d_{33} was found to increase with the increase in the degree of texturing in $[001]_{pc}$ orientation. In order to confirm the phase and structural differences, synchrotron diffraction patterns were recorded on textured and randomly oriented counterparts of NBT-BT in transmission geometry. Figure 6.6(b) shows the 1-D diffraction patterns for textured and randomly oriented specimens and the corresponding 2-D images are shown in Figures 6.6(c) and (d). The diffraction results confirmed that both the systems were crystallized in similar phase which can be described in

terms of rhombohedral symmetry. The difference in the intensity of Bragg peaks in the 1-D synchrotron data and Debye-Scherrer rings in 2-D data reflects the presence of strong [001] (pseudo cubic)/[012] (rhombohedral) texture enforced by present synthesis technique. Figure 6 (e) and f show the Rietveld fits to the synchrotron diffraction patterns. The refined rhombohedral lattice parameters were 5.5017 Å and α=60.28 for the randomly oriented specimens vs. 5.4909 and α=60.99 for the textured specimen. The data shows that strong texturing results in extra structural distortions manifested by a decreasing lattice parameter and increasing rhombohedral angle (α). The enhanced structural distortion revealed by synchrotron diffraction supports the higher piezoelectric response observed in textured specimen.

6.1.3.4 Electrical properties and domain structure analysis

Figure 6.7(a) shows the temperature dependence of the relative permittivity and loss tangent for the poled textured specimen. The depoling temperature (T_d) and temperature of maximum relative permittivity (T_m) were found to be ~90-100^{o}C and ~300^{o}C, respectively. On the other hand, T_d and T_m were found to be 125 ^{o}C and 350 ^{o}C for the randomly oriented specimen. It should be noted here that T_d increases on either side of MPB and thus by moving into rhombohedral or tetragonal regime once can improve the operating regime. From the processing point of view, these single phase compositions are much simpler to synthesize. The textured and randomly oriented specimens were found to exhibit characteristic diffuse nature of the phase transition. Figure 6.7(b) shows the *P-E* hysteresis loops at 1 kHz for NBT-BT ceramics with different crystallographic texture. The randomly oriented specimen exhibited a square loop with high coercive field while textured specimens were found to exhibit pinched hysteresis loop. The specimen with 92% texturing was found to show $2P_r$ ~65 pC/N.

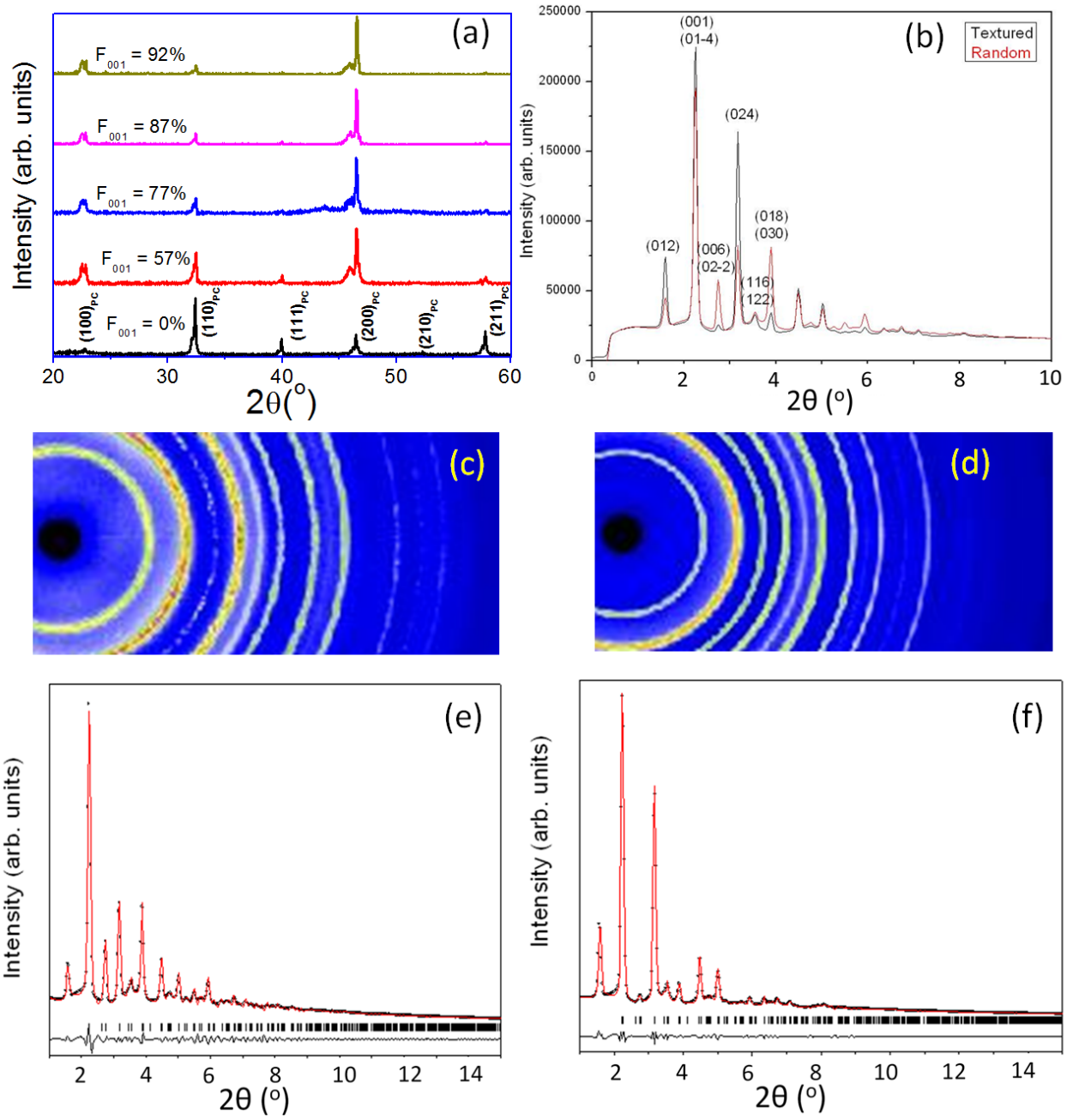

Figure-6.6 (a) XRD data taken at room temperature for various specimens of NBT-BT. Note increasing relative intensity of $(001)_{PC}$ Bragg reflections (equivalent to (012) reflection in rhomohedral symmetery setting) for textured specimens. (b) Synchrtoron diffraction (~115 keV, wavelength = 0.10798 Å) patterns of T-NBT-BT and R-NBT-BT showing strong texture along the $\{012\}_h$ reflection of the underlying rhombohedral structure (c) and (d) 2-D diffraction images corresponding to the synchrotron data in (b) for T-NBT-BT and R-NBT-BT; (e and f) Rietveld fits to the synchrotron diffraction patterns of R-NBT-BT and T-NBT-BT, respectively.

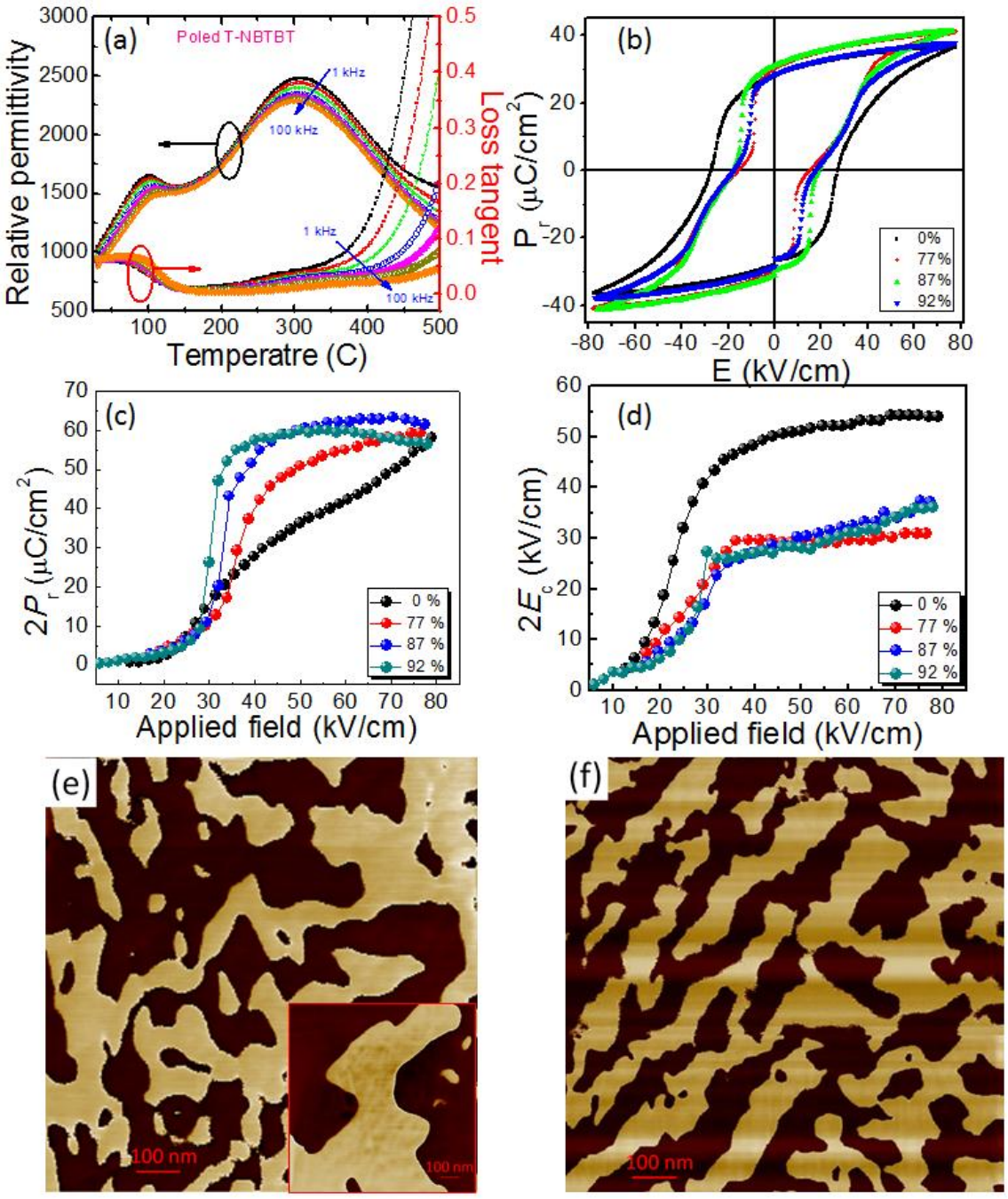

Figure-6.7 (a) Temperature dependence of relative permittivity and loss tangent of poled textured NBT-BT specimen, (b) *P*-*E* hysteresis of various NBT-BT textured ceramics with different degree of orientation, (c) remanent polarization (2 *P*r) versus *E*-field for textured and randomly oriented specimen, (d) coercive field ($2E_c$) versus *E*-field field for textured and randomly oriented specimen, (e) piezoresponse force microscopic (PFM) image of domains in randomly oriented NBT-BT, inset is close-up view, (f) PFM phase image depicting domains in textured NBT-BT.

Figure 6.7(c) and (d) show the remnant polarization and coercive fields as a function of the *E*-field respectively. The randomly oriented specimen shows an almost monotonous increase in the remnant polarization with increasing *E*-field. However, in the case of the textured specimen, the remnant polarization was found to increase sharply after a certain field and then saturate to a constant value. To understand ferroelectric behavior and domain structure of textured and randomly oriented specimen, piezoresponse force microscopy (PFM) was employed. Figure 6.7(e) and (f) shows the PFM image (corresponding height and amplitude images are provided in supplementary data) of ferroelectric domains for randomly oriented and textured specimen. These results clearly reveal the domain structure difference in randomly oriented and textured samples of NBT-BT. The textured specimen exhibits smaller size domains as compared to its randomly oriented counterpart. Also, the domains in textured specimen are more ordered and homogeneous. The low coercivity and sudden increase in the remnant polarization in the textured specimen indicates a coherent nature of domain switching due to smaller size distribution and higher mobility. However, the randomly oriented NBT-BT specimen was found to show wide distribution of domain sizes as observed in Figure 6.7(e). Recent *in-situ* neutron diffraction study has revealed that the pseudo-cubic nature of the bulk lattice was maintained in the textured specimen subsequent to the application of *E*-field [222]. In contrast, significant distortions in diffraction peak profiles were observed in the randomly oriented specimen, indicating coexistence of phases with rhombohedral and tetragonal symmetries. The absence of *E*-field induced structural phase transformation in the textured NBT-BT was attributed to the smaller coherence length scales of PNRs and/or an inhibition due to internal stress generated by domain switching which precedes the structural

transformation. These results clearly demonstrate that the textured ceramic provides higher electromechanical response by facilitating domain switching at smaller applied fields.

6.1.4 Chapter summary

The synthesis $[001]_{pc}$/$[012]_{Rh}$ textured lead-free piezoelectric $0.93(Na_{0.5}Bi_{0.5}TiO_3)$-$0.07BaTiO_3$ (NBT-BT) using a novel processing technique that employs NBT seeds has been performed sucessfully. The 92% textured NBT-BT specimen exhibits 200% improvement in the longitudinal piezoelectric constant (d_{33}). The piezoelectric response increases monotonously with the incease in the degree of texturing. The experimental evidence and theoretical estimates explaining the mechanism of textured grain growth on the NBT seeds has been provided. The interface of the NBT seeds and the textured grain was found to be coherent and defect free facilitating the domain wall motion. Also, the textured specimens exhibited a lower coercive field and coherent nature of domain switching. The present chapter demonstartes the importance of texturing in lead-free piezoelectric materials for achieving a high piezoelectric response comparable to their single crystal counterparts. The experimental information provides all the details required to synthesize textured ceramics.

6.2 Enhanced piezoelectricity and nature of electric-field induced structural phase transformation in textured lead-free piezoelectric $Na_{0.5}Bi_{0.5}TiO_3$-$BaTiO_3$ ceramics [e]

This chapter provides a comparative description of the properties of textured and randomly oriented poly- crystalline lead-free piezoelectric $0.93(Na_{0.5}Bi_{0.5}TiO_3)$-$0.07BaTiO_3$ (NBT-BT) ceramics. A high longitudinal piezoelectric constant of (d_{33}) ~ 322 pC/N was obtained in $(001)_{PC}$ textured NBT-7BT ceramics, which is almost ~2x times the d_{33} coefficient reported for randomly oriented ceramics of the same composition. *In situ* neutron diffraction experiments revealed that characteristically different structural responses are induced in textured and randomly-oriented NBT-BT ceramics upon application of electric fields (*E*), which are likely related to the varying coherence lengths of polar nano regions and internal stresses induced by domain switching.

6.2.1 Background:

Structural transformations in functional materials under external stimuli are known to impart exotic responses and play an important role towards controlling material properties [279]. Such behaviors find applications in many devices such as sensors and actuators [1]. Relaxor-based piezoelectric single crystals have been widely investigated with regard to electric (*E*)-field-induced phase transitions that result in large strains [280]. To exemplify, synchrotron x-ray diffraction studies by Noheda et al. [206] and neutron diffraction studies of Ohwada et al. [281] on 92% $Pb(Zn_{1/3}Nb_{2/3})O_3$ – 8% $PbTiO_3$ (PZN-8%PT) show that under the application of electric (*E*) fields, the crystal goes through an irreversible rhombohedral-to-monoclinic A-type-to-

[e] Reprinted with permission from [222]. Copyright 2012, American Institute of Physics.

monoclinic C-type (R-M_A-M_C) transformation sequence. In this case, it was proposed that the ferroelectric polarization initially moves on the R-T (tetragonal) path but then changes irreversibly to the (orthorhombic) O-T path, finally settling on a ground state with M_C symmetry. Furthermore, it was proposed from optical measurements that in the M_C state the polarization vector rotates within the *ac* plane under the application of an electric field [282]. It was hypothesized that the rotation of the polarization vector causes a large coupling between the polarization and electric field, thereby resulting in a giant piezoresponse [282].

Recently, due to environmental concerns, lead-free piezoelectric materials have gained tremendous importance [202]. However, the properties of lead-free piezoelectric materials are far inferior to those of lead-based systems [283]. Out of the various possibilities, lead-free $(Na_{0.5}Bi_{0.5}TiO_3)$-$BaTiO_3$ (NBT-BT) system has emerged as a potential candidate to replace lead-based piezoelectric systems [174,177,284]. The phase transformation behavior of NBT and its solid solutions with BT as a function of *E*-field has been investigated recently in many studies. Different variants of phase diagrams for NBT-BT have been proposed that consists of ferroelectric rhombohedral and tetragonal phases as end components, and an antiferroelectric or ferrielectric orthorhombic component as an intermediate phase[216,217,285,286]. Coexistence of rhombohedral and tetragonal phases has been observed over a broad range of temperatures and *E*-fields. While the orthorhombic phase is proposed to have an antiferroelectric (AFE) characteristic [23,217]' recent studies instead describe it as a relaxor phase with polar nanoregions[287,288]. The high piezoelectric response and *E*-field induced strain in NBT based systems has been attributed to structural phase transitions under the application of *E*-field [289-291]. Similar to NBT-BT systems, NBT-KBT [292] and NBT-BT-KNN [Ref. 217] systems were also found to show structural phase transformations under *E*-field. Recently, the time dependent

nature of these types of structural phase transitions under external *E*-field has also been reported [292].

Building upon these prior studies, the *E*-field induced structural changes in randomly oriented and $(001)_{PC}$ textured polycrystalline ceramic specimens of NBT-7BT are presented. It should be noted here that very few researchers [40] have been successful in growing the (001) textured NBT-BT ceramics. The randomly oriented and textured specimens of the same composition were found to show drastically different piezoelectric responses, as well as different polarization-electric field (*P*-*E*) hysteresis and phase transformation behaviors under applied E-fields. Specifically, the textured specimens show pinched *P*-*E* hysteresis loop at room temperature in contrast to normal ferroelectric *P*-*E* loops observed for randomly oriented specimens. In the past, the origin of pinched loop has been associated with various factors including the presence of AFE phase, acceptor doping, aging effect, internal-bias and presence of polar nano-regions. In this study, examination of *in-situ* bulk neutron diffraction patterns revealed that the pseudo-cubic nature of the bulk lattice was maintained in the textured specimen subsequent to the application of *E*-field. In contrast, significant distortions in diffraction peak profiles were observed in the randomly oriented specimen, indicating coexistence of phases with rhombohedral and tetragonal symmetries. Although the $(001)_{PC}$ textured specimen exhibits no electric-field-induced phase transformation, it shows a much higher d_{33} (~ 320 pC/N) than that of the randomly oriented specimen (~160 pC/N). Based on these observations, it could be asserted that the structural instability, at least on a bulk scale, is not a necessary prerequisite to obtain large piezoelectric properties in NBT-BT ceramics. The enhanced piezoelectric behavior of the $(001)_{PC}$ textured specimen[38] could be partially attributed to it's domain engineered state, as well as preservation of the "relaxor" nature due to the existing polar nanoregion.

6.2.2 Experimental

Synthesis of randomly oriented polycrystalline ceramics of NBT-BT was performed using conventional solid state reaction method. For texturing, NBT–platelets were aligned in the powder matrix of NBT-BT using the tape casting technique followed by lamination and binder burnout. All the specimens were sintered in air at 1150-1200 ^{o}C. The degree of $(001)_{PC}$ texture, as calculated by the Lotgering factor method[117], was found to be ~92%. Both textured and randomly oriented specimens were found to have a similar composition within 1.0 at%, as confirmed by elemental analysis using EDS. For electrical measurements, silver electrodes were fired on the flat faces of the specimens. The specimens were poled along the thickness and the macroscopic piezoelectric properties were measured using the Berlincourt method along the same direction (which was the $(001)_{PC}$ oriented direction of the textured NBT-BT specimen). The *P-E* hysteresis measurements were performed using a Precision II ferroelectric testing system. Incremental electric fields were applied to the randomly oriented and $(001)_{PC}$ textured samples in steps of 0.5 kV/mm to a maximum of 1.5 kV/mm. The randomly oriented polycrystalline sample was 5 mm × 5mm × 2.4 mm in dimensions and the electric field was applied across the 2.4 mm thickness. The textured sample was 5 mm × 5mm × 2.3 mm in dimensions and the electric field was applied across the 2.3 mm thickness. Neutron diffraction patterns, parallel and perpendicular to the direction of the applied electric field, were collected *in-situ* at the VULCAN beamline of the Spallation Neutron Source at the Oak Ridge National Laboratory [293]. The experimental setup is schematically illustrated in Figure 6.8. The incident neutron beam was 3.0 mm in width for both the samples.

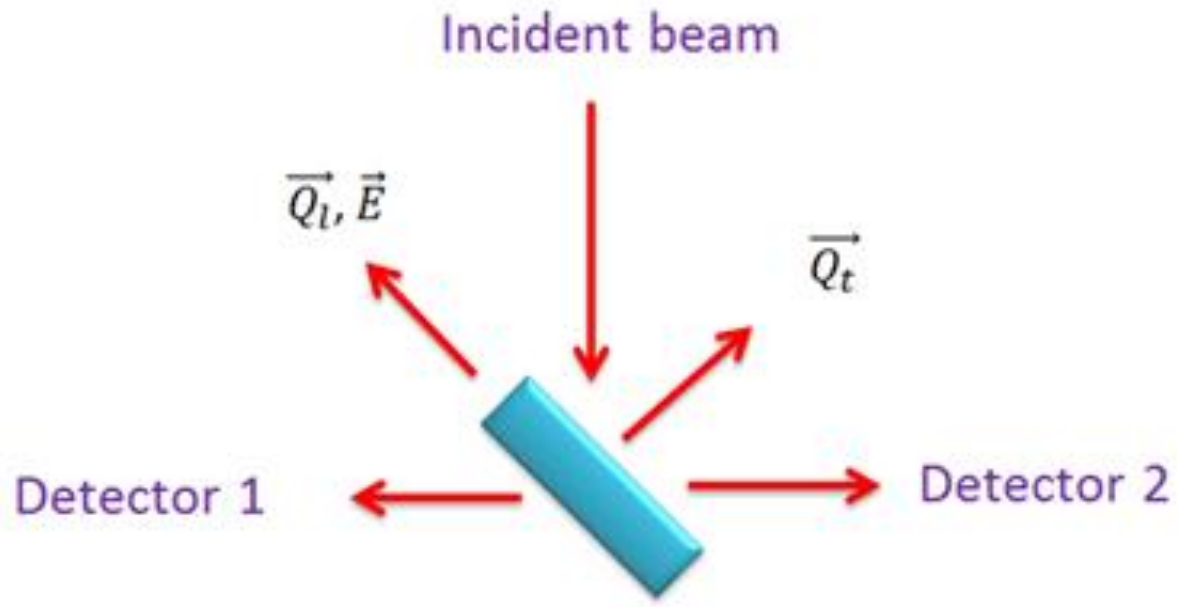

Figure 6.8: Schematic of *in situ* neutron diffraction experiment at VULCAN. Detector 1 measures diffracted neutrons with momentum transfer along $\overrightarrow{Q_l}$, parallel to the direction of applied electric field $\vec{E}$. Detector 2 measures diffracted neutrons with momentum transfer along $\overrightarrow{Q_t}$, transverse to the direction of applied electric field $\vec{E}$.

6.2.3 Results and discussion:

6.2.3.1 Electrical measurements:

Figures 6.9 (a) and (b) depict the *P*-*E* hysteresis loops under cyclic electric fields for the randomly oriented and the $(001)_{PC}$ textured polycrystalline specimens. The remnant and maximum polarizations attained by the application of external field was found to be similar in both the cases. The coercive field (E_C) of the randomly oriented specimen was higher than that of the textured specimen (Fig.6.10). The textured specimen was also found to exhibit a pinched hysteresis loop at RT. The remnant polarization ($2P_r$) and its first derivative as a function of applied electric field are depicted in Fig. 6.9(c) and (d) for the randomly oriented and textured

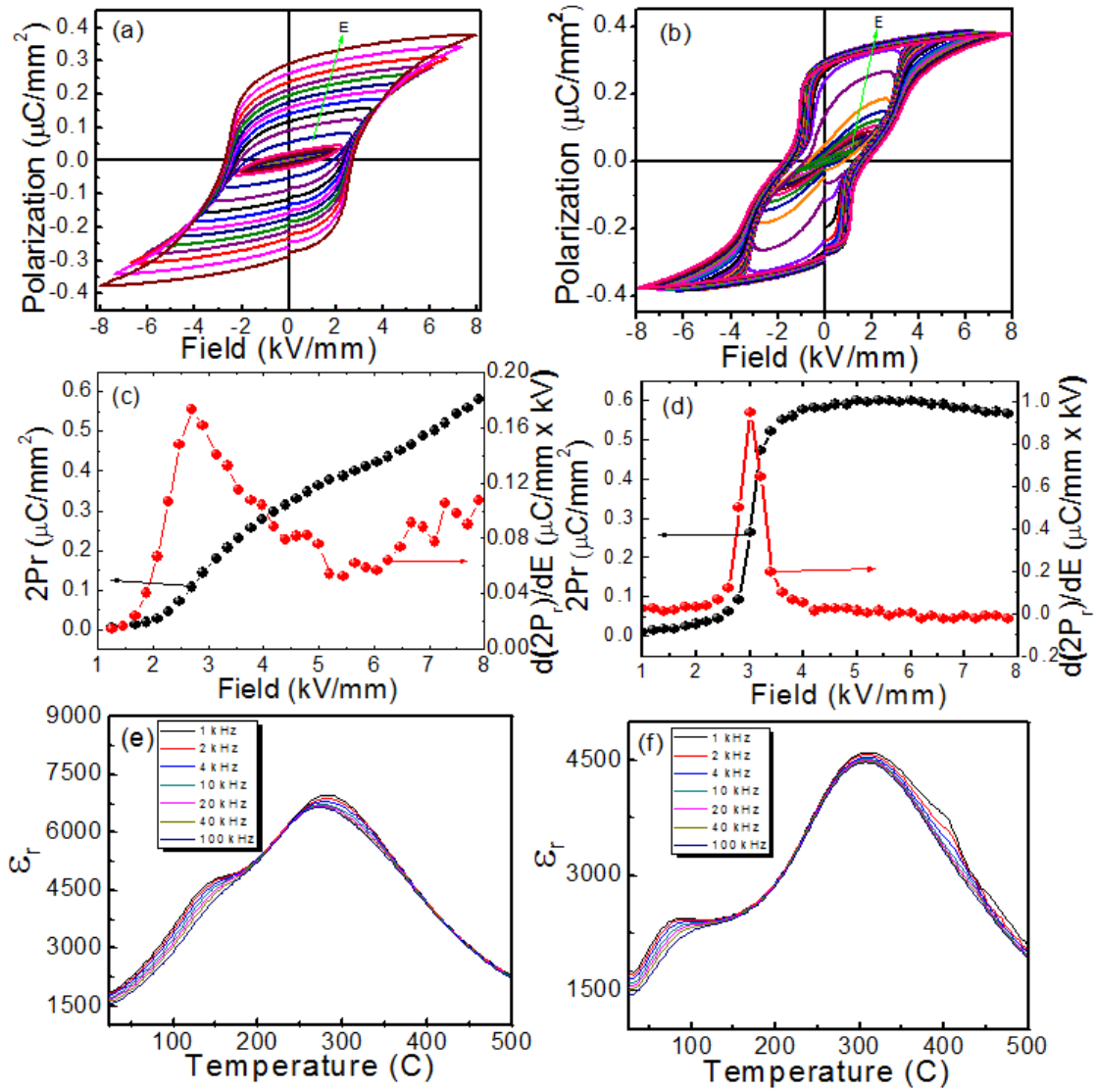

Figure-6.9: PE hysteresis loops at 1 kHz for NBT-BT polycrystalline ceramics (a) randomly oriented (b) textured. The field dependence of $2P_r$ and its derivative with respect to applied electric field for (c) randomly oriented (d) textured. The sharp peak in the dP_r/dE plots of textured specimen indicates coherent switching of the specimen. Temperature dependence of relative permittivity for (e) randomly oriented, (f) textured polycrystalline NBT-BT ceramics

specimens, respectively. It can be seen from these plots that the rate of increase in P_r with respect to increase in applied electric field amplitude is small in the case of the randomly oriented specimen. However in the case of the textured specimen, there is a clear jump in the value of P_r

above the coercive field regime followed by a plateau. This sudden increase in remnant polarization and a sharp peak in the *dP*/*dE* vs. *E* plot for the textured specimen depict a coherent nature of the domain switching in this sample.

Figures 6.9 (e) and (f) depict the temperature dependence of relative permittivity at various frequencies for the randomly oriented and the textured polycrystalline ceramics in their unpoled states. The small anomaly observed at low temperatures is related to the depoling temperature (T_d) in NBT-BT. The value of T_d was found to be ~ 90 and ~ 130 ^{o}C for the textured specimen and the randomly oriented ceramics, respectively. At higher temperatures, a broad peak depicting the diffused nature of phase transition (*DPT*) could be observed for both the specimens. The shifting of T_m (temperature corresponding to the maximum relative permittivity) with a change in the frequency of applied electric field depicts the relaxor nature of this material and can be attributed to the presence of polar nano-regions (*PNRs*).

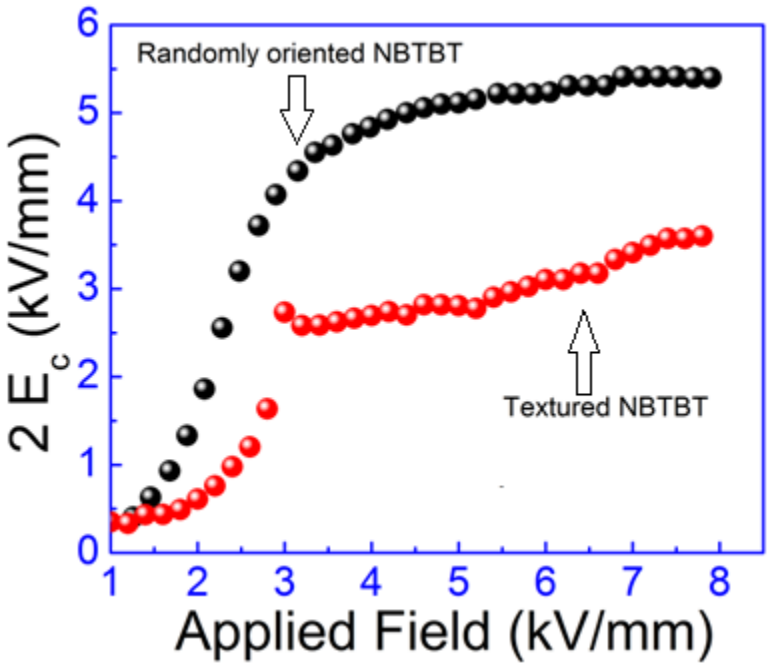

Figure 6.10: Comparative plots of coercive fields (E_c) versus applied electric field (E) for textured and randomly oriented polycrystalline NBT-BT ceramics.

6.2.3.2 In-situ neutron diffraction measurements:

Figure 6.11 (a) shows the changes in the $(200)_{PC}$ diffraction peak profile of the randomly oriented polycrystalline specimen as a function of applied electric field amplitude. Results are shown only for fields of 1 kV/mm and higher to clarify the differences in the diffraction profiles. A distortion of the $(200)_{PC}$ peak parallel to the direction of the applied electric field was observed for a field amplitude of 1.5 kV/mm. A similar distortion of the $(200)_{PC}$ diffraction peak profile was also observed along the direction transverse to the direction of the applied *E*-field, as shown in Fig. 6.11(b). The $(111)_{PC}$ diffraction peak shows gradual appearance of a shoulder with increasing amplitude of applied E-field, for directions both parallel and transverse to the *E*-field, as shown in Figs. 6.11(c) and 6.11(d) respectively. The *in-situ* bulk diffraction patterns reveal the development of structural distortions within the pseudocubic phase of the randomly oriented specimen upon application of an *E*-field. Subsequent distortions in both $(200)_{PC}$ and $(111)_{PC}$ diffraction peaks with increasing *E*-fields could be attributed to further changes in the volume fractions of coexisting phases with tetragonal and rhombohedral symmetries, as well as changes in the volume fractions of non-180° ferroelectric domains of the two coexisting phases. This result is consistent with previous reports on bulk diffraction measurements showing *E*-field-induced phase transformations in NBT-BT ceramics near the MPB [Ref.217].

In contrast to the behavior observed for the randomly oriented specimen, no evidence of *E*-field-induced phase transformation was evident in the $(001)_{PC}$ textured specimen from the *in-situ* neutron diffraction patterns collected at different electric field amplitudes, as shown in Fig. 6. Remarkably, the $(200)_{PC}$ peak profile shows no significant distortion for field amplitudes up to 1.5 kV/mm, as shown in Figs. 6.12(a) and (b). The $(111)_{PC}$ peak profile for the textured sample

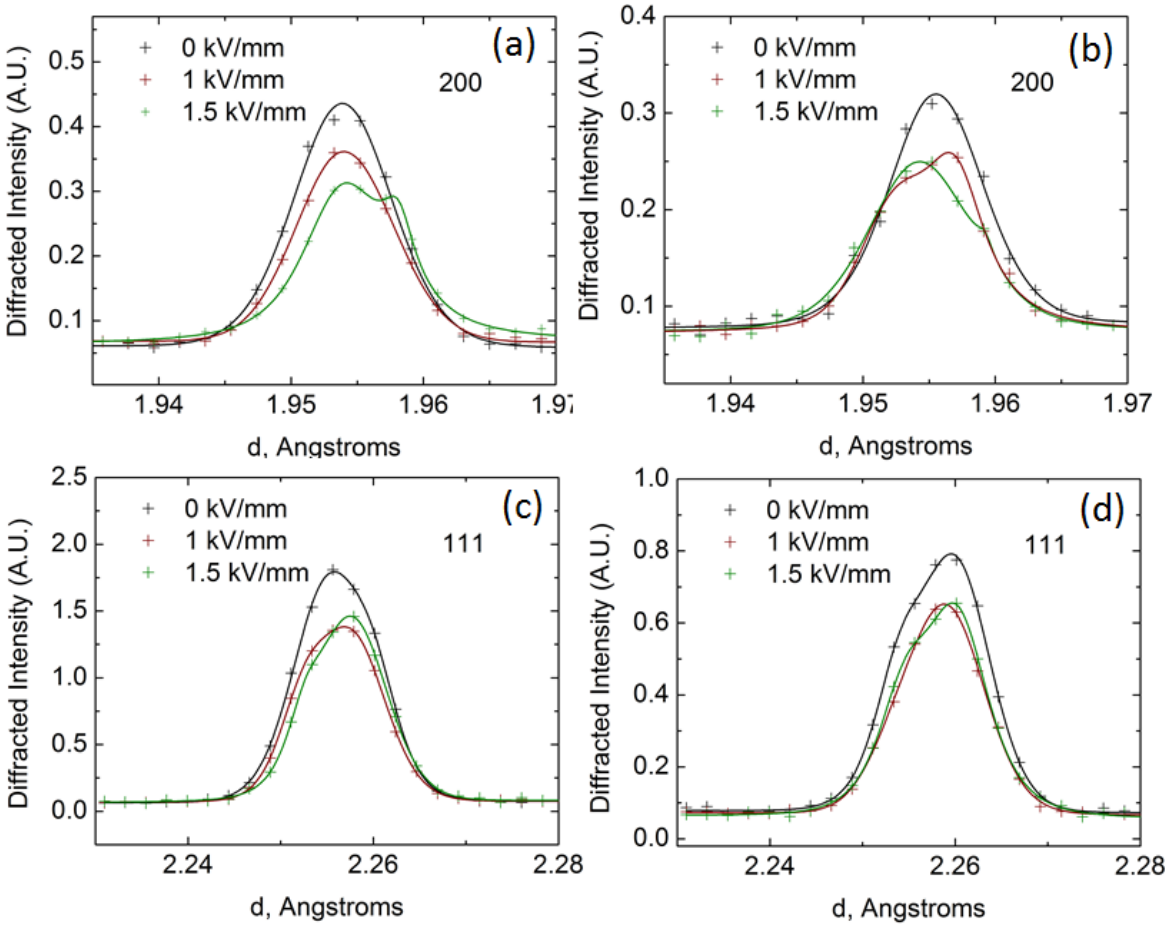

Figure 6.11: Changes in the $(200)_{PC}$ diffraction peak profile for the randomly oriented polycrystalline specimen, (a) parallel, and (b) transverse, to the direction of the applied electric field. Figures (c) and (d) show changes in the $(111)_{PC}$ diffraction peak profile for the same specimen, parallel, and transverse to the applied electric field direction, respectively

measured along the direction of the applied electric field also shows no structural distortions. In the transverse direction, the intensity of $(111)_{PC}$ peak was much lower to draw any significant conclusion, and therefore is not shown here. These results reveal that phase instability under the application of electric fields do not play a significant role towards enhanced piezoelectric properties of the $(001)_{PC}$ textured NBT-BT ceramics. It is pointed out here that creation of phase instabilities is often considered as a guiding principle for the enhancement of dielectric and piezoelectric properties of ferroelectric materials [294,295]. It is therefore interesting that the

randomly-oriented NBT-BT ceramics (that exhibit electric-field-induced phase transformation) have a lower d_{33} coefficient as compared to the $(001)_{PC}$ textured ceramics of the same composition which exhibit no such phase transition. Next, the possible causes for a difference in the *E*-field induced phase transformation behavior of the randomly oriented and the $(001)_{PC}$ textured NBT-7BT ceramics were explored.

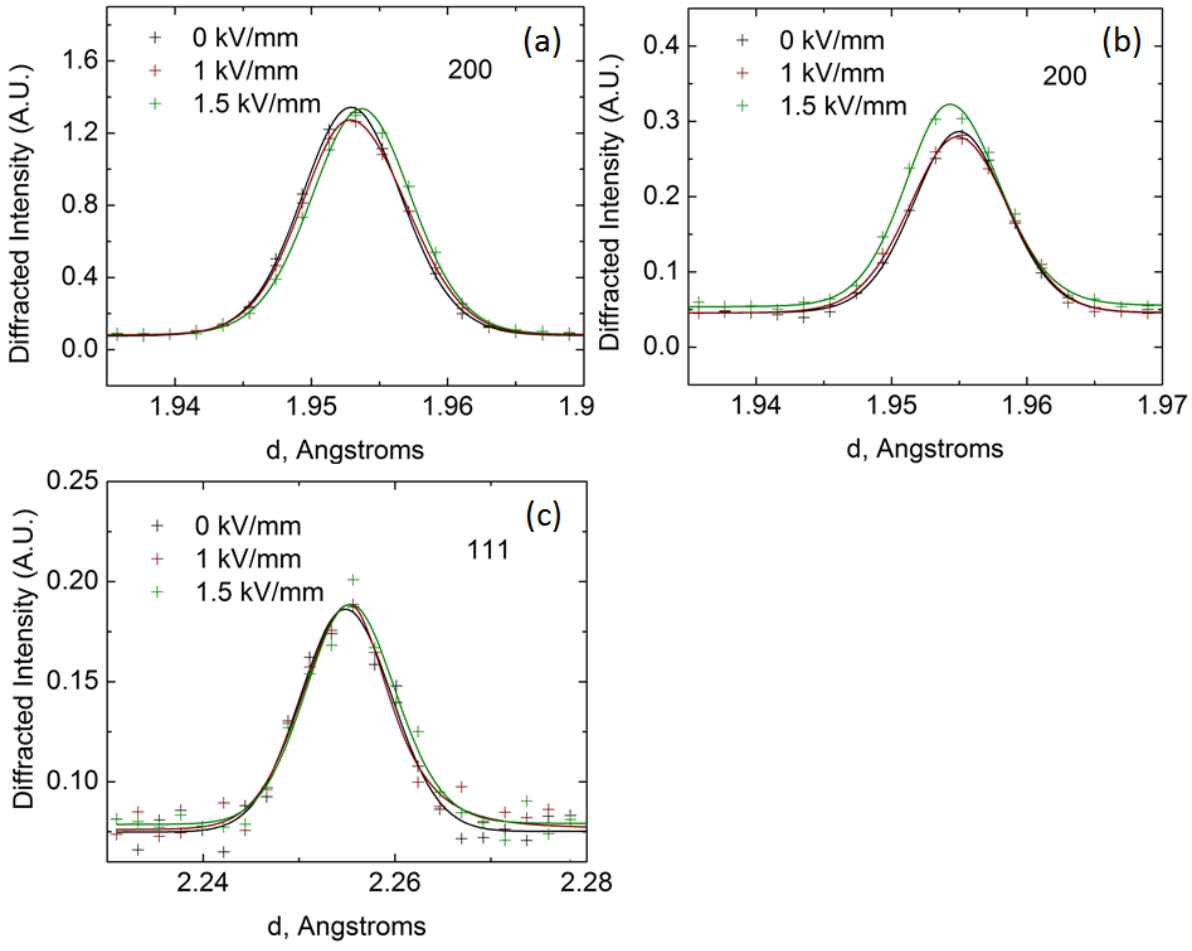

Figure 6.12: Changes in the $(200)_{PC}$ diffraction peak profile for the 100 textured specimen, (a) parallel, and (b) transverse, to the direction of the applied electric field. Fig. (c) show changes in the $(111)_{PC}$ diffraction peak profile for the same specimen, parallel to the direction of applied electric field.

Recently, it has been demonstrated that although Rietveld refinement of bulk neutron diffraction pattern of NBT-7BT indicates a rhombohedral R3c symmetry, the structure is

monoclinic at a local scale [Chapter 5.2]. The local symmetry of the PNRs can arise from localized displacements of Bi^{3+}, Ba^{2+} and Na^{+} away from the $[111]_R$ (R stands for rhombohedral phase) direction towards $[100]_T$ (T stands for tetragonal phase). Since the coherence length of such displacements is of the order of several nanometers, the local displacements towards $[100]_T$ are compensated over larger length scales, and the bulk structure appears almost pseudo-cubic with slight rhombohedral distortion. It was proposed earlier that the observed electric field induced phase transformation behavior in NBT-BT is a consequence of relaxor-to-ferroelectric transformation brought about by changes in the coherence length of the PNRs [Ref.222]. The difference in the observed phase transformation behaviors of the randomly oriented and the textured specimens can be proposed as a consequence of the evolution of coherence length of the PNRs within these two specimens, as explained below. While the $(001)_{PC}$ textured specimen essentially retains a relaxor character with shorter coherence length even after the application of electric fields, such is not the case for the randomly oriented specimen. This hypothesis is consistent with the observed pinched *P-E* loops and a smaller E_c for the $(001)_{PC}$ textured specimens, both of which are characteristic of a relaxor-like behavior. On the contrary, the randomly oriented specimen shows normal ferroelectric P-E loops and therefore does not exhibit a predominant relaxor behavior.

Another possible explanation for the difference in E-field induced phase transformation behavior could be due to internal stresses generated during domain switching. In NBT–KBT based system, a faster rate of applied electric field rate was found to induce structural transformations [292]. The absence of a structural transformation under slower field rate was attributed to internal stresses caused by domain switching during poling (which occurs at the coercive field), because poling before structural transformation increases the required field for

phase transformation to a large extent. Internal stresses can be generated during the poling process due to differences in non-180° domain switching behavior of adjacent grains with different orientations [296]. Therefore, it is proposed that the lower coercive field observed in the textured NBT-BT (Fig. 6.10) specimen facilitates poling, and the resultant internal stresses inhibit further structural transformation. Due to the pseudocubic nature of the diffraction peaks of the textured specimen, non-180° domain switching cannot be clearly identified from structural measurements during the application of electric fields. Nevertheless, large strain associated with non-180^{o} domain switching has been found to play a vital role in the overall structural behavior of various other ferroelectric systems [297-300]. Further examination of the physical origins for such different behaviors of both the types of specimens is currently underway from TEM investigations and detailed Rietveld refinements of neutron diffraction data.

6.2.4 Chapter summary:

In summary, the lead-free piezoelectric ($Na_{0.5}Bi_{0.5}TiO_3$)-$BaTiO_3$ (NBT-BT) textured in $(001)_{PC}$ orientation was found to depict a high longitudinal piezoelectric constant of 322 pC/N contrary to ~160 pC/N observed in randomly oriented NBT-BT ceramics. *In-situ* neutron scattering experiments revealed electric field induced structural phase transformation in the randomly oriented NBT-7BT ceramic, which was however absent in the textured ceramic of the same composition. The absence of *E*-field induced structural phase transformation in the textured NBT-7BT is tentatively attributed to smaller coherence length scales of PNRs and/or inhibition due to internal stress generated by domain switching which precedes a structural transformation. Furthermore, it could be concluded that the phase instability is not a necessary condition to achieve enhanced piezoelectric response in NBT-BT.

Chapter-7

Mechanism of enhanced piezoelectric instability in (1-x) $BaTiO_3$ – x $A(Cu_{1/3}Nb_{2/3})O_3$ (A = Sr, Ca, Ba) solid solutions

This chapter provides fundamental understanding of the enhanced piezoelectric instability in piezoelectric (1-x) $BaTiO_3$-x$A(Cu_{1/3}Nb_{2/3})O_3$ (A: Sr, Ba and Ca and x = 0.0-0.03) solid solutions. These compositions were found to exhibit large d_{33} ~330 pC/N and *kp* ~ 46% at room temperature. The piezoelectric instability in these compositions was found to increase with x despite monotonous decrease in the long range polar ordering. High energy X-ray diffraction coupled with atomic *PDF*s indicated increase in local polarization. Raman scattering analysis revealed that substitutions on A and B-site both substantially perturbed the local octahedral dynamics and resulted in localized nano polar regions with lower symmetry. These localized polar distortions were found to persist much above the Curie temperature (T_c). Polarization – electric field (*P-E)* hysteresis loop analysis indicated presence of the internal bias that was found to be correlated with the formation of polar defects. This defect structure was found to modulate the domain structure resulting in nano domains and broad domain walls with higher mobility as revealed through analysis from HR-TEM and PFM. The presence of nano domains and local structural distortions smears the Curie peak resulting in diffuse order-disorder type phase transitions. The *EPR* investigations revealed that substitution of Cu^{2+} takes place on octahedral sites that are distorted due to *Jahn-Teller* effect. The A-sites were distorted by substitution of Sr and Ca on Ba-site possessing different ionic radii and electronegativity. The effect of these distortions on the variations in physical property was modeled and analyzed within the context of nanodomains and phase transitions.

7.1. Background

Piezoelectric materials with broad range of functional properties are utilized in numerous applications such as high voltage sources, sensors, actuators, energy harvesters and nonvolatile memory elements. Compositional modification of piezoelectric materials is a principal technique used for tuning the magnitude of the electromechanical response. These compositional modifications perturb the atomic-scale structure and global microstructure, modulate the phase transition behavior and influence the evolution of the domain structure. Relaxor-based piezoelectrics are known to exhibit diffuse phase transition (DPT) behavior owing to the existence of polar nano domains. These materials are often characterized by high piezoelectric and dielectric responses [152,153]. However, comprehensive studies accounting for compositional effect on local dynamics/distortion and further on the domain structure and microstructure and their correlation with functional response are limited for lead – free relaxor piezoelectrics. Table 7.1 summarizes the important findings from the literature. In this study, novel lead-free piezoelectric (1-x) $BaTiO_3$ – x $A(Cu_{1/3}Nb_{2/3})O_3$ (A: Ba, Sr and Ca) compositions were synthesized. Subsequently, the local structural distortions, phase transition behavior, microstructure, domain structure and associated changes in functional response of the system were investigated to provide fundamental understanding of A-site instability on piezoelectricity.

The perovskite type $Ba(Cu_{1/3}Nb_{2/3})O_3$ (BCN) material possesses tetragonal unit cell with lattice parameters a = 4.0464 Å and c = 4.1807 Å (c/a = 1.033) suggesting the presence of long-range ferroelectric ordering [301]. The B-site of this system is occupied by Cu and Nb atoms in the ratio of 1:2. This material was found to exhibit high Curie temperature (T_c)~ 793 K as confirmed by XRD-analysis and temperature dependence of the relative permittivity plots [302]. However, ferroelectric and piezoelectric properties were difficult to be measured due to low electrical

resistivity. Interestingly, blending of these materials (higher conductivity) with $BaTiO_3$ (semiconducting) resulted in materials with high resistivity and high piezoelectric response (d_{33}~330 pC/N and k_p~46%). Furthermore, it was observed that with subtle change in composition, the Curie temperature can be modulated and the phase transition becomes diffuse due to the presence of localized regions with polar structural distortions.

In randomly oriented polycrystalline ceramics, the domain size has been found to be dependent on the grain size [303], consequently affecting piezoelectric response of the corresponding system (Table I) [304-307]. The systems with smaller domain size due to high domain density exhibits enhanced piezoelectric response [308]. These systems also exhibit substantial concomitant change in ferroelectric phase transition behavior, which could be noticed in terms of variations in critical exponent (n) (Table 7.1). However below critical grain size, the motion of domain boundaries is confined by geometrical restrictions [303,304]. Thus, the functional properties of piezoelectric materials are a complex function of grain size, tetragonality, Curie temperature, domain structure and local structural distortions. However, studies describing the perturbation in local structural distortions and dynamics on macroscopic functional response are scarce especially for lead-free piezoelectric systems. The atomic PDF and Raman spectroscopy are the powerful tools for the study of local structure in crystalline, quasicrystalline and non-crystalline materials, yielding crucial information about atomic and nano-scale structures of materials.

Table-7.1: List of various lead-free relaxor-type piezoelectric ceramics and their properties with critical exponent (n) obtained by modified Curie-Weiss law [1].

Materials	Composition	Grain size (μm)	d_{33} (pC/N)	Pr ($\mu C/cm^2$)	n	Domain state	Tm (^oC)
BTO[309]	Hf (9 mol%)	9	--	5	1.17		95
NKNS-LT-xBT[310]	X=0.01	----	---	16	1.51	Macro domain	247
	X=0.025	----	----	13	1.69	Tweed-like domains	178
	X=0.050	----	----	5	1.92	Nano domains	111
(1-x)NKN-xCT[311]	X=0.0	0.2	125	---	1.2	----	413
	X=0.03	0.2	137	----	1.31	----	345
	X=0.05	1 .0	237	---	1.40	Increased mobility	306
	X=0.07	< 1.0	80	---	1.54	----	265
0.8BT-(0.2-x)BS-xPT[312]	X=0	---	---	---	1.58	---	85
	X=0.05	---	---	1.17	1.52	----	65
	X=0.10	---	---	3.13	1.44	----	60
	X=0.015	----	---	8.56	1.40	MPB region	60
	X=0.017	---	---	5.16	1.22	----	105
	X=0.20	---	---	---	1.00	----	155
(0.95-x)BT-xCT-0.05ST[313]	X=0.5	5.00	---	---	1.74	---	108
$BaZr_xTi_{1-x}O_3$, MgO 5wt%[314]	X=0.2	---	---	---	2.00	---	-81
$(Ba_{0.65}Sr_{0.35})(Zr_{0.35}Ti_{0.65})O_3$[315]	----	---	---	0.5	2.00	---	-115
(1-x)KNLNS-xBT[316]	X=0.005	2.0	269	---	1.88	---	349
0.94NBT-0.06BT[317]	Nd_2O_3 (0.4 wt%)	---	175	39	1.66	---	300
$Bi_{0.5}(Na_{0.68}K_{0.22}Li_{0.1})TiO_3$[318]	La_2O_3 (0.1 wt%)	2.0	192	29.1	1.70	---	345
KNTN-La_x[319]	X=0.015	2.0	98	9.5	1.59	---	269
$Ba(Ti_{0.9}Zr_{0.1}V_{0.02})O_3$[320]	V	53	----	9.0	1.7	---	97
$(K_{0.5}Na_{0.5})_{1-3x}La_xNbO_3$[321]	La	1-2	135	15	1.52	---	400
(KNN-xBZT + 1 mol% MnO_2	X=0.06	2	234	---	1.26	---	318
(1-x)KNN-xBS[322]	X=0.01	10-20	----	40	1.42	---	379
	X=0.02	1-3	---	28	1.44	---	340
	X=0.03	1-3	---	22	1.58	---	315
	X=0.04	1	---	12	2.0	---	275
(1-x)NBT-xBKT[323]	X=0.18	--	144	---	1.9	---	330
(1-x)KNN-xNBT[324]	X=0.06	1	---	6.0	1.96	---	325
(1-x)KNN-x$AgSbO_3$+0.75 mol% MnO_2	X=0.08	--	190	---	1.88		240

This study provides fundamental understanding about the origin of enhanced piezoelectric instability and its correlation with the average and local structural changes. The microstructure – domain structure – defect chemistry – physical property relationships in complex lead – free perovskite solid solutions given by the formulation (1-x)$BaTiO_3$-x$A(Cu_{1/3}Nb_{2/3})O_3$ (BT-xACN, x = 0.0-0.03, A=Ba, Sr, Ca) were explained. The average and local structural changes were investigated by high-energy X-ray diffraction coupled with PDFs analysis, Raman spectroscopy

and EPR spectroscopy. The temperature dependence of the relative permittivity was used to investigate the modulation in ferroelectric phase transition behavior due to substitutions on A-site and B-site. Microstructural and morphological investigations were performed using scanning electron microscopy (SEM) and transmission electron microscopy (TEM). Domain structure was investigated using HR-TEM and PFM. The chapter is expected to provide a new understanding of *lead–free* piezoelectric materials that would be helpful in designing better compositions.

7.2 Experimental

(1-x)$BaTiO_3$-x$Sr(Cu_{1/3}Nb_{2/3})O_3$ (x=, 0.0, 0.01, 0.015, 0.02, 0.025, 0.03 and 0.035; termed as BT, BT-0.01SCN, BT-0.015SCN, BT-0.020SCN, BT-0.025SCN, BT-0.030SCN, BT-0.035SCN) ceramics were synthesized using conventional solid state reaction method [325]. Stoichiometric amounts of TiO_2 (Alfa aesar, 99.0%), CuO (Alfa aesar, 99.0%), $BaCO_3$ (Alfa aesar,99.0%), Nb_2O_3 (Alfa aesar, 99.0%) and $SrCO_3$ (Alfa aesar, 99.0%) were used as starting reagents. In order to synthesize (1-x) $BaTiO_3$-x$Ca(Cu_{1/3}Nb_{2/3})O_3$ (x=0.01, 0.015, 0.02, 0.025, 0.03; termed as BT-0.01CCN, BT-0.015CCN, BT-0.020CCN, BT-0.025CCN, BT-0.030CCN) and (1-x)$BaTiO_3$-x$Ba(Cu_{1/3}Nb_{2/3})O_3$ (x=0.01, 0.015, 0.02, 0.025, 0.035; named as BT-0.01BCN, BT-0.015BCN, BT-0.020BCN, BT-0.025BCN, BT-0.030BCN, BT-0.035BCN), additional salts corresponding to $CaCO_3$ (Alfa aesar, 99.0%) and $BaCO_3$ (Alfa aesar, 99.0%) were added.

Traditional XRD patterns were recorded to confirm the phase evolution in all samples using PANalytical X'Pert Pro powder X-ray diffractometer with *CuKα* radiation (λ =1.5418 Å). The scans were conducted in the range of 20 - 60^o (2θ) operating at 45 *kV* and current of 40 *mA*. For grain size measurements, SEM images were collected using *LEO (Zeiss) 1550* microscope operating at accelerating voltage of 5 kV. For electrical measurements, silver electrodes were

applied on flat faces of sintered pellets. Computer controlled HP 4192A impedance analyzer coupled with high temperature oven was used to measure the dielectric response as a function of temperature at various frequencies with oscillation level of 500 mV. The ceramic disks were poled under DC electric field of 3-4 kV/mm in silicone oil bath for 1 hr at RT. The d_{33} values were measured using Berlincourt d_{33}-meter (APC International) and values of k_p were measured by resonance anti-resonance method using HP 4194A impedance analyzer. Room temperature micro Raman studies were conducted in the backscattering geometry using a Jobin-Yvon T6400 Triplemate instrument utilizing laser radiation of 514.5 nm from a coherent Innova 99 Argon source. The green laser light was focused in ~2 μm-diameter by using a Raman microprobe with a 50X objective. A charge-coupled device (CCD) system collected and processed the scattered light. The integration time of the spectrum and the slit width and laser beam power were adjusted in order to achieve a high signal to noise ratio. The typical spectral resolution for the Raman system with an 1800 grooves/mm grating and 1-in CCD was less than 1 cm^{-1}. The instrument was calibrated with Si spectra before and after recording the spectra of the actual samples. Raman spectra of all the samples were taken at different geometrical positions; the results presented here were same throughout the matrix. Conventional TEM images were recorded using Philips 420 transmission electron microscope and HR-TEM imaging was performed using FEI Titan 80-300 transmission electron microscope. For this purpose, the electron transparent foils were prepared by standard polishing technique, i.e. mechanical grinding, dimpling and Ar ion beam milling. Electron paramagnetic resonance (EPR) spectra (X-band) were recorded using a Bruker D200 ER spectrometer, equipped with a TE_{102} cavity at room temperature (~21^{o}C).

7.3. Results and discussion

7.3.1 Piezoelectric and dielectric response

The electromechanical response as a function of composition for all the series of samples is shown in Figure-7.1(a), (c) and (e). The magnitude of d_{33} and k_p increases with x going through a maximum. The maximum d_{33} (330 – 333 *pC/N*) was found to occur at x =0.025 for BT-xBCN and x= 0.015 for BT-xSCN. In the case of BT-xCCN, the maximum d_{33} ~ 260 pC/N was found to occur at x =0.020. These values are comparable to that of hard PZT indicating their potential for industrial applications. The variation of k_p with composition was similar to that of d_{33}. The highest values of k_p ~43% and ~46% were measured in x=0.025 for BT-xBCN and x =0.015 for BT-xSCN respectively. However, the BT-xCCN series was found to exhibit a relatively smaller value of k_p~ 35%. The high magnitude of the piezoelectric responses was found to correspond well with the lower values of the loss tangent factor (see Figure 7.1(b), (d) and (f)) in poled specimens for all series. The relative permittivity (ε_{33}) of poled specimens measured at 1 kHz was found to increase monotonously with the increase in the value of x for all compositions. The maximum value of d_{33} and k_p was observed at x =0.015 for BT-SCN and at x =0.025 for BT-xBCN (for the case of BT-xCCN compositions the value of maximum d_{33} was ~270 pC/N for x=0.02). Next, the high energy x-ray diffraction coupled with atomic PDFs, Raman scattering and EPR analysis were performed to understand the mechanism of the enhanced piezoelectric instability at the optimum compositions and its correlation with the average and local structural changes.

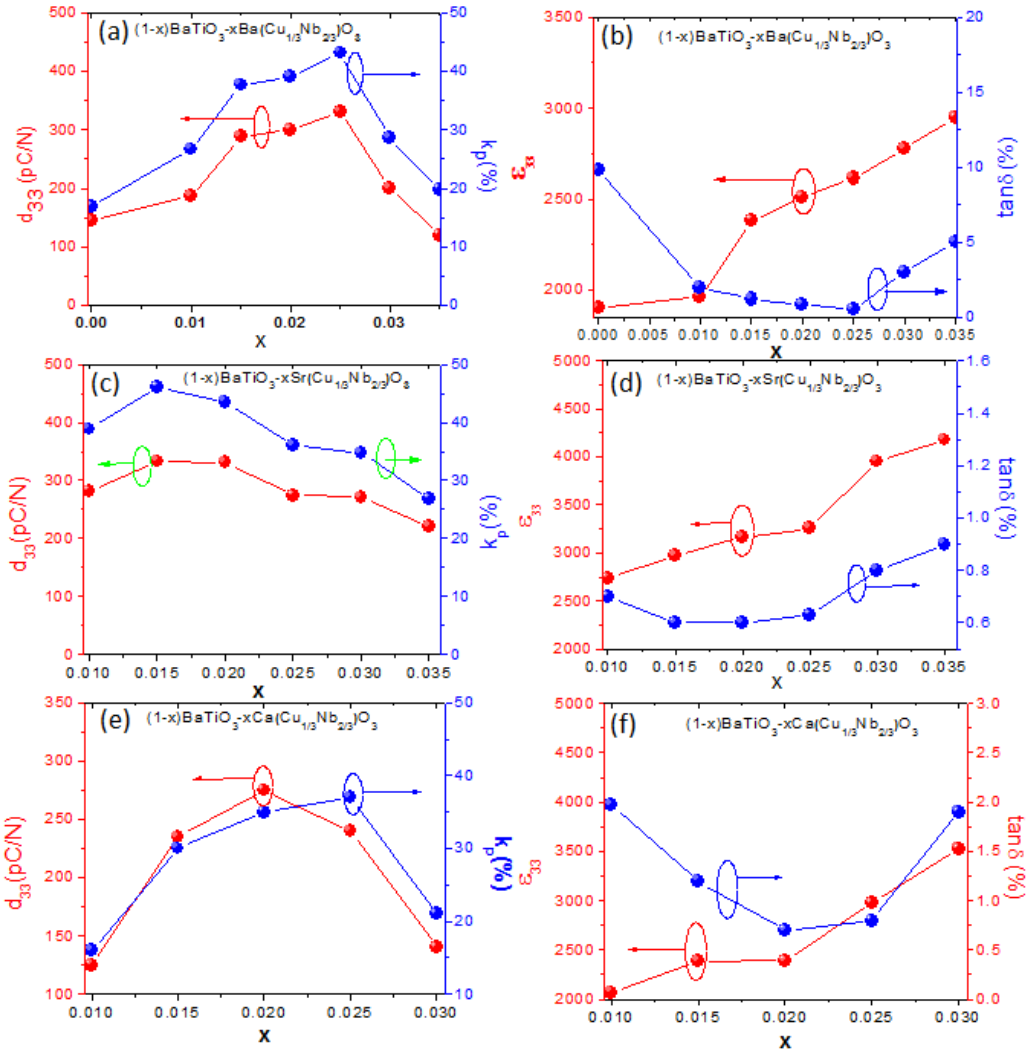

Figure-7.1: Compositional dependence of d_{33} and k_p for (a) (1-x)$BaTiO_3$-xA$(Cu_{1/3}Nb_{2/3})O_3$ with A-site ion as (a)Ba, (c)Sr and (e)Ca. Compositional dependence of ε_{33} and tanδ plots for (1-x)$BaTiO_3$-xA$(Cu_{1/3}Nb_{2/3})O_3$ with A-site ion as(b) Ba, (d) Sr and (f)Ca

7.3.2 X-ray diffraction and atomic pair distribution function analyses

The structural stability of ABO_3 type perovskite can be estimated using a tolerance factor, $t = (r_O + r_A)/\sqrt{2}(r_O + r_B)$, where r_O, r_A, r_B are the effective ionic radii of O, A, and B ions[326]. Classical ferroelectrics like $BaTiO_3$ (tetragonal) possess t > 1 (1.06) and are referred as B-site driven systems because the smaller size B-site cations possess large space to displace.

Other similar perovskite like $SrTiO_3$ and $CaTiO_3$ possess tolerance factor of ~1.00 and 0.98, respectively. Both $SrTiO_3$ and $CaTiO_3$ are incipient ferroelectrics and so do not exhibit polar ordering in normal conditions [327,328]. Generally, materials with lower tolerance factor exhibit lower macroscopic symmetry as a result of the octahedra tilting and ionic displacement due to the smaller ionic radii of A-site species[329,330]. The polar form of pure $BaTiO_3$ possesses a tetragonal structure with space group P4mm and atomic positions: Ba at (000); Ti at (1/2, 1/2, z), O1 at (1/2, 1/2, z); and O2 at (1/2, 0, z) [331]. In the present research, $BaTiO_3$ is blended with diluted concentrations of $Ba(Cu_{1/3}Nb_{2/3})O_3$(BCN), $Sr(Cu_{1/3}Nb_{2/3})O_3$(SCN), and $Ca(Cu_{1/3}Nb_{2/3})O_3$ (CCN). The substitution of Sr^{2+} and Ca^{2+} is expected to occur on Ba^{2+}-site, however the substitution of Cu^{2+} and Nb^{5+} is expected to occur on Ti^{4+}-site. The variation in the tolerance factor (*t*) with the compositional changes is presented in Figure 7.2. An increased level of blending of these complex perovskites leads to systematic decrease in the tolerance factor. However, the rate of decrease in the tolerance factor is higher in the case of substitution of SCN and CCN due to the smaller ionic radius of Sr^{2+} and Ca^{2+} *on* the Ba^{2+} *-site.* The substitution of Sr^{2+} and Ca^{2+} with smaller ionic radii on the Ba-site is expected to reduce the unit cell volume and so decrease the freedom of B-site cation movement eventually leading to reduction of the off-center displacement and the overall long range ordering. The level of distortion from the ideal perovskite structure has been considered as a major factor in imparting ferroelectricity to that system [332]. However, in present case, the decrease in the tolerance factor is very small with the lowest value of 1.057 which is close to 1.0615 of pure $BaTiO_3$. In such cases it is not expected to observe substantial rotational distortion of octahedra [333], even though very intriguing enhancement in the piezoelectric instability in some of specimens studied here was observed.

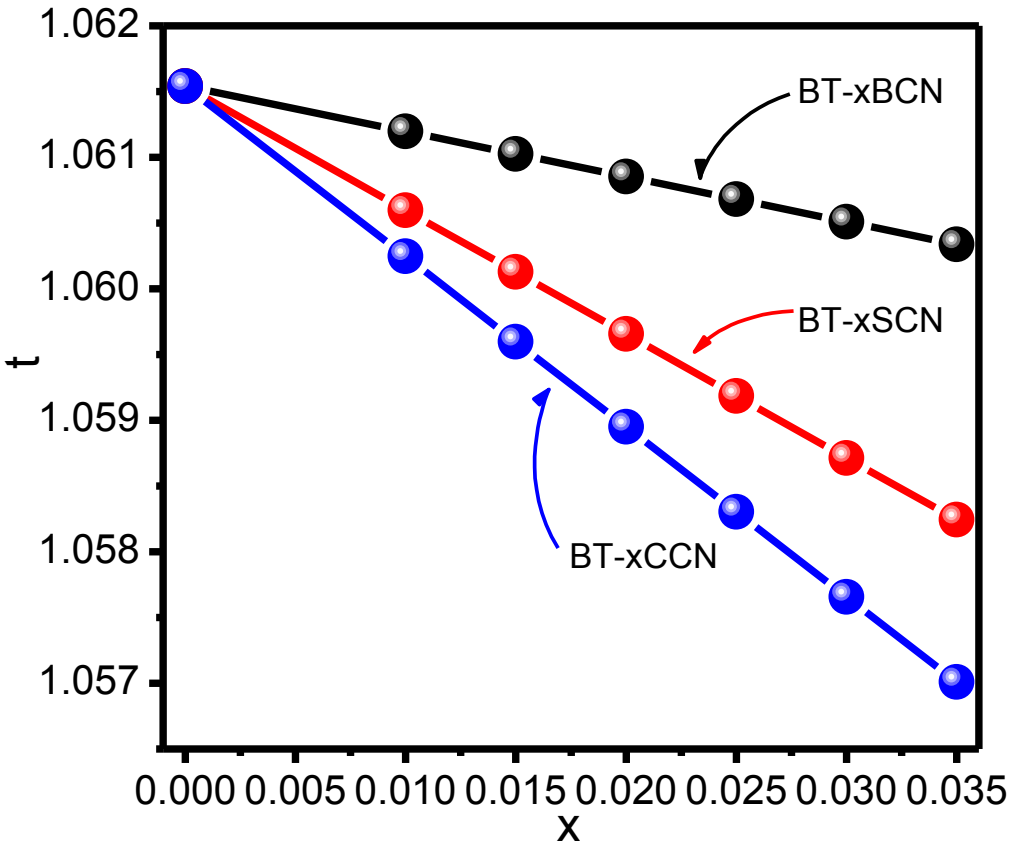

Figure-7.2 Tolerance factor (t) as a function of compositions of different series showing a higher rate of decrease for the compounds having an isovalent substitution on A-sites and aliovalent substitution on B-sites.

Figure-7.3(a), (c) and (e) show the traditional XRD-patterns recorded at RT for various compositions of BT-*x*BCN, BT-*x*SCN and BT-*x*CCN, respectively. This data clearly demonstrates that all the compositions crystallize in pure perovskite phase. The splitting of (200) Bragg reflections suggested tetragonal macroscopic symmetry indicative of the presence of long range ferroelectric ordering. The magnified view of the variation in (002) and (200) Bragg peaks

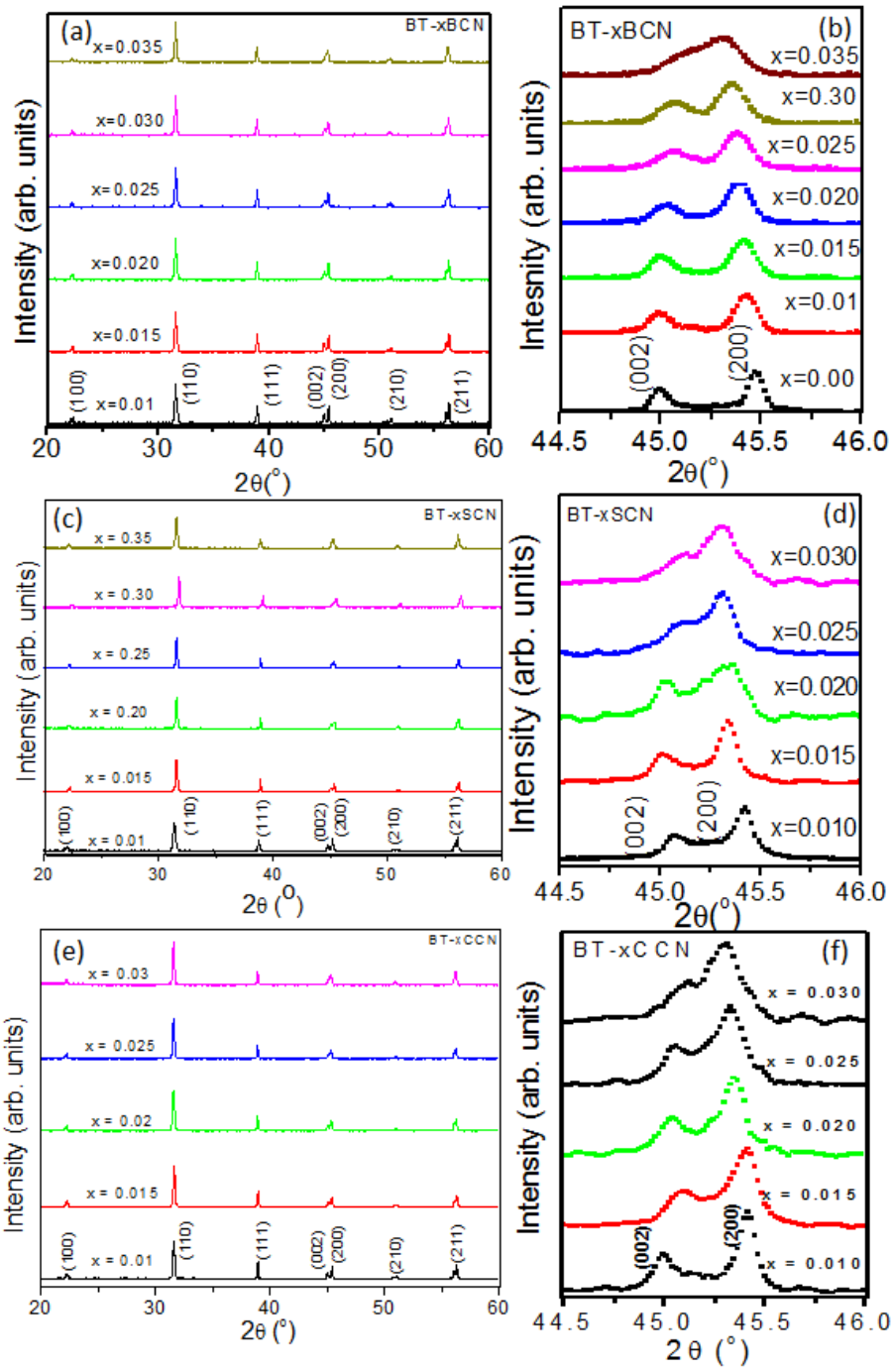

Figure 7.3 XRD-spectra recorded at RT for BT-xACN with A-site ion as (a) Ba (b) Sr (c) Ca, variation in {200} Bragg reflections with A-site ion as: (d) Ba, (e) Sr, (f) Ca

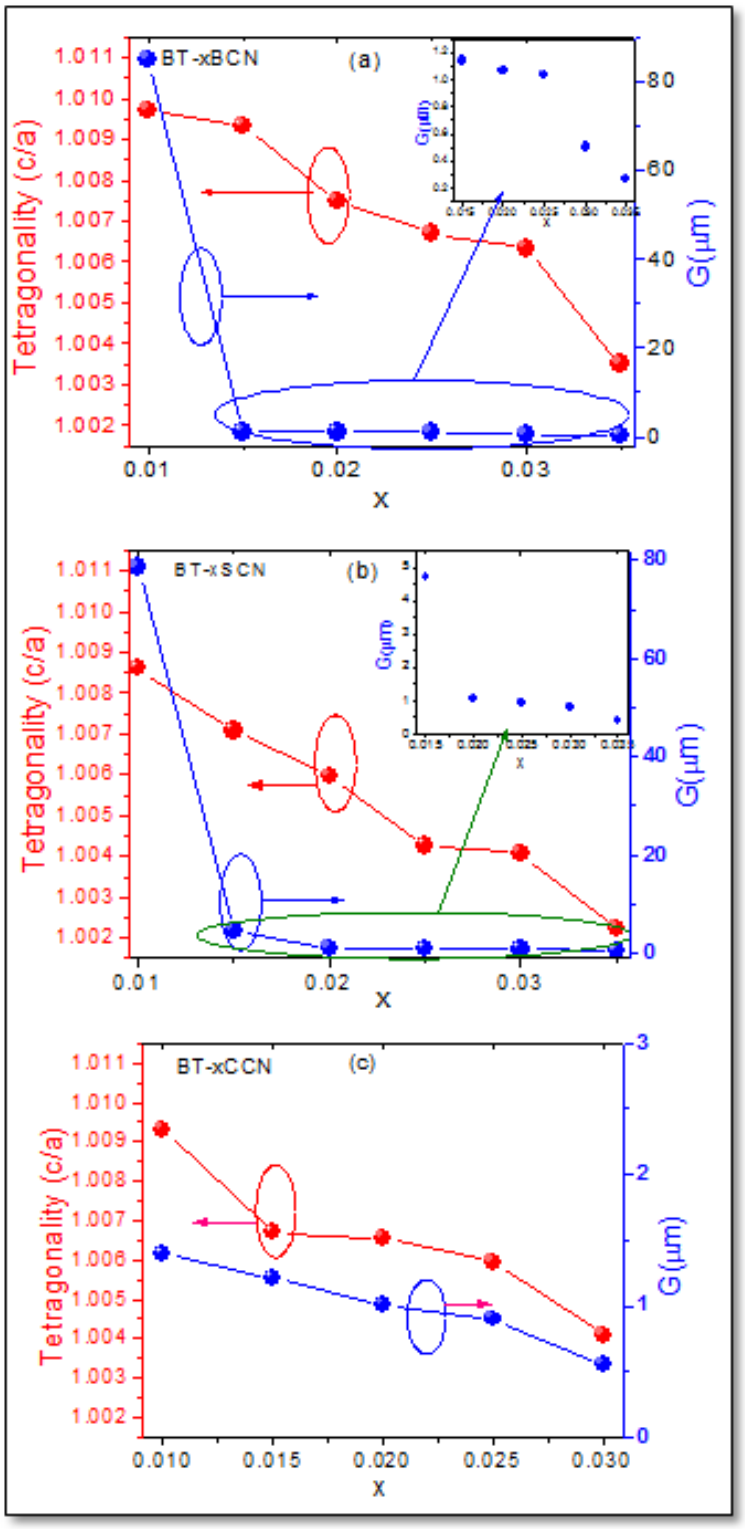

Figure-7.4 Tetragonality and grain size as a function of composition in BT-xACN with A: (a) Ba (b) Sr and (c) Ca

with the change in compositions for all three series of samples is shown in Figure 7.3(b), (d) and (f). As can be seen here that with increase in the value of x, the (002) Bragg peak shifts to higher values of 2θ and the (200) Bragg peak shifts towards the lower values of 2θ indicating increase in the value of the lattice parameter '*a'* and decrease in the value of the lattice parameter '*c'*. This suggests a monotonous decrease in the long range ferroelectric ordering in the corresponding systems. The d-spacing of (200) and (002) peaks was used to calculate tetragonality (c/a) of the specimens. Figure 7.4(a), (b) and (c) show the variation of tetragonality (c/a) and grain size for all modified $BaTiO_3$ compositions. The grain size for pure $BaTiO_3$ was measured to be 28 μm (tetragonality (c/a) = 1.0104) which further increases up to 90 and 80 μm for x=0.01 in BT-*x*BCN and BT-*x*SCN. The large grain size of Sr-doped $BaTiO_3$ is comparable to the values reported earlier [334]. Also, the small concentration of Nb and Cu substitution gives rise to large grain sizes [335,336]. On further increasing the values of x, the grain size decreases monotonously, which can be attributed to the increased concentration of Nb^{5+} and Cu^{2+} [Ref. 337]. The average grain size for BT-*x*CCN compounds was found to be smaller than that of the compositions of the other two series. The detailed discussion about the effect of microstructure on functional response is presented in forthcoming section. Next, high energy x-ray diffraction analysis coupled with atomic PDFs analysis was performed on selected specimens to understand the local structure.

Figure-7.5(a) shows high energy powder x-ray diffraction patterns recorded at RT using Ag-*Kα* (λ =0.559A) radiation for pure $BaTiO_3$ and some selected specimens from the three series of compositions. This data was further reduced to atomic PDFs shown in Fig. 7.5(b). Recently high-energy XRD and atomic PDFs analysis have gained tremendous importance to the

understanding of the local structure of various functional materials and its correlation with their functional properties [178]. The PDF is defined as [178]: $G(r) = 4\pi r[\rho(r) - \rho_o]$, where $\rho(r)$ and ρ_o are the local and average atomic number densities, respectively, and r is the radial distance. The value of atomic PDFs comes from the fact that they consider all components of the diffraction, including sharp Bragg peaks and diffuse scattering, and so are sensitive both to the average and atomic-scale structure. Also, atomic PDFs do not imply any periodicity so that materials of any degree of structural coherence are possible to be studied on the same footing. The experimental PDFs peak at real space distances, where well defined atomic pairs exist and can be easily used to test and refine structural models. Figure 7.5(b) shows the atomic pair distribution functions G(r) (solid line in black) extracted from the 2θ range of the XRD patterns presented in Fig. 7.5(a). The PDF for pure $BaTiO_3$ and its derivatives shows a series of well-defined peaks to high interatomic distances reflecting the presence of a sequence of well-defined coordination spheres in these crystalline materials. These PDF for pure $BaTiO_3$ was matched very well with a structure model featuring a tetragonal perovskite structure (line in red) with space group P4mm. The high-r part of the experimental PDFs of Fig. 7.5(b) is depicted in Figure 7.6. Due to the cooperative off-centering of Ti atoms in the tetragonal/polar phase the intensity distribution of several peaks in the atomic PDFs (red line) is different from that in the PDF (blue line) for the cubic/non-polar phase. For example in the cubic phase the PDF doublet at 26 Å has its low-r component stronger in intensity than the higher-r component. Again in the cubic phase, the PDF doublet at 28 Å has its low-r component stronger in intensity when compared to the higher-r one. The situation is very different with the polar/tetragonal phase. Here the PDF doublet at 26 Å has two components of equal intensity, and the intensity distribution in the PDF doublet at 28 Å is reverse when compared to the case of the non-polar phase. These observations

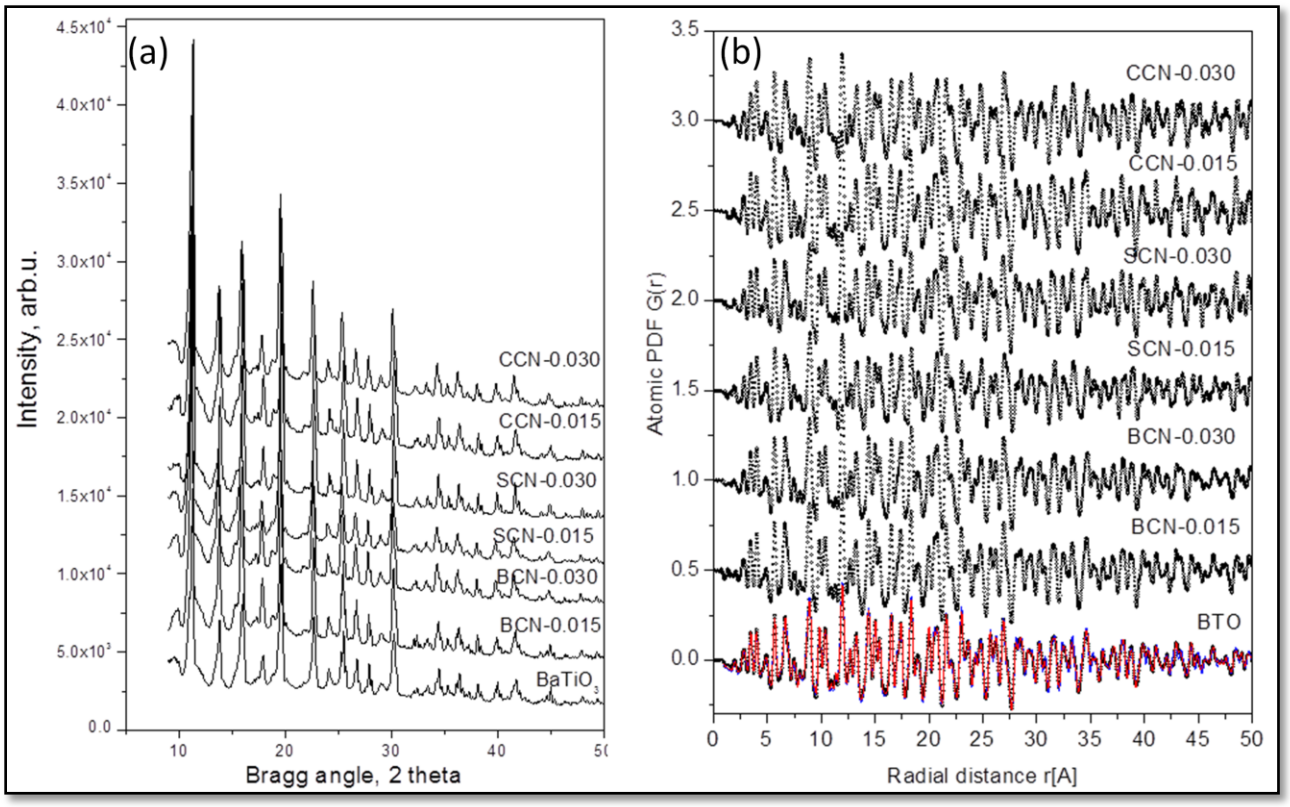

Figure-7.5 (a) Experimental XRD patterns taken with Ag Ka (λ=0.559 A) radiation. Note XRD data quality is optimized for atomic PDFs analysis, (b) experimental atomic PDFs. The PDF for $BaTiO_3$ (BTO) is very well reproduced by a model (line in red) based on a tetragonal (polar/ferroelectric) structure.

are summarized using blue descending arrows for the case of a non-polar/cubic phase and red ascending arrows for the case of a polar/tetragonal phase and used here to differentiate between them. Note a similar analysis based on PDF data for $BaTiO_3$ has been reported by Petkov et al.[338].The PDF peaks at 25.7 and 26.25 Å for the polar structures have similar intensity while those in the PDF of the non-polar structure go like high-low (follow the blue arrows). Moreover, the PDF peaks at 28.25 Å and 28.5 Å for the polar structure go like low-high intensity (follow the arrows in red) while those in the PDF for non-polar go like high-low. From this PDF data it can be seen that the polar distortions survive and even become somewhat stronger with increase composition in BT-*x*BCN, survive in SCN_15 (BT-0.015SCN) but not in SCN_30 (BT-

0.030SCN), and do not survive in CCN_15 (BT-0.015CCN) but reemerge in CCN_30 (BT-0.030CCN). Thus at lower concentrations of Cu^{2+} and Nb^{5+}, the substitution of Sr^{2+} on Ba^{2+}-site

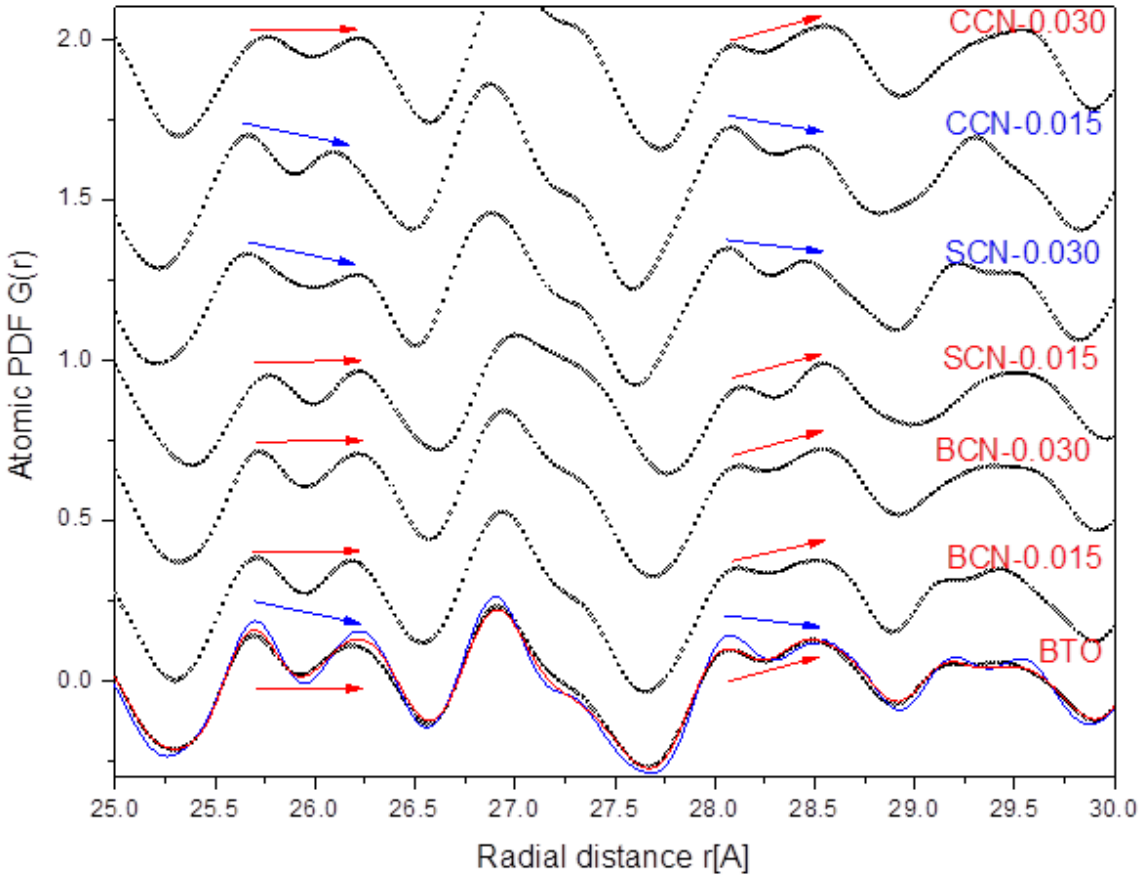

Figure-7.6 Higher-r part of the experimental atomic PDFs (symbols). Model PDFs for tetragonal (line in red) and cubic (line in blue) structures of BTO are shown as well. Note the different behavior of particular PDF peaks in the case of polar (tetragonal) and non-polar (cubic) structures. The PDF peaks at 25.7 Å and 26.25 Å for the polar structure have similar intensity (follow the red arrow) while those in the PDF of the non-polar structure go like high-low (follow the blue arrow).

maintains increased polar character of the specimen (SCN_15). However, the substitution of Ca^{2+} having smaller ionic radii reduces the polar nature of the corresponding specimen (i.e. CCN_15) due to the constrained off-centering of B-site cations. On the other hand for the

specimens (i.e. CCN_30) with higher concentration of Cu and Nb, the substitution of Ca on Ba-site maintains the polar character. This is in line with the pronounced hyperfine splitting observed in higher magnetic field regime of EPR spectrum of heavily Ca substituted specimen CCN_30. Furthermore, the 4d transition ions (Nb^{5+}) are more covalently bound to oxygen than 3d transition ions resulting in a strong off-centered axially perturbed octahedral crystal field[339] influencing local phonon dynamics as explained in Raman scattering results. The increased polar nature explains the enhanced piezoelectric instability in BT-*x*BCN and BT-*x*SCN compositions. At a certain small grain size, domain motion is confined by geometrical restrictions and the system subsequently loses piezoelectric response. The same phenomena is anticipated to occur in BT-*x*CCN where despite high local polar character revealed by the experimental PDF data, a decrease in the piezoelectric response is observed for x=0.03 composition. To understand further the perturbation of the localized dynamics, polar distortions and their correlation with the piezoelectric instability, Raman spectroscopy was employed.

7.3.3 Raman spectroscopic analysis

Raman spectroscopy is a versatile technique for detection of subtle structural distortions in perovskites and an excellent probe for the local structure due to its shorter characterization length. At RT tetragonal $BaTiO_3$ has C_{4v} symmetry, which allows $3(A_1+E)+1(B_1+E)$ Raman active optical modes and $1(A_1+E)$ acoustic modes. There is further splitting in A_1 and E modes to transverse optic (*TO*) and longitudinal optic (*LO*) modes due to long range electrostatic force associated with lattice iconicity. In tetragonal $BaTiO_3$ phase Raman active modes are: $3A_1(TO)+3A_1(LO)+3E(TO)+3E(LO)+1E(LO+TO)+1B_1$. Further optical modes can be seen in the Raman spectra due to dielectric anisotropy.

Figure 7.7(a)-(c) shows Raman spectra for various compositions of BT-*x*ACN (Ba, Sr and Ca). The Raman spectra of pure $BaTiO_3$ (x = 0) depicts an over-damped transverse mode $E_1(TO)$ as observed by continuous increase in the scattered intensity below 150 cm^{-1}. The A_1 (TO_1), $A_1(TO_2)$, $A_1(TO_3)$ and $A_1(LO_3)$ modes were observed at ~ 170, 272, 517 and 720 cm^{-1}, respectively. The interference of the sharp $A_1(TO_1)$ mode at 170 cm^{-1} with the broad $A_1(TO_2)$ mode at 272 cm^{-1} results in an anti-resonance effect in terms of a dip at ~181 cm^{-1}. The $E(TO_2)$ mode was observed at 305 cm^{-1}. In solid solution of BT-*x*ACN, Sr^{2+} and Ca^{2+} easily occupy A-site (Ba^{2+}-site) whereas B-site (Ti^{4+} (0.605Å)) octahedra becomes more complex with the substitution of Cu^{2+} and Nb^{5+} which in turn gives splitting in the phonon modes between 700-800 cm^{-1}. Interestingly, a mode with very small intensity appears in the high frequency regime ~ 840 cm^{-1} for the A-site substituted specimens (BT-xSCN and BT-xCCN). The modes at 170, *305* and *720* cm^{-1} are signature of the tetragonality of the specimens. It can be seen that with the increase in x values, these modes subside. This change is consistent with the decrease in the tetragonality as observed in the XRD spectra which was accompanied with a reduction in the grain size for heavily doped compositions and shifting of T_c towards RT. Furthermore, the confinement of phonons in materials with distorted octahedra and small grains leads to a breakdown of the long range order, allowing phonons not belonging to the center of the Brillouin zone ($k \sim 0$) to become active leading to broadening of the Raman modes[340,341]. The lower frequency Raman mode was found to soften with the increase in compositions 'x' (Fig. 7.8). The rate softening of the mode was higher for the specimen with Ba and Sr on A-site for lower concentrations. However, the substitution of Ca on Ba-site reduces the rate of softening of this mode with compositional change, which could be attributed to increased covalent nature of Ca-O bonds.

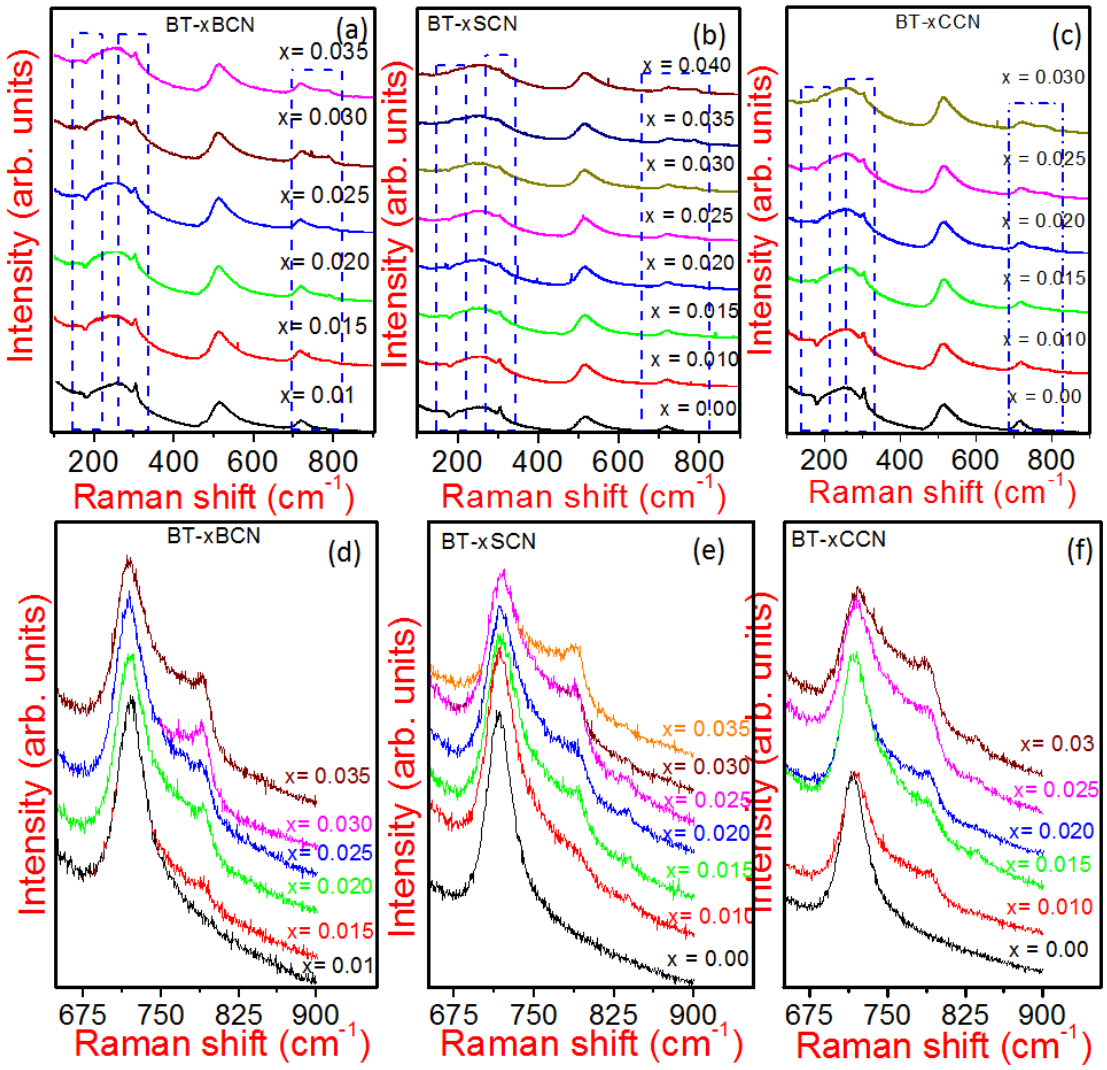

Figure-7.7 Raman spectra recorded at RT for various compositions of (a) BT-*x*BCN, (b) BT-*x*SCN, (c) BT-*x*CCN. High frequency Raman modes at RT for (d) BT-*x*BCN, (e) BT-*x*SCN and (f) BT-*x*CCN.

An ideal (primitive Pm-3m) cubic ABO_3 perovskite structure does not permit any Raman active mode in its first-order vibrational spectra; since each ion is at an inversion center and all long-wavelength vibrational modes are of odd parity. However many complex perovskites like PFN exhibit first-order Raman spectra over a wide temperature range [342]. Higher mode varies in complex perosvkite compounds as a function of the perovskite unit cell and the changes in the ionic radii. So, these high frequency modes have been found to be sensitive towards the change

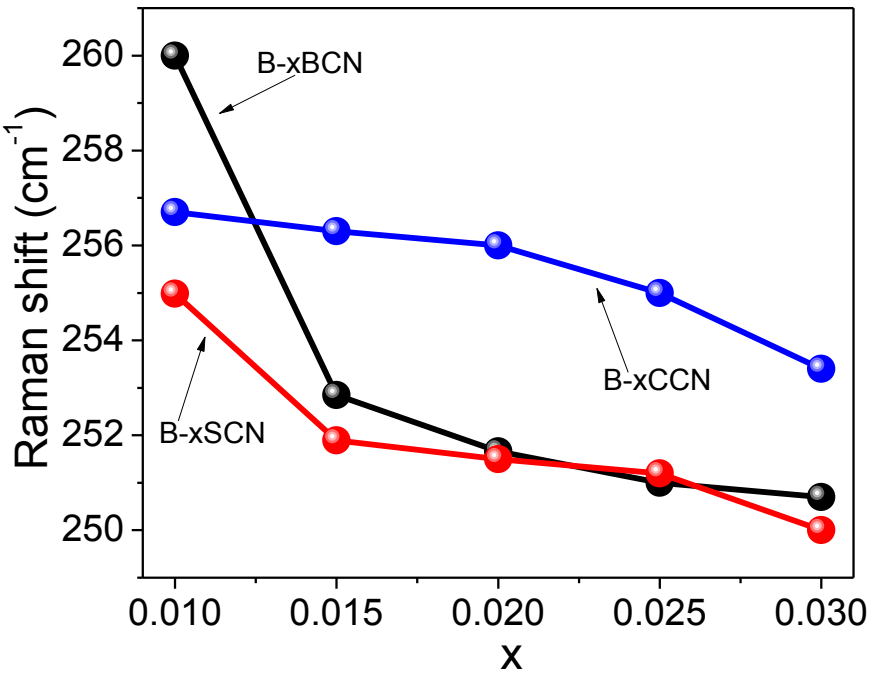

Figure-7.8: Variation in peak position of low frequency Raman mode with the change in compositions.

in the local crystal symmetry related to the presence of polar nano regions[343]. Although neither *A*, *B′*, nor *B″* ions move in this A_{1g} vibration, the mode still reflects subtle changes in the perovskite structure. Only the oxygen ions move, but their spacing and bonding and, hence, frequencies change with the size of the other ions involved. The low Raman band 720 cm^{-1} corresponds to *Ti-O* stretching whereas the 792 cm^{-1} band represents *Nb-O* stretching[344]. In such system the vibration associated with two band modes do not couple due to their different chemical origin. The appearance of a mode at 792 cm^{-1} was considered as local counterpart of the $A_1(LO_3)$ mode appearing at 720 cm^{-1} in pure BT and is related to the internal deformation of the BO_6 octahedra due to the different cation substitutions on B site. The difference in the ionic radii of Cu^{2+} (0.73 A) and Nb^{5+} (0.64A) substituted on Ti^{4+} (0.605A) site would give rise to

elastic dipole like distortion in the surrounding region. Moreover, a small mode observed at high frequency 840 cm^{-1} (marked with arrow) could be attributed to local modes of distorted octahedra due to substitution of Sr and Ca on the A-sites, because this mode was found to be absent in BT-xBCN. The appearance of new modes in the Raman spectra of modified BT has been interpreted as a presence of localized region with lower symmetry[345], which sometimes is referred as polar nano regions giving rise to a diffuse nature of the phase transitions in the relative permittivity versus temperature plots.

To further analyze the splitting of the high frequency modes in various compositions, their magnified view is shown in Figure -7.7 (d), (e) and (f) for BT-*x*BCN, BT-*x*SCN and BT-*x*CCN, respectively. It can be seen that the mode due to TiO_6 octahedra is sharp in the case of BT-*x*BCN and is rather diffuse in the case of substitution of Sr^{2+} and Ca^{2+} on Ba^{2+} -site suggesting increased damping due to enhanced phonon anharmonicity. Moreover, the ratio of the intensities of modes corresponding to TiO_6 octahedra and NbO_6 octahedra decrease with the substitution of Sr^{2+} and Ca^{2+} on the Ba-site. It is very interesting to observe how the substitution on A-sites perturbs the local surrounding of the B-sites. These kinds of local distortions due to substitution on the Ba-sites make the atoms surrounding these sites to coherently shift away from the octahedra centers resulting in nucleation of small polar clusters or regions[346]. The ferroelectric active Nb^{5+} ions are more involved in this process leading to a significant distortion of the B-site cation shell of Ba^{2+}, Sr^{2+} and Ca^{2+} ions when surrounded predominantly by Nb^{5+} [346]. This is reflected in the appearance of new high frequency Raman modes. The PDF analysis also revealed enhanced polar distortions with the increase in the B-site substitution, which was further modulated by substitution of Ca and Sr.

As discussed in PDF analysis, the B-site substitution by Nb^{5+} ions is more covalently bound to oxygen than Ti^{4+} ions and Cu^{2+} ions resulting in a strong off-centered axially perturbed octahedral crystal field, this perturbation can also be seen in A_{1g} modes of Raman spectra of all the investigated systems. This can be rationalized by considering that atomic positional disorder in general; and of niobium and copper in particular at the lower concentration of Cu^{2+} and Nb^{5+}; increases as the population of polar to non-polar phase evolves. The perturbation of nano-polar regions is higher with increased concentration of B-site transition metal ions. The asymmetry in the intensities of different A_{1g} modes, change in the spacing and bonding among the B-site ions with oxygen ions, change in Raman modes positions with the size substituting ions are equally supported by the observation of non-polar high-low intensity and polar low-high intensity PDF analysis qualitatively. Raman analysis also indicates an increase in the spatial range to which local tetragonal distortions can propagate coherently with increase in B-site substitutions which in turns increases the mean free path of the phonons associated with those distortions observed in PDF analysis. It is interesting to note that such a small compositional changes substantially modulate the local dynamics and distortions favoring a piezoelectric instability.

To understand the nature of the phonon instabilities with the change in temperature, Raman spectra for pure $BaTiO_3$ (BT) and BT-0.03BCN, BT-0.03SCN and BT-0.03CCN are shown in Figure-7.9 (a)-(d) in the temperature range of 81 – 573K with 20 K interval. The low frequency mode observed at 305 cm^{-1} and high frequency mode at 720 cm^{-1} vanishes above the Curie temperature in pure $BaTiO_3$. Comparative plots of Raman spectra at various temperatures for pure $BaTiO_3$ and BT-0.03BCN, BT-0.03SCN and BT-0.03CCN are shown in Figure-7.10(a)-(c). In order to investigate the effect of temperature on the local dynamics of TiO_6 and NbO_6

octahedra, a magnified view of the high frequency modes at 81, 298 and 573 K is shown in Figure-7.10(d)-(f). Figure-7.11 shows softening of the Raman mode with respect to change in the

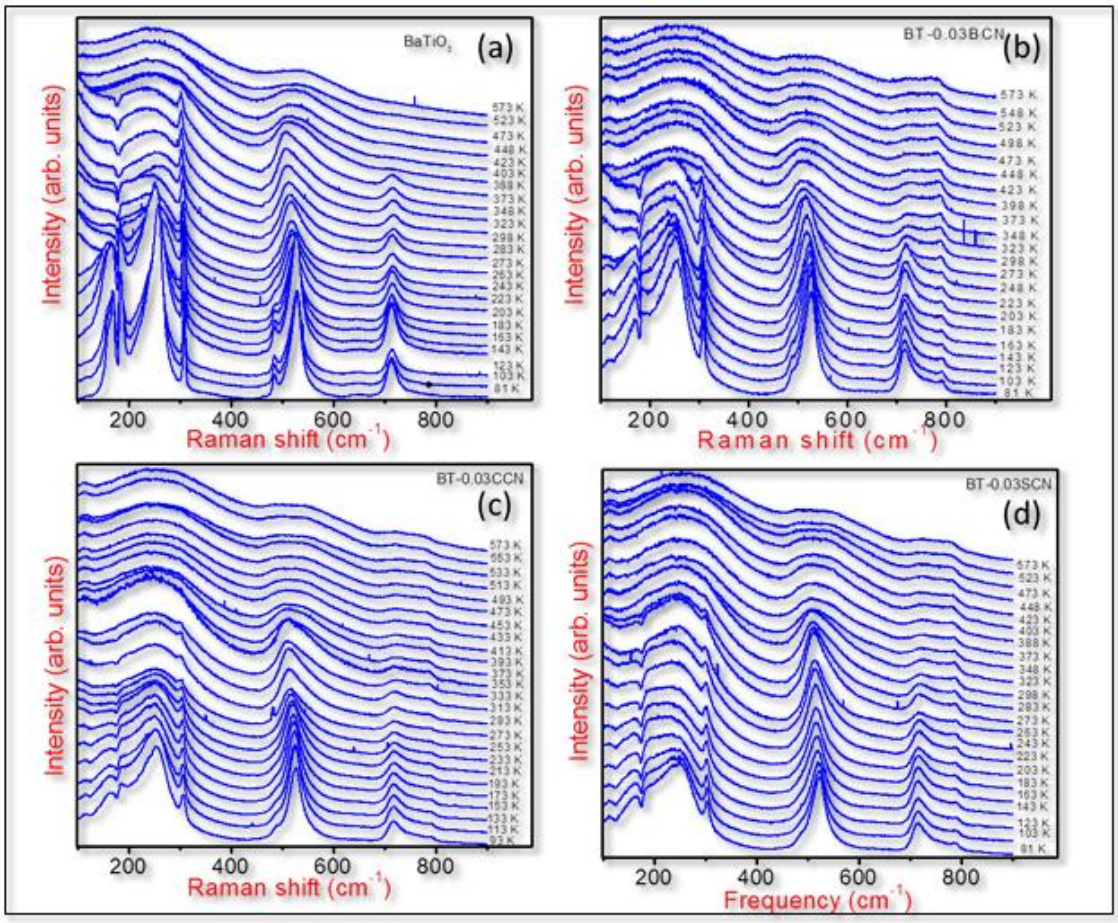

Figure-7.9 Temperature dependence of Raman spectra for (a) BT, (b) BT-0.03BCN, (c) BT-0.03CCN and (d) BT-0.03SCN.

temperature for various compositions. The higher slope of BT-0.03BCN reflects increased degree of softening of the mode with respect to change in temperature, which is however reduced for Sr and Ca substituted derivatives suggesting local structural distortions are less vulnerable to temperature variations in these compositions. From these spectra the following observations can be made: (i) The Raman modes get smeared with the substitution of Cu and Nb on Ti-site, with a

further broadening when Sr^{2+} and Ca^{2+} are substituted on the Ba-sites, as observed in Fig. 7.10 (a) and (b). Also, the monotonous suppression of the mode at 305 cm^{-1} at 81 and 298 K suggests

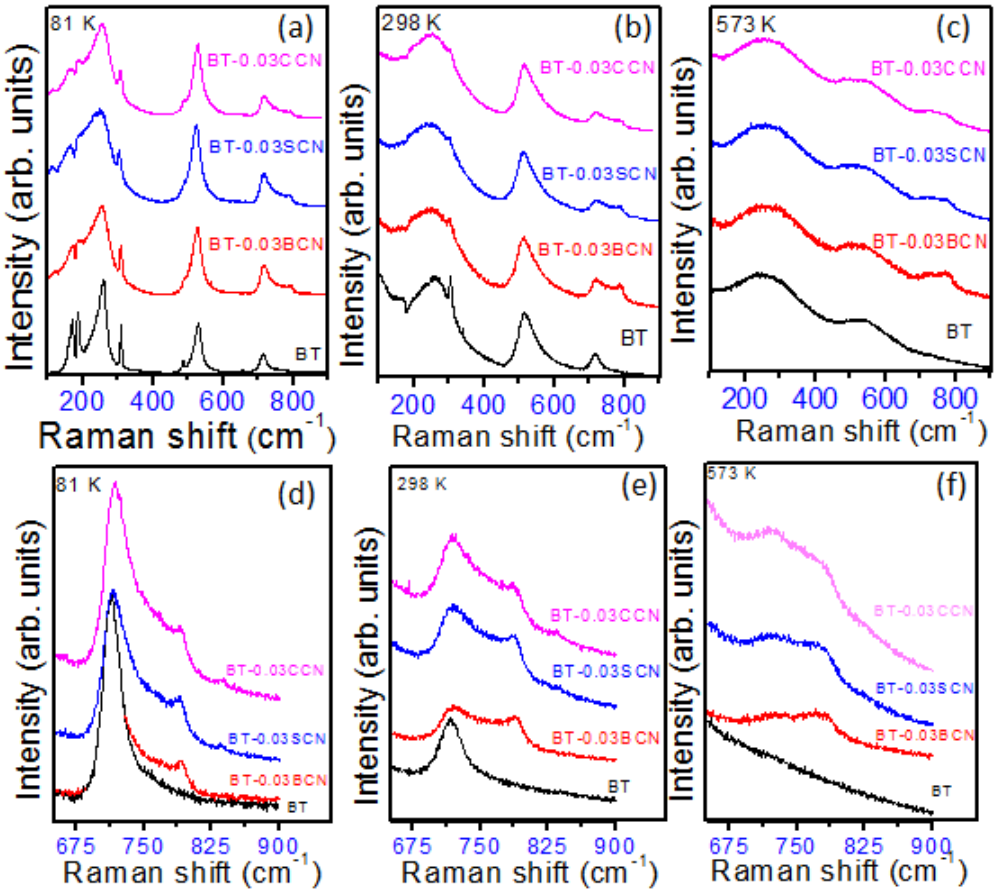

Figure-7.10 Raman spectra of various compositions at (a) 81 K, (b) 298 K and (c) 573 K. Magnified high frequency regime for various compositions at (d) 81, (e) 298 and (f) 573 K.

a reduction of the long range ferroelectric ordering in the following sequence: BT > BT-*x*BCN > BT-*x*SCN > BT-*x*CCN. (ii) Though the Raman mode at 305 cm^{-1} vanishes, the high frequency modes at 720 and 792 cm^{-1} persist up to much higher than the Curie temperature indicating that nucleation of polar nano regions occurs much above that temperature. (iii) In the case of all three modified compositions, the intensity of both high frequency peaks decreases with the increase in x. However, in the case of BT-*x*BCN the rate of decrease in the intensity of the mode due NbO_6 octahedra is lower than that of TiO_6 octahedra and, consequently, the corresponding Raman

mode has a stronger intensity at 573 K. This phenomenon could be attributed to the NbO_6 moieties [347], which play the role of stable pillar for the structure. (iv) The weak mode observed at 840 cm^{-1} at 298 K is more pronounced at low temperature 81 K. Though this mode is absent in the high temperature spectra at 573 K for all compositions stressing its relation with the local octahedral distortions. (v) Appearance of a new mode at low frequency of 113 cm^{-1} in the case of all the modified compositions in the low and high temperature regime (up to 573 K). This mode is not very clear near room temperature probably due to the increase in intensity of the over-damped transverse mode. The observation of this mode in BT-*x*BCN (do not have A-site substitution), suggests that its origin is in the perturbation of the local dynamics due to the B-site substitutions. The appearance of a similar lower frequency mode has been attributed to localized

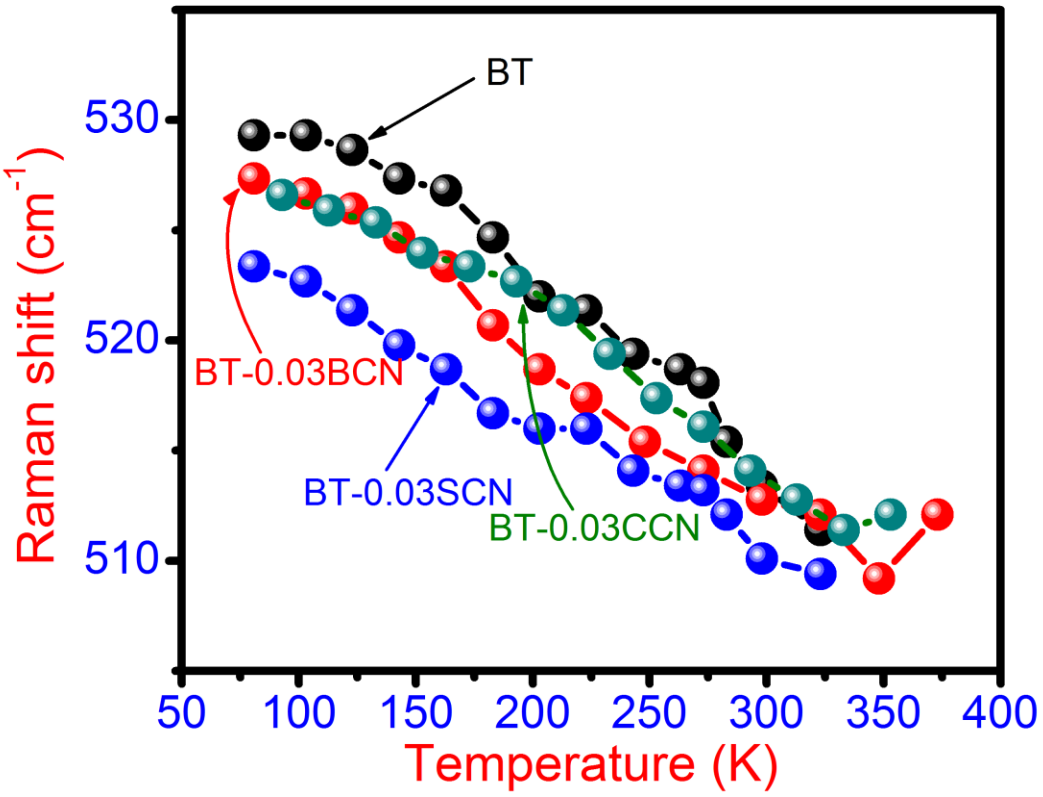

Figure-7.11 Change in the position of Raman mode with the temperature variation for BT, BT-xBCN, BT-xSCN and BT-xCCN.

regions with rhombohedral local symmetry[348]. These localized polar regions or nano polar regions play an important role towards enhanced piezoelectric response of the specimen and result in diffuse nature of phase transition (DPT). Information about the local crystal field around Cu^{2+} is important to understand the localized distortions and defect structure. Fortunately Cu^{2+} have unfilled d-orbitals, which make them EPR active.

7.3.4 Electron paramagnetic resonance spectroscopy and defect chemistry

Magnetically diluted Cu^{2+} centers ($3d^9$) with an electron spin S=1/2 can be represented by a spin Hamiltonian[349]: $H = \mu_B B_o . g . S - \mu_n g_n B_o . I + S . A . I$, where g_n is the corresponding nuclear g factor and μ_B and μ_n are the Bohr and nuclear magnetons, respectively. The first term represents the electronic, while second term represents the Zeeman interactions and B_o denotes the external field. The third term corresponds to copper hyperfine interaction with I^{Cu} = 3/2 for both copper isotopes. X-band EPR spectra recorded at room temperature (RT) for samples having lower (x=0.01) and higher (x=0.03) concentration form BT-xBCN, BT-xSCN and BT-xCCN series are shown in Fig. 7.12(a) and (b), respectively. The shape of the EPR spectra is characteristic of axially distorted octahedral copper (II) ($3d^9$, S = 1/2, I = 3/2) complexes at RT. The EPR spectra contained two major peaks, corresponding to g_{II},which was split into four peaks due to hyperfine interactions with the copper (II) nucleus (I= 3/2), and $g_{\perp}$, which was the sharp central feature in the spectrum. This confirms the Cu^{2+} ($3d^9$) oxidation state of copper. Copper has two isotopes with natural abundances Cu^{63}: 69.09% and Cu^{65}: 30.91%, but both isotopes possess similar magnetic moment and a nuclear spin I = 3/2, giving rise to a nearly identical EPR signal [349]. From the EPR spectra, it could be noticed that the hyperfine lines (g_{II}) are relatively sharp for the BT-*x*BCN specimens (BT-0.01BCN and BT-0.03BCN), and become rather smeared for the compounds having Sr^{2+} and Ca^{2+} on Ba^{2+}-site. This could be due to a local distortion

created by the isovalent substitution of Sr^{2+} and Ca^{2+} on the Ba^{2+} sites coming from the different ionic radii. Likewise, the central peak corresponding to $g_{\perp}$ also appeared to contain hyperfine splitting (encircled region in the higher magnetic field regime of Fig 7.12(a) and (b)), which was more pronounced for the Ca^{2+} than for the Sr^{2+} or Ba^{2+}-sites. Therefore, the effect of A-site substitution on B-site is clearly observable in the EPR, Raman spectra and PDF analysis. In a powder sample, only an averaged EPR spectrum could be observed due to the random orientation of crystallites, which results in the so called parallel and perpendicular orientations. By nature, the parallel part of the spectrum remains much weaker than the perpendicular part of the EPR spectrum and, hence, the observed EPR spectra conforms to the axial symmetry of the copper complex i.e. $g_x = g_y = g_{\perp}$ and $g_z = g_{||}$. In the present case, $g_{||}$= 2.302 and $g_{\perp}$=2.01. The value of the hyperfine splitting constant $a_{||}$= 101G. The values of the g factor were found to vary as $g_{||} > g_{\perp} > 2$, which suggests that the ground state of the Cu^{2+} ion in the distorted octahedral (tetragonal) complex is dx^2-y^2 [350]. Measured values of $g_{||}$ and $g_{\perp}$ are characteristic of Cu^{2+} coordinated by six ligands that form an octahedron elongated by tetragonal distortion along its c-axis [351]. The observed distorted octahedral symmetry of the copper complexes suggests that copper occupies Ti^{4+} site with divalent oxidation state (Cu^{2+}), which results in a lowering of the local symmetry due to the Jahn-Teller effect [349]. These localized distortions with lower symmetry have been found to modulate extensively the macroscopic functional response of the corresponding systems.

According to the chemical formulation of BT-*x*ACN, the overall charge neutrality should be maintained by Cu^{2+} and Nb^{5+} doping on the Ti-sites. For the rather diluted concentrations studied here, these ions are statistically distributed in the perovskite lattice leading to charged

nano regions. For electroneutrality, the acceptor doping of Cu^{2+} on the Ti^{4+} -sites gives rise to an equivalent number of oxygen vacancies $V_o^{\bullet\bullet}$ (Kröger–Vink notation) given as:

$$BaO + CuO \rightleftharpoons Ba_{Ba}^{\times} + Cu_{Ti}'' + V_o^{\bullet\bullet} + 2O_o^{\times} \quad (7.1)$$

$Ba_{Ba}^{\times}$ is the Ba sitting on Ba-site with neutral charge. The oxygen vacancies $V_o^{\bullet\bullet}$ impact the domain wall mobility. The Cu_{Ti}'' vacancies are immobile contrary to the moblie $V_o^{\bullet\bullet}$ at ambient temperature [352]. The substitution of Nb^{5+} occurs on the Ti^{4+} sites as:

$$2BaO + Nb_2O_5 \rightleftharpoons 2Ba_{Ba}^{\times} + 2Nb_{Ti}^{\bullet} + 2e' + 6O_o^{\times} + 1/2O_2(g) \quad (7.2)$$

where $Nb_{Ti}^{\bullet}$ and $e'$are the singly charged dopant ions occupying the titanium sites and the electrons in conduction band, respectively. For higher concentration of Nb, the ionic charge compensation occurs though formation of vacancies at the Ba-sites (V_{Ba}''):

$$BaO + Nb_2O_5 \rightleftharpoons Ba_{Ba}^{\times} + 2Nb_{Ti}^{\bullet} + V_{Ba}'' + 6O_o^{\times} \quad (7.3)$$

The vacancies V_{Ba}'' do not contribute significantly to the conduction. On the other hand the increased impurity scattering (due to Nb ions) leads to an increase in the resistivity. In the present case, the formation of V_{Ba}'' appears to be less favorable due to the small concentration of the dopants and the co-doping with copper on the same sites. However their presence cannot be ruled out. Furthermore, for larger values of x, the negatively charged Cu_{Ti}'' would start interacting with the positively charged $V_o^{\bullet\bullet}$ leading to the formation of defect complexes [353]:

$$Cu_{Ti}'' + V_o^{\bullet\bullet} \rightleftharpoons (Cu_{Ti}'' - V_o^{\bullet\bullet})^{\times} \quad (7.4)$$

The $(Cu_{Ti}'' - V_o^{\bullet\bullet})^{\times}$ defect dipoles have been found to be oriented along the crystallographic c-axis [353]. The schematic representation of the formation of defect dipoles is shown in Figure

7.12(c) and (d). However, for donor doping, the formation of defect complexes between the donor ion and the cation vacancies was not observed [352]. This type of defect complexes has been found to result in high electromechanical coupling and substantially affect the fatigue behavior [354]. In previous sections, the effect of elemental substitutions on local structural modulations and phonon dynamics was studied. Concomitantly, the elemental substitution induced defect structure modulates the evolution of microstructure and domains structure, which consequently affects the overall piezoelectric response.

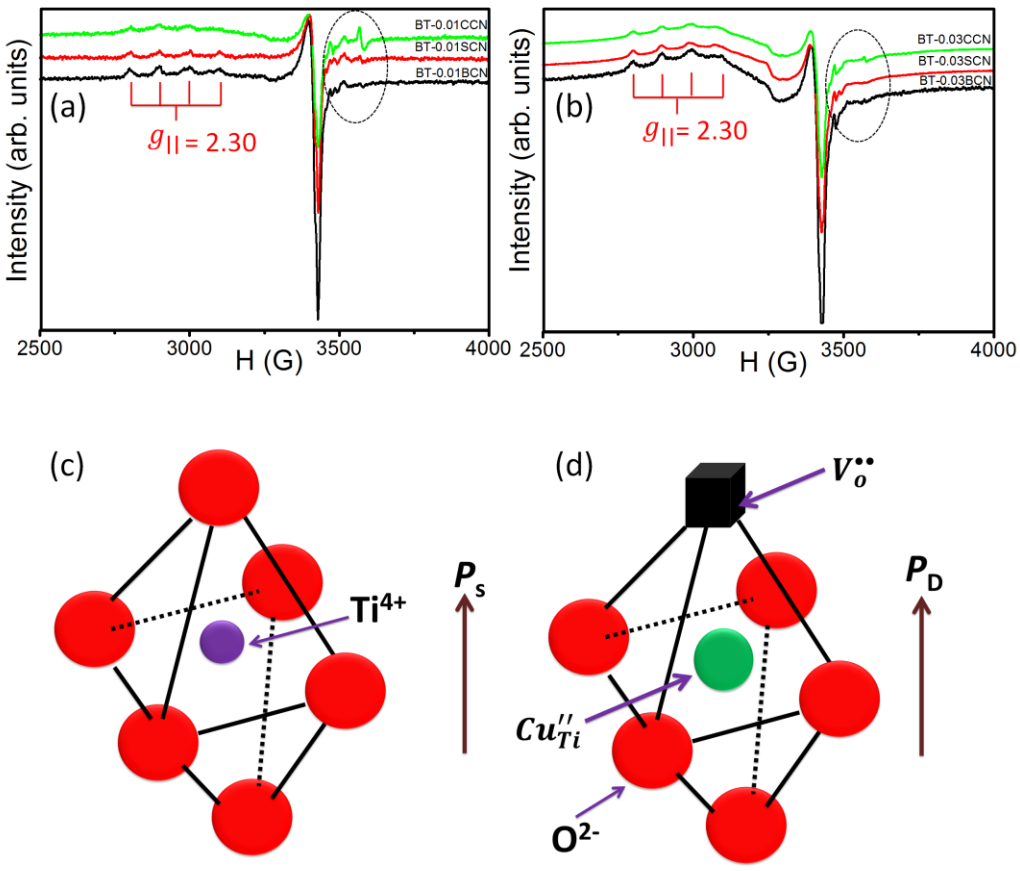

Figure-7.12 EPR spectra recorded at RT for (a) x=0.01 and (b) x=0.03 compositions of different series. Schematic representation of the structural model (c) T^{4+} sites surrounded by oxygen octahedra in case of pure $BaTiO_3$, (d) the $(Cu_{Ti}'' - V_o^{\bullet\bullet})^{\times}$ defect dipole oriented along the crystallographic c –axis, creating axial center.

7.3.5 Microstructure and domain structure

For various compositions of BT-*x*ACN (Sr, Ca, Ba), the tetragonality (c/a) was found to decrease monotonously with the increase in the values of x (Figure 7.4) accompanied by reduction in grain size. The defects resulting from the isovalent and aliovalent substitution impede the grain boundary mobility during the synthesis process at higher temperature resulting in a smaller grain size [352] especially for higher concentrations of doping. Smaller grain size has been reported to result in miniaturized domain state and an increased domain density, which has been considered to be key factor for achieving high piezoelectric response. The grain size (~28 μm) of pure BT was found to be much higher than that of its modified counterparts as discussed earlier (Figure-7.4). Figures 7.13 (a)-(d) and (e)-(h) show piezoresponse force microscopy (PFM) phase images exhibiting domain switching under applied DC bias for $BaTiO_3$ and BT-0.025BCN, respectively. From these images it could be seen that the domain size in BT-0.03BCN with smaller grain size is much smaller than in pure BTO. The bigger domain size in pure $BaTiO_3$ was also confirmed through bright field TEM images (Figure -7.18) explained in forthcoming section. In order to investigate the switching behavior of domains in BT and BT-0.025BCN, a DC bias of 0, 2, 4, 6, 8, 10, and 12 V was applied using scanning tip on both the specimens of same thickness (~100 μm). The area chosen for applying DC bias was 20x20 μm^2 for $BaTiO_3$ and 4x4 μm^2 for BT-0.025BCN. The effect of applied voltage on the domain switching could be clearly seen from the disappearance of dark regions inside the rectangular region marked in the images. From these images, it could be noticed that the switching of domains in BT-0.025BCN occurs at comparatively lower *E*-field. This phenomenon reflects higher domain mobility in BT0.025BCN leading to higher piezoelectric response. At low *E*-field switching of 180^o domains occurs, while switching of 90^o domains requires higher *E*-field

resulting in higher electromechanical response. The values of *E*-field required to switch particular domains varies from system to system. Therefore, the polarization reversal by the nucleation and migration of 90^{o} domain walls instead by just direct 180^{o} switching cannot be ruled out at higher fields [355]. The coercive field for 90^{o} domain reversal increases substantially with the reduction in grain size after certain extent and seen as a reduction of the hysteresis. However, the restoring force provided by symmetry conforming point defects (like oxygen vacancies) that facilitate non 180^{o} domain switching could considerably contribute to the enhanced electromechanical response of the ceramics systems [354]. These 90^{o} domain walls are expected to vanish at 400 nm, however at grain size >10 μm, the domain size becomes constant [308].

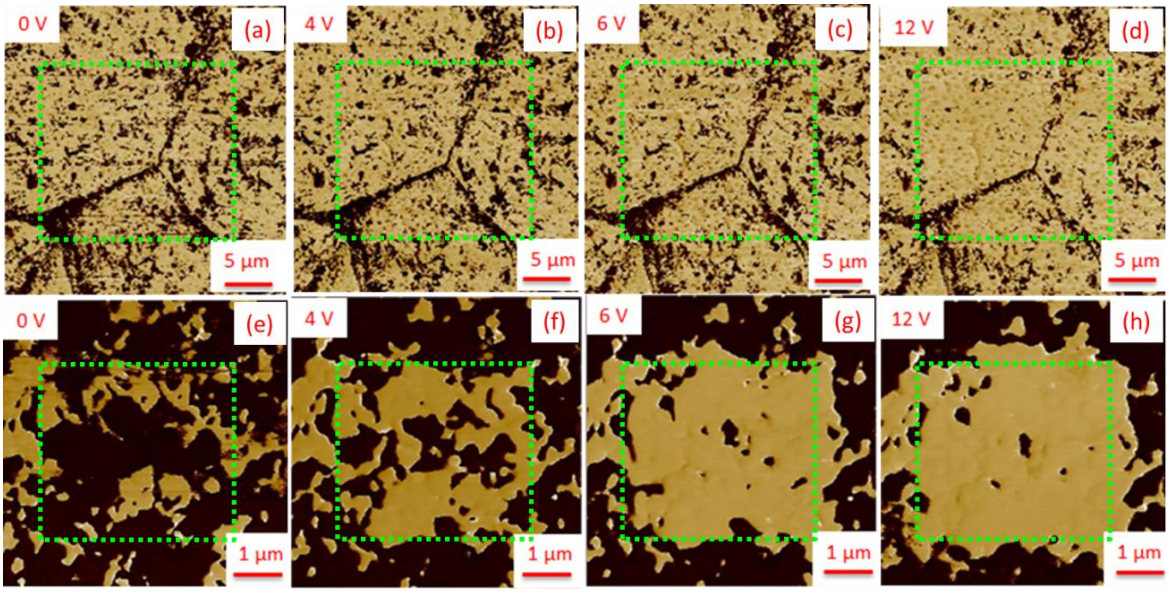

Figure-7.13: Piezoresponse force microscopic images of domains switching under applied DC bias for (a)-(d) BaTiO3, (e)-(h) BT-0.025BCN, the values of DC bias are mentioned on the images.

The actual angle of the 90^{o} domain wall can be given by $2tan^{-1}\left(\frac{1}{\frac{c}{a}}\right)$. Therefore in pure $BaTiO_3$, the actual angle of 90^{o} walls is 89.4^{o}. However, the angle of domain wall is forced to be 90^{o} instead of 89.4^{o} which results in localized strained regions whose strength varies with the

grain size [308]. The localized strained regions can also act as nucleation sites for domain switching. In the case of $PbTiO_3$, the higher teragonality (c/a=1.06) results in the domain wall angle having a value of 86.66^o. This kind of local strain could influence the converse piezoelectric response. The spontaneous strain can be directly estimated from the tetragonal splitting and defines the maximum achievable strain in the corresponding system. Therefore, the long range polar ordering have been found to decrease monotonously with the decrease in the grain size as evident from the decrease in the tetragonality[356] at higher values of *x*. Interestingly, the piezoelectric response increases up to a certain extent with the increase in the value of x and then drops (Fig. 7.1(a), (c) and (e)) exhibiting a trend that is different than that of the monotonous reduction in the long range polar ordering (Figs. 7.4) and reduction in tolerance factor (Fig. 7.2). However, the increased degree of local polar distortions was observed in PDF and Raman spectroscopic analysis. Despite presence of polar character at local length scales, systems with smaller grain size exhibit almost negligible piezoelectric response due to geometric restrictions imposed on domain wall mobility as explained earlier. Therefore, along with the increase in the local polar distortion enhanced domain wall mobility plays an important role in imparting superior functional response to a piezoelectric system. This high piezoelectric response could be attributed to the decreased activation energy (Fig. 7.15(d)) of the domain switching, the high nano domain density and the local polar distortions arising from the higher mobility as observed in PFM switching results (Fig. 7.13). As explained in the next section, domain broadening has an enormous effect on the mobility of the domain walls eventually leading to high piezoelectric response. At some critical grain size, grain boundary starts impeding the domain wall motion reducing the macroscopic functional response of the system. However, the

polar distortion at local length scales still persists in these systems. The effect of these elemental modifications on the phase transition and ferroelectric properties is investigated in next section.

7.3.6 Ferroelectric properties and phase transitions

In order to understand the nature of the ferroelectric phase transition, the temperature dependence of the relative permittivity plots were recorded. Figure-7.14 shows the temperature dependence of the relative permittivity and the loss tangent at 1 kHz for various compositions. It can be observed that with the increase in the values of x for all specimens, the *Curie* temperature (T_c) decreases and the *Curie* peak gets smeared reflecting an increasing diffuse nature of the phase transitions (DPT). However, the rate of shift of the Curie temperature towards RT is higher in case of BT-xCCN in comparison to BT-xBCN and BT-xSCN series. Moreover, the Curie peaks in case of BT-*x*BCN specimens are comparatively sharper than those of the compounds having same value of x in BT-*x*SCN and BT-*x*CCN series. The substitutions of Sr^{2+} and Ca^{2+} on the Ba-sites does not appear to favor long range ordering the tetragonality as discussed in the previous sections.

The diffuse nature of the phase transition can be attributed to a perturbed localized dynamics and polar structural distortions of the octahedra due to the substitution on the A- and B-sites as discussed in PDF, Raman spectra and EPR analysis. The state of systems with lower T_c could be understood in analogy with the state of systems at temperature closer to T_c. As the composition of BT in the solid solution approaches some critical value of x, titanium ion is expected to move in a shallower potential well. Therefore, any displacement from the center of this well results in a large displacement once a number of adjacent moments are pointed in the same direction by external stimuli. A local field of the Mosotti type increases the polarization and displaces the potential minimum towards one of the oxygen ion [357].This phenomenon is

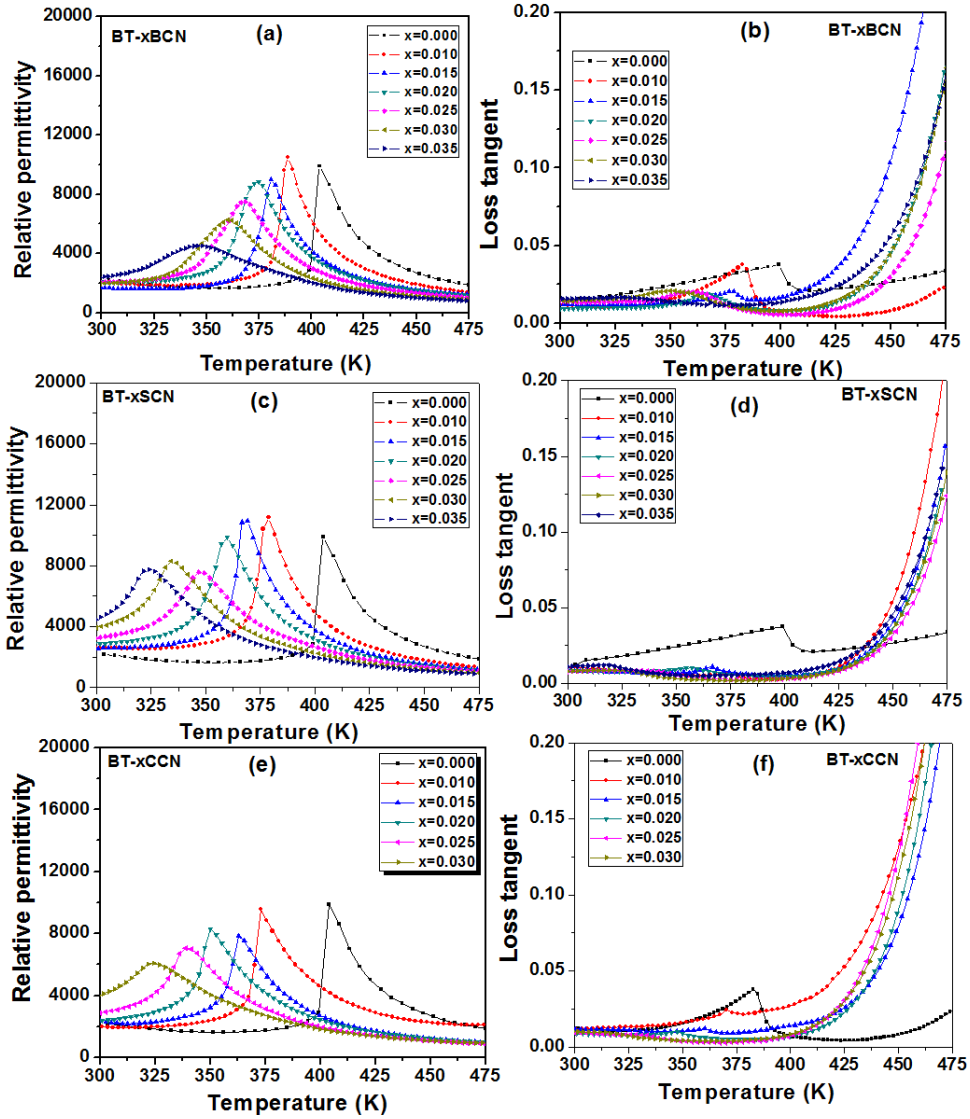

Figure -7.14: Temperature dependence of dielectric response at 1 kHz for various compositions of BT-xACN with A as (a-b) Ba, (c-d) Sr,(e-f) Ca.

supported by the PDF results where the increase in the polar distortions could be observed in case of BT-*x*BCN specimens (Fig. 7.6). The shallower potential well reduces the activation energy ΔF for polarization switching with increased domain mobility imparting higher functional response to the system as shown in PFM switching results. However, for heavily doped

compositions, ΔF becomes negligible i.e there is no macroscopic switchable polarization (Figure-7.15(d)) and the system acquires a center of symmetry.

The local field of the Massotti type could be given as: $E^{loc} = (\gamma/3\varepsilon_o)P$, where P is the polarization, γ is the Lorentz factor, ε_o is the permittivity of free space. Suppose, the ionic polarizability of ion Ti is α, the dipole moment of the unit cell of this system could be given as[1]: $\mu = (\alpha\gamma/3\varepsilon_o)P$. The total energy of this dipole moment (dipole – dipole coupling) for N number of dipoles can be written as: $F_{dip} = Nw_{dip} = -N\mu.E^{loc} = -(N\alpha\gamma^2/3\varepsilon_o^2)P^2$. For the sake of brevity, the increased elastic energy due to the displacement of the B-site ions from their equilibrium positions can be given as [358]:

$$F_{elas} = N[\left(\frac{k}{2}\right)u^2 + \left(\frac{k'}{4}\right)u^4] \quad (7.5)$$

where 'u' is the displacement, k and k' are force constants. k' (higher order force constant) assumes positive value. Substituting $P = Nqu$ in the above equation leads to:

$$F_{elas} = \left(\frac{k}{2Nq^2}\right)P^2 + \left(\frac{k'}{4N^3q^4}\right)P^4 \quad (7.6)$$

Therefore, the total energy of the system could be given as:

$$F_{total} = F_{dip} + F_{elas} = \left[\left(\frac{k}{2Nq^2}\right) - \left(\frac{N\alpha\gamma^2}{9\varepsilon_o^2}\right)\right]P^2 + [\frac{k'}{4N^3q^4}]P^4 \quad (7.7)$$

The schematic representation of F_{dip} and F_{elas} and F_{total} is given in Figure- 7.15 (a)-(c). The two minima of potential depict the two states of switchable polarization. Figure 7.15(d) shows the schematic variation in the potential well with respect to the change in composition. The coefficient of P^2 in equation (7.7) is related to the Curie –Weiss law as:

$$\left[\left(\frac{k}{2Nq^2}\right) - \left(\frac{N\alpha\gamma^2}{9\varepsilon_o^2}\right)\right] = \frac{(T-T_c)}{\varepsilon_o C} = \frac{1}{\varepsilon_o \varepsilon} = a \qquad (7.8)$$

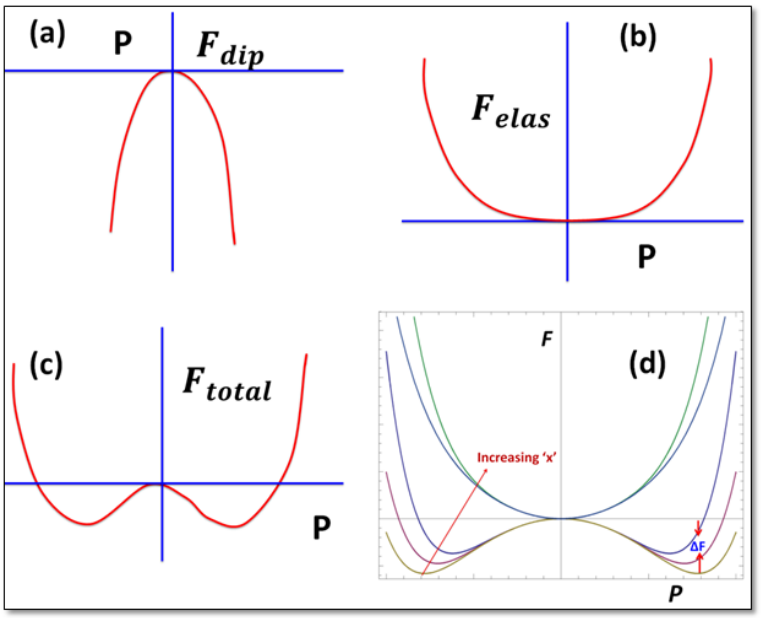

Figure -7.15 The schematic of potential well for (a) dipolar energy F_{dip}, (b), elastic energy F_{elas}, (c) total energy $F_{total} = F_{dip} + F_{elas}$. (d) Schematic of variation in potential wells of total energy for different compositions. As the T_c decreases with the change in composition (x) the potential well becomes shallow depicting the decrease in activation energy for polarization switching.

Figure-7.16 (a), (c) and (e) show the temperature dependence of the inverse relative permittivity at 1 kHz for all compositions. The value of the coefficient 'a' in equation (8) was calculated from the temperature dependence of the inverse relative permittivity for all compositions (Table-7.2). The coefficient '*a*', Curie constant (C) and Curie temperature (T_c) were calculated by fitting the linear regions in the data sets. The Curie Constant (*C*) of pure $BaTiO_3$ varies over a broad range: $C=1.56\times10^5$ K and $C=1.73\times10^5$ K. In the present case it was calculated to be $C = 1.59\times10^5$ K (Table -7.2). As can be seen from the values listed in this table the coefficient 'a' is initially positive and then becomes negative. The negative value of the

Table-7.2 Various parameters calculated from temperature dependence of permittivity plots at 1 kHz

Sample	T_c (K)	T (K)	Curie constant (C)	$a=(T-T_c)/\varepsilon_o C$	Critical exponent (n)
BT-xBCN					
x=0.000	393	403	1.59×10^5	7.4×10^6	1.08
x=0.01	386	388	1.26×10^5	1.28×10^6	1.14
x=0.015	370	381	1.23×10^5	9.92×10^6	1.15
x=0.020	369	375	1.22×10^5	5.01×10^6	1.19
x=0.025	363	366	1.15×10^5	2.73×10^6	1.26
x=0.030	358	360	1.04×10^5	1.90×10^6	1.27
x=0.035	352	345	9.99×10^4	-7.92×10^6	1.48
BT-xSCN					
x=0.01	375	378	1.37×10^5	2.4×10^6	1.1
x=0.015	370	371	1.34×10^5	1.2×10^6	1.17
x=0.020	362	359	1.31×10^5	-2.1×10^6	1.3
x=0.025	354	346	1.29×10^5	-6.7×10^6	1.33
x=0.030	348	334	1.24×10^5	-12.7×10^6	1.36
x=0.035	340	324	1.21×10^5	-15.3×10^6	1.39
BT-xCCN					
x=0.010	365	372	3.65×10^5	5.3×10^6	1.14
x=0.015	357	363	1.23×10^5	5.9×10^6	1.26
x=0.020	348	350	1.18×10^5	9.5×10^6	1.28
x=0.025	341	339	1.14×10^5	-1.8×10^6	1.34
x=0.030	326	324	1.10×10^5	-2.0×10^6	1.46

coefficient ‘a’ indicates that the system is not in a true paraelectric state and so the Curie –Weiss law for a classical ferroelectric is not valid. The expression in the parenthesis on the left hand

side of equation (7.8) suggests that as the polarizabilty of the B-site ions increases with decreasing temperature, this term can assume negative value leading to a ferroelectric phase transition for the system. In the present case, the B-site is substituted by Cu^{2+} and Nb^{5+} (with different ionic radii and electronegativity) and, therefore, the localized regions or polar nano regions with different ions would behave differently i.e. the system would exhibit different Curie points for the different localized regions resulting DPT as discussed in the previously. The Lorentz factor would also assume different value for various compositions due to change in crystal structure. Also, the local environment as seen by PDF, Raman scattering and EPR is perturbed from the A-site substitutions that could also contribute towards the phase transition behavior, including increasing its diffuse nature. These localized polar regions or nano domains increase the domain /dipole density. However, in present case, the value of 'a' with respect to the change in the composition was investigated and its negative value could be due to the increased number of dipoles per unit volume (*N*) i.e. high density of dipoles. The diffuseness of the phase transition of a ferroelectric could be modeled using a modified Curie-Weiss law [1]:

$$\frac{1}{\varepsilon} - \frac{1}{\varepsilon_m} = \frac{(T-T_m)^n}{C_1} \tag{7.9}$$

where, n (critical exponent) is the degree of relaxation, $1<n>2$ and C_1 was assumed to be constant, T_m is the temperature corresponding to the maximum relative permittivity (ε_m). The limiting values of n = 1 and n = 2 reduce the expression to the Curie –Weiss law valid for the case of classical ferroelectric and to the quadratic dependence valid for an ideal relaxor

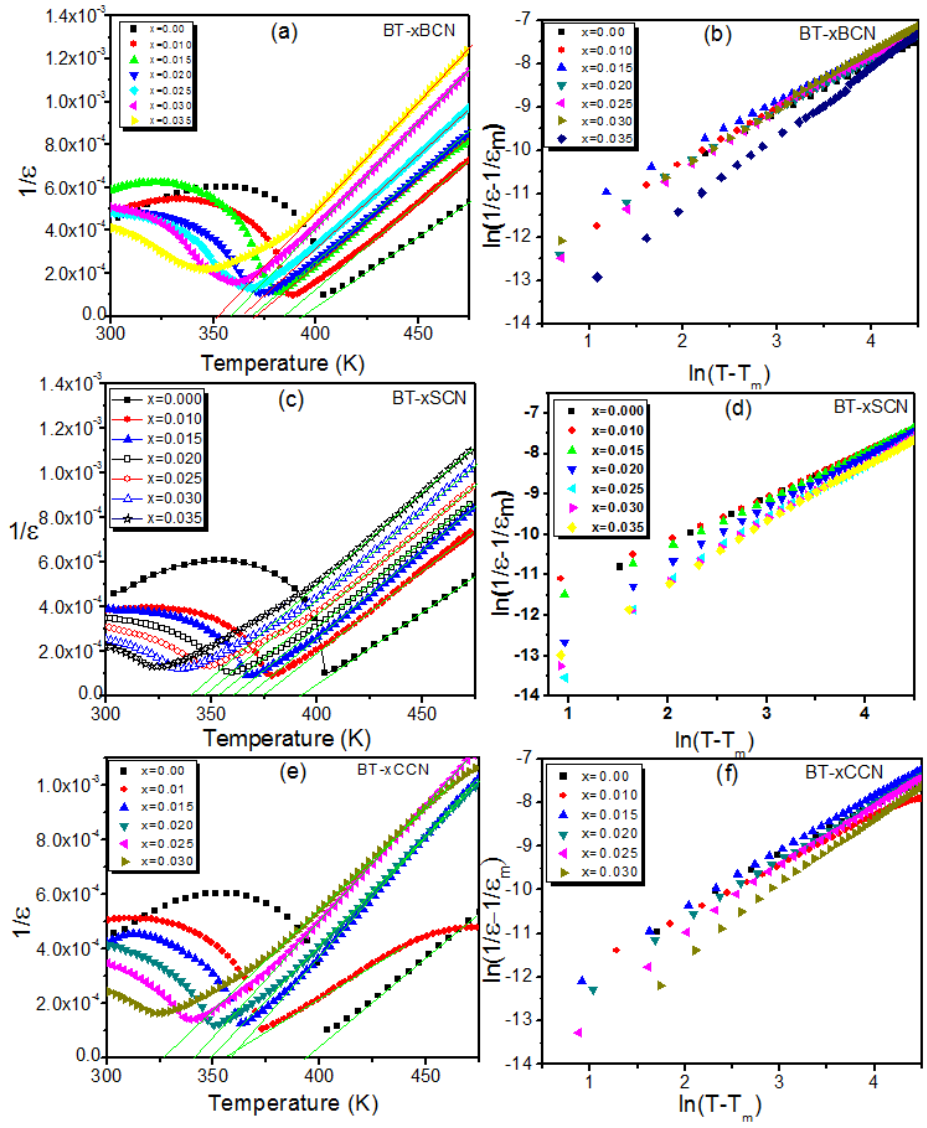

Figure -7.16: Temperature dependence of inverse relative permittivity (1/ε) at 1 kHz for various compositions of BT-*x*ACN with A as (a) Ba, (c) Sr and (e)Ca. The ln(1/ε -1/ ε m) versus ln(T-Tm) plots for various compositions of BT-*x*ACN with A as(b) Ba, (d) Sr and (f)Ca.

ferroelectric, respectively[1]. The values of n' obtained by fitting curves to the data sets in Figure 7.16(b), (d) and (f) are summarized in Table 7.2. It can be seen that in all cases with the increase in the value of x, the Curie temperature decreases and the Curie peak becomes diffuse resulting in a monotonous increase in the value of the critical exponent (n). The ferroelectric-paraelectric transition in these systems is characterized not by an abrupt structural transition, but rather by a

gradual, diffuse transition which occurs over a temperature range i.e. also known as a Curie range. The diffuse nature of phase transition is the outcome of local polar structural distortions and miniaturized domains states. Figure-7.17(a) shows the variation of the difference in the permittivity at T_m and RT for various compositions of BT-*x*SCN at 1 kHz. This difference decreases for the highly doped specimens indicating a decrease in ε_m (the maximum value of relative permittivity at the ferroelectric phase transition) and an increase in ε_{RT} (relative permittivity at room temperature). The relative permittivity (ε_{33}) of poled specimen (Fig. 7.1(b), (d) and (f)) was also found to increase monotonously with the increase in the value of x for BT-xACN, which could be attributed to the internal stress and increased domain wall density as well as lattice instability due to the lower T_c [Ref.359]. Moreover in Fig. 7.14, the maximum value of the relative permittivity at the transition temperatures was found to decrease along with increased broadening of Curie peak as a result of increased local disorder due to elemental substitutions. The systems with higher substitutions were also found to exhibit almost monotonous decrease in the grain size, long range ordering, Curie temperature (T_c) and increased local polar distortions as explained earlier.

Figure-7.17(b) shows *P-E* hysteresis at 10 Hz using bipolar triangular signal for all compositions of (1-x)$BaTiO_3$-x$Sr(Cu_{1/3}Nb_{2/3})O_3$. The inset of this plot shows well saturated *P-E* hysteresis loops of pure $BaTiO_3$ having macro-size ferroelectric domains (Fig. 7.18). The high remnant polarization reflects the cooperative nature of the ferroelectricity in $BaTiO_3$. Also, with the increase in the value of x, the remnant polarization and coercive field decrease, and the system starts showing relaxor-type slim *P-E* loops. The asymmetric shape of *P-E* loops could be attributed to polar defects and defect complexes created by the aliovalent doping on the B-sites

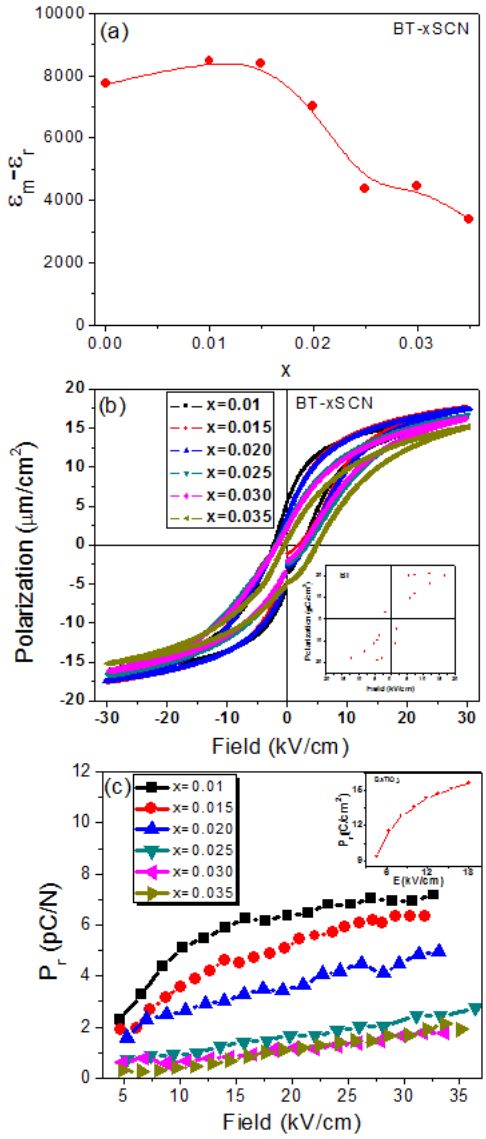

Figure-7.17: (a) Variation in difference of relative permittivity at T_c and RT with respect to change in composition of BT-*x*SCN, (b) *P*-*E* hysteresis loop of BT-*x*SCN at 10 Hz, Inset is showing *PE*-hysteresis loop of pure $BaTiO_3$, (c) remnant polarization (P_r) as a function of maximum applied electric field (E) at 10 Hz, Inset is showing electric field dependence of P_r for pure $BaTiO_3$.

as explained earlier by invoking defect chemistry. The shifting of the *P*-*E* loops on the x-axis indicates a presence of internal bias due to the presence of polar defects. Figure 7.17(c) shows remnant polarization as a function of the maximum applied electric field for BT-*x*SCN. The inset of this figure shows the remnant polarization (P_r) vs. electric field (E) plot for pure $BaTiO_3$.

These plots show that for the BT-*x*SCN specimens having higher value of x, the remnant values change linearly with the applied electric field. The compositions with the higher values of x exhibit relaxor-like slim hysteresis loops characteristic of materials having miniaturized domains and local polar regions, which, under the application of high electric field, can be oriented resulting in a large polarization. After removing the field, the majority of polar regions retrace their original orientation giving rise to a weaker remnant polarization (Fig. 7.17(c)). The defect structure substantially modulates the hysteresis behavior playing an important role in providing enhanced functional response of the system and contribute to the DPT in ε(T) plots.

7.3.7 Domain size – defect chemistry – ferroelectric property relationships

As the system cools down from high temperature cubic to ferroelectric tetragonal phase, formation of domains takes place to accommodate stress. The equilibrium size of the domain structure is governed by minimization of the total energy of the system. However, the domain structure is substantially influenced by the nature of defect distribution as well. Defects influence the minimum domain size that is comparable to the average distance between the defects. On the other hand, weakly interacting defects set the size of the fluctuation of the defect concentration. In either case, the domain size (nano domains) is significantly smaller than that of the mean equilibrium width of the domains (macro domains) in a perfect system like pure $BaTiO_3$. The bright field TEM image of macro-sized domains of pure $BaTiO_3$ is depicted in Figure –7.18(a) and (b) with the electron beam coming down from [111] zone axis obtained by indexing SAED (Fig. 7.18(c)) corresponding to the same area.

The formation of a nano-domain structure has been especially found to be associated with polar defects. Near the Curie point the structure of ferroelectrics becomes extremely susceptible

to external stimuli. Defect dipole contribute towards polarization of the lattice and induce a chaotic distribution of electric fields (E_d) resulting in local region with different contrast or nano polar regions as evident in HR-TEM image of BT-0.02SCN with (111) zone axis (Figure 7.19(a)-(b)). The zone axis was obtained by indexing the fast Fourier transform (FFT) pattern (shown in the inset) corresponding to Fig. 7.19 (a). These local regions with different contrast can be clearly seen in inverse fast Fourier filtered images (IFFT) shown in Fig. 7.19(b). The presence of an internal field due to polar defect structure is evident from the translation of the

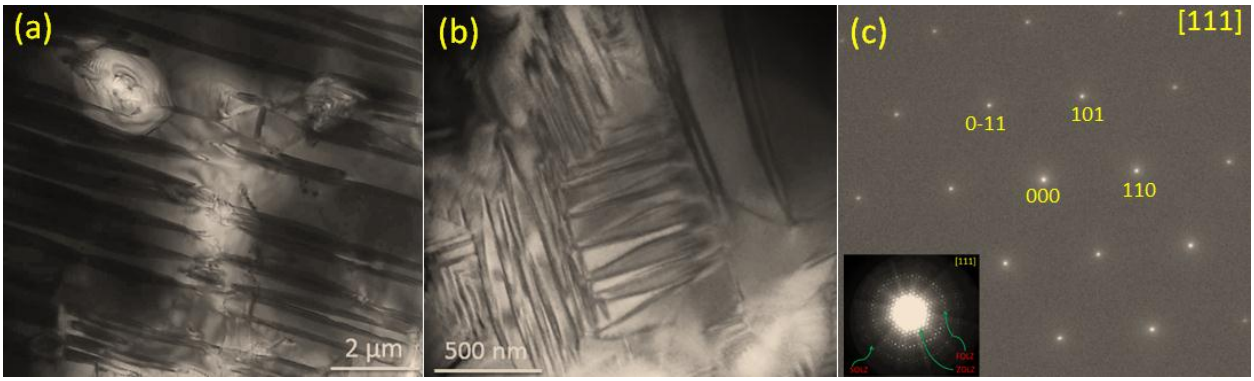

Figure-7.18 (a)-(b) Bright field TEM images of domains in BaTiO3, (c) SAED corresponding to the area presented in (a) and (b). The inset of figure 7.18 (c) shows the higher order diffraction from the same area.

PE-hysteresis loops on the *x*-axis (Fig. 7.17(b)) as explained in previous section. Furthermore, in the case of systems with T_c closer to RT, the domain structure is not homogeneous due to finite interaction with the defects. The decrease in temperature rapidly increases the domain wall energy $\sim(\Delta T)^{3/2}$ (ΔT is the distance from Curie point) in comparison with the temperature dependence of volume energy $\sim E_d P \sim(\Delta T)^{1/2}$[Ref.360], which in turn yields formation of domains on defects. These two energies compete with each other. In case these energies are equal [360]: $\gamma = 2PE_d d$, the domain structure loses its stability. In such systems, the interaction of the domain boundary with defects of the crystalline lattice results in a deformation of its shape and, consequ-

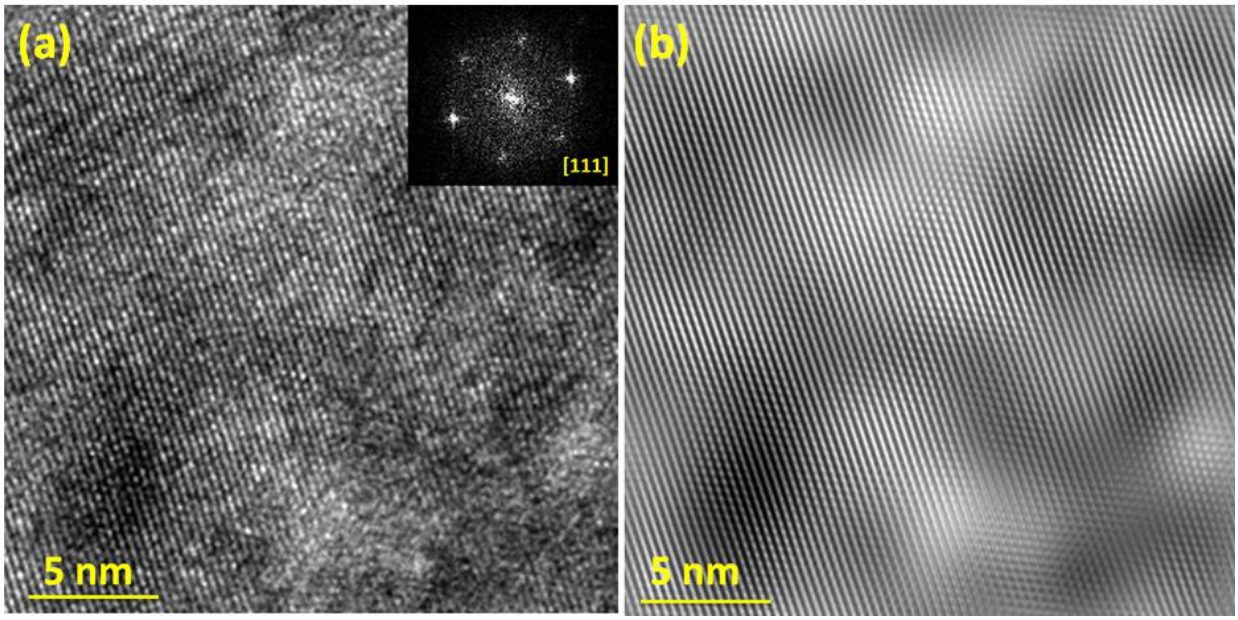

Figure 7.19 (a) The HR-TEM image of lattice fringes of BT-0.025SCN depicting contrast change due to presence of defects, the inset is depicting FFT pattern corresponding to rectangular region. (b) Depicts inverse fast Fourier transform image of (a).

-ently, as in the case of thermo-fluctuations on the profile of domain wall, the effective thickness of the transition layer between the domains increases. Also, the interaction of domain walls with crystal defect leads to a domain wall broadening. The velocity of lateral motion of domain walls depends on various parameters [360]:

$$v = v_{\infty}\exp\{-w\ exp\left\{-\frac{3\pi^2\delta}{4a}\right\}\} \qquad (7.10)$$

$$\text{with , } w = 2(\gamma a^2)(\varepsilon)^{-\frac{1}{2}}T^{-1}(8\pi^4\gamma)^{\frac{3}{4}}(\delta/a)^{9/4}E^{-1}$$

where, γ is the surface energy of the domain wall, δ domain wall width, a is the size of elementary cell, ε is the permittivity, T is the temperature and E is the applied field. Equation (7.10) shows that the velocity of domain wall in the given regime very strongly depends on its width (a functional dependence of exponent in exponent). Therefore, even a relatively small increase in the width of the walls results in a considerable increase in the velocity of the wall v

resulting in an enhanced piezoelectric response of the system. The increased ease of domain switching for BT-0.025BCN was clearly observed in PFM switching results (Fig. 7.13) as explained earlier.

The domain structure was investigated using HR-TEM. For this purpose, two compositions (1-x)$BaTiO_3$-x$Sr(Cu_{1/3}Nb_{2/3})O_3$, x=0.020 and (1-x)$BaTiO_3$-x$Ba(Cu_{1/3}Nb_{2/3})O_3$, x=0.025 having high piezoelectric response were selected. Figures 7.20 (a) and 7.21 (a) show TEM images of the domain structures at nano scale. Figures 7.20(b) and 7.21(b) show lattice fringes across the domains and the corresponding fast Fourier transform (FFT) patterns are indexed with $[1\bar{1}0]$ and [111] zone axis in Fig. 7.20(c) and 7.21(c), respectively. The splitting of the diffraction spots in FFT (Fig. 7.20(c)) shows an existence of nano twins with small mutual misorientation. The broad domain walls as marked in Figs 7.20(b) and 7.21(b) can be observed in both systems. The width of domain walls considerably perturbs the domain wall mobility. For the sake of clarity, inverse fast Fourier transform (IFFT) images are provided in Figs. 7.20(d) and 7.21(d). These images clearly indicate broadened domain walls, and the degree of broadening is approximately similar for both systems. The higher domain wall width and the nano size of the domains give rise to high piezoelectric response in corresponding systems. These nano domains also play an important role in the onset of a relaxor-like diffuse phase transition.

Thus, the substitutions on A-site and B-site result in local polar distortions up to certain extent despite monotonous decrease in long range ordering. The increased piezoelectric instability in BT-*x*ACN with the change in composition (x) is supported by the increase in local polar distortions and change in phonon instability. Moreover, the aliovalent elemental substitution results in formation of defect complexes and polar defects giving rise to the presence of internal bias fields modulating the ferroelectric hysteresis behavior. The polar defects due to

elemental substitutions substantially change domain structure giving rise to the formation of nano domains with varying domains wall width and higher mobility resulting in enhanced piezoelectric response in the specimen. The local structural distortions and miniaturized domain structure results in relaxor-like diffuse phase transition and enhanced functional response. Presence of point defects due to aliovalent substitution also inhibits the grain boundary mobility resulting in reduced grain size in modified BT systems. However at certain small size due to geometrical restrictions, domain mobility is reduced exhibiting reduction in piezoelectric response in the corresponding system. Therefore to achieve enhanced functional response in a piezoelectric system, enhanced structural polar distortion and higher domain wall mobility are equally important factors.

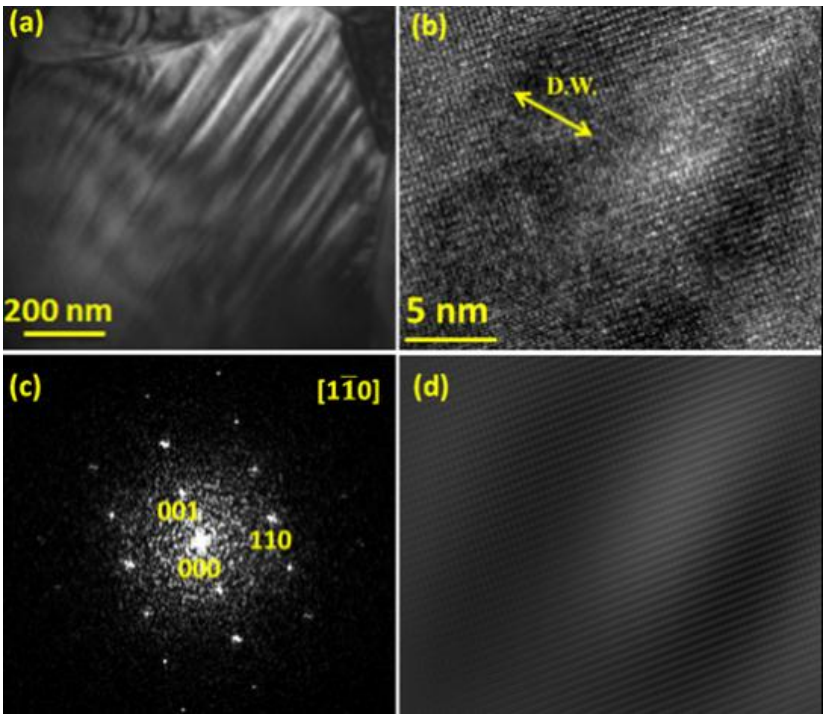

Figure-7.20 (a) TEM image of BT-xSCN with x = 0.02, (b) HR-TEM image of lattice fringes across domains, the arrows marked shows broad domain wall, (c) FFT pattern corresponding to lattice fringes depicted in (a), (d) Inverse fast forier transform (IFFT) of (b) clearly depicting domain wall.

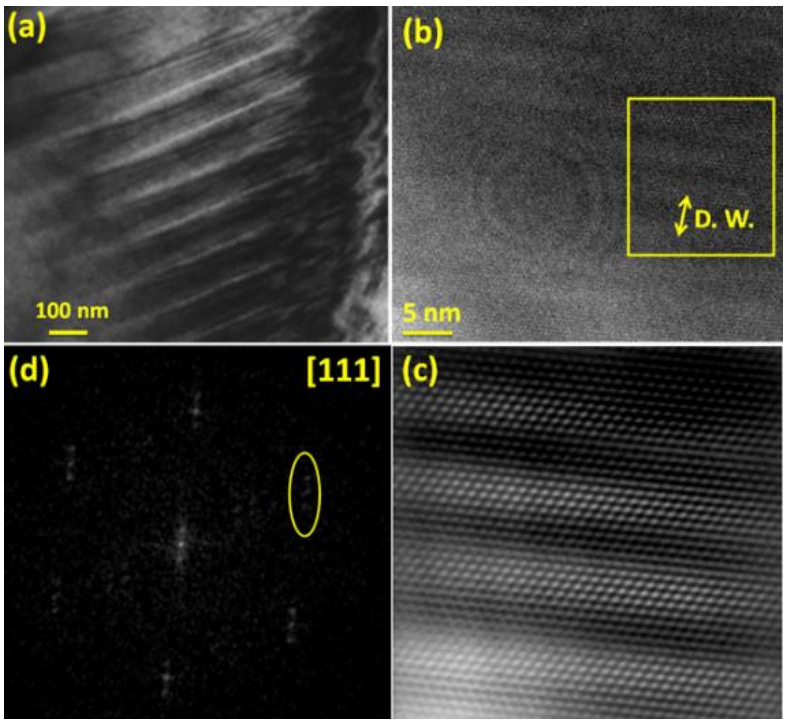

Figure-7.21(a) TEM image of BT-*x*BCN with x = 0.025, (b) HR-TEM image of lattice fringes across domains, the arrows marked shows broad domain wall, (c) FFT pattern corresponding to lattice fringes depicted in rectangular box marked in (a), triple spots encircled depict presence of nano twins, (d) magnified view of IFFT of the area in rectangular box clearly depicting domain wall.

7.4 Chapter summary

Series of new lead-free piezoelectric (1-x) $BaTiO_3$-x$A(Cu_{1/3}Nb_{2/3})O_3$ (A: Sr, Ba and Ca) ceramics were developed. The piezoelectric instability in these compositions was found to increase with the increase in the value of x up to certain extent and then drop. Interestingly, long range polar ordering was found to decrease monotonously with the increase in the value of x suggesting that the origin of the enhanced piezoelectric instability is not a simple function of the long range polar ordering. Instead it may be associated with localized polar distortions. High energy x-ray diffraction coupled with atomic PDFs analysis suggests increased polar nature and

well explains the enhanced piezoelectric instability. Raman scattering studies revealed that not only substitution of Cu^{2+} and Nb^{5+} on the Ti^{4+}-sites but also substitution of Sr^{2+} and Ca^{2+} on the Ba^{2+} -sites substantially modifies the octahedral dynamics as well as significantly distorts the octahedral cage resulting in localized distorted regions of lower symmetry, in line with the atomic PDFs results. The high temperature stability of high frequency Raman modes suggests that these local polar regions exist well above the Curie temperature. Electron paramagnetic resonance (EPR) spectroscopy confirms that Cu^{2+} occupies distorted octahedral sites thus creating oxygen vacancies to maintain charge neutrality. The EPR spectra also suggest that the A-site substitution of Sr^{2+} and Ca^{2+} substantially changes the crystal field surrounding the Cu^{2+} ions. This substitution results in the formation of defect dipoles $(Cu''_{Ti} - V_o^{\bullet\bullet})^{\times}$ oriented along the c-axis of the perovskite lattice inducing strong internal bias that translates the PE-hysteresis loop on the *E-field* axis. The local defect structure substantially modulates the domain structure resulting in nano domains with broad walls with higher domain mobility, which has been considered to be a key factor in imparting enhanced piezoelectric response to the systems studied here. The presence of nano domains and local structural distortions induce diffuse phase transitions indicating a subsidence of the long range polar ordering.

The piezoelectric instability follows well the local polar distortions that enhance it. However, after certain extent of modification the macroscopic functional response is suppressed due to confinement of the domain walls within the geometrical restrictions of the grain boundaries, though sufficient strong polar distortions still persists locally.

Chapter-8

High dielectric composition in the system Sn – modified (1-x)$BaTiO_3$-x$Ba(Cu_{1/3}Nb_{2/3})O_3$, x = 0.025 for multilayer ceramic capacitors[f]

This chapter deals with the synthesis and characterization of $BaTiO_3$ (BT) based high dielectric compositions that are promising for Y5V type multilayer ceramic capacitors (MLCCs). Solid solution with nominal composition (1-x)$BaTiO_3$-x$Ba(Cu_{1/3}Nb_{2/3})O_3$ (BCN) (x = 0, 0.025) was synthesized by conventional mixed oxide route, followed by compositional modification with varying concentration of Sn, as given by the formulation: 0.975 $BaTi_{1-y}Sn_yO_3$ – 0.025 $Ba(Cu_{1/3}Nb_{2/3})O_3$ (y = 0.05, 0.06, 0.075, 0.1). Room temperature XRD patterns showed decrease in tetragonality of BT after modifying with BCN (BTBCN). Modifications with Sn lead to further decrement in tetragonality and the room temperature structure became cubic at 6.0 at% doping level. The decrement in tetragonality was accompanied by lowering of Curie temperature (T_c). BTBCN doped with 6 and 7.5 at% Sn were found to exhibit diffuse phase transition accompanied by high dielectric constant ≥ 7000, low loss tangent ≤ 1% and grain size in the submicron regime (≤ 1 μm).

8.1 Background

Multilayer ceramic capacitor (MLCC) technologies require continuous development of high dielectric constant material in order to meet the growing demand of miniaturization, high volume efficiency, lifecycle, and low cost[361]. In order to meet these requirements, thickness of each layer is a critical factor. Dielectric layers less than 3μm thickness require sub-micron grain

[f] Reproduced with permission from [57]. Copyright 2010, the American Ceramic Society

size with good densification [361,362].Modified barium titanate compositions are widely used in MLCCs due to their high dielectric constant and low loss [9]. To exemplify, $BaTiO_3$–$CaZrO_3$ ceramics have been used for Y5V-type MLCC exhibiting a large magnitude of dielectric constant (ε_r) of 15,000 (EIA code[363]: $-82\% < \Delta\varepsilon_{r(T-25\ ^\circ C)}/\varepsilon_{r(25\ ^\circ C)} < 22\%$ in the temperature range from −30 to 85°C). However, these compositions have large grain sizes (>3.0 μm) restraining them for being used in MLCCs with thinner layers [361,364,365] Generally, $BaTiO_3$ (BT) is modified by doping rare earths and MgO to achieve smaller grain sizes ranging from 0.2 – 0.4 μm as in X7R-type capacitors (EIA code [363]: $-15\% < \Delta\varepsilon_{r(T-25\ ^\circ C)}/\varepsilon_{r(25\ ^\circ C)} < 15\%$ in the temperature range from −55 to 125°C). However, these compositions are characterized by small magnitude of dielectric constant (2000–4000) and hence not very efficient for next generation MLCCs requiring ultrahigh capacitance [365-367] and high volume efficiency. Various attempts have been made to synthesize dielectrics with smaller grain sizes using diverse processing methods [368-372] but there has been limited success in achieving large relative permittivity with smaller grain sizes. Prior research has shown that Sn doping not only results in lowering of Curie temperature but also induces diffuse phase transition[9,373-377]. Both these characteristics can be exploited in tailoring the dielectric response of ceramics suitable for MLCCs. Further, the magnitude of dielectric constant in these prior studies was found to lie in the range of 5000 – 7000 and loss tangent factor between 2 – 5% around room temperature. However, the details on grain size and temperature coefficient of capacitance (TCC) were not provided which restricts the ability to quantify the suitability of these compositions for MLCCs.

In present study, the composition 0.975 $BaTiO_3$ – 0.025 $Ba(Cu_{1/3}Nb_{2/3})O_3$ exhibits ferroelectric – paraelectric (FE-PE) transition at 80^{o}C, while the microstructure shwos significantly small grain size. FE-PE transition was further shifted towards room temperature

(RT) by modification with Sn, while at the same time enhancing the diffuseness in phase transition. In this chapter, the Sn-modified compositions in the system 0.975 $BaTi_{1-y}Sn_yO_3$ – 0.025 $Ba(Cu_{1/3}Nb_{2/3})O_3$ exhibits dielectric constant higher than 7000, dielectric loss factor less than 1%, grain size less than 1 μm and TCC suitable for Y5V type MLCCs.

8.2 Experimental

(1-x)$BaTiO_3$ – x$Ba(Cu_{1/3}Nb_{2/3})O_3$ (x = 0.0, and 0.025; BT and BTBCN) ceramics were synthesized using conventional mixed oxide processing method. Stoichiometric concentrations of CuO (Alfa Aesar, 99.0%), TiO_2 (Alfa Aesar, 99.5%), Nb_2O_5 (Alfa Aesar, 99.5 %) and $BaCO_3$ (Alfa Aesar, 99.8 %) were mixed by ball milling for 24h with ZrO_2 balls in polyethylene bottle and calcined in the range of 800 – 1000^oC for 2h. Calcined powder was again ball milled, pelletized, and sintered at 1350^oC for 2h. In order to synthesize Sn-doped 0.975$BaTi_{1-y}Sn_yO_3$-0.025$Ba(Cu_{1/3}Nb_{2/3})O_3$ ceramics (y = 0.05, 0.06 0.075, 0.1; denoted as SBTBCN-1, SBTBCN-2, SBTBCN-3, SBTBCN-4); stoichiometric concentration of SnO_2 (Alfa Aesar, >99%) was added to the base matrix before first ball milling. Thermal etching was performed at 1250 ^oC for 15 min on all specimens used for microscopy and subsequently the average grain size was calculated by line intercept method. For electrical and piezoelectric measurements, silver paste was applied on flat surfaces of sintered and polished ceramic disks (diameter ~ 10.28 mm, thickness ~ 1.0 mm) and fired at 650^oC. These samples were poled at 3-4 kV/mm for 1h at room temperature (RT). The d_{33} values were measured using d_{33}-meter and resonance response was measured by using HP 4194A impedance analyzer. Dielectric constant and tangent loss factor were determined as a function of temperature at selected frequencies using an inductance-capacitance-resistance (LCR) meter (HP 4284A), connected to a computer controlled high temperature furnace. P-E (polarization vs. field) measurements were made using a modified Sawyer-Tower bridge. This

system was computer controlled and capable of automatic determinations of standard P-E measurement compensation parameters.

8.3 Results and discussion

8.3.1 X-ray diffraction and SEM analysis:

Figure 8.1 shows the XRD patterns for all synthesized compositions measured at RT using Philips Xpert Pro X-ray diffraction system. These XRD patterns were measured on powders obtained after crushing the unpoled sintered ceramic pellets. There was no trace of secondary peak suggesting the formation of homogeneous solid solution for all the compositions with perovskite phase. The inset of Fig. 8.1 shows that (200) and (002) peaks merged into a broad symmetrical peak after modification with BCN, indicating decrease in tetragonality (c/a ratio). Modification of BTBCN with Sn further decreased the tetragonality as observed by continued reduction of the FWHM (full width of half maxima) for SBTBCN-2, SBTBCN-3 and SBTBCN-4, showing cubic symmetry. For SBTBCN-1, one can still notice minor splitting in the (200) peak suggesting very low tetragonality at RT. The magnitude of c/a ratio was calculated from XRD patterns shown in Fig. 8.1 for BT, BTBCN and SBTBCN-1 and found to be 1.010, 1.004, 1.002 respectively, displaying decrease in tetragonality upon modification with BCN and Sn.

Figure 8.2(a)-(d) shows the SEM images measured on thermally etched sintered samples using LEO Zeiss 1550 microscope. Dense microstructure was obtained in all the cases and samples exhibited ≥ 95% theoretical density measured using Archimedes principle. It was found that sintered BTBCN had grain size on the order of ~1 μm, which is much smaller than that observed for pure $BaTiO_3$ ~28μm under identical sintering conditions. The occupancy of Nb^{5+} on

Ti^{4+} site will result in the formation of metal vacancies as preferred ionic compensation mechanism[378]. However, occupancy of Cu^{2+} on Ti-site will result in formation of oxygen vacancies in order to maintain the charge electroneutrality[379]. It is suspected that the segregation of these vacancies on the grain boundaries inhibits the grain coarsening phenomena resulting in smaller grain size for BTBCN. Modification with Sn further decreases the grain size to submicron regime and the grain sizes for SBTBCN-1, SBTBCN-2, SBTBCN-3 and SBTBCN-4 were found to be 0.93, 0.85, 0.74 and 0.37 μm, respectively**.**

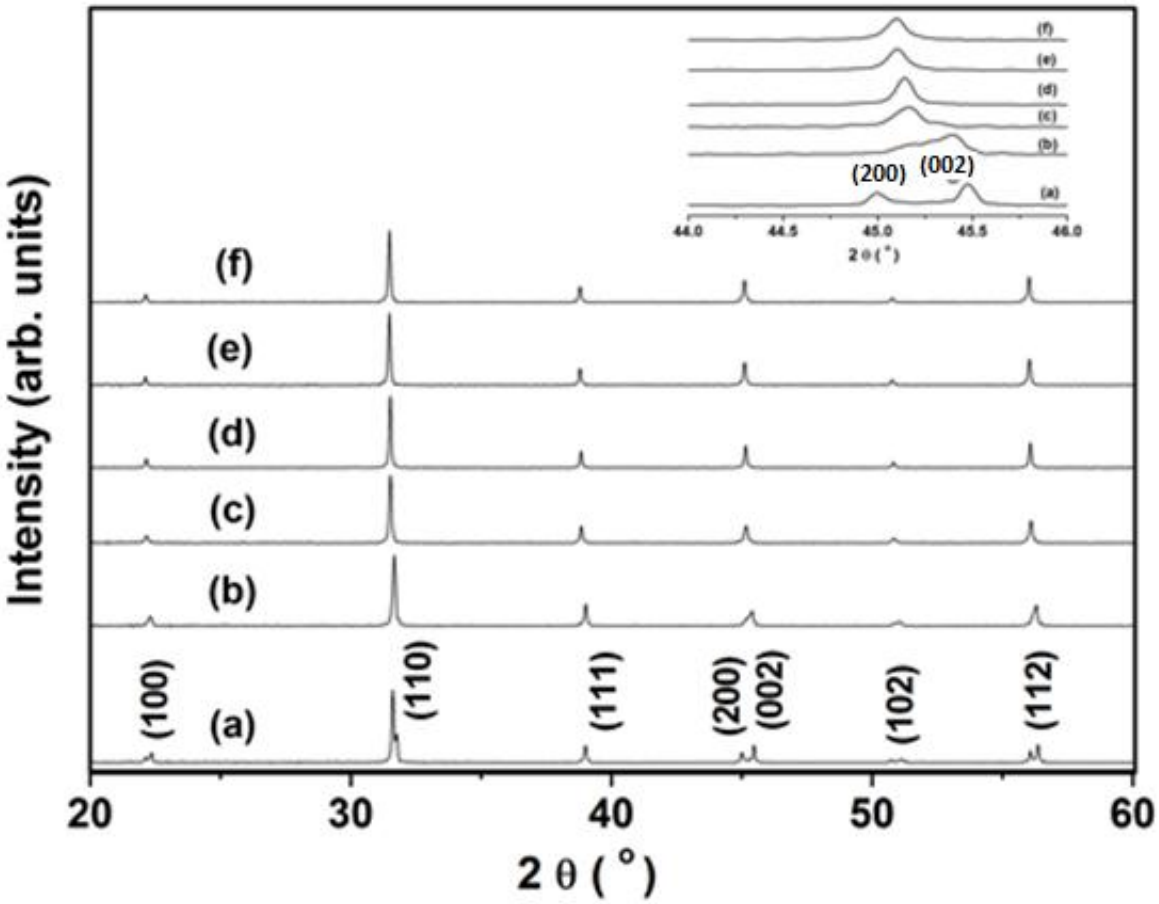

Figure 8.1- Room temperature XRD patterns for: (a) BT, (b) BTBCN, (c) SBTBCN-1, (d) SBTBCN-2, and (e) SBTBCN-3 (f) SBTBCN-4

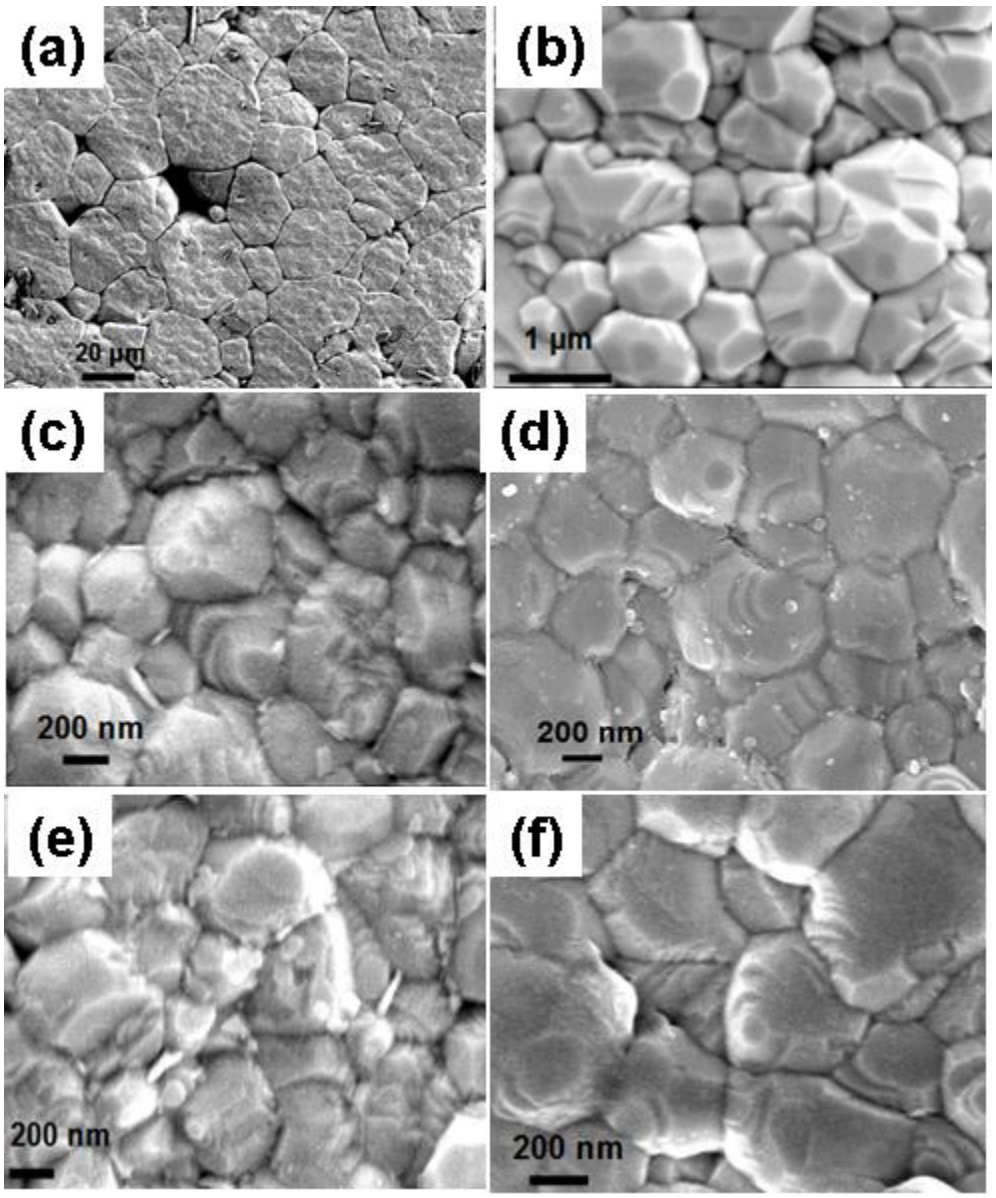

Figure 8.2- SEM images of thermally etched sintered ceramic samples of (a) BT (b) BTBCN (c) SBTBCN-1 (d) SBTBCN-2 (e) SBTBCN-3 (f) SBTBCN-4.

A decrease in the grain size leads to the decrease in maximum magnitude of dielectric constant and transition temperature [380].

8.3.2 Electrical measurements:

Figure 8.3 shows the variation of d_{33} and radial mode coupling factor (k_p) as a function of Sn content in the base composition (BTBCN). A high d_{33} value of 330 pC/N and k_p of 0.43 was

obtained for BTBCN. This value is consistent with the recently reported data on this composition [381]. The magnitudes of d_{33} and k_p were found to decrease rapidly with the increase in Sn content for SBTBCN-1, SBTBCN-2, SBTBCN-3 and SBTBCN-4. The magnitude of d_{33} and k_p for pure BT was found to be 144 pC/N and 0.17 which is similar to that reported in the literature. The rapid decrease in d_{33} and k_p with increase in Sn content can be explained by decrease in tetragonality as the crystal approaches paraelectric cubic phase.

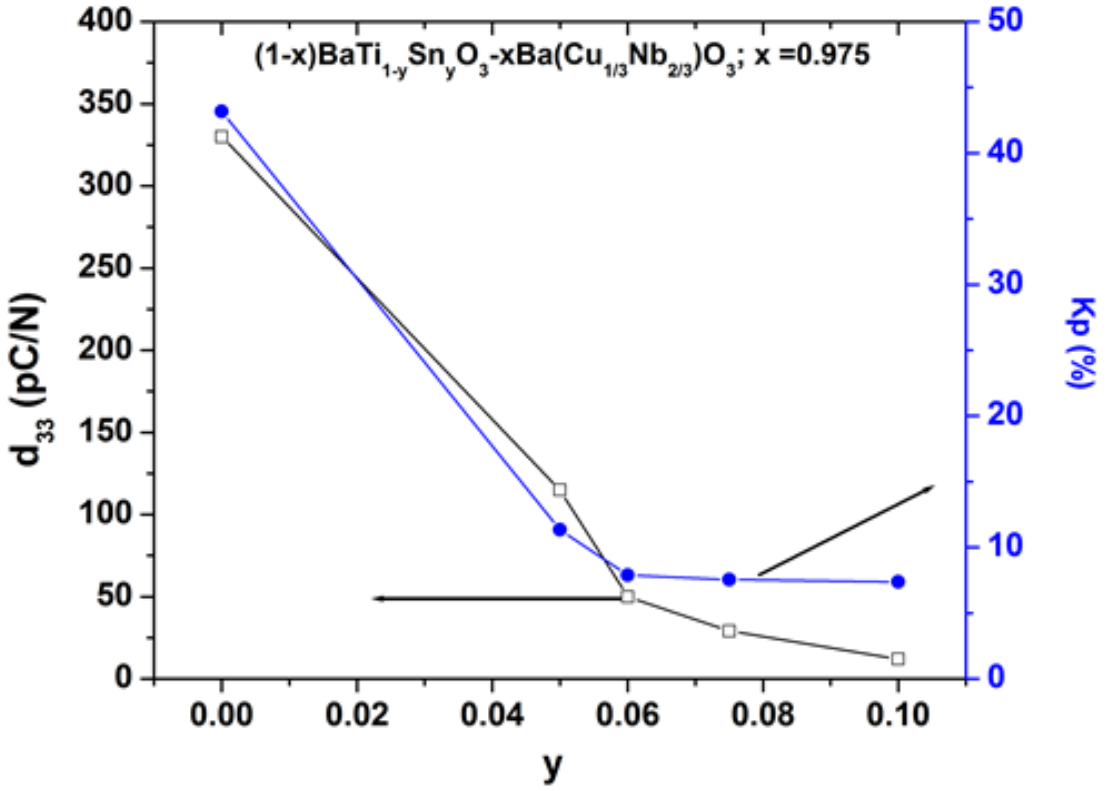

Figure 8.3- Variation of d_{33} and k_p as a function of Sn content.

Figure 8.4 shows the *P-E* hysteresis loop at 1 Hz at room temperature for all the synthesized compositions. The magnitude of remnant polarization ($2P_r$) calculated from *P-E* hysteresis was found to be on the order of 0.32, 0.11, 0.08, 0.03, 0.03, and 0.03 C/m^2 for BT, BTBCN, SBTBCN-1, SBTBCN-2, SBTBCN-3, and SBTBCN-4 respectively. The area under the loop gradually reduces upon modification with BCN and further reduces upon modification with

Sn. The shape of the loops became slim, indicating that the compositions are approaching the paraelectric phase. This result is in agreement with that observed using XRD, that upon modification with BCN and Sn the phase increasingly becomes cubic. The hysteresis originates from energy requirement for reversal of metastable dipoles during electric field application, hence the area under the loop is directly proportional to the energy dissipated inside the specimen. For all the Sn-modified specimens a small hysteresis area was measured.

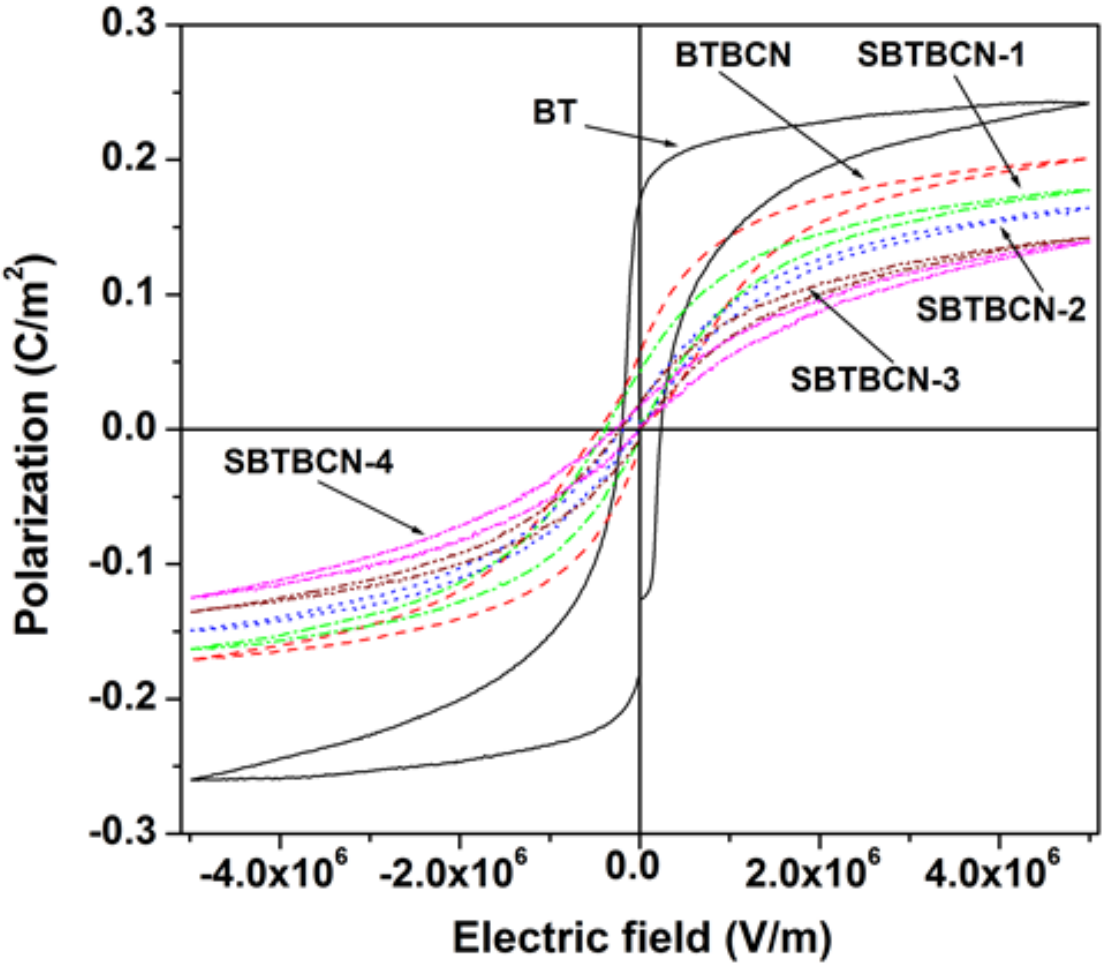

Figure 8.4- P-*E* hysteresis loops for synthesized compositions.

Figure 8.5(a) and 8.5(b) show the variation of dielectric constant (ε_r) and loss tangent (tanδ) as a function of temperature in the range of -50 to 150 ^oC, measured at 1 kHz for all the compositions. The Curie temperature (T_c) was found to shift towards room temperature on forming solid solution with BCN. Upon modification with Sn, the T_c further shifted towards room temperature and peak broadening was observed. The broadening of peak was found to increase with Sn content in the base matrix, indicating increase in diffuseness of phase transition. The tangent loss factor (tanδ) was below 2% in a wide temperature range (-50 to 180^oC) for all the Sn – modified compositions which is desired for MLCC application according to EIA specification [363]. As listed in Table 8.1, SBTBCN-2 and SBTBCN-3 were found to show very high dielectric constant of 9580 and 7440 respectively at RT along with very small loss factor < 0.6 %. Using the data for capacitance vs. temperature, TCC (temperature coefficient of capacitance) was calculated for both SBTBCN-2 and SBTBCN-3 and listed in Table 8.1. These values show the suitability of these two compositions for Y5V type of multilayer chip capacitors.

All the Sn-doped compositions were found to exhibit broad peak indicating diffuse nature of phase transitions. Figure 8.6(a) shows the temperature dependence of dielectric constant (ε_r) and loss tangent (tanδ) at various frequencies for SBTBCN-2. Figure 8.6(b) shows $1/\varepsilon_r$ as a function of temperature at 1 kHz for SBTBCN-2. The deviation from Curie-Weiss law can be defined as:

$$\Delta T_m = T_{dev} - T_m \tag{8.1}$$

where T_{dev} is the temperature at which ε_r starts to deviate from Curie-Weiss law. From Fig. 8.6(b), T_m and T_{dev} were found to exhibit values of 23 and 90°C respectively, thereby indicating a ΔT_m value on the order of 67°C. A modified Curie-Weiss law has been proposed to describe the diffuseness of phase transition as [1]:

$$1/\varepsilon_r - 1/\varepsilon_m = (T - T_m)^n/C \qquad (8.2)$$

where n and C are constant with $1 \leq n \leq 2$. The limiting value of n = 1 and n = 2 corresponds to the Curie-Weiss law for normal ferroelectric and to the quadratic dependence of relaxor ferroelectric respectively. From the above equation, the value of n for SBTBCN-2 was found to be 1.74, indicating diffuse nature of phase transition. This is expected considering the fact that

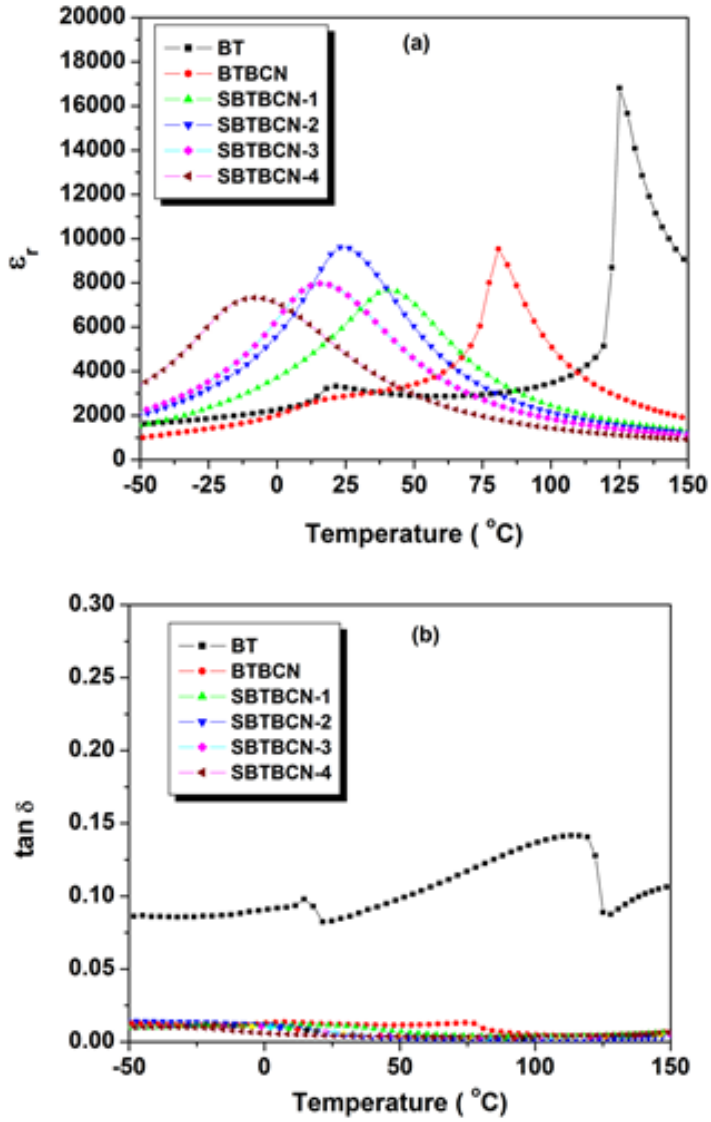

Figure 8.5- Temperature dependence of (a) ε_r and (b) tanδ at 1 kHz.

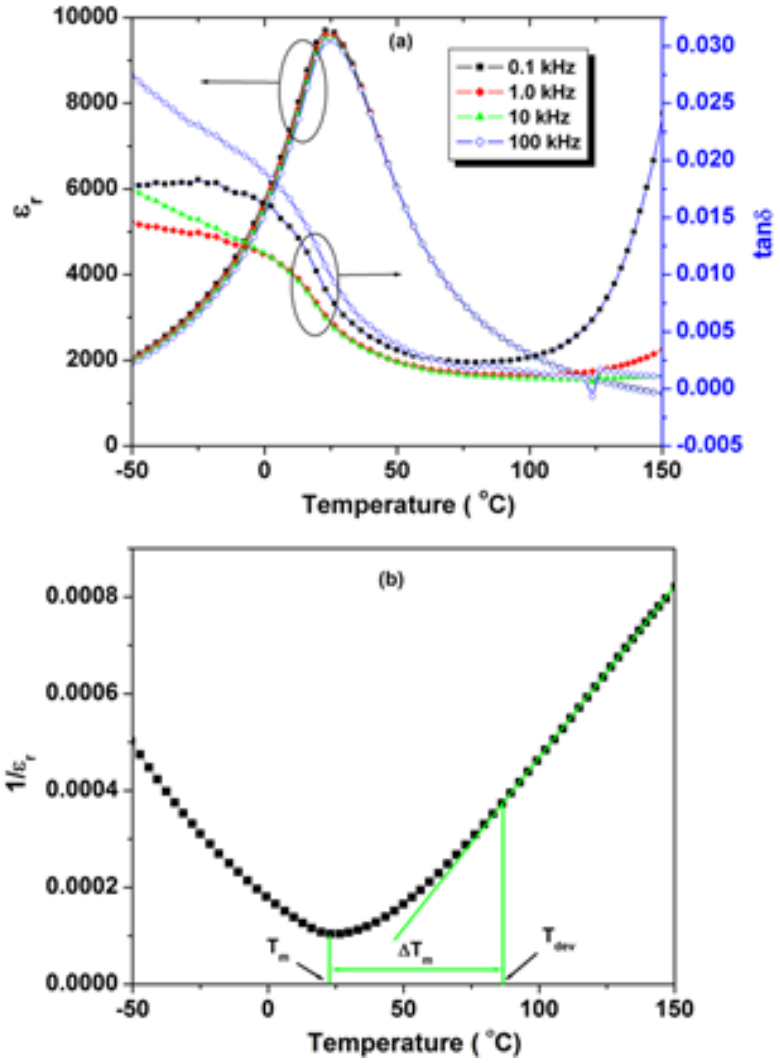

Figure 8.6- (a) ε_r and tanδ versus temperature at various frequencies (b) $1/\varepsilon_r$ versus temperature at 1 kHz for SBTBCN-2.

substitution of Ti^{+4} site by Cu^{+2}, Nb^{+5}, and Sn^{+2} will result in heterogeneity creating point defects as required for charge compensation. Thus, polarization switching occurs by heterogeneous nucleation in the vicinity of the local fields of randomly distributed point defects. Accordingly, polarization switching does not occur by the creation and motion of coherent micron-sized

domains, but rather by the creation of polar clusters within the domains. Originally, Imry and Ma pointed out that local fluctuations of these quenched microscopic fields results in the stability of domain states in cases where the phase transformation is driven by an order parameter with continuous symmetry[382]. On application of electric field, long-range ferroelectric order breaks down and results in the formation of polar clusters. TEM investigations for La-modified PZT and PMN-PT ceramics revealed the breakdown of normal micron-sized ferroelectric domains into tweed-like structures and polar clusters with increasing ac electrical drive for $E < E_c$, rather than movement or growth micron-sized domains and the dielectric behavior investigations revealed the development of ac induced relaxor ferroelectric characteristics [383]. The similar behavior is expected to be present in the SBTBCN ceramics. Table 8.1 summarizes the values of ε_r, tanδ, T_m, ΔT_m (^oC), n and TCC (Temperature Coefficient of Capacitance) and tetragonality (c/a) for all the studied compositions.

Table 8.1- ε_r, tanδ, T_m, ΔT_m (^oC), n, TCC at 1 kHz and tetragonality for the synthesized compositions.

Sample	**ε_r**	**tanδ(%)**	**T_m(^{o}C)**	**ΔT_m(^{o}C)**	**n**	**$\Delta\varepsilon_{r(T-25\,^\circ C)}/\varepsilon_{r(25\,^\circ C)}$ (%)**		**Tetragonality (c/a)**
						-30 ^{o}C	**85 ^{o}C**	
BT	3290	8.0	125	0	1.10	-44	-6	1.010
BTBCN	2850	1.0	80	43	1.30	-53	209	1.004
SBTBCN-1	6180	1.0	40	60	1.72	-65	-48	1.002
SBTBCN-2	9580	0.5	23	67	1.74	-70	-71	-----
SBTBCN-3	7440	0.6	15	80	1.77	-58	-69	-----
SBTBCN-4	4780	0.4	-8	90	1.84	11	-64	-----

The results in Table 8.1 clearly show that Sn-modified BTBCN compositions exhibit desired magnitude of TCC with high dielectric constant and low dielectric loss as required for MLCCs. Further, it is worth to note that all Sn-doped compositions have small grain size on the order of submicron under normal sintering conditions.

8.4. Chapter summary

In summary, $BaTiO_3 - Ba(Cu_{1/3}Nb_{2/3})O_3$ (BTBCN) solid solution was modified with Sn to achieve compositions with high dielectric constant ≥ 7000, low loss factor ≤ 1 % and grain size in submicron regime. Sn-doped compositions denoted as SBTBCN-2 and SBTBCN-3 were found to exhibit very high dielectric constant of 9580 and 7440 respectively at RT along with low loss tangent of < 0.6%. These compositions have potential application in Y5V type MLCCs.

Chapter-9

Dielectric and ferroelectric response of compositionally graded bilayer and trilayer composites of $BaTiO_3$ and $0.975BaTiO_3$-$0.025Ba(Cu_{1/3}Nb_{2/3})O_3$[g]

This chapter focuses on the dielectric and ferroelectric response of compositionally graded bilayer and trilayer composites consisting of $BaTiO_3$ (BT) and $0.975BaTiO_3$-$0.025Ba(Cu_{1/3}Nb_{2/3})O_3$ (BTBCN). Two types of graded bilayer samples were synthesized, one with same thickness of BT and BTBCN while other with different layer thicknesses. The graded trilayer sample consisted of BT layer sandwiched between two BTBCN layers of equal thickness. SEM and TEM images showed a sharp interface with needle-shape domains across the interface. The domain size on BT-side was found to be larger than that on BTBCN-side. The temperature dependence of dielectric response for all composite systems was found to exhibit shifting of characteristic Curie peak compared to constituent material which was associated to coupling between layers. Moreover, the differences in grain size, tetragonality, domain mobility of each layer was found to perturb the electrical response of composite. The polarization mismatch between uncoupled BT and BTBCN established internal electric field in composite specimen and defined new polarization states in each layer by perturbing free energy functional of the composite specimen. Dynamic hysteresis behaviors and power-law scaling relations of all specimens were determined from polarization – electric field hysteresis loop measurements as a function of frequency. All systems were found to exhibit similar dynamic scaling relationships. Hysteresis area $<A>$, P_r and E_C decreased with increasing frequency due to delayed response, but increased with increasing applied electric field due to enhancement of driving force. Trilayer

[g] Reprinted with permission from [325]. Copyright 2010, American Institute of Physics.

system was found to exhibit strong internal-bias field and double hysteresis behavior. The coupling effect resulting due to polarization mismatch between layers had substantial influence on the dynamic hysteresis behavior and power-law scaling relations.

9.1 Background

Ferroelectric random access memory (FeRAM) has been gaining interest as it can provide nonvolatile memory operation with fast writing time while reducing the power requirement[384]. Ferroelectric materials are also being used as gate in ferroelectric memory field-effect transistor (FeMFET)[385-387] providing a nondestructive readout operation with high density. The stored dipole moments in the ferroelectric material can adjust the threshold voltage of a FeMFET, and thus drain current of each switching state can be discriminated and identified as a logic state in memory [384]. In these applications, the switching capability and energy loss during the operation of ferroelectric gate is quite important. Both of these parameters are dependent upon the hysteresis behavior of ferroelectric material. Ideally, one would like to achieve a slim hysteresis loop with large remanence and low coercivity.

In order to develop ferroelectric materials with adequate hysteresis behavior as required for new generation of memories, efforts have been made on developing graded structures in the form of bilayer, trilayer and multilayers[388-390]. Such structures offer the possibility of tuning the hysteresis loops by modulating the parameters such as leakage current, sharpness of the interface and ferroelectric – anti-ferroelectric exchange coupling. However, most of the work in this area has been limited to thin films where besides material parameters and interface phenomenon, additional factors such as clamping from the substrate, residual stress due to difference in thermal expansion, and epitaxy influences the overall hysteresis behavior. Therefore in this chapter, the bulk graded ferroelectrics were investigated for two specific

reasons: (i) to better understand the physics governing the dynamic hysteresis behavior, and (ii) to deterministically model the hysteretic scaling relationships. The prediction of hysteresis behavior with applied electric field amplitude and frequency can be accomplished by constructing the dynamic hysteresis and scaling rules [1,391,392]. Dynamic hysteresis model provides the changes in hysteresis area $<A>$, coercive field (E_c) and remnant polarization (P_r) as function of amplitude of applied field (E_o) and frequency (f)[393]. The synthesis of bilayer and trilayer ferroelectric graded structures were performed with following variations: (i) single layer thick film of pure $BaTiO_3$ (BT) with thickness of 1 mm, (ii) bilayer structure with equal layer thickness of 0.5 mm for BT and $0.975BaTiO_3$-$0.025Ba(Cu_{1/3}Nb_{2/3})O_3$ (BTBCN), (iii) bilayer structure with unequal thickness of 0.650 mm for BT and 0.350 mm for BTBCN, and (iv) trilayer structure with 0.40 mm layer of BT sandwiched between two layers of BTBCN with thickness of 0.30 mm. All these structures are schematically shown in Fig. 9.1. It was observed that coupling resulting due to polarization mismatch between layers changes the free energy function and influences the dynamic hysteresis behavior and power-law scaling relations.

9.2 Experimental

BT and BTBCN were synthesized by using mixed oxide route. Calcined powders were mixed with binder system and used for tape casting. Dried tapes of thickness 60 μm were cut to desired dimensions and laminated to fabricate bilayer and trilayer structures. Laminated stacks were sintered at 1350^oC for 2h. Phase evolution for all specimens was determined by using Philips Xpert Pro XRD system (Almelo, the Netherlands). Dielectric constant and tangent loss factor was determined as a function of temperature at selected frequencies using HP 4284A LCR meter connected to a computer-controlled high temperature furnace. The surface microstructure

of sintered samples was observed using Zeiss Leo Scanning Electron Microscope (SEM). Transmission electron microscopy (TEM) was performed by using FEI Titan 300 on specimen prepared by using focused ion beam (FEI Helios 600 NanoLab). Polarization – electric field (*P-E*) hysteresis measurements were conducted by using modified Sawyer-Tower bridge Precision II (Radiant Technologies). All the measurements were repeated on at least three samples to confirm the repeatability.

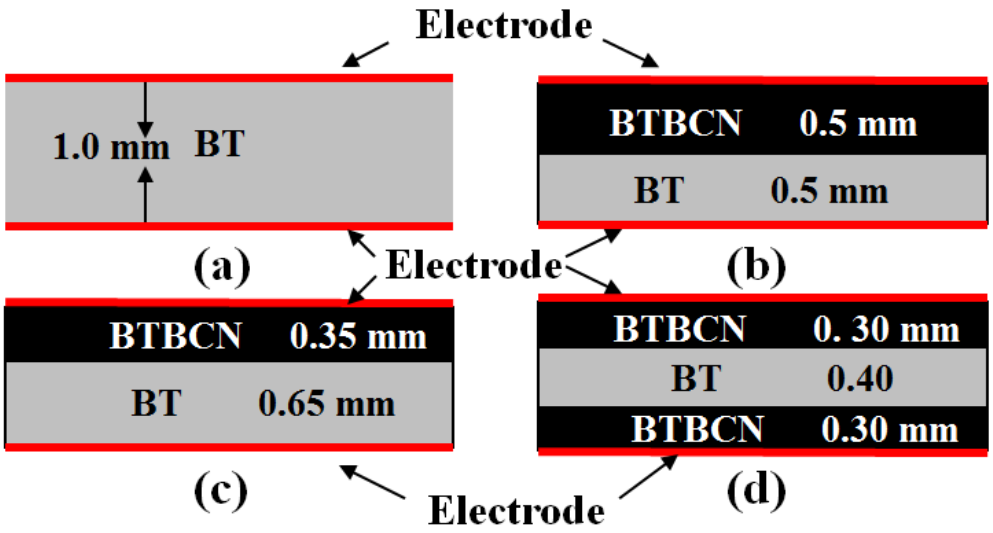

Figure-9.1 Schematic representation of the bilayer and trilayer thick films (a) BT (b) Bilayer with equal thickness of BT and BTBCN layer (0.5 mm each) (c) Bilayer with higher thickness of BT (0.65 mm) and BTBCN (0.35 mm) (d) Trilayer with 0.3 mm thickness of each BTBCN layer and 0.4 mm BT layer sandwiched in between them.

9.3 Results and discussion

9.3.1 Domain and interface structure

Figure 9.2 shows the room temperature (RT) X-Ray diffraction (XRD) patterns for bilayer specimen from both BT and BTBCN sides. It can be seen that both the layers crystallized in perovskite phase with tetragonal symmetry. However, the splitting of (200) peak was

prominent in the XRD pattern recorded on BT side. The tetragonality (c/a) calculated using (200) and (002) peaks was found to be 1.01 and 1.006 for BT and BTBCN side respectively. The decrease in tetragonality was generally coupled with lowering of transition temperature and decrease in grain size [1], which is consistent with SEM micrographs and ε(T) plots explained later. This difference in tetragonality between BT and BTBCN defines difference in principle strain S_s, given as $S_s = (c/a - 1)$. The magnitude of S_s was found to be 0.01 for BT and 0.006 for BTBCN resulting in strain gradient across the interface between the two coupled layers in bilayer.

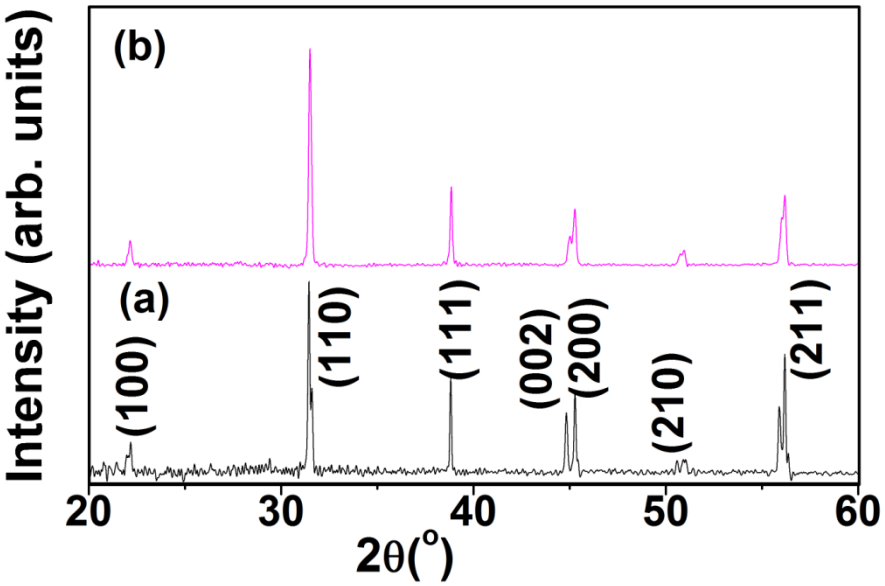

Figure 9.2 -XRD patterns recorded at RT on (a) BT and (b) BTBCN side of the bilayer.

Figure 9.3(a) – (c) show the SEM micrograph of interface at various magnifications. There is clear difference in the average grain size across the interface (shown by solid line), where grains on BT side were found to be much larger ~32 μm than that on BTBCN side ~0.64 μm (computed using line-intercept method). The magnified view of interface region in Fig.9.3(c) depicts a sharp interface indicating that there was limited diffusion of Cu and Nb across the

interface. EDS detector in SEM analysis was not able to find any trace of Cu and Nb across the interface. Using Fig. 9.3(d), the effective thickness of interface can be estimated to be ~75 nm in case of bilayer, and ~150 nm in the case of trilayer with two interfaces. Figure 9.3(d) shows the TEM image of specimen across the interface. Selected area electron diffraction (SAED) pattern

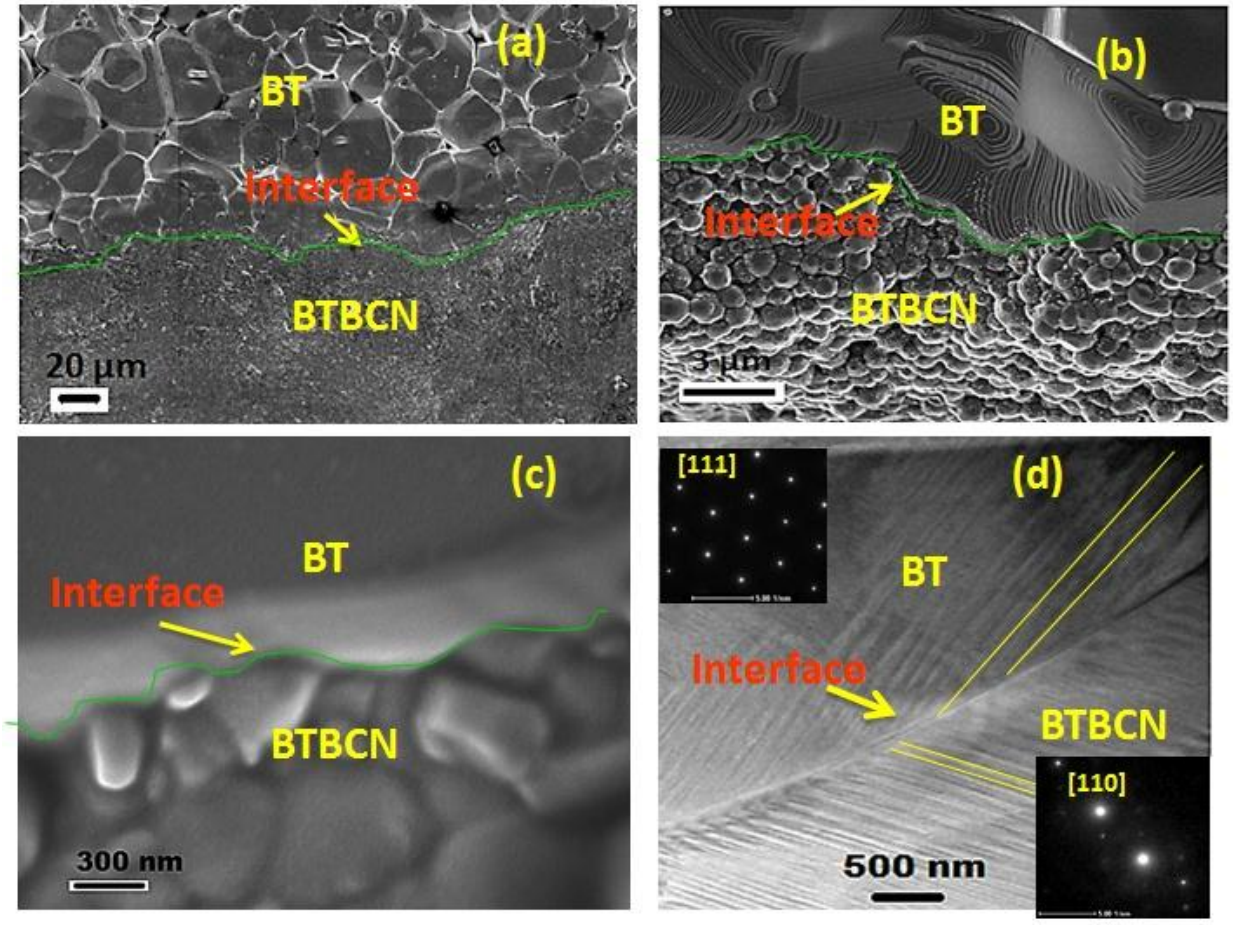

Figure-9.3 (a)-(c) SEM micrographs of the interface at various magnifications, (d) TEM image of the domain structure across the interface (inset showing SAED pattern).

of corresponding sides are shown in inset of Fig. 9.3(d). In these SAED patterns, the zone axis of BT side was [111] and that of BTBCN side was [110]. Needle shaped domain structure was found to be formed on both BT and BTBCN side, however domains on BT side had larger width than that on BTBCN side. This is quite interesting observation and provides us the key to modify

the polarization response. The difference in grain size (as observed in SEM images) results in the variation of domain size and width, which in turn influences the polarization. In randomly oriented polycrystalline ceramics, the domain size (D) is related to grain size (G) as [304]:

$$D \propto G^{p} \tag{9.1}$$

where $p < 1/2$ for $G > 10\ \mu m$

$p = 1/2$ for $10\ \mu m > G > 1\ \mu m$

$p > 1/2$ for $G < 1\ \mu m$

Using Eq.(9.1), one can approximate the domain size of BT material by taking $p = 1/3$ (typical value) in the case of grain size > 10 μm[303,304].Substituting the value of grain size calculated from SEM micrographs in Eq. (9.1) and rewriting the above equation to find the exponent p for BTBCN material as:

$$D_{BT} / D_{BTBCN} = (32)^{1/3} / (0.64)^{p} \tag{9.2}$$

The domain size obtained from TEM analysis was used to determine the ratio in Eq. (9.2), which was roughly found to be 4. Thus, the exponent p for BTBCN material with grain size of 0.64 μm was calculated to be 0.52. This difference in the domain exponent results in the varying polarization across the interface. Combined with strain – gradient, this result indicates the formation of graded structure.

Figure 9.4(a) and (b) show the piezoresponse force microscopy (PFM) images of BT and BTBCN side respectively, where the variation in contrast indicates regions with different piezoelectricity. If the sample was single domain structure than the image produced would be all of same color. Comparing the two images, it can be seen that there is difference in the magnitude of the piezoelectric response, with BTBCN exhibiting higher piezoelectric response than that of BT. Using Berlincourt d_{33} meter, the piezoelectric coefficient of individual layers of BT and

BTBCN was found to be 144 and 330 pC/N. These measurements were in agreement with the PFM information showing higher piezoelectric activity for the BTBCN phase.

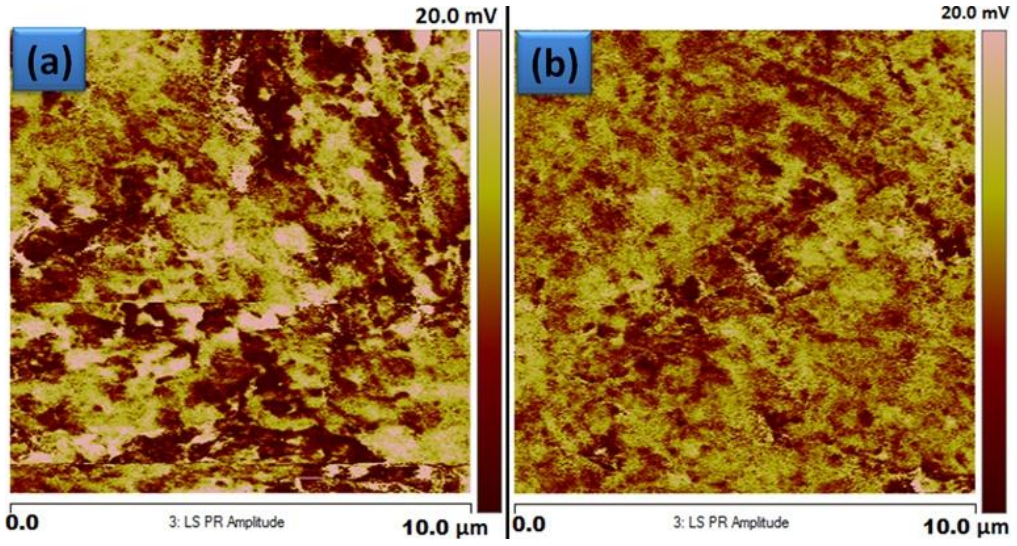

Figure-9.4 PFM image of (a) BT side and (b) BTBCN side

Figure 9.5(a) – (e) shows the variation of dielectric constant (ε) and tangent loss factor (tanδ) as a function of temperature (T) at different frequencies for various specimens. It is known that BT and BTBCN have Curie temperature (T_c) of 125^{o}C and 80^{o}C respectively[381] The characteristic transition peaks of BT and BTBCN can be marked in the $\varepsilon(T)$ plots as shown in Fig. 9.5(a) and (b). The transition temperatures of BT and BTBCN can be found in the graded bilayer and trilayer specimens with minor shifts. The Curie temperature of BT was shifted towards lower temperature (~117 ^{o}C) while that of BTBCN was shifted towards higher temperature (~ 90^{o}C), which can be attributed to strain gradient present across the interface. The magnitude of maxima in dielectric constant, $\varepsilon(T_m)$, was found to decrease for the composite specimens. In the case of graded trilayer, the peak in the dielectric curve due to BTBCN was

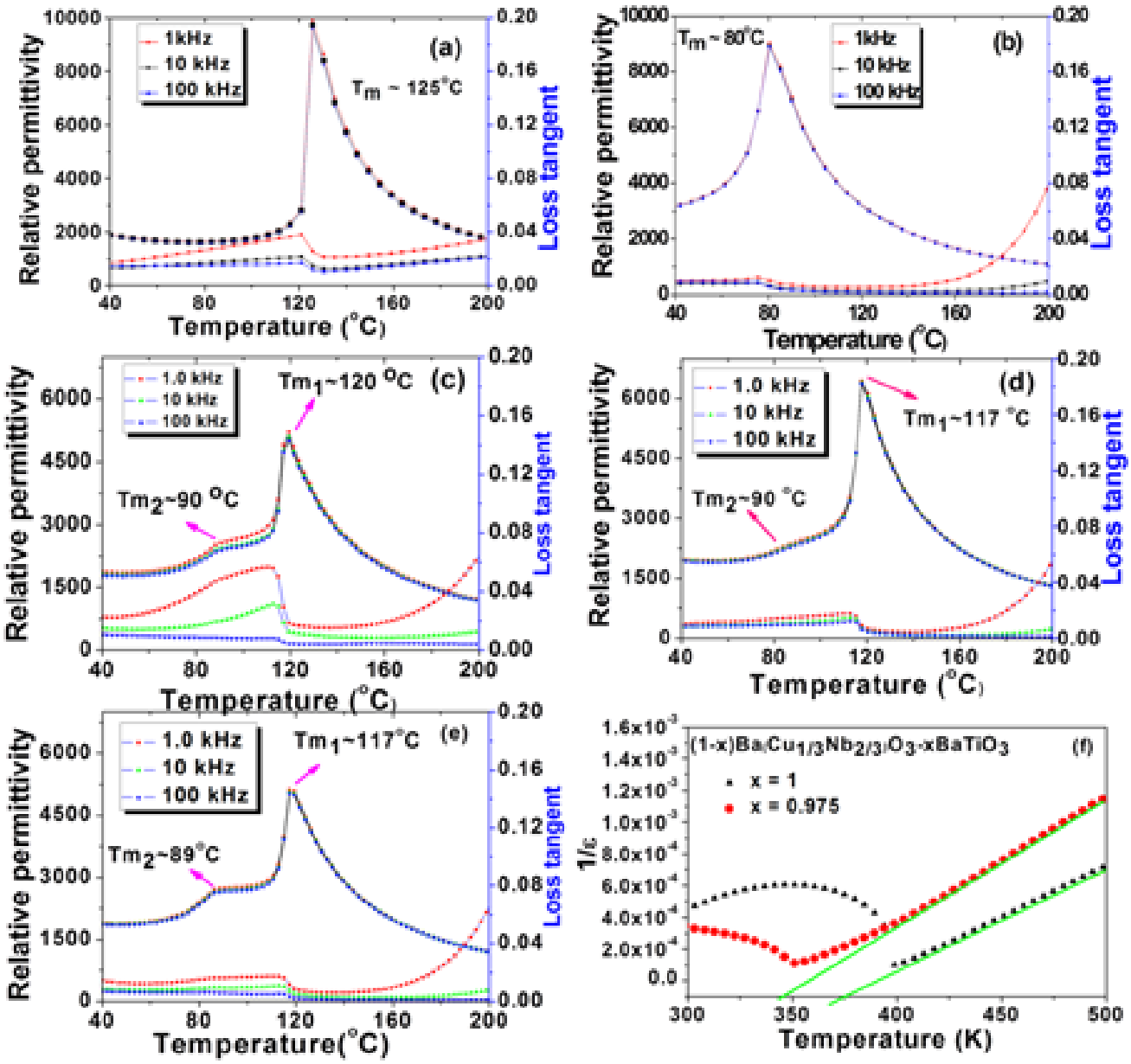

Figure 9.5 Temperature dependence of relative permittivity for (a) BT (b) BTBCN (c) Bilayer with equal thickness (d) Bilayer with unequal thickness (e) Trilayer with BT layer sandwiched between two BTBCN layers (f) 1/ε versus temperature plot.

more obvious due to higher effective thickness of two BTBCN layers. These results clearly show that there was influence of interface on the overall system properties and dielectric response of the composite was a combination of individual components. Further these results combined with

the gradient in domain size and widths confirm the formation of graded structure. More information on grading and interface coupling could be obtained by invoking phenomenology.

For an uncoupled and unconstrained tetragonal BT, the free energy in terms of polarization can be expressed as [394]:

$$G_1 (P, T) = G_{o1}(T) + 1/2a_1P_1^2 + 1/4a_2P_1^4 + 1/6a_3P_1^6 \quad (9.3)$$

where $G_o(T)$ is the energy in paraelectric state. For the isothermal case, the electric field acting on the ferroelectric material, expressed in terms of P_1, can be obtained as:

$$E_1 = dG_1/dP_1 = a_1P_1 + a_2P_1^3 + a_3P_1^5 \quad (9.4)$$

Similarly for BTBCN the electric field is given as:

$$E_2 = dG_2/dP_2 = b_1P_2 + b_2P_2^3 + b_3P_2^5 \quad (9.5)$$

where G_1 andG_2 are free energy of layer *1* and *2* in its high-temperature PE state, P_1 and P_2 are the polarizations of layers 1 and 2 and a_1, a_2, a_3, b_1, b_2, b_3 are the Landau coefficients. The coefficients a_1 and b_1 have temperature dependence given by the Curie-Weiss law as $a_1 = (T_o - Tc_1)/\varepsilon_o C_1$ and $b_1 = (T_o - Tc_2)/\varepsilon_o C_2$, where ε_o is the permittivity of free space, Tc_1, Tc_2 and C_1,C_2 are the Curie-Weiss temperature and constant of uncoupled layer *1* and *2*. The other coefficients in free energy function are assumed to be temperature independent. By equating Eq.(9.5) and (9.6) to zero, spontaneous polarization *(P)* corresponding to two polarization states of each layer can be obtained. Figure 9.5(f) was used to compute the magnitude of $(T_o - Tc_1) \sim -24.15$ K for BT layer and $(T_o - Tc_2) \sim -5.88$ K for BTBCN layer. The values of Curie constant calculated from experimental data were found to be $\sim 1.6 \times 10^5$ K for BT and $\sim 1.4 \times 10^5$ K for BTBCN.

After coupling of both layers in graded bilayer and trilayer structure, the free energy (G) and electric field (*dG/dP)* values would be different as observed in terms of differences in *ε(T)*

plots. Suppose $E_{i,1}$ and $E_{i,2}$ are the internal electric fields in BT and BTBCN layers given as[395,396]:

$$E_{i1} = -1/\varepsilon_0(P_1-<P>) = \alpha/\varepsilon_0(P_2-P_1) \quad (9.6)$$

and

$$E_{i2} = -1/\varepsilon_0(P_2-<P>) = (1-\alpha)/\varepsilon_0(P_1-P_2) \quad (9.7)$$

where P_1 and P_2 are new polarization states in layer 1 and layer 2 respectively after coupling, $<P>= (1-\alpha)P_1+\alpha P_2$ is the average polarization and α is the relative volume fraction. The total free energy function incorporating the potential energies of internal fields E_1 and E_2 is given by [395]:

$$G_\Sigma = (1-\alpha)[G_1(P_1) - EP_1-1/2\ \xi E_{i1}P_1] + \alpha[G_2(P_2) - EP_2 - 1/2E_{i2}P_2] + G_S/h + G_{el} - JP_1P_2 \quad (9.8)$$

where G_{el} is the elastic energy of the polarization-free misfit. The energy of interface G_S/h can be neglected due to very small correlation length of ferroelectric [397] in comparison to the total thickness of bilayer (~1000 μm). The last term in above equation is interlayer (interfacial) coupling and J is the coupling coefficient (interfacial exchange interaction coefficient) given as [395]:

$$J = \alpha\ (1-\alpha)\xi/\varepsilon_0 \quad (9.9)$$

Above relation demonstrates that the coupling between layers can be controlled by either the volume fraction of each layer or by modifying the free carrier content quantified by coefficient ξ. *"ξ"* is measure of the free charge density with respect to the bound charge at the interlayer interface given as $\xi = 1-\rho_f/\rho_b$, ρ_b is the bound charge density and ρ_f is the free charge density. The two limiting values, $\xi = 1$ and $\xi = 0$ correspond to perfect insulating and semiconducting ferroelectric bilayers. Assuming polarization $\vec{P}$ varies from point to point within the interfacial region, the resulting bound charge density can be written as:

$$\rho_b = -\vec{\nabla} \cdot \vec{P} \tag{9.10}$$

Using differential form of Gauss's law, the divergence of electric field is given as:

$$\vec{\nabla} \cdot \vec{E} = \frac{\rho}{\varepsilon_o} = \frac{\rho_b + \rho_f}{\varepsilon_o} \tag{9.11}$$

Combining Eq. (9.10) and (9.11), one can derive the relation for free charge density as:

$$\overrightarrow{\nabla} \cdot \varepsilon_o \vec{E} = -\vec{\nabla} \cdot \overrightarrow{P} + \rho_f$$

or,

$$\rho_f = \overrightarrow{\nabla} \cdot \varepsilon_o \vec{E} + \vec{\nabla} \cdot \overrightarrow{P} = \vec{\nabla} \cdot (\varepsilon_o \vec{E} + \overrightarrow{P}) = \vec{\nabla} \cdot \overrightarrow{D} \tag{9.12}$$

where $\overrightarrow{D} = (\varepsilon_o \vec{E} + \overrightarrow{P})$ is the displacement vector. In quasi-static frequency regime (< 1 Hz) and below sub-coercive field, the contribution from free charge polarization is dominant. In saturated field and quasi-static frequency regime, alignment of domains contributes to resultant polarization, which provides estimation of bound charge density. Table 9.1 lists the values of polarization for sub-coercive field (E_{c-} = 1 kV/cm) and maximum polarization in saturated field (E_{c+}) regime for layered systems at 0.1 Hz. Taking the ratio of the polarization magnitudes in E_{c-} and E_{c+} regime, an indication for the changes in free and bound charge density can be obtained ($\sim \rho_f / \rho_b$). The polarization ratio shown in Table 9.1 indicates a significant drop for the graded bilayer with unequal thickness and trilayer structure which reflects the increase in coupling coefficient. This analysis neglects the contribution from interface which is not realistic but it does provide an explanation for the changes observed in hysteresis behavior as explained later. Further, this analysis confirms the observation on influence of graded structure on ferroelectric properties.

Table 9.1. Magnitude of polarization in quasi-static frequency (0.1 Hz) regime.

Systems	**P_r (μC/cm^2) in sub-coercive field (E_{c-}) regime (1 kV/cm)**	**P_{max}(μC/cm^2) in saturated field (E_{c+}) regime**	**Polarization ratio = $P_r(E_{c-})$ / $P_{max}(E_{c+})$**
BTBCN single layer	0.15	19.2	0.00781
BT single layer	0.11	16.8	0.00655
Bilayer with equal thickness	0.14	16.5	0.00848
Bilayer with unequal thickness	0.07	15.2	0.00461
Trilayer	0.07	12.1	0.00579

9.3.2 Ferroelectric hysteresis behavior

The hysteresis profiles with various frequencies (f) and electric fields (E_0) were obtained for BT single layer, BT-BTBCN graded bilayer with equal and unequal thicknesses and BTBCN-BT-BTBCN graded trilayer ceramic systems. Examples of hysteresis profiles are shown in Fig. 9.6 (a) and (b) for BT single layer system. Other systems, i.e. graded bilayer with equal and unequal thicknesses and trilayers, exhibited very similar behaviors. At fixed E_0, the hysteresis loop area $<A>$, remnant polarization (P_r) and coercive field (E_C) decreased with an increase of frequency (Fig. 9.6(a)) because of the delayed response of domain switching and polarization reversal which diminishes hysteresis loop size[398]. At fixed f, remnant polarization (P_r) increases with an increase of E_0 (Fig. 9.6(b)) as larger E_0 provides higher level of driving force responsible for switching of ferroelectric domains. Higher driving force enhances the domain volume and consequently total polarization including hysteresis parameters [393].

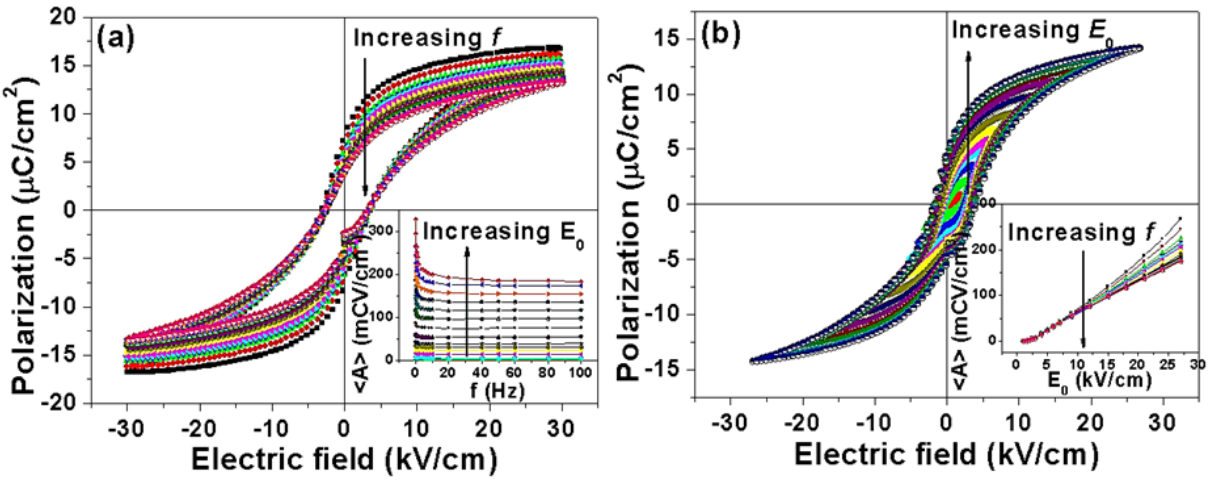

Figure 9.6 P-E hysteresis loops of BT single layer system (a) various f with fixed E_0 = 30 kV/cm, and (b) various E_0 with fixed f = 10 Hz.

Figure 9.7(a) compares the P-E hysteresis loop of BTBCN with BT. Both these compositions are ferroelectric with tetragonal perovskite structure at room temperature and as seen in this figure, the polarization of BTBCN is higher than that of BT. Hysteresis loops of both materials were found to be shifted towards positive side on electric field axis implying the presence of internal-bias field mainly arising from electronic defects. The polarization switching mechanisms in BT single crystals have been attributed to nucleation of anti-parallel domains and their growth by domain wall motion [399-401]. In polycrystalline ceramics, the polarization switching is strongly influenced by presence of grain boundaries, space charges, charged defects and surfaces [402-407]. Presence of charged defects will result in the formation of internal bias field as commonly observed for the hard piezoelectric materials by pinning the domain boundaries. The coercive field broadness ($2E_C$) of BTBCN was larger than that of BT. The P-E hysteresis loops of BT single layer and BT-BTBCN layers formed as graded bilayer and trilayer ceramic systems are compared in Fig. 9.7(b). The polarization value of graded trilayer ceramic system was lowest as compared with rest of the cases but it possesses the largest coercive field

(E_C). The coercive field (E_C) value on positive side was higher than that on negative side for all systems which is further indication of built-in internal-bias field [364].

To quantify internal-bias field in each system, following relations was used [364]:

$$E_1 = E_C + E_i \tag{9.13}$$

$$E_2 = -E_C + E_i \tag{9.14}$$

thus, $$E_i = (E_1 + E_2)/2 \tag{9.15}$$

where E_1 and E_2 are electric field intercepts on positive and negative side respectively, E_C is the magnitude of coercive field with no internal-bias and E_i is the magnitude of internal-bias field. The effect of internal-bias field on the coercive field can be determined by expressing the rate of motion of domain boundaries as:

$$v = \mu E \tag{9.16}$$

and

$$\mu = (3\delta)/2P_0\Gamma \tag{9.17}$$

where μ is the mobility of domain wall, δ is its half-width, Γ is the viscosity of domain wall motion, and P_0 is the spontaneous polarization[360] The switching time was characterized by the time of inter-growth of domain to the crystallite half-width $d/2$ given by the relation:

$$t = d/(2v(E_C)) = 1/f \tag{9.18}$$

Combing Eqs. (9.19) – (9.21):

$$E_C = (P_0\Gamma df)/\delta \tag{9.19}$$

which is a linear dependence of internal-bias field modified coercive field on frequency[360].

Table 9.2 Magnitude of coercive field broadness ($2E_C$) and internal-bias field for various composite systems.

System	Coercive field broadness, $2E_C$ (kV/cm)	Internal-bias field (kV/cm)
BTBCN single layer	7.2	2.9
BT single layer	6.2	1.0
Bilayer with equal thickness	8.2	2.1
Bilayer with unequal thickness	5.1	1.2
Trilayer	8.8	2.5

The coercive field broadness ($2E_C$) of BTBCN single layer was found to be 7.2 kV/cm, however for BT single layer it was 6.2 kV/cm. In multilayer systems, if they are in uncoupled state behaving like capacitors in series, normally the coercive field broadness should be between 6.2 kV/cm and 7.2 kV/cm. This was not the case for graded bilayer and trilayer systems as shown in Table 9.2. The lower coercive field broadness value found in bilayer with unequal thickness system and higher coercive field broadness values found in bilayer with equal thickness and trilayer systems implies that there was finite interaction across the layers. The polarization mismatch provides direct contribution to internal-bias field which increases from bilayer to trilayer system. In order to achieve domain reversal, the system needs additional energy to overcome barrier due to internal-bias field. Consequently, high coercive field is characteristics of system with high internal-bias field. This explains why the coercive field of trilayer system is highest and it reduces sequentially for bilayer with equal and unequal thickness

systems respectively as shown in Table 9.2. It can be noticed that coercive field for bilayer with unequal thickness system is less than that for BT single layer. This reflects the effect of interface coupling between layers in bilayer with unequal thickness system which enhances domain wall mobility.

The graded trilayer ceramic system was found to exhibit double hysteresis loop-like behavior which normally occurs in anti-ferroelectric materials [408-412]. Prior studies have also found similar behavior and it was attributed to presence of multiple domain states when two factors are simultaneously occurring, (i) the coupling strength (J) between layers is sufficient and (ii), both layers have almost equal polarization values in anti-parallel direction ($P_1 = -P_2$ or vice versa). The polarization of each layer depends on layer thickness, so in the case of same material the layer thickness should be $L_1 \approx L_2$ (where L_1 and L_2 are thickness of layer 1 and layer 2 respectively) to provide equal polarization in opposite direction. In case of bilayers with equal thickness of same material, when coupling strength is small the overall polarization ($P = P_1 + P_2$) is non-zero and the system is in weak ferroelectric phase. As the strength of coupling increases, P approaches zero, and thus the system will exhibit double loop behavior. In the case of graded bilayers consisting of two different materials, the polarizations P_1 and P_2 are variable with coupling strength [409]. The graded trilayer system has two interfaces between BTBCN-BT and BT-BTBCN. Since each couple layers composes of the same materials with same layer thickness, thus it is possible that each couple induces equal polarization but in different direction, which can explain the origin of double hysteresis loop-like behavior. Bilayers with equal and unequal thicknesses did not show double hysteresis loop-like behavior which could be related to smaller effective interface thickness.

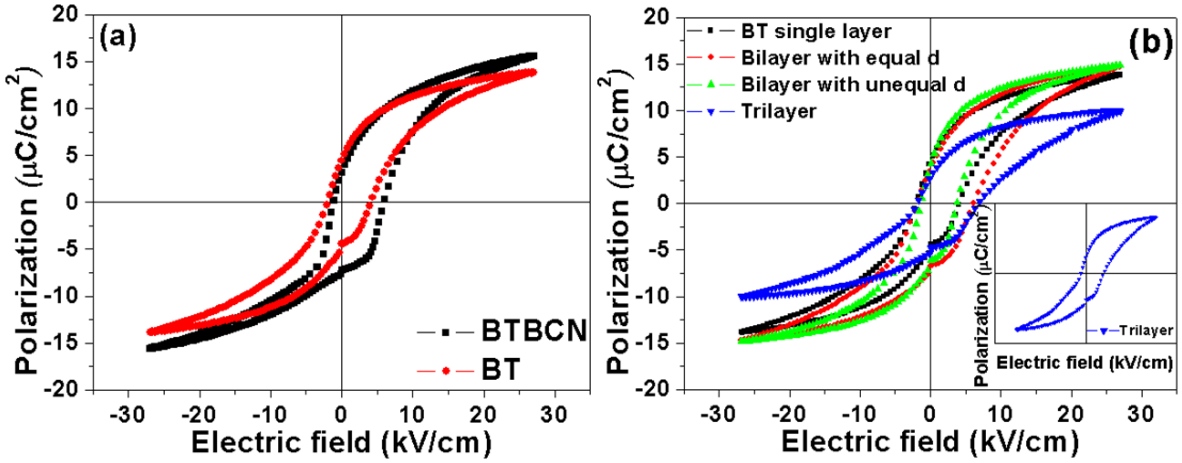

Figure 9.7 (a) P-E hysteresis loops of BTBCN and BT layers at fixed f = 50 Hz and E_0 = 27 kV/cm, and (b) P-E hysteresis loops of multilayer systems with fixed f = 50 Hz and E_0 = 27 kV/cm.

Figure 9.7(a) shows that the polarization of BTBCN is higher than that of BT. Since polarization is directly proportional to layer thickness[409], uncoupled state bilayer system with equal thickness should have higher polarization than that of bilayer system with unequal thickness (lower volume fraction of BTBCN). However results show that the polarization of bilayer system with unequal thickness was almost similar to that of bilayer with equal thickness at 50 Hz. Only at lower frequencies of 0.1Hz, the polarization recorded for bilayer with equal thickness is higher than that of bilayer with unequal thickness (Table-9.1). This again suggests that there is finite coupling occurring in the layered structure which is frequency dependent. This result can be explained by considering the coupling of two layers which establishes new polarization state in each layer due to internal bias field arising from polarization mismatch [395]. BTBCN possess higher polarization than that of BT, thus smaller thickness of BTBCN in bilayer system with unequal thickness can reach the polarization of BT. By adjusting the thickness of BTBCN, a slight polarization mismatch in graded bilayer could be created, which could result in weak internal bias field that would be subsequently affect the domain reversal. By

tailoring the thickness of layers, a higher polarization in graded bilayer system with unequal thickness could be obtained as shown in Fig. 9.7(b). For the composite having equal thickness of BT and BTBCN, net polarization value in BTBCN layer will be higher as compared to that of BT giving rise to polarization mismatch. As explained in earlier sections, the trilayer specimen possesses higher exchange coupling and increased internal bias due to finite interaction across the layers. Hence, polarization can expected to be lowest in trilayer as compared with single layer and bilayer systems. Hence, polarization can expected to be lowest in trilayer as compared with single layer and bilayer systems. This was experimentally confirmed in Fig. 9.7(b).

9.3.3 Dynamic scaling relationships

In ferromagnetic materials, the variation of hysteresis area <*A*> with frequency (ω) and magnetic field (h) have been established as power-law scaling relation $A = A_0 + h_0^{\alpha}\omega^{\beta} g\left(\frac{\omega}{h_0^{\gamma}}\right)$ with the exponents α, β, and γ and with a function g having a suitable nonmonotonic form such that $g(x)\rightarrow 0$ as $x\rightarrow 0$ or ∞[413,414]. Here A_0 is the loop area at the zero frequency limit. Similarly in ferroelectric materials, hysteresis area <*A*> also responds to applied frequency (f) and electric field (E_0). Therefore, to model relation of hysteresis area with these parameters, power-law scaling relation is applied:

$$<A> \propto f^{m} E_0^{n} \tag{9.20}$$

where m and n are exponents that depend on the dimensionality and symmetry of the system. By plotting <*A*> against f at fixed E_0, one obtains the exponent m. The exponent n can be obtained by plotting <*A*> against E_o at fixed f [393]. This method can be repeated for all the cases studied here to extract the magnitude of exponent m and n. After obtaining f-exponent m and E_0-

exponent *n*, the scaling of hysteresis area <*A*> against frequency *f* and field amplitude E_0 can be obtained as shown in Fig. 9.8(a) – (d). Noticeably, for each case the scaling relations can be divided into two regimes corresponding to sub-coercive field and saturated field condition which possess different domain switching mechanisms. The reversible 180º domain switching mechanism is responsible for changes occurring in sub-coercive field condition whereas the irreversible non-180º domain switching mechanism dominates in saturated field condition[415].

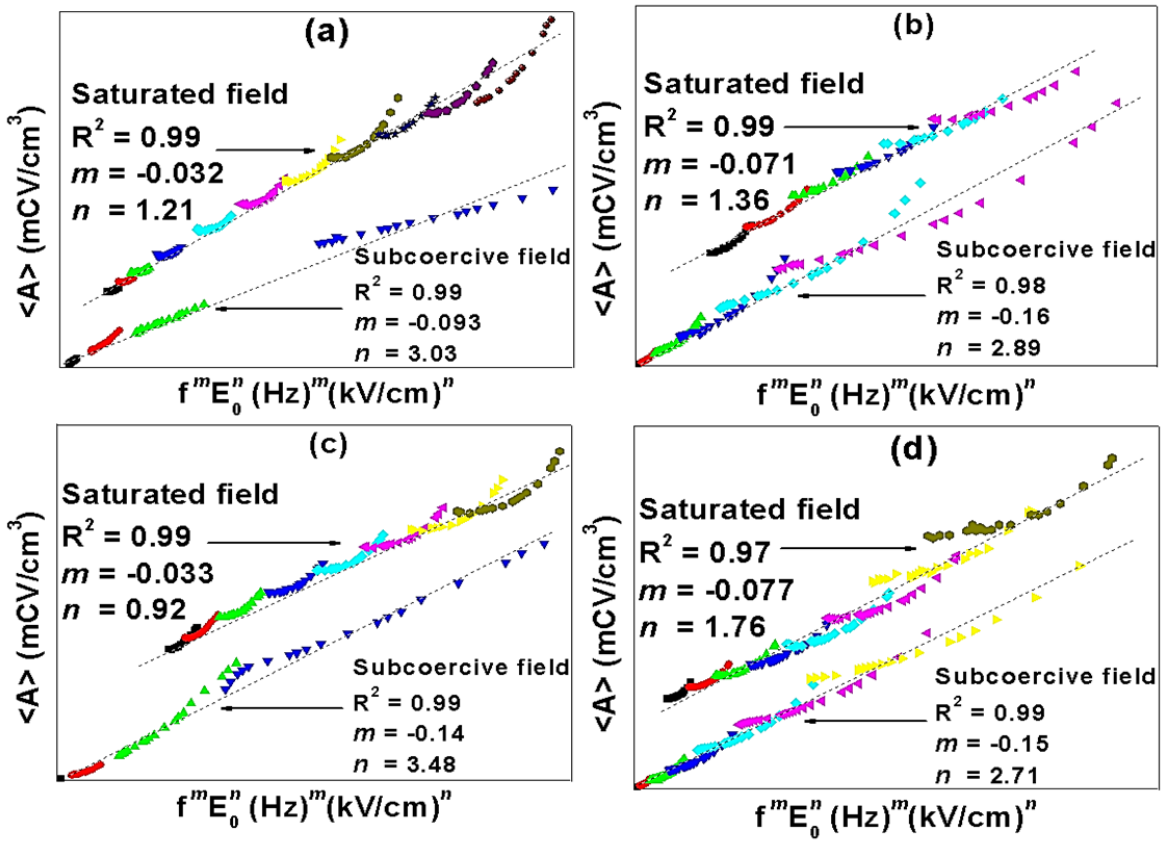

Figure 9.8: Scaling relations for sub-coercive and saturated field conditions (a) BT single layer system, (b) bilayer with equal thickness system, (c) bilayer with unequal thickness system, and (d) trilayer system. Dotted lines indicate linear relations fitted to data in each regime.

In describing the physical meaning of scaling exponents, the *f*-exponent *m* refers to how quickly the domain can switch corresponding to frequency *f* of electric field switching. A higher

negative magnitude for exponent *m* implies longer switching time where the ferroelectric domains cannot follow the applied AC electric field. Several variables may cause the delay in domain switching including charged defects and space charges [416]. The polarization and hysteresis area <*A*> decrease rapidly with increase in negative coefficient of *m*. On the other hand, if exponent *m* has lower negative coefficient, this implies that the switching time is short. The ferroelectric domains can follow the applied AC electric field, so the polarization and hysteresis area <*A*> decreases slowly. The E_0-exponent *n* refers to the ease of domain wall motion. The high exponent *n* value refers to the ability of domain in following the applied electric field direction, so that hysteresis parameters (<*A*>, P_r, E_C) increase sharply with increasing E_0. Conversely, the low exponent *n* refers to the poor ability of domain switching in following the direction of applied electric field, so hysteresis parameters increase slowly [393].

Table 9.3 shows the power-law scaling exponent *m* and *n* for sub-coercive and saturated field conditions for all cases. Comparatively, the exponent *m* of BT single layer system under sub-coercive field condition has lower negative value (-0.093) than that of BT bulk ceramic [415]. Generally, domains of material with smaller grain size would respond to switching field slowly than that of material with larger grain size because it possess high density of grain boundaries. However in this case, BT single layer with smaller grain size was found to exhibit lower negative value of exponent *m* than that of BT bulk ceramic possessing larger grain size. This could be explained by considering exponent *m* as rate of decrease of domain response with increasing frequency *f*. Generally, as frequency increases the domain response will be delayed. This effect is further amplified in materials with smaller grain size. Since domain wall velocity is already small, a further increase in frequency does not have much effect. This is why exponent *m*

of BT single layer has lower negative coefficient than that of BT bulk ceramic. In addition, exponent *m* of BT single layer has the lowest negative value compared with that of graded

Table 9.3 List of exponent *m* and *n* in power-law scaling relations for various composite systems.

System	Sub-coercive field		Saturated field	
	Exponent *m*	**Exponent *n***	**Exponent *m***	**Exponent *n***
BT single crystal (Previous work[402])	$1.667E_0-2.804$	4.157	-0.195	0.95
BT bulk ceramic (Previous work[415])	-0.36	3.64	-0.23	0.87
BT Single layer	-0.093	3.03	-0.032	1.21
Bilayer equal thickness	-0.16	2.89	-0.071	1.36
Bilayer unequal thickness	-0.14	3.48	-0.033	0.92
Trilayer	-0.15	2.71	-0.077	1.76

bilayer and trilayer ceramic systems. This can be related to internal bias field in this system as discussed earlier. The exponent *n* in sub-coercive field condition for BT single layer is smaller than that of BT single crystal and BT bulk ceramic. Basically, domain switching mechanism in sub-coercive field condition is related to reversible 180º domain switching [415] or amount of domain volume which is proportional to grain size. Consequently, BT single layer possessing smaller grain size should have smaller exponent *n* value. Surprisingly, exponent *n* of BT single layer was not the highest when compared with bilayer and trilayer systems. The highest value of

exponent *n* was found to be for graded bilayer with unequal thickness as listed in Table 9.3. This could be caused by enhancement in domain wall mobility occurring from coupling between layers. The exponent *n* of trilayer composite was lowest owing to its high internal bias which pins the domain wall motion.

In saturated field condition, the exponent *m* of BT single layer had lower negative value compared to both BT single crystal and BT bulk ceramic. Upon comparison with bilayer and trilayer composites, exponent *m* of BT single layer had distinctively lower negative value than that of bilayer with equal thickness and trilayer systems but similar to that of bilayer with unequal thickness. This phenomenon can be attributed to strength of internal bias field. BT single layer and bilayer with unequal thickness systems have weak and similar internal bias field value as listed in Table 9.2, thus exponent *m* has lower negative value. The internal bias field for bilayer with equal thickness and trilayer composites is quite large so exponent *m* has higher negative coefficient. From Table 9.3, it can be seen that the exponent *n* for BT single layer was higher than that for BT single crystal and bulk ceramic. Since hysteresis behavior near saturated polarization does not change much, BT single layer may have distinct exponent *n* than that in BT single crystal and bulk ceramics which were measured below the saturated field condition. Comparing bilayer and trilayer composites, the exponent *n* was highest for trilayer while the smallest for bilayer with unequal thickness. It is very interesting that exponent *n* values of both systems invert from sub-coercive field condition. The trilayer composite with lowest exponent *n* under sub-coercive field condition possess the highest value under saturated field condition, while the bilayer with unequal thickness has the highest *n* coefficient under sub-coercive field condition but it changes to lowest one under saturated field condition. This may be related to the magnitude of internal bias field which is highest for trilayer as shown in Table 9.2. Thus, these

composites provide a wide range of tuning capability of ferroelectric polarization, coercive field and hysteresis area, by varying the grading and number of layers.

9. 4. Chapter summary:

In summary, graded bilayer and trilayer bulk composite of BT and BTBCN were synthesized with different thickness of individual layer while keeping the same overall effective thickness. TEM and SEM images depicted a sharp interface with needle shape domains across the interface. The domain size was found to be larger on BT side as compared to that on BTBCN side. Temperature dependence of dielectric response for all composite systems was found to exhibit shifting of Curie peak with respect to each constituent material due to coupling between layers. Polarization mismatch between uncoupled BT and BTBCN resulted in internal electric field in composite specimen which produces new polarization states in each layer by perturbing free energy of the composite specimen. Further, the differences in grain size, tetragonality, and domain mobility of each layer also perturbs the electrical response in coupled layered composites. The dynamic hysteresis behavior and power-law scaling relations of BT single layer, bilayer with equal and unequal thickness, and trilayer ceramic systems were derived. All cases exhibited similar trends where hysteresis area $<A>$, remnant polarization (P_r) and coercive field (E_C) was found to decrease with increasing frequency due to delayed response. But, the magnitude of these hysteresis parameters was found to increase with increase in applied electric field due to enlargement of electrical driving force. Graded trilayer system was found to possess the strongest internal bias field while graded bilayer with unequal thickness system had the lowest magnitude. The trilayer composite was found to exhibit a double hysteresis loop due to polarization mismatch between layers.

Chapter-10 Summary and future work

10.1 Summary

The objective of this research was to design, synthesize and characterize the lead-free piezoelectric materials with enhanced functional properties and to understand their structure-property relationships. Following are the important accomplishments and learning achieved in this thesis:

1. In order to improve the piezoelectric properties, a novel method for synthesis of lead-free piezoelectric NBT-BT ceramics was developed. This process was based on structural transformation of NTO whiskers to piezoelectric NBT-BT. A detailed microstructural study was conducted to understand the sintering at various stage of processing. This novel method for synthesizing the NBT-BT ceramics opens the possibility of achieving varying grain shape and sizes with certain degree of texturing resulting in enhanced piezoelectric response.
2. Nanostructured ferroelectric NBT-BT whiskers with high aspect ratio were synthesized topochemically using NTO as a host structure. High energy x-ray diffraction coupled with PDF and Raman scattering analyses was used to demonstrate that the average structure of NBT-BT whiskers was rhombohedral, i.e. a ferroelectricity enabling type. HRTEM analysis revealed local monoclinic-type structural distortions indicating a modulated structure at the nanoscale in the MPB composition of NBT-BT whiskers. The structural rearrangement during the synthesis of NBT-BT whiskers was found to occur via the translation of edge shared octahedra of NTO into a corner sharing coordination. The high temperature morphological changes depicting disintegration of isolated

whiskers into individual grains due to higher grain boundary energy were found to occur in a close analogy with Rayleigh-type instability.

3. The local structural distortions coupled with elastic degrees of freedom results in hierarchical domain structure in MPB composition of NBT-BT. The local polar distortions with lower symmetry in A-site disordered NBT-BT systems are different than that of lead-based B-site disordered relaxors. The dynamics of ferroelectric nano domains were found to be constrained by ferroelastic domains in NBT-BT. The nano-beam electron diffraction revealed higher deviation in g vectors suggesting lower local symmetry in NBT-BT which were however found to be compensated over larger length scales. To delineate the contribution from inter-domain interactions and surrounding numerous grains, polycrystalline NBT-BT whiskers with same compositions were investigated. The HRTEM analysis revealed presence of a local monoclinic symmetry as monoclinic lattice with higher degree of freedom can easily adopt local stress. However, the neutron diffraction analysis suggested an average rhombohedral phase. The presence of monoclinic domains within rhombohedral domains can easily act as bridging phase. Small size of nanotwins was found to facilitate the piezoelectricity due to easy accommodation of the macroscopic strain induced by external stimuli. The short range crystallographic distortions in NBT-BT were found to provide explanation for the different phase transitions that have been reported for this material around the MPB.

4. $[001]_{pc}/[012]_{Rh}$ textured piezoelectric NBT-BT ceramics were synthesized using a novel processing technique that employs NBT seeds. The 92% textured NBT-BT specimen was found to exhibit 200% improvement in the value of d_{33}. The piezoelectric response was found to increase monotonously with the increase in the degree of texturing. The

experimental evidence and theoretical estimates explaining the mechanism of textured grain growth on the NBT seeds was provided. The interface of the NBT seeds and the textured grain was found to be coherent and defect free facilitating the domain wall motion resulting in higher piezoelectric response. Also, the textured specimens exhibited a lower coercive field and coherent nature of domain switching.

5. The piezoelectric NBT-BT textured in $(001)_{PC}$ orientation was found to depict high d_{33} ~322 pC/N compared to ~160 pC/N observed in randomly oriented NBT-BT ceramics. I*n-situ* neutron scattering experiments revealed electric field induced structural phase transformation in randomly oriented polycrystalline NBT-BT, which was however absent in textured NBT-BT. The absence of electric field induced structural phase transformation in textured NBT-BT was attributed to smaller coherence length scales of PNRs and /or inhibition due to internal stress induced by domain switching prior to structural transformation.

6. A series of new piezoelectric (1-x) $BaTiO_3$-x$A(Cu_{1/3}Nb_{2/3})O_3$ (A: Sr, Ba and Ca) ceramics were developed. The piezoelectric instability in these compositions was found to increase with the increase in the value of x up to certain extent and then drop. Interestingly, long range polar ordering was found to decrease monotonously with the increase in the value of x suggesting that the origin of the enhanced piezoelectric instability is not a simple function of the long range polar ordering. Instead it may be associated with localized polar distortions. High energy x-ray diffraction coupled with atomic PDF analysis suggested an increased polar nature that well explains the enhanced piezoelectric instability. Raman scattering studies revealed that not only substitution of Cu^{2+} and Nb^{5+} on the Ti^{4+}-sites but also substitution of Sr^{2+} and Ca^{2+} on the Ba^{2+} -sites

substantially modifies the octahedral dynamics as well as significantly distorts the octahedral cage resulting in localized distorted regions of lower symmetry, in line with the atomic PDFs results. The high temperature stability of high frequency Raman modes suggested that these local polar regions exist well above the T_c. The EPR spectroscopy confirmed that Cu^{2+} occupies distorted octahedral sites thus creating oxygen vacancies to maintain charge neutrality. The EPR spectra also suggested that the A-site substitution of Sr^{2+} and Ca^{2+} substantially changes the crystal field surrounding the Cu^{2+} ions. This substitution results in the formation of defect dipoles $(Cu''_{Ti} - V_o^{\bullet\bullet})^{\times}$ oriented along the c-axis of the perovskite lattice inducing strong internal bias that translates the PE-hysteresis loop on the *E-field* axis. The local defect structure substantially modulates the domain structure resulting in nano-domains with broad walls with higher domain mobility. The presence of nano domains and local structural distortions induce diffuse phase transitions indicating a subsidence of the long range polar ordering. The piezoelectric instability followed well the local polar distortions that enhance it. However, after certain extent of modification the macroscopic functional response is suppressed due to confinement of the domain walls within the geometrical restrictions of the grain boundaries, though sufficient strong polar distortions still persisted locally.

7. The $BaTiO_3 - Ba(Cu_{1/3}Nb_{2/3})O_3$ (BTBCN) solid solution was modified with Sn to achieve compositions with high dielectric constant ≥ 7000, low loss factor ≤ 1 % and grain size in submicron regime. Sn-doped compositions denoted as SBTBCN-2 and SBTBCN-3 were found to exhibit very high dielectric constant of 9580 and 7440 respectively at RT along with low loss tangent of < 0.6%. These compositions have potential application in Y5V type MLCCs.

8. The graded bilayer and trilayer bulk composite of BT and BTBCN were synthesized with different thickness of individual layer while keeping the same overall effective thickness. TEM and SEM images depicted a sharp interface with needle shape domains across the interface. The domain size was found to be larger on BT side as compared to that on BTBCN side. Temperature dependence of dielectric response for all composite systems was found to exhibit shifting of Curie peak with respect to each constituent material due to coupling between layers. Polarization mismatch between uncoupled BT and BTBCN resulted in internal electric field in composite specimen which produces new polarization states in each layer by perturbing free energy of the composite specimen. Further, the differences in grain size, tetragonality, and domain mobility of each layer also perturbs the electrical response in coupled layered composites. The dynamic hysteresis behavior and power-law scaling relations of BT single layer, bilayer with equal and unequal thickness, and trilayer ceramic systems were derived. All cases exhibited similar trends where hysteresis area $<A>$, remnant polarization (P_r) and coercive field (E_C) was found to decrease with increasing frequency due to delayed response. But, the magnitude of these hysteresis parameters was found to increase with increase in applied electric field due to enlargement of electrical driving force. Graded trilayer system was found to possess the strongest internal bias field while graded bilayer with unequal thickness system had the lowest magnitude. The trilayer composite was found to exhibit the double hysteresis loop due to polarization mismatch between layers.

10.2 Future work

1. The neutron diffraction coupled with PDF would be interesting tool to obtain further insights about the octahedral disorder and nano-scale structural distortions in NBT-BT system.
2. The intermediate phase transition has been observed in NBT-BT with A-site disorder and PMN-PT with B-site disorder. However, above intermediate phase transition temperature (T_d), NBT-BT loses its piezoelectric response contrary to that of PMN-PT. A comparative structural analysis should be performed to understand these differences in the nature of phase transition and piezoelectricity.
3. Electrical measurements should be performed on the individual nanostructured lead-free NBT-BT whiskers to confirm their ferroelectric and piezoelectric nature.
4. NBT-BT randomly oriented polycrystalline and textured specimen exhibit different structural phase transformation behavior under the application of *E*-field. In order to provide in-depth understanding of this behavior, detailed neutron diffraction studies coupled with PDF analysis and HR-TEM needs to be performed.
5. Analysis of domains structures at various length scales should be performed on the single crystal specimen of NBT-BT across MPB. The average and local structural changes should be investigated to understand functional response across MPB in A-site disordered NBT-based systems.
6. Synthesis of (1-x) $BaTiO_3$-x$A(Cu_{1/3}Nb_{2/3})O_3$ (A: Sr, Ba and Ca and x = 0.0-0.03) solid solutions should be extended to the higher concentrations to investigate the presence of a tricritical point. Materials at the tricritical point exhibit high piezoelectric response. This

study would also be helpful in understanding the role of A-site cation in $BaTiO_3$, $CaTiO_3$ and $SrTiO_3$ systems.

7. Synthesis of multilayer structure of Sn-doped $BaTiO_3$ – $Ba(Cu_{1/3}Nb_{2/3})O_3$ ceramics should be performed to achieve low temperature coefficient of capacitance (LTCC).
8. In order to understand the effect of coupling at the interface in a bulk composite, synthesis of graded thin film multilayer structures of $BaTiO_3$ and $BaTiO_3$–$Ba(Cu_{1/3}Nb_{2/3})O_3$ should be performed.

Publications

(a) Papers in Journals:

i. *Giant Piezoelectric Response in Grain-Oriented lead-free piezoelectric* $Na_{0.5}Bi_{0.5}TiO_3$-$BaTiO_3$ *Ceramics*, Deepam Maurya, Yuan Zhou, Yongke Yan, and Shashank Priya. (Submitted)

ii. *Mechanism of enhanced piezoelectric instability in lead–free (1-x)* $BaTiO_3 - x\ A(Cu_{1/3}Nb_{2/3})O_3$ *(A = Sr, Ca, Ba) solid solutions,* Deepam Maurya, V. Petkov, Ashok Kumar, J. E. Mahaney, R. S. Katiyar and Shashank Priya. (Submitted)

iii. *Origin of high piezoelectric response in A-site disordered morphotropic phase boundary systems*, Deepam Maurya**,** M. Murayama, A. Pramanick, W. T. Reynolds Jr, Ke An, and Shashank Priya**.** (Submitted)

iv. *Enhanced Piezoelectricity and nature of electric-field induced structural phase transformation in textured lead-free piezoelectric* $Na_{0.5}Bi_{0.5}TiO_3$-$BaTiO_3$ *ceramics*, Deepam Maurya, A. Pramanick, Ke An and Shashank Priya, *Appl. Phys. Lett*. 100, (2012) 172906

v. *Nanostructured Lead – Free Ferroelectric* $Na_{0.5}Bi_{0.5}TiO_3$-$BaTiO_3$ *Whiskers: Synthesis Mechanism and Structure,* Deepam Maurya, Velari Petkov, Ashok Kumar, and Shashank Priya, *Dalton Trans*., 41 (2012), 5643

vi. *Synthesis and characterization of* $Na_2Ti_6O_{13}$ *whiskers and their transformation to (1-x)* $Na_{0.5}Bi_{0.5}TiO_3$-$xBaTiO_3$ *ceramics,* Deepam Maurya, M. Murayama, Shashank Priya, *J. Am. Ceram. Soc*., 94 (2011) 2857

vii. *Magnetoelectric intercations in lead based and lead-free composites*, M. I. Bichurin, V. M. Petrov, A.Yu. Zakharov, D. V. Kovalenko, S. C. Yang, Deepam Maurya, V. Bedekar, and S. Priya, *Materials, 4*(4), (2011), 651-702,

viii. *Dielectric and Ferroelectric Response of Compositionally Graded Bilayer and Trilayer composites of $BaTiO_3$ and $0.975BaTiO_3$-$0.025Ba(Cu_{1/3}Nb_{2/3})O_3$,* Deepam Maurya, N. Wongdamnern, R. Yimnirun and S. Priya, *J. Appl. Phys.*, **108**, (2010), 124111

ix. *High Dielectric Composition in the System Sn-Modified $(1-x)BaTiO_3$–$xBa(Cu_{1/3}Nb_{2/3})O_3$, $x=0.025$ for Multilayer Ceramic Capacitor*, Deepam Maurya, Cheol-Woo Ahn, Shujun Zhang, Shashank Priya, *J. Am. Ceram. Soc*., 93, (2010), 1225

x. *A generalized rule for large piezoelectric response in perovskite oxideceramics and its application for design of lead-free compositions,* Cheol-Woo Ahn, Deepam Maurya, Chee-Sung Park, Sahn Nahm, and Shashank Priya, *J. Appl. Phys.* 105, 114108 (2009)

(b) Presentations in Conferences/ Seminars/Symposia:

Invited presentations:

i. *Design and fabrication of piezoelectric ceramics for sensors and actuators*, Deepam Maurya and Shashank Priya, Department of Physics and Astronomy, Indiana University South Bend, Nov. 3, 2011

ii. New Processing Technique for NBT-BT Ceramics, Deepam Maurya and Shashank Priya, NSF INAMM, August 7, 2011, The Hotel Roanoke & Conference Center, Roanoke, VA

iii. *Synthesis of Various Templates and Their Effect on Texture Evolution in (1-x) $Na_{0.5}Bi_{0.5}TiO_3$-$xBaTiO_3$ Ceramics*, Deepam Maurya and Shashank Priya, Materials Science and Technology Conference, George R. Brown Convention Centre, Houston, Texas, October 17-21, 2010

iv. *KNN based lead free piezoelectricc*, Cheol Woo Ahn, Deepam Maurya, Shashank Priya, presented in 14th US-Japan Seminar on Dielectric and Piezoelectric Materials, Welches, Oregon, USA, October 11-14, 2009

Contributed presentations:

i. Origin and Role of Hierarchal Domain Structure in $(Na_{1/2}Bi_{1/2})TiO_3$-$xBaTiO_3$ Single Crystals, Deepam Maurya and Shashank Priya, MRS Fall meeting, Hynes Convention Center, Boston, MA, Nov 28 – Dec 2, 2011

ii. *Lead Free Piezoelectric Cearmics*, Deepam Maurya, Shashank Gupta, Yongke Yan, and Shashank Priya, IWPMA, August 7-11, 2011, The Hotel Roanoke & Conference Center, Roanoke, VA

iii. *Flux growth and electrical properties of* $(1-x)Na_{0.5}Bi_{0.5}TiO_3$-$xBaTiO_3$ *single crystal*, Deepam Maurya, Shujun Zhang and Shashank Priya, Electronic Materials and Application Meeting programmed by Electrocnic Devision and Basic Sceince Devision of the American ceramic Society, lake Baena Vista, FL, USA, January 19-21, 2011

iv. *Synthesis and characterization of lead free piezoelectric* $(1-x)\ BaTiO_3$-$xA\ (Cu_{1/3}Nb_{2/3})O_3$ *(A = Ba, Ca and Sr) ceramics*, Deepam Maurya and Shashank Priya, IWPMA , Antalya, Turkey, October 10-14, 2010

v. *Texturing of lead free* $(1-x)Na_{0.5}Bi_{0.5}TiO_3$-$xBaTiO_3$ *piezoelectrics using RTGG and TGG method*, Deepam Maurya, Yongke Yan, Shashank Priya, IWPMA , Antalya, Turkey, October 10-14, 2010

vi. Synthesis of 0.93 $Na_{0.5}Bi_{0.5}TiO_3$-$0.07BaTiO_3$ *textured ceramics using sodium hexa-titanate whiskers as templates,* Deepam Maurya, Shashank Priya, Electronic Materials and

Application Meeting programmed by Electrocnic Devision and Basic Sceince Devision of the American ceramic Society, lake Baena Vista, FL, USA, January 20-22, 2010

vii. *Synthesis of (1-x)$Na_{0.5}Bi_{0.5}TiO_3$-x$BaTiO_3$ lead-free textured ceramics*, Deepam Maurya, Cheol-Woo Ahn and Shashank Priya, Materials Science and Technology Conference, David L. Lawrence Convention Centre, Pittsburgh, Pennsylvania, October 25-29, 2009

Papers in refereed conference proceedings:

(i) *Structural and electrical characterization of lead free (1-x)$Na_{0.5}Bi_{0.5}TiO_3$-x$BaTiO_3$ piezoelectric ceramics*, Deepam Maurya, Cheol-Woo Ahn and Shashank Priya, Advances in Electroceramic Materials II, Vol. 221 (2010), DOI: 10.1002/9780470930915.ch5

(ii) *Lead-Free Piezoelectric Materials for Sensors*, Capacitors, and Actuators, Cheol-Woo Ahn, Deepam Maurya, Alex O. Aning and Shashank Priya, Advances in Electroceramic Materials II, Vol. 221 (2010), DOI: 10.1002/9780470930915.ch15

References:

1. K. Uchino, Ferroelectric Devices, 2009, (CRC Press, 2009).

2. T. Ikeda, Fundamentals of Piezoelectricity (Oxford University Press, New York, 1990).

3. D. Damjanovic, Rep. Prog. Phys. 61, 1267 (1998).

4. J. F. Nye, Physical Properties of Crystals, Their Representation by Tensor and Matrices (Oxford University Press, 1957).

5. G. H. Haertling, J. Am. Soc., 82, 797 (1999).

6. M. E Lines and A. M. Glass, Principal and Applications of Ferroelectrics and Related Materials (Claredon Press, Oxford, 1977).

7. Y. Xu, Ferroelectric Materials and Their Applications (North-Holland, Amsterdam, 1991)

8. R. Blinc and B. Zeks, Soft Modes in Ferroelectrics and Antiferroelectrics (North-Holland, Amsterdam, 1974).

9. B. Jaffe,W.R. Cook, and H. Jaffe, Piezoelectric Ceramics, (Academic, New York, 1971).

10. B. Noheda, A. Gonzalo, L.E. Cross, R. Guo, S.E. Park, D.E. Cox, G. Shirane, Phys. Rev. B61, 8687, (2000).

11. M.J. Hoffman, H. Kungl, J-Th. Reszat, S. Wagner, in Polar Oxides roperties, Characterization, and Imaging,ch.7, p. 137, ed. by R. Waser, U. Böttger, S. Tiedke (Wiley-VCH)].

12. S. Wada, K. Yako, H. Kakemoto, T. Tsurumi, and T. Kiguchi, J. Appl. Phys. 98, 014109 (2005)

13. Wei-Feng Rao and Yu U. Wang, Appl. Phys. Lett. 90, 041915 (2007)

14. G.A. Samara, in Solid State Physics, edited by H. Ehrenreich and F. Spaepen, Vol. 56 (Academic Press, New York, 2001).

15. G.A. Smolensky, A.I. Agranovskaya, Sov. Phys.Solid State, 1, 1429, (1959).

16. L. E. Cross, Relaxor ferroelectrics. In Robert Hull, Jürgen Parisi, R.M.Osgood Jr., HansWarlimont (Eds), Piezoelectricity, p.131, Springer-Verlag Berlin Heidelberg, 2008.

17. G. A. Smolenskii, V. A. Isupov, A. I. Agranovskaya, and N. N. Krainik, Soviet Physics-Solid State 2, 2651 (1961).

18. G. O. Jones and P. A. Thomas, Acta Crystallographica Section B-Structural Science 58, 168-178 (2002).

19. J. Suchainicz, K. Roleder, A. Kania, and J. Handerek, Ferroelectrics 77, 107 (1998).

20. K. Roleder, J. Suchanicz, and A. Kania, Ferroelectrics 89, 1 (1989).

21. J. Suchanicz, Ferroelectrics 172, 455 (1995).

22. C. S. Tu, S. -H. Huang, C. –S. Ku, H. –Y. Lee, R. R. Chien, V. H. Schmidt. H Luo, Appl. Phys. Lett., 96, 062903, (2010).

23. V. Dorcet, G. Trolliard, and P. Boullay, Chem. Mater., 20, 5061 (2008).

24. T. Takenaka, K. Maruyama, and K. Sakata, J. Jap. Phys. Part 1-Rgular Papers Short Notes & Review Papers 30, 2236, (1991).

25. S. Kuharuangrong and W. Schulze, Journal of the American Ceramic Society 78, 2274, (1995).

26. O. Elkechai, M. Manier, and J. P. Mercurio, Physica Status Solidi a-Applied Research, 157, 499 (1996).

27. T. Takenaka, K. Sakata, and K. Toda, Ferroelectrics 106, 375, (1990).

28. P. Marchet, E. Boucher, V. Dorcet and J. P. Mercurio, J. Eur. Ceram. Soc., 26, 3037, (2006).

29. H. Nagata and T. Takenaka. Jpn. J. Appl. Phys. Part I, 36, 6055, (1997).

30. H. Nagata and T. Takenaka. Ferroelectrics, 229, 273, (1999).

31. Y Li, W. Chen, J. Zhou , Q. Xu, H. Sun, R. Xu, Mater. Sci. Engg. B., 112, 5, (2004).

32. Y. S. Sung, J. M. Kim, J. H. Cho, T. K. Song, M. H. Kim, H. H. Chong, T. G. Park, D. Do, and S. S. Kim, Appl. Lett., 96, 022901, (2010).

33. Q. Xu, D. –P. Huang, M. Chen, Han –Xing Liu, Bok –Hee Kim, J. Alloys and Compounds, 471, 310, (2009).

34. X. X. Wang, X. G. Tang and H. L. Chan, Appl. Phys. Lett., 85, 036951, (2004)

35. B.-J. Chu, D.-R. Chen, G.-R. Li, and Q.-R. Yin, Journal of the European Ceramic Society, 22, 2115, (2002).

36. Q. Xu, M. Chen, W. Chen, H. X. Liu, B. H. Kim, and B. K. Ahn, Acta Materialia 56, 642, (2008).

37. T. Takenaka, H. Nagata, and Y. Hiruma, IEEE Transactions on Ultrasonics Ferroelectrics and Frequency Control, 56, 1595, (2009).

38. G. L. Messing, S. Trolier-McKinstry, E. M. Sabolsky, C. Duran, S. Kwon, B. Brahmaroutu, P. Park, H. Yilmaz, P. W. Rehrig, K. B. Eitel, E. Suvaci, M. Seabaugh, and K. S. Oh, Crit. Rev. Solid State Mater. Sci., 29 [2], 45 (2004).

39.Y. Saito, H. Takao, T. Tani, T. Nonoyama, K. Takatori, T. Homma et al., Nature ,432**,** 84-87 (2004).

40. H. Yilmaz, G. L. Messing and S. Trolier-McKinstry, J. Electroceram., 11, 207 (2003).

41. Y. K. Yan, H. P. Zhao, D. Liu, *J*. Electroceram, 21, 246, (2008).

42. T. Motohashi, T. Kimura, J. Euro. Ceram. Soc., 27, 3633, (2007).

43. T. Tani, T. Kimura, Advances in Applied Ceramics, 105, 55, (2006).

44. T. Tani, E. Fukuchi, T. Kimura, J. Jpn. Soc. Powder Metall., 49, 198, (2002).

45. J. B. Babu, G. Madeswaran, M. He, D. F. Zhang, X. L. Chen, and R. Dhanasekaran, Journal of Crystal Growth 310, 467, (2008).

46. R. Sun, Q. Zhang, B. Fang, J. Jiao, X. Li, X. Zhao, D. Lin, D. Wang, and H. Luo, Appl. Phys. A,103,199,(2011).

47. Y. Chen, X. P. Jiang, H. S. Luo, J. Y, Dai, H. L. W. Chan, IEEE Transactions on Ultrasonics, Ferroelctrics, and frequency control, 57, 2601, (2010).

48. S. T. Zhang, A. B. Kounga, E. Aulbach, H. Ehrenberg, J. Rödel, Appl. Phys. Lett., 91, 112906, (2007).

49 S. T. Zhang, A. B. Kounga, E. Aulbach, T. Granzow, W. Jo, H. –J. Kleebe, J. Rödel, J. Appl. Phys., 103, 034107, (2008).

50. S. T. Zhang, A. B. Kounga, E. Aulbach, W. Jo, T. Granzow, H. Ehrenberg, J. Rödel, J. Appl. Phys., 103, 034108, (2008).

51. J. E. Daniels, W. Jo, J. Rodel and J. L. Jones, Appl. Phys. Lett., 95, 032904, (2009).

52. W. Jo, T. Granzow, E.Aulbach, J. Rödel, D. Damjanovic, J. Appl. Phys., 105, 094102, (2009).

53. S.-T. Zhang, A. B. Kounga, E. Aulbach, H. Ehrenberg, and J. Rödel, Appl. Phys. Lett. 91, 112906, (2007).

54. X. Tan, E. Aulbach, W. Jo, T. Granzow, J. Kling, M. Marsilius, H. –J. Kleebe, J. Rodel, J. Appl. Phys., 106, 044107,(2009).

55. M. Bichurin, V. Petrov, A. Zakharov, D. Kovalenko, S. C. Yang, D. Maurya, V. Bedekar, and S. Priya, Materials, 4, 615, (2011).

56. K Kusumoto, Proceedings of the Application of Ferrolectrics, ISAF 2007, Sixteenth IEEE International Symposium, Nara. Japan, 27-31 May 2007, pp. 686-687, DOI 10.1109/ISAF.2007.4393370 (2007).

57 D. Maurya, C. W. Ahn, S. J. Zhang, and S. Priya, Journal of the American Ceramic Society 93, 1225, (2010).

58. Y. Yuan, S. R. Zhang, X. H. Zhou, and J. S. Liu, Japanese Journal of Applied Physics Part 1-Regular Papers Brief Communications & Review Papers 45, 831 (2006).

59. T. Takenaka and H. Nagata, J. Eur. Ceram. Soc., 25, 2693, (2005).

60. M. Chen, Q. Xu, B. H. Kim, B. K. Ahn, J. H. Ko, W. J. Kang, and O. J. Nam, J. Eur. Ceram. Soc. 28, 843, (2008).

61. C. G. Xu, D. M. Lin, and K. W. Kwok, Solid State Sciences 10, 934, (2008).

62. T. Oh and M. H. Kim, Mater. Sci. Eng. B -Solid State Materials for Advanced Technology 132, 239, (2006).

63. D. X. Zhou, H. Li, S. P. Gong, Y. X. Hu, and K. Han, Journal of the American Ceramic Society 91, 2792, (2008).

64. J. R. Gomah-Pettry, E. Said, P. Marchet, and J. P. Mercurio, Journal of the European Ceramic Society 24, 1165, (2004).

65. D. Lin, K. W. Kwok, and H. L. W. Chan, Solid State Ionics 178, 1930, (2008).

66. D. M. Lin, D. Q. Xiao, J. G. Zhu, and P. Yu, Journal of the European Ceramic Society 26, 3247, (2006).

67. Z. Yang, B. Liu, L. Wei, and Y. Hou, Materials Research Bulletin 43, 81 (2008).

68. K. Yoshii, Y. Hiruma, H. Nagata, and T. Takenaka, Japanese Journal of Applied Physics Part 1-Regular Papers Brief Communications & Review Papers 45, 4493 (2006).

69. S. C. Zhao, G. R. Li, A. L. Ding, T. B. Wang, and Q. R. Yin, Journal of Physics D-Applied Physics 39, 2277, (2006).

70. Y. R. Zhang, J. F. Li, and B. P. Zhang, Journal of the American Ceramic Society 91, 2716, (2008).

71. Y. Hiruma, K. Yoshii, H. Nagata, and T. Takenaka, Journal of Applied Physics 103, 084121 (2008).

72. T. Oh, Japanese Journal of Applied Physics Part 1-Regular Papers Brief Communications & Review Papers 45, 5138-5143 (2006).

73. R. E. Jaeger and L. Egerton, J. Am. Ceram. Soc. 45, 209 (1962).

74. G. H. Haertling, J. Am. Ceram. Soc. 50, 329 (1967).

75. L. Egerton and D. M. Dillon, J. Am. Ceram. Soc. 42, 438 (1959).

76. E. Hollenstein, M. Davis, D. Damjanovic, and N. Setter, Applied Physics Letters 87 (2005).

77. S. B. Lang, W. Y. Zhu, and L. E. Cross, Ferroelectrics 336, 15-21 (2006).

78. R. P. Wang, R. J. Xie, K. Hanada, K. Matsusaki, H. Bando, T. Sekiya, and M. Itoh, Ferroelectrics 336, 39-46 (2006).

79 R. P. Wang, R. J. Xie, K. Hanada, K. Matsusaki, H. Bando, and M. Itoh, Physica Status Solidi a-Applications and Materials Science 202, R57 (2005).

80. Y. P. Guo, K. Kakimoto, and H. Ohsato, Materials Letters 59, 241 (2005).

81. Y. P. Guo, K. Kakimoto, and H. Ohsato, Applied Physics Letters 85, 4121, (2004).

82. G. Z. Zang, J. F. Wang, H. C. Chen, W. B. Su, C. M. Wang, P. Qi, B. Q. Ming, J. Du, and L. M. Zheng, Appl. Phys. Lett., 88, 212908, (2006).

83. Michel W. Barsoum "Fundamentals of ceramics", Mc Graw Hill Book Co., 1997.

84. M. D. Graff and M. E. McHenry, "Structure of Materials" Cambridge University Press, 2007

85. Michel Le Bellac, "Quantum Physics", Cambridge University Press, 2006.
86. X. L. Wang, T. M. Holden, G. Q. Rennich, A. D. Stoica, P. K. Liaw, H. Choo, and C. R. Hubbard, Physica B: Condensed Matter, 385, 673 (2006).
87. A. C. Larson and R. B. Von Dreele, (1995). General Structure Analysis System (GSAS). Los Alamos National Laboratory, NM, USA
88. H. M. Rietveld, J. Appl. Crystallogr.,2, 65(1969)
89. T. Egami and Simon J. L. Billinge, Underneath The Bragg Peaks, Pergamon An Imprint of Elsevier, 2003
90. Valeri Petkov, Milen Gateshki, Markus Niederberger, and Yang Ren, Chem. Mater., 18 ,814, (2006)
91. H. P. Klug, L. E. Alexander, In X-ray diffraction procedures for Polycrystalline Materials, Wiley: New York 1974.
92. J. R. Ferraro, K. Nakamoto, C. W. Brown, "Introductory Raman Spectroscopy" Academic Press, California, 2003
93. J.F. Scott, Rev. Mod. Phys., 46, 83 (1974).
94. P. S. Dobal, R. R. Das, R. S. Katiyar, D. C. Agrawal, .J. Am. Ceram. Soc., 83, 1953 (2000).
95. Yuhuan Xu, *Ferroelectric Materials and Their Applications*, (North-Hallad Publishing Co., Amesterdam, 1991).
96. Q. Xu, S. Chen,W. Chen, S.Wu, J. Lee, J. Zhou, H. Sun, Y. Lee, J. Alloys Compd., 381, 221, (2004).
97. J.R. Gomah-Pettry, S. Said, P. Marchet, J.P. Mercurio, J. Eur. Ceram. Soc., 24, 1165, (2004).
98. K H Hong, S E Park. J. Appl. Phys., 79, 388, (1996).

99. J. W. Waanders, Piezoelectric Ceramics-Properties and Applications (Philips Components, Eindhoven, 1991)

100. Y. J. Ma, J. H. Cho, Y. H. Lee, B. I. Kim, Mater. Chem. Phys., 98, 5 (2006).

101. Y. Liu, Y. Lu, S. Dai, J. Alloys and Compounds, 484, 801 (2009).

102. J. Hao, X. Wang, R. Chen, L. Li, Mater. Chem. Phys. 90**,** 282, (2005).

103. Q. Xu, X. Chen, W. Chen, S. Chen, B. Kim, J. Lee, , Mater. Lett., 59, 2437, (2005).

104. D. Z. Jin, X. M. Chen, Z. C. Xu, Mater. Lett., 58, 1701-1705, (2004).

105. J. Qi, Li. Sun, Peng Du and Longtu Li, J Am. Ceram. Soc., 93, 1044, (2010).

106. E. Aksel and J. L. Jones, J Am Ceram. Soc., 93, 3012, (2010).

107. A. Loachim, M.I. Toacsan, M. G. Banciu, L. Nedelcu, H. Alexandru, C. Berbecaru, D. Ghetu, G. Stoica, Materials Science and Engineering B, 109, 183 (2004).

108. A. Herabut, A. Safari, J. Am. Ceram. Soc., 80, 2954, (1997).

109. Y. Lin, S. Zhao, N. Cai, J. Wu, X. Zhou, C. W. Nan, Materials Science and Engineering B, 99, 449 (2003).

110. H. Nagata, T. Takenaka, J. Euro. Ceram. Soc., 21, 1299, (2001).

111. A Watcharapasorn, S. Jiansirisomboon, T. Tunkasiri, Mater. Lett., 61, 2986 (2007).

112. A Watcharapasorn, S. Jiansirisomboon, Ceramics International, 34, 769 (2008).

113. Y. Saito, H. Takao, T. Tani, T. Nonoyama, K. Takatori, T. Homma et al., "Lead-free piezoceramics," Nature ,432**,** 84 (2004).

114. Y. K. Yan, H. P. Zhao, D. Liu, J. Electroceram, 21, 246, (2008)

115 W. Zhao, Jing Ya, Ying Xin, Lie E and Dan Zhao, Heping Zhou, *J. Am. Ceram. Soc*., **92**, 1607, (2009).

116. Z. L. Wang and Z. C. Kang, *Functional and Smart Materials*, Plenum Press, New York, ,pp.93, 1998.

117. F. K. Lotgering, J. Inorg. Nucl. Chem., 9,113, (1959).

118. S. Andersson, A. D. Wadsley, Acta Cryst., 15, 194, (1962).

119. L. Liu and H. Fan, J. Electroceram., 16, 293-296 (2006).

120. S. B. Vakhrushev, B. G. Ivanitskii, B. E. Kvyatkovskii, A. N. Maistrenko, R. S. Malysheva, N. M. Okuneva, N. N. Parfenova, 25, 2613, (1983)

121. B. D. Cullity, *Elements of x-ray diffraction* (second edition), Addison-Wesley publishing company Inc., Philippines, 1978.

122. M. -K. Kang, D. –Y. Kim, N. M. Hwang, J. Eur. Ceram. Soc., 22, 603, (2002).

123. M. N. Rahaman, *Ceramic Processing*, Taylor & Fransis Group, FL (USA), 2007.

124. S.-M. Lee and S.-J. L. Kang, Acta Mater., 46, 3191, (1998).

125. S. H. Kim, J. –D. Byun, Won- Park, Y. Kim, J. Mater. Sci., 34, 3057, (1999).

126. S. J. P. Longworth, K. M. Knowles and R. E. Dunin-Borkowski, J. Phys.: Conference Series, 26, 235, (2006).

127. Imaging and microanalysis of ceramic materials with a scanning ion microprobe, K.K. Soni, J. M. Chabala, R. Magilevsky, R. Levi-Setti, K. Zhang, W. S. Wolbach, S. R. Bryan, Surface and Interface Analysis, 21, 117, (1994).

128. G. Grzinic and L. A. Bursill, J. Solid State Chem., 74, 151, (1983).

129. G. D. Fallon and B. M. Gatehouse, J. Solid State Chem.,49, 59, (1983).

130. R. E. Newnham, Mat. Res. Bull., 2, 1041, (1967).

131. E. C. Subbarao, J. Phys. Chem. Solids, 2, 665, (1962).

132. B. Aurivillius, Arkiv For Kemi, 2, 519 (1950).

133. R. Trivedi, "Theory of Capillarity" pp. 135-163 in *Lectures on the Theory of Phase transformations (2nd Edition)*, Edited by Hubert I. Aaroson, A Publication of The Minerals, Metals and Materials Society, Warrendale, Pennsylvania (1999).

134. J. M. Howe, *Interfaces in Materials*; pp. 83–86. Wiley, New York, 1997.

135. D. P. Woodruff, *The Solid–Liquid Interface*; pp. 3–5. Cambridge University Press, London, U.K., 1973.

136. B.-J. Fang, H.-Q. Xu, T.-H. He, H.-S. Luo, Z.-W. Yin, Journal of crystal growth , 244, 318-326 (2002).

137. M. Dong, Z.G. Ye, J. Crystal Growth, 209, 81, (2000).

138. B.J. Fang, H.Q. Xu, T.H. He, H.S. Luo, Z.W. Yin, J. Crystal Growth, 244, 318, (2002).

139. A. Khan, F.A. Meschke, T. Li, A.M. Scotch, H.M. Chan, M.P. Harmer, J. Am. Ceram. Soc., 82, 2958, (1999).

140. T. Li, A.M. Scotch, H.M. Chan, M.P. Harmer, J. Am. Ceram. Soc., 81, 244, (1998).

141. P.T. King, E.P. Gorzkowski, A.M. Scotch, D.J. Rockosi, H.M. Chan, M.P. Harmer, J. Am. Ceram. Soc., 86, 2182, (2003).

142. J.-Song Pan, X.-Wen Zhang, Ke-Pi Chen, J. Cryst. Growth, 284, 275, (2005).

143. X.Y. Liu, E.S. Boek, W.J. Briels and P. Bennema, Nature, 374, 342, (2005).

144. J. P. van der Eerden, "Crystal Growth Mechanism*";* pp.3111-475 in *Hand-book of crystal growth Fundamentals Part A: Thermodynamics and Kinetics*, Edited by D. T. J. Hurle. North Holland, Amsterdam, 1993.

145. J. W. Martin and R. D. Doherty, PP. 210-2, *Stability of Microstructure in Metallic Systems*, Cambridge University Press, London, 1976.

146. Takao Motohashi and Toshio Kimura, J. Am. Ceram. Soc., 91, 3889, (2008)

147. M. Upmanyu, D.J. Srolovitz, A.E. Lobkovsky, J.A. Warren, W.C. Carter, Acta Materialia, 54, 1707, (2006).

148. L. Zhou and H. Y. Sohn, Ind. Eng. Chem. Res., 35, 954, (1996).

149. J.-K. Liou, M.-H. Lin, Hong -Yang Lu, J. Am. Ceram. Soc., 85, 2931, (2002).

150. K.-S. Moon and S.-J. L. Kang, J. Am. Ceram. Soc., 91, 3191, (2008).

151. M. Demartin and D. Damjanovic, Appl.. Phys. Lett., 68, 3046, (1996).

152. G. A Samara and E. L. Venturini, Phase transitions, 79, 21-40, (2006).

153. L. E. Cross, Ferroelectrics, 76, 241, (1987).

154. Nina Balke, Torsten Granzow and Jurgen Rodel, J. Appl. Phys., 104, 054120, (2008).

155. J. F. Scott *Ferroelectr. Rev*., 1,1, 1998.

156. S. O'Brien, L. Brus, C. B. Murray, J. Am. Chem. Soc. 123,12085, (2001).

157. C. Liu, B. Zou, A. J. Rondinone, Z. J. Zhang, J. Am. Chem. Soc. 123, 4344, (2001).

158. B. Jiang, J. L. Peng, L. A. Bursill, W. L. Zhong, J. Appl. Phys., 87, 3462, (2000).

159. M. Alexe, C. Harnagea, W. Erfurth, D. Hesse, U. Gösele, Appl. Phys. A, **70**, 247, (2000).

160. S. A. Morin, M. J. Bierman, J. Tong, S. Jin, Science, 328, 476(2010).

161. Y. Xia, P. Yang, Y. Sun, Y. Wu, B. Mayers, B. Gates, Y. Yin, F. Kim, H. Yan, *Adv. Mater*., 15, 353, (2003).

162. H. Q. Cao, Y. Xu, J. M. Hong, H. B. Liu, G. Yin, B. L. Li, C. Y. Tie, Z. Xu, Z. *Adv. Mater*., 13, 1393, (2001).

163. Y. J. Zhang, N. L. Wang, S. P. Gao, R. R. He, S. Miao, J. Liu, J. Zhu, X. Zhang, Chem. Mater. 14, 3564(2002).

164. Y. Y. Wu, P. D. Yang, J. Am. Chem. Soc.**,** 123, 3165, (2001).

165. M. S. Gudiksen, C. M. Lieber, J. Am. Chem. Soc., 122, 8801 (2000).

166. X. Wang and Y. Li, *J. Am. Chem. Soc*.,124, 2880, (2002).

167. X. G. Peng, L. Manna, W. D. Yang, J. Wickham, E. Scher, A. Kadavanich, A. P. Alivisatos, Nature, 404, 59, (2000).

168. C. Pacholski, A. Kornowski, H. Weller, *Angew Chem. Int. Ed.* 41,1188, (2002).

169. Y. Yin, B. Gates, Y. Xia, *Adv. Mater*., 12,1426, (2000).

170. M. Granahan, M. Holmes, W. A. Schulze, R. E. Newnham J. Am. Ceram. Soc. **64**, C68, (1981).

171. C. C. Li., C. C. Chiu, S. B. Desu, J. Am. Ceram. Soc., 74,42, (1991).

172. Y. Seno and T. Tani, Ferroelectrics, 224, 365, (1999).

173. S. F. Poterala, R. J. Meyer Jr, and G. L. Messing, 94**,** 2323, (2011).

174. D. Maurya, C.-W. Ahn and S. Priya, Advances in Electroceramic Materials II, 221, 47, (2010).

175. W. Cao and L. E Cross, Phys. Rev. B, 47, 4825, (1993).

176. A. J. Bell, J. Mater. Sci., 41, 12, (2006).

177. D. Maurya, M. Murayama, S. Priya, J. Am. Cearm. Soc., 2011, 94, 2857-2871

178. V. Petkov, *Materials Today*,11, 28, (2008).

179. M. Gateshki, S. Yin, Y. Ren, and V. Petkov, Chem. Mater., 19, 2512, (2007).

180. C. E. Bamberger and G. M. Begun, J. Am. Ceram. Soc., 70, C48, (1987).

181. T. Kasuga, M. Hiramatsu, A. Hoson, T. Sekino, K. Niihara, Adv. Mater., 11, 1307, (1999).

182. Y. Su, M. L. Balmer, B. C. Bunker, J. Phys. Chem. B, 104, 8160, (2000).

183. M. Ocana, J. V. Garcia-Ramos, C. J. Serna, J. Am. Ceram. Soc., 75, 2010, (1992).

184. B. Mihailova, M. Gospodinov, B. Güttler, R. Stosch, and U. Bismayer, *J. Phys. : Condens. Matter*, 19, 275205, (2007).

185. J. Kreisel, A. M. Glazer, P. Bouvier, and G. Lucazeau, Phys. Rev. B, 63, 174106, (2001).

186. D. A. Porter and K. E. Easterling, *Phase Transformation in Metal and alloys*, 2nd edition, CRC Press, UK, 1992.

187. C. N. R. Rao, Mater. Sci. Eng.: B, 18,1, (1993).

188. W. D. Kingery, H. K. Bowen, D. R. Uhlmann, *Introduction to Ceramics*, 2nd edition, John Wiley & Sons, Inc.: New York, 1976.

189. B. Noheda, and D. E. Cox, Phase Transitions, 79, 5, (2006).

190. D. E. Cox, B. Noheda G. Shirane, Y. Uesu, K. Fujishiro, Y. Yamada, Appl. Phys. Lett., 79, 400, (2001).

191. J. M. Kiat, Y. Uesu, B. Dkhil, M. Matsuda, C. Malibert, G. Calvarin, Phys. Rev. B, 65, 064106 (2002).

192. M. Iwata, T. Araki, M. Maeda, I. Suzuki, H. Ohwa, N. Yasuda, H. Orihara, Y. Ishibhashi, Jpn. J. Appl. Phys. 41, 7003, (2002).

193. A. S. Bhalla, R. Guo, R. Roy, Mat Res. Innovat. 4, 3, (2000).

194. K. Tkacz-Smiech, A. Kolezynski, W. S. Ptak, Solid State Comm. 127, 557, (2003).

195. L. Klinger and E. Rabkin, *Materialwissenschaft und Werkstofftechnik*, 36, 505, (2005).

196. W. W. Mullins, J. Appl. Phys. 28, 333, (1957).

197. J. W. Martin and R. D. Doherty, *Stability of Microstructure in Metallic Systems*, Cambridge University Press: London, 1976.

198. T. Motohashi and T. Kimura, J. Am. Ceram. Soc. 91, 3889, (2008).

199. S. Karim, M. E. Toimil-Molares, A. G. Bologh, W. Ensinger, T. W. Cornelius, E. U. Khan and R. Neumann, Nanotechnology, **17**, 5954, (2006).

200. D. Duft, T. Achtzehn, R. Müller, B. A. Huber, and T. Leisner, Nature (London), 412, 128, (2003).

201. D. J. Srolovitz and C. V. Thompson, Thin Solid Films, 139, 133, (1986).

202. J. Rodel, W. Jo, K. T. P. Seifert, E. M. Anton, and T. Granzow, J. Am. Ceram. Soc. 92, 1153 (2009).

203. S. Gorfman, P. Thomas, J. Appl. Cryst, 43, 1409, (2010).

204. E. Aksel, J. S. Forrester, J. L. Jones, P. A. Thomas, K. Page, and M. R. Suchomel, Appl. Phys. Lett., 98, 152901, (2011).

205. H. Fu, R. E. Cohen, Nature 403, 281 (2000).

206. B. Noheda, D. E. Cox, G. Shirane, R. Guo, B. Jones, and L. E. Cross, Phys. Rev. B, 63, 014103 (2000).

207. B. Noheda, D. E. Cox, G. Shirane, S. –E. Park, L. E. Cross and Z. Zhong, Phys. Rev. Lett. 86, 3891 (2001).

208. W. Cao and L. E Cross, Phys. Rev. B, 47, 4825 (1993).

209. M. J. Hoffmann, M. Hammer, A. Endriss, and D. C. Lupascu, Acta Mater. 49,1301(2001).

210. R. Guo, L. E. Cross, S-E. Park, B. Noheda, D. E. Cox, and G. Shirane, Phys. Rev. Lett. 84, 5423–5426 (2000).

211. Ilya Grinberg, Valentino R. Cooper & Andrew M. Rappe, Nature, 419, 909 (2002).

212. F. Cordero, F. Craciun, F. Trequattrini, E. Mercadelli, and C. Glassi, Phys. Rev. B 81, 144124 (2010).

213. I. P. Aleksandrova, A. A. Sukhovsky, Yu. N. Ivanov, Yu. E. Yablonskaya, and S. B. Vakhrushev, Phys. Sold State, 50, 496(2008).

214. B. Wylie-Van Eerd, D. Damjanovic, N. Klein, N. Setter, and J. Trodahl, Phys. Rev. B 82, 104112 (2010).

215. J. Yao, L. Yan, W. Ge, L. Luo, J. Li, and D. Viehland, Phys. Rev. B 83,054107 (2011).

216. Wook Jo, John E. Daniels, Jacob L. Jones, Xiaoli Tan, Pamela A. Thomas et al. J. Appl. Phys. 109, 014110 (2011).

217. John E. Daniels, Wook Jo, Jürgen Rödel**,** Veijo Honkimaki, Jacob L. Jones, Acta Materialia, 58**,** 2103 (2010).

218. G. Trolliard and V. Dorcet, Chem. Mater. 20, 5074, (2008).

219. Wook Jo, Silke Schaab, Eva Sapper, Ljubomira A. Schmitt, Hans-Joachim Kleebe et al., J. Appl. Phys. 110, 074106 (2011).

220. C. Ma, X. Tan, E. Dul'kin, and M. Roth, J. Appl. Phys., 108, 104105 (2010).

221. Y. Guo, Y. Liu, R. L. Withers, F. Brink, and Hua Chen., Chem. Mater., 23, 219 (2011).

222. D. Maurya, A. Pramanick, K. An, S. Priya, Appl. Phys. Lett. 100, 172906, (2012).

223. N. Waeselmann, B. Mihailova, B. J. Maier, C. Paulmann, M. Gospodinov, V. Marinova, and U. Bismayer, Phy. Rev. B 83, 214104 (2011).

224. K. H. Ahn, T. Lookman and A. R. Bishop, Nature, 428, 401, (2004).

225. G. Xu, J. Wen, C. Stock, and P. M. Gehring, Nature Materials, **7**, 562 (2008).

226. J. Yao, W. Ge, L. Luo, J. Li, D. Viehland, and H. Luo, Appl. Phys. Lett., 96, 222905 (2010).

[227] G. Xu, Z. Zhong, Y. Bing, Z.-G.Ye, and G. Shirane, Nature Materials, 5, 134 (2006)

228. A. R. Bishop, T. Lookman, A. Saxena and S. R. Shenoy, Europhys. Lett., 63, 289 (2003).

229. J. Y. Li, R. C. Rogan, E. Ustundag, K. Bhattacharya, Nature Material, 4, 776 (2005).

230. F.X. Li, R.K.N.D. Rajapakse, Acta Materialia 55, 6472, (2007).

231. Y. Hosono, K. Harada and Y. Yamashita, Jpn. J. Appl. Phys., 40, 5722 (2001).

232. X. L. Wang, T. M. Holden, G. Q. Rennich, A. D. Stoica, P. K. Liaw, H. Choo, and C. R. Hubbard, Physica B: Condensed Matter 385-386, 673 (2006).

233. A. C. Larson and R. B. Von Dreele, (1995). General Structure Analysis System (GSAS). Los Alamos National Laboratory, NM, USA

234. E. K. H. Salje, S. A. Hayward, W. T. Lee, Acta Cryst. A 61, 3 (2005).

235. Krzysztof Parlinski, Computer Physics Reports, 8, 153 (1988).

236. E. Salje, B. Kuscholke, B. Wruck, Phys. Chem. Min., 12, 132 (1985).

237. E.K.H. Salje, *Phase transitions in feroeleastic and co-elastic crystlas*, Cambridge University Press, Cambidge, 1990.

238. A. G. Khachaturyan, S. M. Shapiro, and S. Semenovskaya, Phys. Rev. B 43, 10832 (1991).

239. Y. M. Jin, Y. U. Wang, A. G. Khachaturyan, J. F. Li and D. Viehland, Phys. Rev. Lett., 91, 197601-1 (2003)

240. R. Theissmann, L. A. Schmitt, J. Kling, R. Schierholz, K. A. Schönau, and H. Fuess, J. Appl. Phys. 102, 024111,(2007).

241. R. Schierholz and H. Fuess, J. Appl. Cryst. 45, 766 (2012).

242. X. Z. Liao, Y. H. Zhao, S. G. Srinivasan, Y. T. Zhu, R. Z. Valiev and D. V. Gunderov, J. Appl. Phys., 84, 592 (2004).

243. C. A. Randall, D. J. Barber, R. W. Whatmore, J. Mater. Sci., 22, 925, (1987).

244. V. A. Zhirnov, Sov. Phys. JETP 35, 822 (1959).

245. S. Ii, K. Yamauchi, Y. Maruhashi, M. Nishida, Scripta Materialia 49, 723 (2003).

246.J. F. Nie, Acta Materialia, 52, 795(2004).

247. S. Gorfman, P. A. Thomas, J. Appl. Cryst. 43, 1409 (2010).

248. D. Pandey, A. K. Singh and S. Baik, Acta Cryst. A 64, 192 (2008).

249. J. Kreisel, P. Bouvier, B. Dkhil, P. A. Thomas, A. M. Glazer, T. R. Welberry, B. Chaabane, and M. Mezouar, Phys. Rev. B 68, 014113 (2003).

250. M. Hinterstein, M. Knapp, M. Hölzel, W. Jo, A. Cervellino, H. Ehrenberg , H. Fuess, J. Appl. Cryst. 43, 1314, (2010).

251. A. M. Glazer, Acta Cryst. A 31, 756 (1975).

252. D. I. Woodward and I. M. Reaney, Acta Cryst. B 61, 387 (2005).

253. I. Levin and I. M. Reaney, Adv. Funct. Mater. 22, 3445, (2012).

254. V. Dorcet, G. Trolliard, Acta Materialia, 56, 1753(2008).

255. D. I. Woodward, J. Knudsen, and I. M. Reaney, Phys. Rev. B 72, 104110 (2005).

256. Yu. U. Wang, Phys. Rev. B. 73, 014113(2006).

257. S. Kaufmann, U. K. Rößler, O. Heczko, M. Wuttig, J. Buschbeck, L. Schultz, and S. Fähler, Phy. Rev. Lett., 104, 145702 (2010).

258. C. –S. Tu, C. –M Hsieh, R. R. Chien, V. H. Schmidt, F. –T. Wang, and W. S. Chnag, J. Appl. Phys., 103, 074117(2008).

259. W. S. Chang, L. C. Lim, P. Yang, H. Miao, C. –S. Tu, Q. Chen, A. K. Soh, Appl. Phys. Lett. 94**,** 202907(2009).

260. Y. Sato, T. Hirayama, and Y Ikuhara, Phys. Rev. Lett. 107, 187601 (2011).

261. T. R. Shrout and S. J. Zhang, J. Electroceram., 19, 111, (2007).

262. W. Liu and X. Ren, Phys. Rev. Lett., 103, 257602, (2009).

263. Ben Wylie-van Eerd, Dragan Damjanovic, Naama Klein, Nava Setter, and Joe Trodahl, Phys. Rev. B, 82,104112, (2010).

264. P Fu, Z. Xu, R. Chu, W. Li, G. Zang, J. Hao, Mater. Sci. Engg. B, 167, 161, (2010).

265. H. Li, C. Feng, P. Xiang, Jpn. J. Appl. Phys., 42, 7387, (2003).

266. H. Li, C. Feng, W. Yao, Mater. Lett., 58, 1194, (2004).

267. W. Lang, D. Xiao, L. Dunmin, Z. Jianguo, Y. Ping, L. Xiang, Jpn. J. Appl. Phys., 46, 7382, (2007).

268. R. Zuo, C. Ye, X. Fang, J. Li, J. Eur. Ceram. Soc., 28, 871, (2008).

269. X.X. Wang, H. Chan, C. L. Choy, Appl. Phys. A: Mater. Sci. Process., 80, 333, (2005).

270. M. S. Yoon, Y. G. Lee, S. C. Ur, J. Electroceram., 23, 564, (2009).

271. Y. Saito, H.Takao, T. Tani, T. Nonoyama, K. Takatori, T. Homma, T. Nagaya and M. Nakamura, Nature, 432, 84, (2004).

272. S. Kwon, E. M. Sabolsky, G. L. Messing, S. Trolier-McKinstry, J. Am. Cearm. Soc., 88, 312, (2005).

273. W. Zhao, H. Zhou, Y. Yan, and D. Liu, J. Am. Ceram. Soc., 91, 1322, (2008).

274. W. Ge, H. Liu, X. Y. Zhao, B. J. Fang, X. B. Li, F. F. Wang, D. Zhou, P. Yu, X. M. Pan, D. Lin, and H. S. Luo, J. Phys. D: Appl. Phys., 41, 115403, (2008).

275. Q. Zhang, Y. Zhang, F. Wang, Y. Wang, D. Lin, X. Zhao, H. Luo, W. Ge, and D. Viehland, Appl. Phys. Lett., 95, 102904, (2009).

276. S. Kwon, E. M. Sabolsky, G. L. Messing, S. Trolier-McKinstry, J. Am. Cearm. Soc., 88, 312, (2005).

277. Deepam Maurya, Valeri Petkov, Ashok Kumar and Shashank Priya, Dalton Trans., 41, 5643, (2012)

278. M. A. Herman, W. Richter, H. Sitter, *Epitaxy: Physical Principles and Technical Implementation*, Springer-Verlag Berlin Heidelberg, 2004.

279. X. Tan, J. Frederick, C. Ma, W. Jo, and J. Rödel, Phys. Rev. Lett., 105, 255702 (2010).

280. S. Priya, K. Uchino and D. Viehland, Appl. Phys. Lett. 81, 2430 (2002).

281. K. Ohwada, K. Hirota, P. W. Rehrig, P. M. Gehring, B. Noheda, Y. Fujii, S. –E. Park and G. Shirane, J. Phys. Soc. Jpn. 70, 2778 (2001).

282. D. –S. Paik, S. –E. Park, S. Wada, S. –F. Liu and T. R. Shrout, J. Appl. Phys. 85, 1080, (1999).

283. T. R. Shrout and S. J. Zhang, J. Electroceram., 19, 111 (2007).

284. Ben Wylie-van Eerd, Dragan Damjanovic, Naama Klein, Nava Setter, and Joe Trodahl, Phys. Rev. B 82, 104112 (2010).

285. F. Cordero, F. Craciun, F. Trequattrini, E. Mercadelli, and C. Glassi, Phys. Rev. B 81, 144124 (2010).

286. J. Yao, L. Yan, W. Ge, L. Luo, J. Li, and D. Viehland, Phys. Rev. B 83,054107 (2011).

287. Wook Jo, Silke Schaab, Eva Sapper, Ljubomira A. Schmitt, Hans-Joachim Kleebe, A. J. Bell, J. Rödel, J. Appl. Phys. 110, 074106 (2011).

288. C. Ma, X. Tan, E. Dul'kin, and M. Roth, J. Appl. Phys., 108, 104105 (2010).

289. M. Davis, D. Damjanovic, and N. Setter, J. Appl. Phys., 97, 064101 (2005).

290. Y. Guo, Y. Liu, R. L. Withers, F. Brink, and Hua Chen., Chem. Mater., 23, 219 (2011).

291. Q. Zhang, Y. Zhang, F. Wang, Y. Wang, D. Lin, X. Zhao, H. Luo, W. Ge, and D. Viehland, Appl. Phys. Lett. 95, 102904 (2009).

292. A. J. Royals, A. J. Bell, J. E. Daniels, S. J. Milne, and T. P. Comyn, Appl. Phys. Lett., 98, 182904 (2011).

293. X. L. Wang, T. M. Holden, G. Q. Rennich, A. D. Stoica, P. K. Liaw, H. Choo, and C. R. Hubbard, Physica B: Condensed Matter 385, 673 (2006).

294. D. Damjanovic, Appl. Phys. Lett., 97, 062906 (2010).

295. D. Damjanovic, J. Am. Ceram. Soc., 88, 2663(2005).

296. D. A. Hall, A. Steuwer, B. Cherdhirunkorn, T. Mori, and P. J. Withers, J. Appl. Phys. 96, 4245 (2004).

297. C. T. Nelson, P. Gao, J. R. Jokisaari, C. Heikes, C. Adamo, A. Melville, S. –H Baek, C. M. Folkman, B. Wichester et al., Science, 334, 968 (2011).

298. J. Y. Li, R. C. Rogan, E. Üstündag and K. Bhattacharya, Nature Materials, 4, 776 (2005).

299. A. A. Bokov and Z. –G Ye, J. Appl. Phys., 91, 6656, 2002.

300. S. Teranishi, M. Suzuki, Y. Noguchi, M. Miyayama, C. Moriyoshi, Y. Kuroiwa, K. Tawa, and S. Mori, Appl. Phys. Lett., 92, 182905 (2008).

301. S. Priya, A. Ando and Y. Sakabe, J. Appl. Phys. 94, 1171 (2003).

302. W. Zhang, N. Kumada, Y. Yonesaki, T. Takei, N. Kinomura, T. Hayashi, M. Azuma, M. Takano, J. Solid State Chem. 179, 4052 (2006).

303. W. Cao and C. A. Randall, J. Phys. Chem. Solids, 57(10), 1499 (1996).

304. C. A. Randall, N. Kim, J. –P. Kucera, W. Cao, and T. R Shrout, J. Am. Ceram. Soc., 81, 677 (1998).

305. D. Damjanovic, J. Am. Ceram. Soc., **88**, 2663 (2005).

306. V. Petkov, V. Buscaglia, M. T. Buscaglia, Z. Zhao, and Y. Ren, Phys. Rev. B **78**, 054107 (2008).

307. V. Bovtun, S. Kamba, S. Veljko, D. Nuzhnyy, J. Kroupa, M. Savinov, P. Vanek, J. Petzelt, J. Hole, M. Kosec, H. Amorin, and M. Alguero, Phys. Rev. B **79**, 014111 (2009).

308. G. Arlt and P. Sasko, J. Appl. Phys. 51, 4956 (1980).

309. L Mitoseriu, V Tura, M. Curteanu, D. Popovici and A. P. Anghel, 8, 500 (2001).

310. R Zuo, J. Fu, S. Lu, and Z. Xu, J. Am. Ceram. Soc., 94 (12), 4352, (2011).

311 H. –Y Park, K. –H Choo, D. –S Park, S. Nahm, H. –G. Lee, D. –H. Kim, J. Appl. Phys., 102, 124101 (2007).

312 Z. Yao, H. Liu, Y. Liu, Z. Li, X. Cheng, M. Cao, H. Hao, J. Ceram. Soc. Jap., 116, 1150 (2008).

313. L. Zhang, X. Wang, W. Yang, H. Liu, X. Yao,J. Appl. Phys., 104, 014104 (2008).

314. T. Maiti, R. Guo and A. S. Bhalla, J. Phys. D: Appl Phys., 40, 4355 (2007).

315. X. G. Tang, X. X. Wang, K. –H. Chew, H. L. W. Chau, Solid Sate Comm., 136, 89, ((2005)

316. W. Wu, D. Xiao, J. Wu, J. Li, J. Zhu, B. Zhau, Cearmic International, (2011), doi:10.1016/j.ceramint.2011.10.079

317. P Fu, Z. Xu, R. Chu, W. Li, G. Zhnag, J. Hao, Mater. Sci. Engg. B, 167**,** 161 (2010).

318. H. Pan, Y. Hou, X. Chao, L. Wei, Z. Yang, Current Applied Phys., 11, 888 (2011).

319. J. Hao, Z. Xu, R. Chu, W. Li, G. Li, Q. Yin, J. Alloys. And Comp., 484, 233 (2009).

320. F. Maura, A. Z. Simoes, C. –A Paskocimas, M. A. Zaghete, J. A. Varela, E. Longo, Mater. Chem. and Phys., 123, 772-775 (2010).

321. D. Gao, K. W. Kwok, D. Lin, H. L. W. Chan, J. Phys. D. Appl. Phys. 42, 035411 (2009).

322. H. Du, W. Zhou, F. Luo, D. Zhu, S. Qu, Y. Li, Z. Pei, J. Appl. Phys., 104, 044104 (2008).

323. Z. Yang, B. Lin, L. Wei, Y. Hou, Mater. Res. Bull., 43, 81 (2008).

324. H. Du, W. Zhou, D. Zhu and L. Fa, S Qu, Y Li, Z Pei, J. Am. Ceram. Soc., 91, 2903 (2008).

325. D. Maurya, N. Wongdamnern, R. Yimnirun, and S. Priya, J. Appl. Phys. 108, 124111 (2010).

326. W. Zhong and D. Vanderbilt, Phys. Rev. Lett., 74, 2587 (1995).

327. J. H. Haeni, P. Irvin, W. Chang, R. Uecker, P. Reiche, Y. L. Li, S. Choudhury, W. Tian, M. E. Hawley, B. Craigo, A. K. Tagantsev, X. Q. Pan, S. K. Streiffer, L. Q. Chen, S. W. Kirchoefer, J. Levy and D. G. Schlom. Nature, 430, 758 (2004).

328. V. V. Lemanov, A. V. Stonikov, E. P. Smirnova, M. Weihnacht, R. Kunze, Solid State Comm., 110, 611-614 (1999).

329. A. M. Glazer, Acta Cryst. B, 28, 3384 (1972).

330. A. M. Glazer, Acta Cryst. A, 31, 756 (1975).

331. M. B. Smith, K. Page, T. Siegrist, P. L. Redmond, E. C. Walter, R. Sheshadri, L. E. Brus, and M. L. Steigerwald, J. Am. Chem. Soc. 130, 6955 (2008).

332. R. E. Cohen, Nature (London) 358, 136 (1992).

333. I. M. Reaney, E. L. Colla and N. Setter, Jpn. J. Appl. Phys., 33, 3984 (1994).

334. U. M. Pasha, H. Zheng, O. P. Thakur, A. Feteira, K. R. Whittle, D. C. Sinclair, and I. M. Reaney, Appl. Phys. Lett., 91, 062908(1)-3(2007).

335. M. N. Rahaman and R. Manalert, J. Eur. Ceram. Soc., 18, 1063 (1998).

336. H. T. Langhammer, T. Müller, R. Böttcher, H.-P. Abicht, Solid State Sciences, **5**, 965-971 (2003).

337. S. H Yoon and Hwan Kim, J. Mater. Res., 16, 1479 (2001).

338. V. Petkov, V. Buscaglia, M. T. Buscaglia, Z. Zhao, and Y. Ren, Physical Review B, 78, 054107, (2008).

339. P. G. Clem, D. A. Payne, and W. L. Warren, J. Appl. Phys. **77**, 5865, (1995).

340. H. Richer, Z. P. Wang, L Ley, Solid State Comm., 39, 625, (1981).

341. M. S. Chen, Z. X. Shen, S. H. Tang, W. S. Shi, D. F. Cui and Z. H. Chen, J. Phys.: Condens. Mater, 12, 7013, (2000).

342. M. Correa, A. Kumar, S. Priya, R. S. Katiyar, J. F. Scott, Phys. Rev. B, 83, 014302, (2011).

343. F. Jiang, S. Kojima, Changlei Zhao, and Chude Feng, Appl. Phys. Lett., 79, 3938, (2011).

344. Aneta Slodczyk and Philippe Colomban, Materials, 3, 5007, (2010).

345. A. Slodczyk, P. Daniel, and A. Kania, Phys. Rev. B 77, 184114, (2008).

346. N. Waeselmann, B. Mihailova, B. J. Maier, C. Paulmann, M. Gospodinov, V. Marinova, and U. Bismayer, Phys. Rev. B, 83, 214104, (2011).

347. A. Slodczyk and P. Colomban, Materials, 3, 5007 (2010).

348. J. Kreisel, P. Bouvier, M. Maglione, B. Dkhil, and A. Simon, Phys. Rev. B, 69, 092104 (2004).

349. A. Abragam and B. Bleaney, Electron Paramagnetic Resonance of Transition Ions (Clarendon, Oxford, 1970).

350. J. W. Orton, Electron Paramagnetic Resonance (An Introduction to Transition Group Ions in Crystal) (London Iliffe Books, Ltd., London, 1968).

351. I. Yamada, M. Nishi, J. Akimitsu, J. Phys. Condens. Matter.8, 2625, (1996).

352. R. –A. Eichel, Phys. Chem. Chem. Phys., 13, 368, (2011).

353. R. A. Eichel, P. Erhart, P. Träskelin, K. Albe, H. Kungl, and M. J. Hoffmann, Phys. Rev. Lett. 100, 095504 (2008).

354. Xiaobng Ren, Nature Materials, 3, 91-94 (2004).

355. L. Chen, Q. Ouyang, C. S. Ganpule, V. Nagarajan, R. Ramesh, A. L. Rovtburd, Appl. Phys.Lett., 84, 254 (2004).

356. Z. Zhao, V. Buscaglia, Massimo Viviani, M. T. Buscaglia, L. Mitoseriu, A. Testino, M. Nygren, M. Johnsson, and Nanni, Phys. Rev. B., **70**, 024107 (2004).

357. A. Von Hippel, Rev. Mod. Phys. **22**, 221 - 237 (1950).

358. Martin T. Dove, Structure and dynamics (Oxford University Press Inc., New York, 2003).

359. G. Arlt, D. Hennings and G. de With, J. Appl. Phys., **58**, 4 (1985).

360. A. S. Sidorkin, *Domain Structure in ferroelectrics and related materials* (Cambridge International Science Publishing, Cambridge, 2006).

361. *Multilayer Electronic Devices*, edited by Jean Jau-Ho, Gupta T. K., Nair K. M., Niwa K., Ceramic Transaction, Vol. 97, The American Ceramic Soc. Westerville, Ohio 43081.

362. D. Hennigs, A. Schnell, and G. Simon, J. Am. Ceram. Soc. 65, 539, (1982).

363. Electronic Industries Association, Specification No RS198.

364. P. Hansen, D. Hennings, and H. Schreinemacher, J. Am. Ceram. Soc. 81, 1369, (1998).

365. H. Kishi, Y. Mizuno, and H. Chazono, Jpn. J. Appl. Phys., 1, 42, (2003).

366. Y. Sakabe, Y. Hamaji, H. Sano, and N. Wada, Jpn. J. Appl. Phys., 41, 5668, (2002).

367. H. Kishi, N. Kohzu, J. Sugino, H. Ohsato, Yoshiaki Iguchi, and T. Okuda, J. Eur. Ceram. Soc., 19, 1043, (1999).

368. G. Arlt, D. Hennings, and G. de With, J. Appl. Phys. 58, 1619, (1985).

369. S. F. Wang and G. O. Dayton, J. Am. Ceram. Soc., 82, 2677, (1999).

370. W. Zhu, S. A. Akbar, R. Asiaie, and P. K. Dutta, Jpn. J. Appl. Phys., 36, 214, (1997).

371. C.-H. Choi, C.-W. Ahn, and S. Nahm, Appl. Phys. Lett. 90, 132905, (2007).

372. Z. Tian, X. Wang, L Shu, T. Wang, Tae-Ho Song, Z Gui, L Li, J. Am. Ceram. Soc., 92, 830, (2009).

373. Wei Xiaoyong, Feng Yujun, and Yao Xi, Appl. Phys. Lett., 83, 2031, (2003).

374. Wei Xiaoyong, Feng Yujun, and Yao Xi, Appl. Phys. Lett., 84, 1534, (2004).

375. Yun Liu, Ray L. Withers, Xiaoyong Wei, John D. Fitz Gerald, J Solid State Chem., 180, 858, (2007).

376. S. G. Lu, Z. K. Xu, and Haydn Chen, Appl. Phys. Lett., 85, 5319, (2004).

377. N. Baskaran and Hua Chang, J Mater Sci.: Mater. El., 12, 527, (2001).

378. N. Maso´, H. Beltra´n, E. Cordoncillo, D. C. Sinclair, A. R. West, J. Am. Ceram. Soc., 91, 144, (2008).

379. Hans Theo Langhammer, Thomas Müller, Rolf Böttcher , Hans-Peter Abicht, Solid State Sci., 5, 965 (2003).

380. K. Keizer and A. J. Burggraaf, Phys. Stat. Sol., 26, 561, (2006).

381. C.-W. Ahn, D. Maurya, C.-S. Park, S. Nahm, and S. Priya, J. Appl. Phys., 105, 114108 (2009).

382. Y. Imry and S. K Ma, Phys. Rev. Lett. 35, 1399, (1975).

383. Tan, Q. and D. Viehland, Phys. Rev. B, 53, 14103, (1996).

384. H.-T. Lue, C.-J. Wu, IEEE Trans. Electr. Dev. 49, 1790, (2002).

385. S. L. Miller and P. J. McWhorter, J. Appl. Phys. 72, 5999, (1992).

386. M. Ullmann, H. Goebel, H. Hoenigschmid, and T. Hander, IEICE Trans. Electr. 83, 1324, (2000).

387. K. H. Kim, J. P. Han, S. W. Jung, and T. P. Ma, IEEE Electron Device Lett. 23, 82, (2002).

388. J. Wu, J. Zhu, D. Xiao and J. Zhu, Appl. Phys. Lett. 91, 212905, (2007).

389. I. Essaoudi, A. Ainane, M. Saber, J. J. de Miguel, Phys. Stat. Sol. (b) 244, 3398, (2007).

390. Y.-Z. Wu, D.-L. Yao, Z.-Y. Li, Appl. Phys. Lett. 91, 1482, (2002).

391. J. F. Scott, Ferroelect. Rev. 21, 1, (1998).

392. R. Waser, U. Böttger, and M. Grossmann, in *Ferroelectric Random Access Memories*, edited by H. Ishiwara, M. Okuyama, and Y. Arimoto (Springer-Verlag, Berlin, Heidelberg, 2004).

393. N. Wongdamnern, N. Triamnak, M. Unruan, K. Kanchianga, A. Ngamjarurojana, S. Ananta, Y. Laosiritaworn, R. Yimnirun, Phys. Lett. A 374, 391, (2010).

394. K. Chi Kao, "Dielectric Phenomena in Solids", Elsevier Academic Press, San Diego, 2004

395. C. Wood, and D. Jena, Polarization Effects in Semiconductors, published by Springer US, DOI 10.1007/978-0-387-68319-5, (2008).

396. R. Kretschmer, and K. Binder, phys. Rev. B 20, 1065, (1979).

397. B. Strukov and A. Levanyuk, Ferroelectric Phenomena in Crystals. Berlin: Spring-Verlag (1998).

398 N. Wongdamnern, N. Triamnak, A. Ngamjarurojana, S. Ananta, Y. Laosiritaworn, and R. Yimnirun, Ferroelectrics 383, 1, (2009).

399. E. Fatuzzo, and W. J. Merz, in *Ferroelectricity*, 1st ed. edited by E. P. Wohlfarth (Wiley, New York, 1967), Vol. 7, Chap. 1, p. 5.

400. W. J. Merz, Phys. Rev. 95, 690, (1954).

401. A. Picinin, M. H. Lente, J. A. Eiras, and J. P. Rino, Phys Rev B 69, 064117, (2004).

402. N. Wongdamnern, A. Ngamjarurojana, Y. Laosiritaworn, S. Ananta, and R. Yimnirun, J. Appl. Phys. 105, 044109, (2009).

403. K. Okazaki and K. Sakata, Electrotech. J. Jpn. 7, 13, (1962).

404. R. E. Cohen, J. Phys. Chem. Solids 61, 139, (2000).

405. M. H. Lente and J. A. Eiras, J. Phys.: Condens. Matter, 12, 5939, (2000).

406. M. H. Lente and J. A. Eiras, J. Appl. Phys. 89, 5093, (2001).

407. S. Takahashi, Ferroelectrics 41, 143, (1982).

408. L.H. Ong, J. Osman, and D.R. Tilley, Phys. Rev. B 65, 134108, (2002).

409. Y.Q. Ma, J. Shen, and X.H. Xu, Solid State Commun. 114, 461, (2000).

410. K.H. Chew, L.H. Ong, J. Osman, and D.R. Tilley, Appl. Phys. Lett. **77**, 17, (2000).

411. K.H. Chew, Y. Ishibashi, F.G. Shin, and H.L.W. Chan, J. Phys. Soc. Jpn. 72, 2364, (2003).

412. N. Wongdamnern, J. Tangsritragul, A. Ngamjarurojana, S. Ananta, Y. Laosiritaworn, R. Yimnirun, Mater. Chem. Phys., (in press).

413. M. Acharyya, Phys. Rev. E 56, 1234, (1997b).

414. B.K. Chakrabarti, and M. Acharyya, Reviews of Modern Physics, 71**,** 847, (1999).

415. N. Wongdamnern, A. Ngamjarurojana, S. Ananta, Y. Laosiritaworn, and R. Yimnirun, Key Eng. Mater. 421, 399, (2010).

416. R. Yimnirun, R. Wongmaneerung, S. Wongsaenmai, A. Ngamjarurojana, S. Ananta, Y. Laosiritaworn, Appl. Phys. Lett. 90, 112908, (2007).